DESIGN, TOLERANCING, AND EXPERIMENTAL CHARACTERIZATION OF DYNAMIC FREEFORM OPTICAL SYSTEMS

by

Jason Allen Shultz

A dissertation paper submitted to the faculty of
The University of North Carolina at Charlotte
in partial fulfillment of the requirements
for the degree of Doctor of Philosophy in
Optical Science and Engineering

Charlotte

2017

Approved by:

_____
Dr. Thomas J. Suleski

_____
Dr. Matthew A. Davies

_____
Dr. Angela D. Davies

_____
Dr. Glenn D. Boreman

_____
Dr. James E. Amburgey

ABSTRACT

JASON ALLEN SHULTZ. Design, tolerancing, and experimental characterization of dynamic freeform optical systems. (Under the direction of DR. THOMAS J. SULESKI)

Although freeform concepts have been considered for many decades, new fabrication capabilities have enabled new classes of optical components and sparked greatly increased interest in freeform optics. Generally defined as surfaces without rotational symmetry, freeform optics enable complex phase variations due to their asymmetry. One approach for freeform optics utilizes multiple freeform surfaces in close proximity. Light transmitted through these surfaces results in a composite wavefront, which is then dynamically changed through controlled relative motions of the freeform surfaces, thereby dynamically changing the overall optical function of the system. These ‘dynamic freeform optics’ offer advantages such as design miniaturization, decreased manufacturing costs, and optical design flexibility. Examples include the varifocal Alvarez lens and a variable diameter Gaussian to flat-top beam shaper. In these cases the output function is varied through relative lateral shifts. The analytical design procedures for these examples have been well documented in previous work. However, previous cases possess inherent design constraints. For example, the classic Alvarez lens has no optical power when the lateral shift is zero, and both examples are limited to rotationally symmetric output functions and lateral shifts along a single axis. A primary objective of this dissertation is to expand design procedures to overcome these constraints for creation of additional novel dynamic freeform optical systems. The optical performance of several example systems is characterized through experimental testing of diamond-machined freeform elements. Furthermore, as the advantages offered by freeform systems are

realized, there remain unknowns regarding performance sensitivity to several potential errors such as opto-mechanical alignment, surface form accuracy, and surface finish quality. To this end, this dissertation also includes individual tolerance analyses on each of these error sources, enabling the determination of meaningful tolerance specifications for dynamic freeform optical systems.

DEDICATION

This dissertation and all of my academic achievements are dedicated to my beloved parents, Jay and Lisa Shultz. Their constant display of respect and compassion towards one another, while always demonstrating a ‘never say never’ work ethic, has taught me so many valuable life lessons. I could never repay them for these life lessons, nor could I ever thank them enough for all of the sacrifices they have made. If only one thing is made clear throughout this entire dissertation, I want it to be how much I truly appreciate everything they have done for me. It is through their unconditional love and endless support that I am able to overcome my toughest challenges and achieve my biggest goals.

ACKNOWLEDGMENTS

First and foremost, I would like to thank my advisor, Dr. Thomas Suleski, for his continued support and guidance through my research and academic studies. Without his dedication and encouragement, I truly could not have succeeded in completing this dissertation. I would also like to thank Dr. Matthew Davies, not only for his many contributions to this research as a committee member, but also for the original inspiration to pursue my doctoral degree in the field of optics. I am also grateful to my other committee members, Dr. Angela Davies and Dr. Glenn Boreman, and to my colleague Dr. Joseph Owen, as their expertise, feedback, and advice were instrumental in completing this dissertation.

I would like to thank Dr. John Troutman and Brian Dutterer for all of the precision fabrication in this research. I would also like to thank several of my lab mates and colleagues who have all contributed in many ways throughout my graduate career: Paul Smilie, Hamidreza Aryan, Steven Glass, Jonathan Koerber, Sara Moein, Daniel Barnhardt, and Dr. Christopher Wilson.

Lastly, I would like to express my utmost appreciation for the financial support provided by several contributors: The II-VI Foundation through the II-VI Foundation Block Gift Program, the Center for Freeform Optics, and Nanohmics Inc. Without their support, this dissertation would not have been possible.

TABLE OF CONTENTS

LIST OF FIGURES

LIST OF TABLES

LIST OF ABBREVIATIONS

a_{2k}	Base component surface coefficients
b_{2k}	Variability component surface coefficients
CA	Clear aperture
CCD	Charge-coupled device
C_d	Correlation degree
CEA	Combined Error Analysis
d	Relative lateral shift
DOF	Depth of focus
EB	Error Budget
EFA	Edge finding algorithm
F	focal length
FTS	Fast tool servo
HeNe	Helium Neon
HS	Height scale
IR	Infrared
IRG26	Chalcogenide glass
MSF	Mid spatial frequency
MTF	Modular transfer function
n_l	Refractive index
O(1-4)	Orientation(no.)
PMMA	Poly (methyl methacrylate)
PSF	Point spread function
P-V	Peak-to-valley

R	Output radius
R(0-4)	Rotational tolerance class
ROC	Radius of curvature
R_z	Rotational tolerance
R_{CV}	Variation coefficient of the output spot shape deviation
RMS	Root mean square
R_{rms}	Root mean square of the output spot shape deviation
S(0-4)	Displacement tolerance class
S_{xy}	Displacement tolerance
SA	Sensitivity analysis
SPW	Spectral plane wave
SS	Slope scale
STS	Slow tool servo
SWLI	Scanning white light interferometry
T(0-4)	Tilt tolerance class
T_{xy}	Tilt tolerance
U_{CV}	Variation coefficient of the output spot uniformity
U_{rms}	Root mean square of the output spot uniformity
$z(r)$	Desired composite surface
z_b	Base component
Z_c	Composite surface
z_f	Freeform surface
z_v	Variability component

CHAPTER 1: INTRODUCTION

1.1 Background and Motivation

Although freeform concepts have been considered for many decades, new fabrication capabilities have enabled new classes of optical components and sparked greatly increased interest in freeform optics. Generally defined as surfaces without rotational symmetry, freeform optics enable complex phase variations due to their asymmetry. Furthermore, freeform surfaces have an intriguing advantage enabling the manipulation of a given input into a desired output form [1-4]. Example applications which utilize freeforms include aberration correction [5-7], extending depth of field [8-11], beam collimation and beam shaping [12-14], illumination and projection systems [15-24], and conformal optics applications [25-27].

Another approach for freeform optics utilizes multiple freeform surfaces in close proximity. Light transmitted through these surfaces results in a composite wavefront; the overall optical function of the system is dynamically changed through controlled relative motions of the freeform surfaces. These ‘dynamic freeform optics’ offer advantages such as design miniaturization, decreased manufacturing costs, and optical design flexibility. This concept is demonstrated in Fig. 1.1 for relative lateral shifts.

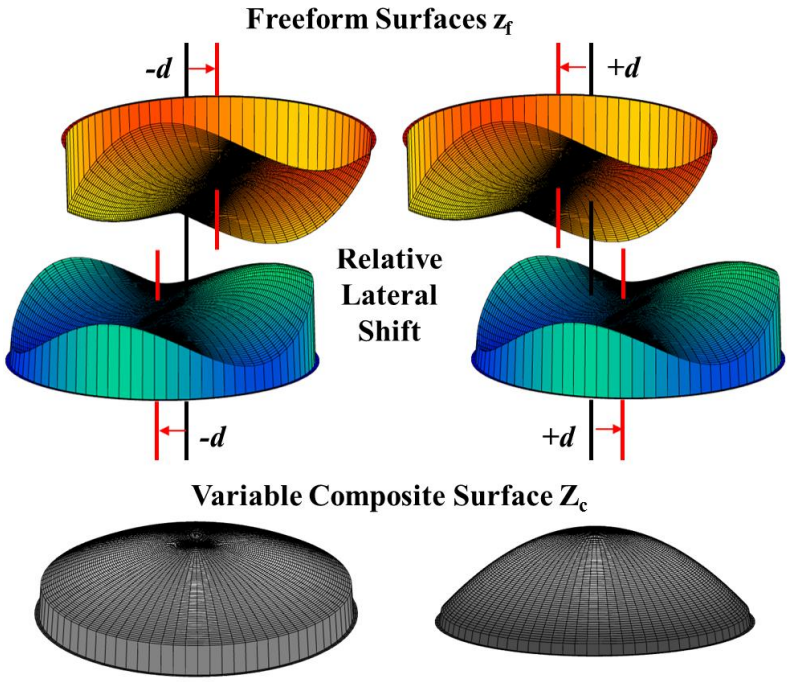

Fig. 1.1: General demonstration of two freeform surfaces with a controlled relative lateral shift, creating a variable composite surface.

The Alvarez lens and Lohmann lens are classic examples in this genre of optical systems, comprised of two superimposed freeforms with matching cubic surface profiles [28-30]. In these specific examples, a refractive lens with a variable focal length is achieved by laterally shifting the freeform components by equal amounts in opposite directions along a single designated axis. Alvarez lens prototypes have been created for visible light and fabricated using diamond turning [31-33]. Smilie *et al*. expanded this concept into the mid and long wave infrared (IR) through the analytical design, fabrication, and experimental characterization of a diamond milled Alvarez lens [34, 35].

Since the introduction of this concept, there have multiple designs presented which incorporate laterally or rotationally translated freeforms for improved varifocal imaging systems [36-43], and variable aberration generation or correction [5, 6, 44-48]. Smilie *et al.* [35, 49-51] further expanded on this design concept through an analytical design for a

novel variable diameter beam shaper. For this device, the energy from an incident source with Gaussian form is redistributed to an output spot with uniform irradiance, defined as a step-function. Varying output diameters are achieved while maintaining the uniform irradiance distribution at a target location by utilizing two laterally shifted freeforms, similar to the Alvarez lens. Fabrication and experimental characterization of this device were recently continued and are presented in this dissertation [51, 52].

While the design procedures for the Alvarez lens and beam shaping examples offer insights to the overall system design, they also have inherent limitations. For example, the analytical design procedure for the 'standard' Alvarez lens results in no optical power when there is no lateral shift in the system, and the composite surface acts a converging lens for negative shifts and as a diverging lens with positive shifts. Researchers have reported limited examples where the systems had optical power at zero relative shift by presetting a lateral offset of the lens apertures [53-55] or through optimization using optical simulation [56] where the procedure was not well defined. A consequence to defining the output irradiance of the variable beam shaper as a step-function is undesirable spikes of energy at the edges of the output spot from the Gibb's phenomenon [57, 58]. A solution to this problem is to implement an output irradiance profile described as a super-Gaussian function as presented by Shealy and Hoffnagle [59]. However, since this is a continuous and more complex function, the analytical solutions previously used to determine the appropriate composite surface do not apply and a more general numerical approach is required. With this in mind, an extended design approach is considered, implementing an extended numerical analysis to avoid the constraints for both devices. This dissertation demonstrates this design procedure through creation of a

super-Gaussian variable diameter beam shaper [50, 51], and an Alvarez lens with a shifted focal range [60]. Fabrication and experimental characterization of these devices are also presented.

The previous designs are also limited to output functions with radial symmetry in which the *x* and *y* parameters are varied simultaneously through a lateral shift along a single axis. For example, it has been demonstrated [42, 61-65] that shifting the Alvarez lens in the orthogonal direction inherently creates an astigmatic function. However, the variability of the *x* and *y* focal lengths are interdependent. As mentioned by Lohmann [30] and later demonstrated by Barbero [42], two crossed variable cylindrical lens pairs create a varifocal lens with appropriate lateral shifts, but independent *x* and *y* output functions were not demonstrated. A diffractive varifocal toric lens has been reported [66]; however, similar to other work, the design procedure was not reported. With this in mind, we consider cases where the output is no longer radially symmetric and cases where *x* and *y* dimensions of the optical output are varied independently of each other. We present three novel optical systems; a variable square output beam shaper with a 1-D shift [51], a variable rectangular output beam shaper with a 2-D shift [51], and a variable toric lens with a 2-D shift [67].

In addition to creating and characterizing novel optical systems, several different tolerance specifications are also investigated in this work. While dynamic freeform optical systems enable variable and compact functionality, the overall optical performance depends on the relative positioning and shape accuracy of the freeform surfaces. The ability to determine specific tolerance specifications precludes the over-tolerancing of the system, where overly tight tolerances could unnecessarily increase

manufacturing costs and tolerances that are too loose could result in poorly functioning systems.

Since there are multiple elements in these systems, tolerances on relative displacement, rotation, and tilt between the surfaces must be understood as part of the design process. As shown in other work [68-71], tolerancing typically utilizes a probabilistic Monte-Carlo approach enabling cross-communication between different errors in the system. However, Monte Carlo methods are computationally intensive and inefficient for systems with large numbers of variables. Tolerancing freeform elements with this kind of approach presents several challenges, as some assumptions made are not valid due to the lack of rotational symmetry. We present a simplified deterministic procedure for defining optomechanical tolerances for dynamic freeform optical systems, demonstrated using imaging and non-imaging examples [72, 73].

The overall optical performance also depends on the surface form accuracy. Surface form error is a low frequency surface deviation from a desired prescription. Related tolerance methods and specifications for rotationally symmetric optical surfaces are well-established through the international ISO 10110 standard [74, 75], which has been recently updated to include freeform surfaces [76]. Researchers have explored ways to develop surface form error specifications for freeforms within the ISO standards [77-81], although much of this previous work is application-specific and does not pertain directly to dynamic freeform systems. In this dissertation, we present a tolerance analysis to determine meaningful surface form accuracy specifications pertinent to both optical design and manufacturing. Both imaging and non-imaging examples of dynamic freeform systems are presented.

Lastly, the fabricated surface finish texture also has a significant impact on overall system performance. Each fabrication technique leaves residual mid-spatial frequency (MSF) surface errors that degrade the surface finish quality, introducing undesired optical artifacts. Though surface form errors and MSF errors are both a product of manufacturing errors, MSF errors are typically periodic with smaller feature sizes, thus requiring different simulation methods to account for diffraction and interference effects. Harvey and Tamkin *et al.* previously showed that the total surface finish can be decomposed into known segments where the effects from each segment are simply combined with one another [82-84]. As with surface form errors, researchers have previously explored the effects of some MSF errors on optical performance e.g. [82-86], but these studies have generally been limited to radially symmetric lenses in imaging systems. With this in mind, we investigate the optical effects of MSF errors on imaging and non-imaging examples, and compare approximated MSF errors resulting from diamond turning and diamond milling [87, 88].

1.2 Dissertation outline

The theory and analytical design procedure used by Smilie *et al.* to create the step-function variable diameter beam shaper are reviewed in Chapter 2. Additionally, Chapter 2 discusses the different methods used to fabricate refractive freeform elements as well as the optomechanical design used for experimental testing. The initial fabrication and experimental test results of the variable beam shaper are presented in Chapter 3, where the overall functionality was confirmed, but the uniformity and overall quality of the output spots were poor. The reason for this poor output spot quality is investigated and discussed. Chapter 3 also introduces a second variable diameter beam shaper with a

super-Gaussian output function. The changes made in this design procedure, along with other key design alterations, are discussed. Fabrication and experimental test results from this system are presented, where the output spots were much improved. Using the same numerical design procedure as for the super-Gaussian beam shaper, an Alvarez lens with a shifted focal range is presented and compared to a ‘standard’ Alvarez lens in Chapter 4. Fabrication and experimental results of this device are also presented.

Chapter 5 presents additional novel dynamic freeform optical systems with non-rotationally symmetric outputs using both one and two dimensional lateral shifts. The theory and analytical design procedure of a square output beam shaper is discussed in detail. Following this, the design of a variable square beam shaper with a 1-D shift and the design of a variable rectangular beam shaper with a 2-D shift are presented. Additionally, the design of a variable toric lens with a 2-D shift is presented.

Chapter 6 discusses the importance of optomechanical tolerancing. Several different performance metric options suitable for these devices are discussed in detail along with a simplified optomechanical tolerancing procedure. This procedure is demonstrated using the Alvarez lens with a shifted focal range from Chapter 4 and the super-Gaussian variable diameter beam shaper from Chapter 3.

A tolerance analysis regarding surface form accuracy is presented in Chapter 7. Different types of surface form error along with several assumptions made throughout the analysis are discussed in detail. This tolerance analysis is demonstrated using the same examples employed in Chapter 6. Additionally, a method for communicating tolerance specifications between a designer and a manufacturer is presented.

The performance effects of residual mid spatial frequency (MSF) surface errors are investigated in Chapter 8. The different characteristic MSF errors resulting from synchronized diamond turning and diamond milling fabrication processes are examined and compared. The optical effects from these MSF errors are demonstrated using a single element imaging lens along with a single element square beam shaper. Relations between these MSF errors and meaningful machining parameters are made, and methods to determine machining parameters balancing cost and performance are discussed.

Chapter 9 summarizes the results from the research performed in this dissertation. Suggestions are given for continued research in the area of dynamic freeform optical systems.

This work is a cooperative effort between the Center for Optoelectronics and Optical Communications and the Center for Precision Metrology at the University of North Carolina at Charlotte. This collaboration takes advantage of available design, fabrication, and testing capabilities to produce and characterize novel dynamic freeform optics.

CHAPTER 2: METHODS AND PROCEDURES

2.1 Design overview of a variable diameter beam shaper

Much of the work discussed in this dissertation was heavily motivated by Paul Smilie's research on the variable diameter beam shaper [35]. Therefore, it is essential to review the analytical design process and design parameters used to create this device.

2.1.1 Introduction

One function of a beam shaper is to redistribute the energy from an incident source with Gaussian form to an output with uniform irradiance. Beam shaping devices of this type are beneficial to several applications such as communications, machining, lithography, medical treatment, scanning, printing, illumination, and holography [89-100]. Such beam shaping devices have been around since 1960 and have expanded over time [14, 101-109]. These devices are static, with a fixed shape determined from the input irradiance and the desired output. Laskin *et al.* [110] later expanded on this concept by creating a variable output using a fixed beam shaper in combination with additional zoom lenses. In contrast, Smilie *et al.* [35, 49] created an analytical design for a novel variable diameter beam shaper utilizing two laterally shifted freeform surfaces. In this particular device, the two freeform elements are shifted laterally by equal amounts d in opposite directions parallel to the x-axis, where relative shifts result in varying output diameters while maintaining the uniform irradiance distribution. Fig. 2.1 shows a

schematic demonstrating a fixed single element beam shaper as well as the variable diameter beam shaper with two freeform elements.

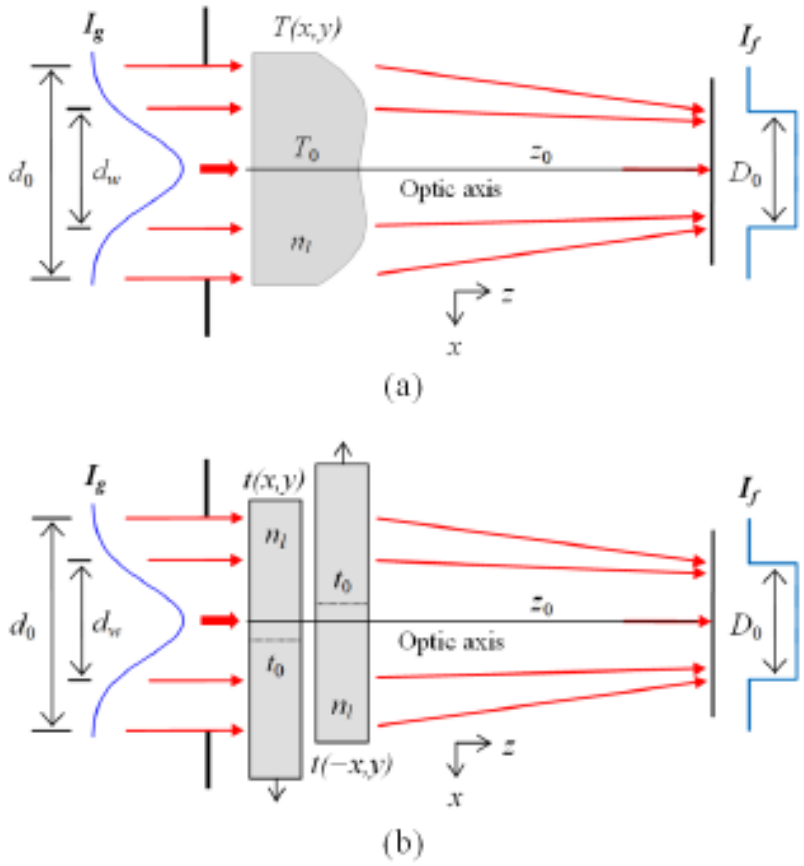

Fig. 2.1: Schematic illustrations comparing (a) a fixed single element beam shaper and (b) the variable diameter beam shaper with two freeform elements.

2.1.2 Analytical design procedure for the variable diameter beam shaper

The general analysis used by Smilie *et al.* began with design of a single element beam shaper, referred to as the desired composite surface *z(r)*. This composite surface represents the base optical function performed by the eventual combination of two appropriately defined freeform surfaces. In order to determine the height profile of the desired composite surface, a ray mapping technique was implemented. This utilizes energy conservation from the input beam $I_1(r)$ to the output beam $I_2(R)$, given by

$$\int_0^{r_0} I_1(r) r dr = \int_0^{R_o} I_2(R) R dR, \tag{2.1}$$

where r is the input radial coordinate and R is the output radial coordinate. Assuming an input irradiance of Gaussian form with waist radius w_0 and a uniform output irradiance defined as a step-function, the integrals can be solved analytically, yielding

$$\int_0^{r_0} I_1(r) r dr = \int_0^{r_o} exp[-2(r/w_0)^2] r dr = \frac{{w_o}^2}{4}\left[1 - exp[-2(r_o/w_o)^2]\right], \tag{2.2}$$

$$\int_0^{R_o} I_2(R) R dR = \frac{1}{2} I_o {R_o}^2. \tag{2.3}$$

Setting Eq. (2.2) equal to Eq. (2.3) and solving for I_0 yields the constant output irradiance for which conservation of energy is achieved:

$$I_o = \frac{{w_o}^2}{2{R_o}^2}\left[1 - exp[-2(r_o/w_o)^2]\right]. \tag{2.4}$$

Next, Eq. (2.2) is again set equal to Eq. (2.3), where this time the output radial coordinate R is solved for while the input radial coordinate r is left as a variable. This inherently creates the aforementioned ray mapping function, given by

$$R(r) = \left[\frac{{w_o}^2}{2I_o}\left[1 - exp[-2(r/w_o)^2]\right]\right]^{1/2}. \tag{2.5}$$

Several rays are then mapped from the input to the output at the target plane, located a distance z_0 away from the center of the beam shaping surface, and used to determine the corresponding relationship between radial coordinates, as demonstrated in Fig. 2.2.

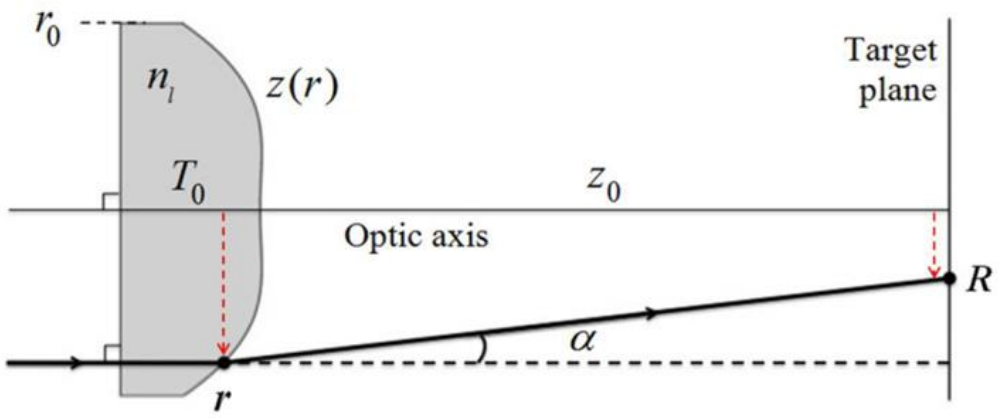

Fig. 2.2: Illustration of the ray mapping concept used to develop the relationship between the input radial coordinate *r* and the output radial coordinate *R*.

Using this coordinate relationship in combination with Snell's law and other geometrical considerations, it was shown in [35] that the slope of the desired composite surface *dz/dr* can be equated to a differential equation dependent on the input radial coordinate *r*, target distance z_0, and material refractive index n_l. This differential equation is given by,

$$\frac{dz}{dr} = \frac{R - r}{(n_1 - 1)(z_o - z(r))}. \tag{2.6}$$

This equation can be solved numerically, creating a list of surface data points representing the desired composite surface. This composite surface can be represented by a general polynomial equation, given by

$$z(r) = \sum_{k=1}^{n} a_{2k}(r)^{2k}. \tag{2.7}$$

The polynomial coefficients a_{2k} are determined in MATLAB® by numerically fitting the surface data from Eq. (2.6) to Eq. (2.7), dependent on the desired input and output parameters. It should be noted that this can be any radially symmetric optical function, as

long as it can be accurately described using this general polynomial equation. However, as discussed in further detail in Chapter 5, this base composite surface can be altered such that asymmetric output functions can also be realized.

Now that a method to define a composite beam shaping surface has been established, the next step is to define the freeform surfaces that create the composite form. In order to develop this general freeform approach, Smilie *et al.* developed a process which implemented the combination of two 'components' with different purposes and functions. The first is the base component z_b which determines the system function with zero lateral shift (d = 0) of the two freeform surfaces. The second is a 'variability' component z_v which changes the composite surface for non-zero shifts. It is the combination of the base and variability components which create the freeform surfaces, demonstrated in Fig. 2.3.

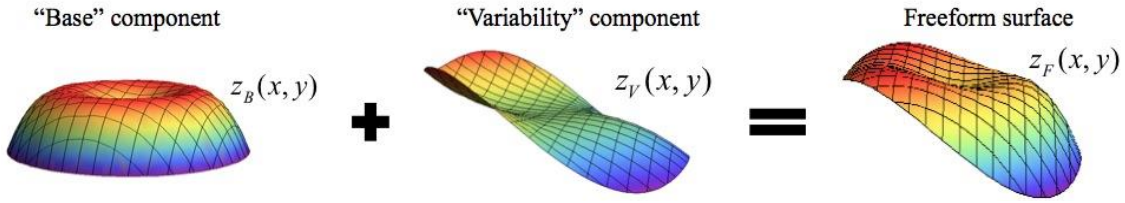

Fig. 2.3: Decomposition of freeform surface into base component and variability component.

The two freeform surfaces z_f involved in this design are flipped 180^o relative to each other along the x-axis and aligned in close proximity along the optical axis (the separation is assumed to be negligible). The two freeforms combine to form the composite surface, defined as,

$$\begin{aligned} Z_c(x,y) &= z_f(x,y) + z_f(-x,y) \\ &= z_b(x,y) + z_v(x,y) + z_b(-x,y) + z_v(-x,y). \end{aligned} \tag{2.8}$$

Looking at Eq. (2.8) more closely, the base component is defined to be rotationally symmetric, meaning $z_b(x,y) + z_b(-x,y) = 2z_b(x,y)$. Because this handles the specific case where there is no lateral shift, the base component is defined using Eq. (2.7), where it is halved because of the eventual combination of the two freeforms. Hence, the base component is defined as,

$$z_b(x,y) = \sum_{k=1}^{n} \frac{1}{2} a_{2k}(x^2+y^2)^k. \tag{2.9}$$

The variability component is more difficult to define, partly due to the fact that it is not rotationally symmetric. As presented by Palusinski [44] for creation of variable aberration generators, when laterally shifting freeform elements, the desired composite surface is the derivative of the freeform surface with other terms. With this in mind, the variability component is defined as the integral of the general polynomial equation,

$$z_v(x,y) = \int z(x,y)dx = \sum_{k=1}^{n} b_{2k} \int (x^2+y^2)^k \, dx, \tag{2.10}$$

where b_{2k} represents the variability coefficients. With both the base and variability components defined, the general freeform surface can be mathematically described as,

$$z_f(x,y) = \sum_{k=1}^{n} \frac{1}{2} a_{2k}(x^2+y^2)^k + \sum_{k=1}^{n} b_{2k} \int (x^2+y^2)^k dx + c_o x, \tag{2.11}$$

where c_0 is a ‘tilt’ term used to minimize the overall sag of the surface without affecting the optical properties.

The next step is to determine the b_{2k} coefficients found in Eq. (2.10) using Eq. (2.8) and Eq. (2.11), and introducing a lateral shift *d* along the *x*-axis. It should be noted that the lateral shift *d* represents the amount of displacement for one freeform lens, meaning the total displacement between both freeform lenses is *2d*. With this in mind, the combined composite surface with the introduced lateral shifts is given by,

$$\begin{aligned} Z_c(x,y,d) &= z_f(x+d,y) + z_f(-(x-d),y) \\ &= \sum_{k=1}^{n} [a_{2k} + 2b_{2k}d](x^2+y^2)^k + \varepsilon(x,y,d) \\ &= \sum_{k=1}^{n} a_{2k}{}' \, (x^2+y^2)^k + \varepsilon(x,y,d), \end{aligned} \tag{2.12}$$

where $\varepsilon(x,y,d)$ represents the combined 'error' terms that are a byproduct of the integration. These error terms are negligible for small lateral shifts, though larger shifts can introduce error terms with more significant impacts on performance.

From Eq. (2.12), the curvature/power of the composite surface is now a function of lateral shift, meaning the 'overall' composite surface coefficients a_{2k}' can be described as

$$a'_{2k}(d) = a_{2k} + 2b_{2k}d. \tag{2.13}$$

As shown in Eq. (2.13), we note that when $d = 0$, the b_{2k} terms go away meaning the composite surface is described solely by the base coefficients a_{2k}, as expected. Further, for non-zero shifts, the composite surface coefficients a_{2k}' have a linear relationship with lateral shift *d*. To develop this linear relationship, several different desired base composite surfaces are created with incremental changes within a defined range of output parameters (output spot diameters), ultimately providing a catalog of varying composite surface coefficients. From this catalog, the average change in surface coefficients Δa_{2k} is

determined for a given linear change in output spot diameter. This average change can be related to the lateral shift by

$$b_{2k} = \frac{\Delta a_{2k}}{2\Delta d}, \tag{2.14}$$

where Δd is the defined amount of lateral shift corresponding to the given change in output spot diameter. This inherently assumes that the desired base composite coefficients vary linearly in correspondence with the linear variation in lateral shift, which is later shown to be a valid assumption.

2.1.3 Optical design of the variable diameter beam shaper

Using this design process, Smilie designed a variable output diameter beam shaper with a round, step-function output irradiance distribution [35, 49]. The waist diameter of the Gaussian input was defined to be 6 mm at a wavelength of 632.8 nm, and the output spot diameter was chosen to be 5 mm for the case with no relative shift in the system (d = 0). The material chosen for the 12 mm diameter freeform surfaces was poly (methyl methacrylate) (PMMA) (n_l = 1.49). The target distance, where the incident light is 'focused' to a uniform distribution, was defined to be 150 mm. The variability component was determined by first defining the output diameter range to be from 3 mm to 7 mm over a lateral shift range +/-300 μm. This means that with every lateral shift of Δd =150 μm will result in a 1 mm change in output diameter. With these design parameters in mind, multiple fixed beam shapers with different output spot diameters were designed. Fig. 2.4 shows each surface profile on the same scale across the 12 mm aperture.

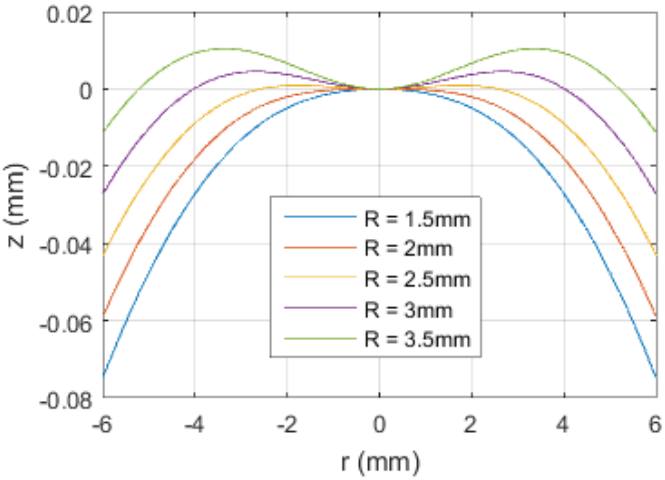

Fig. 2.4: Surface height profiles for multiple fixed beam shapers with various output spot diameters.

For each surface height profile, a set of polynomial coefficients was fit to Eq. (2.7). Each set of coefficients are listed in Table 2.1 along with the average change, Δa_{2k}.

Table 2.1: Surface coefficients for five output spot diameters and the associated changes.

a_{2k} values (mm^{-2k+1})	**Output Diameter**					**Avg. Δa_{2k} (mm^{-2k+1})**
	3 mm (*d*=300um)	**4 mm (*d*=150um)**	**5 mm (*d*=0)**	**6 mm (*d*=-150um)**	**7 mm (*d*=-300um)**	
a_2	-1.99E-03	-3.88E-04	1.22E-03	2.82E-03	4.42E-03	-1.60E-03
a_4	-1.33E-04	-1.78E-04	-2.22E-04	-2.67E-04	-3.11E-04	4.45E-05
a_6	4.09E-06	5.45E-06	6.81E-06	8.17E-06	9.53E-06	-1.36E-06
a_8	-9.87E-08	-1.32E-07	-1.64E-07	-1.97E-07	-2.30E-07	3.28E-08
a_{10}	1.70E-09	2.27E-09	2.83E-09	3.39E-09	3.96E-09	-5.64E-10
a_{12}	-1.84E-11	-2.45E-11	-3.06E-11	-3.67E-11	-4.27E-11	6.09E-12
a_{14}	9.23E-14	1.23E-13	1.53E-13	1.84E-13	2.14E-13	-3.05E-14

This variable beam shaper is designed to have a 5 mm output diameter when there is no lateral shift in the system; therefore, the corresponding coefficients will inherently be defined as the base component coefficients (a_{2k}). The average change in coefficients Δa_{2k} per unit change in lateral shift (Δd = 150 μm) are then used in Eq. (2.14) to determine the variability coefficients b_{2k}. Table 2.2 shows the resulting a_{2k} and b_{2k} coefficients for this design.

Table 2.2: Freeform surface coefficients for variable diameter beam shaper.

Order (k)	a_{2k} Values (mm^{-2k+1})	b_{2k} values (mm^{-2k})
1	1.2153E-03	-5.3454E-03
2	-2.2248E-04	1.4828E-04
3	6.8131E-06	-4.5348E-06
4	-1.6435E-07	1.0930E-07
5	2.8309E-09	-1.8807E-09
6	-3.0574E-11	2.0289E-11
7	1.5346E-13	-1.0174E-13

A performance sweep was then performed on the tilt term to find the point at which the sag of the freeform surface was at a minimum. The resulting tilt term of 0.0484 decreased the sag from 695 µm to 291 µm over the 12 mm aperture diameter. Minimizing the sag make the surfaces easier to manufacture and also allows the two surfaces to be closer together, ultimately minimizing the potential error caused by the stand-off distance. The resulting freeform surface is shown in Fig. 2.5 along with the corresponding base and variability component.

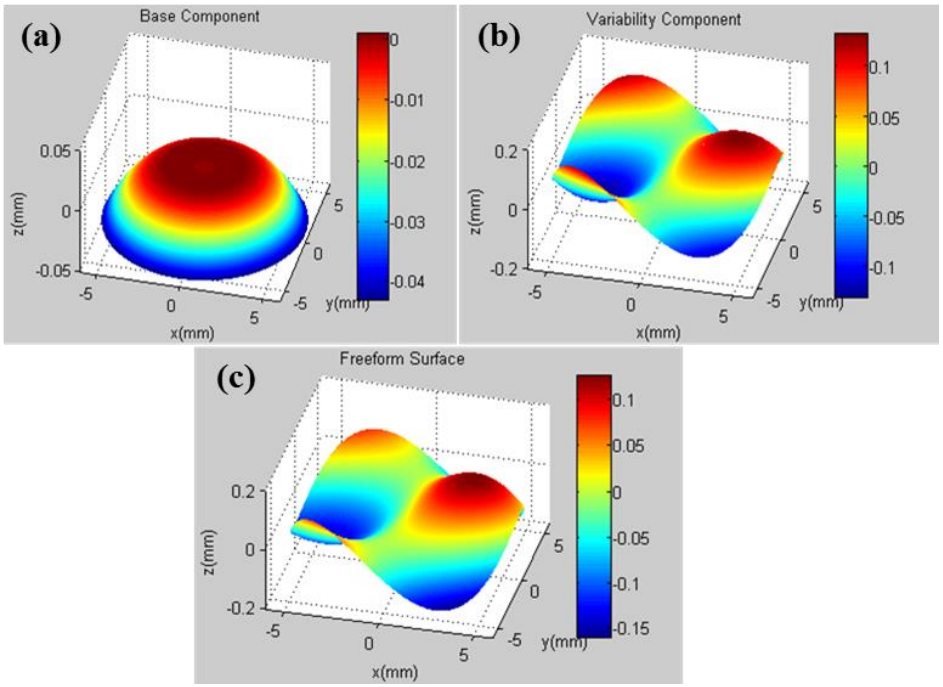

Fig. 2.5: Surface plots showing the (a) base component, (b) variability component, and (c) one of the two freeform surfaces.

2.1.4 Optical modeling of a variable diameter beam shaper

VirtualLab™, a wave-based physical optical simulation software package was employed to simulate this dynamic optical system. In the following simulations, the freeform surfaces were modeled as two plano-freeform surfaces using the surface coefficients defined above. The stand-off distance between both freeform surfaces was set to 200 μm. The combined SPW/Fresnel propagation operator [111] was used as the propagation method for all simulations. The sampling distance of the output light field was set to 9 x 9 μm over a 9 x 9 mm window. The "Beam Parameters" function was used to determine the diameter of the output spot relative to the centroid at the target location (150 mm), which was taken to where the irradiance fell to zero. Table 2.3 shows the constant input diameter with the expected and simulated output diameters relative to the corresponding lateral shift.

Table 2.3: Predicted and modeled input and output spot diameters for several amounts of lateral shift.

Lateral Shift d (μm)	Input diameter (mm)	Predicted Output diameter (mm)	VirtualLab™ Output diameter (mm)
-300	6.0	7.0	6.991
-150	6.0	6.0	5.988
0	6.0	5.0	4.988
150	6.0	4.0	3.982
300	6.0	3.0	2.950

The predicted results were in good agreement with simulated results in VirtualLab™; however, the output diameters do not say anything about the uniformity of the output spot. For this, the "Virtual Screen" detector in VirtualLab™ was used with the same sampling parameters and propagation method as before to simulate an image of the

output spot. Fig. 2.6 shows the input spot, displaying its Gaussian irradiance distribution, along with the simulation results for output spots with lateral shifts of 0 µm, +/-150 µm, and +/-300 µm.

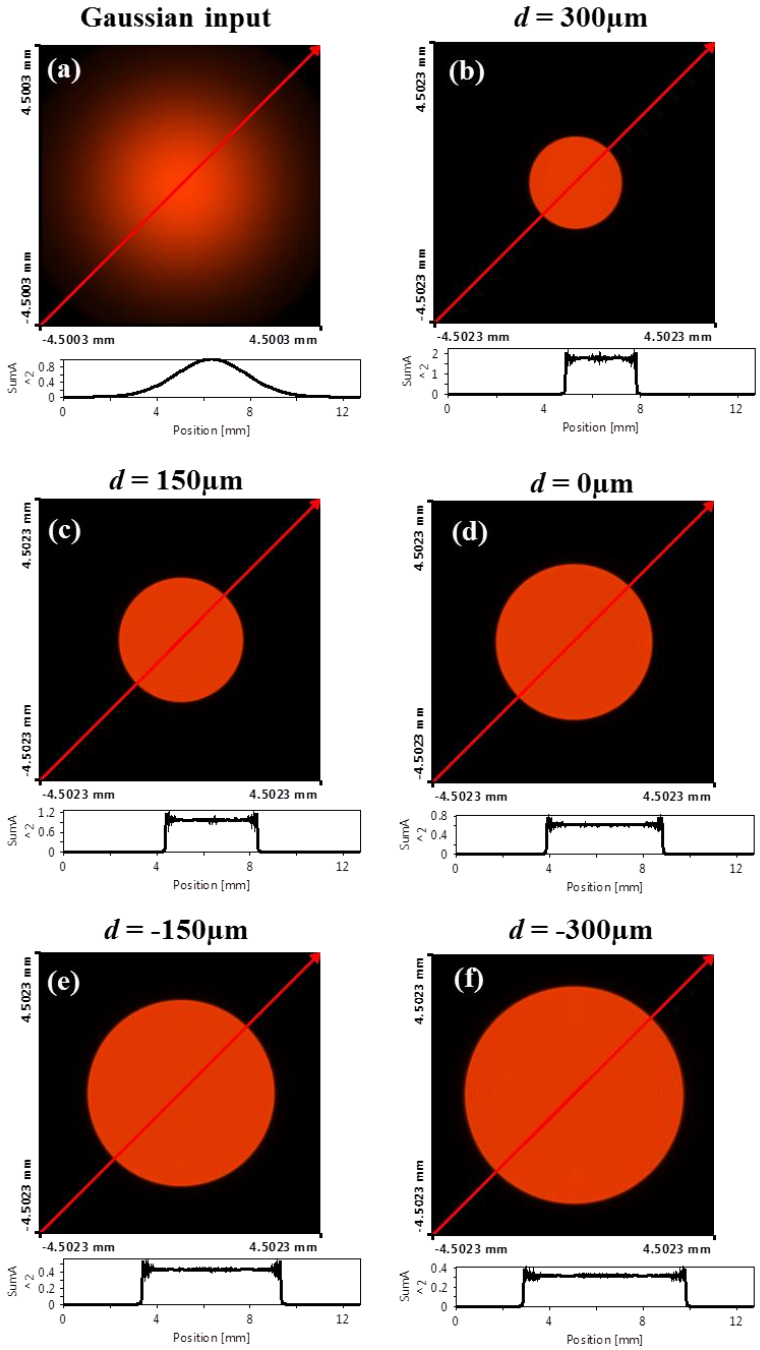

Fig. 2.6: Six VirtualLab™ images and 1-D profiles, (a) Gaussian input, (b) d = 300 µm, (c) d = 150 µm, (d) d = 0.0 mm, (e) d = –150 µm, and (f) d = –300 µm.

From the simulation results, the output spots are highly uniform along the cross section, suggesting the system works as intended; however, we note the undesired spike of energy along the edges of the spot. This is formally known as the Gibb's phenomenon [57, 58] which is a result of using a step function for the output irradiance distribution. To combat this issue, a super Gaussian function [59] may be employed for its desired output irradiance distribution, where the output distribution is described in a continuous manner with controlled edge steepness. This approach is discussed in Chapter 3.

2.2 Fabrication of refractive freeforms

From a manufacturing perspective, the technology used for different optical fabrication methods has advanced tremendously over recent years, expanding overall capabilities while also increasing surface accuracy. Optical grinding and polishing methods are often viewed as 'standard' examples for material removal; however, these techniques are not always conducive to freeform manufacturing. In contrast, diamond machining allows for great design flexibility over a wide range of scales while still offering a high level of surface form accuracy [112, 113]. In conventional diamond turning, an optical workpiece on a rotating spindle is cut by a diamond tool at varying depths, resulting in a radially symmetric surface. Synchronized modulation of the tool depth with the rotating spindle (slow tool servo (STS) or fast tool servo (FTS)) [112, 113] enables cutting of non-symmetric surfaces, illustrated in Fig. 2.7(a). In contrast, diamond milling involves a non-rotating workpiece that is laterally translated relative to a rotating diamond tool (endmill) at varying depths, illustrated in Fig. 2.7(b). In each method, the 'step-over' is a primary machining parameter that has a direct impact on surface finish. For diamond turning the step-over is equivalent to the lateral tool feed rate per revolution of the

workpiece, and for diamond milling the step-over is the lateral translation made between each cutting pass. A smaller step-over results in a better surface finish, but also results in an increase in the machine time which can potentially be costly.

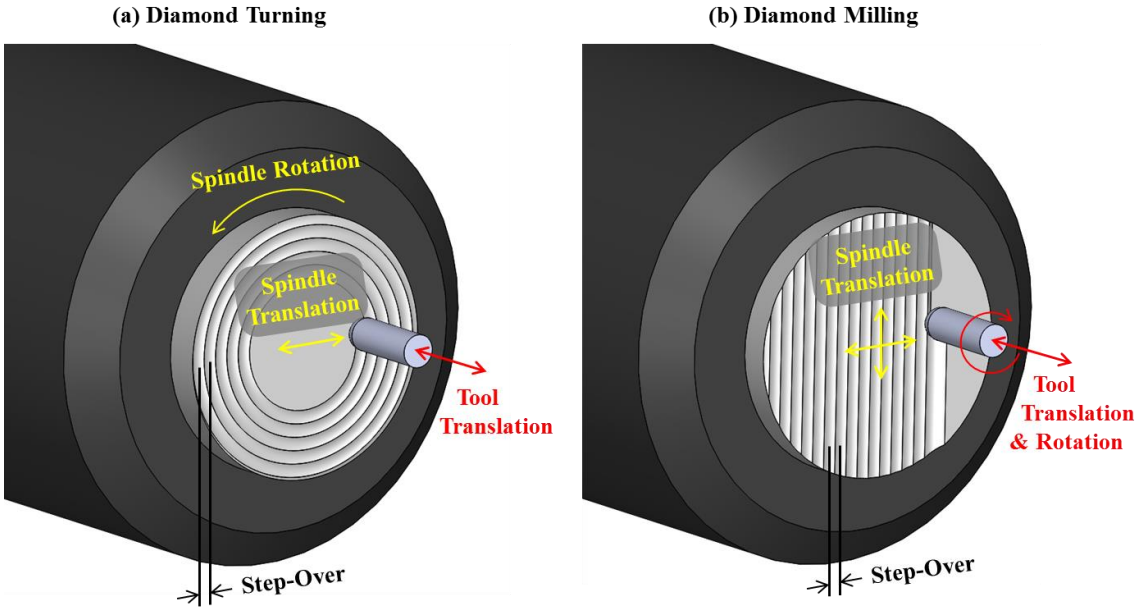

Fig. 2.7: Illustration of material removal methods through the use of (a) diamond turning and (b) diamond micro-milling.

Although both methods possess the ability to fabricate freeform surfaces, they each have relative advantages and disadvantages. Diamond turning has been more commonly used to fabricate freeform surfaces [113-117]. While FTS diamond turning is significantly quicker, providing a major advantage in terms of machine time and relative costs, the maximum allowable surface deviation is smaller than what can be achieved with STS or diamond milling. Additionally, for surface features with high aspect ratios, there can be access problems based on tool geometries for diamond turning that would not exist for diamond milling. Thus, using a diamond milling approach enables, for example, fabrication of monolithic alignment features with freeform optical surfaces. With these advantages and disadvantages in mind, both STS diamond turning and

diamond milling are used to produce the freeform optics presented in this dissertation. Diamond milling is used to fabricate both of the variable PMMA beam shapers presented in Chapter 3. An Alvarez lens with a shifted focal range is fabricated using STS diamond turning in IRG26 chalcogenide glass [118], presented in Chapter 4. All the diamond machining discussed in this dissertation was performed on the Moore Nanotech® 350FG (Fig. 2.8) by students and staff in the UNC Charlotte Center for Precision Metrology. This is a five axis freeform generator with three linear axes (X, Y, and Z) and two rotary axes (B and C).

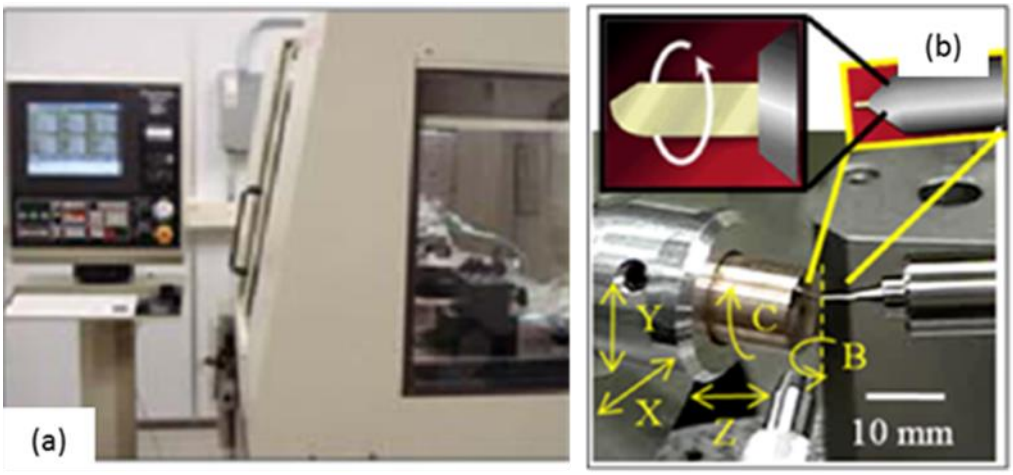

Fig. 2.8: (a) The Moore Nanotech® 350 FG and (b) the spindle head with three linear axes (X, Y, and Z) and two rotary axes (B and C).

In each case, fabrication of the freeform elements began with two diamond turned disks of the respective material, each with a 25.4 mm diameter and an initial thickness of 3 mm. A point cloud describing the respective freeform surface was generated in MATLAB® and used to establish the custom toolpath. The freeform surface was then machined into the substrate; where the area outside of the freeform surface diameter d_0 was machined down further to create a pedestal, illustrated in Fig. 2.9. At the same time, during the fabrication process, mechanical alignment features (slots) were machined into

the pedestal, also illustrated in Fig. 2.9. These monolithic slots were designed to coincide with alignment features in the experimental test setup.

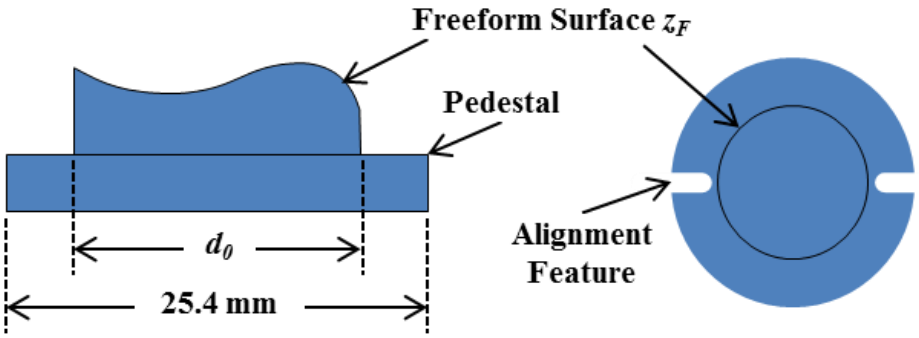

Fig. 2.9: Illustration of the freeform fabrication concept, showing the freeform surface on a pedestal along with the monolithic slots serving as a rotational alignment feature.

2.3 Optomechanical design for experimental tests

A refractive IR Alvarez lens was designed, diamond machined, and experimentally characterized in previous work [34, 35]. A custom mounting assembly was designed and machined by Brian Dutterer for this testing. The optomechanical assembly included two mounting brackets, two mounting rings, and two Newport® M-461 three-axis translation stages enabling linear shifts with 10 μm resolution, shown in Fig. 2.10. The mounting rings were specifically designed to minimize any applied stress in order to prevent any surface warping. Additionally, two locating pins were implemented on each of the mounting brackets, coinciding with monolithic slots machined in the freeform elements to ensure proper rotational alignment. For the examples presented in this dissertation, each of the freeform elements were designed and fabricated such that the existing optomechanical setup could again be utilized.

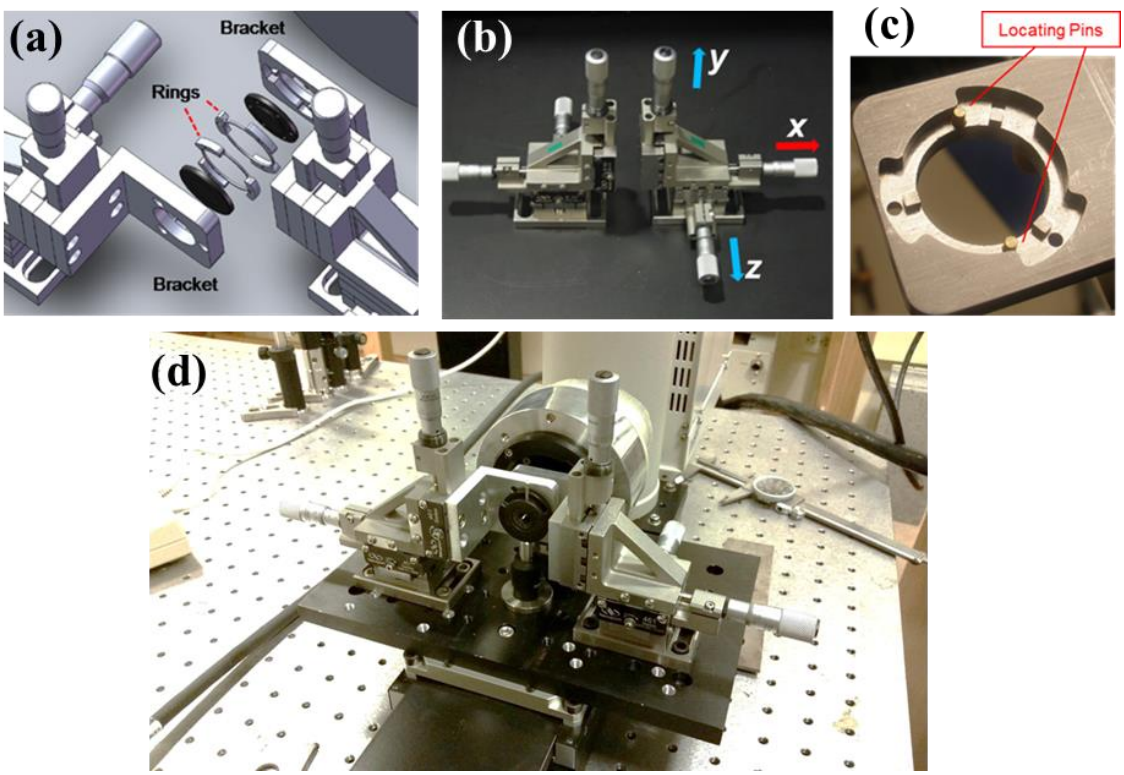

Fig. 2.10: (a) Solidworks© model of the mounting assembly, (b) two three axis translation stages where the mounting brackets are mounted, (c) an close-up image of a mounting bracket displaying the location pins, and (d) an overview image of the entire optomechanical assembly.

CHAPTER 3: VARIABLE DIAMETER BEAM SHAPER

In this chapter, we present the fabrication and experimental test results of a variable diameter beam shaper previously designed by Smilie *et al.* [35, 49]. The analytical design of this device was reviewed in Chapter 2. Additionally, we present the design, fabrication, and experimental test results of a second variable diameter beam shaper with a super-Gaussian irradiance distribution.

3.1 Fabrication results of a step function variable diameter beam shaper

To fabricate this device, a diamond raster micro-milling approach was used, where the non-rotating work piece was translated along the X and Y axes as the tool rotated at high speeds and translated along the Z axis to cut away material. *This device was fabricated at using a Moore Nanotech® 350 FG by Brian Dutterer, machinist at the UNC Charlotte Center for Precision Metrology*. A point cloud describing the surface was generated using MATLAB® and imported into MasterCAM® to establish the toolpath. The radius of the diamond endmill was 1.0 mm and milling step-over was set at 20 μm. Fig. 3.1 displays one of the two fabricated freeform elements.

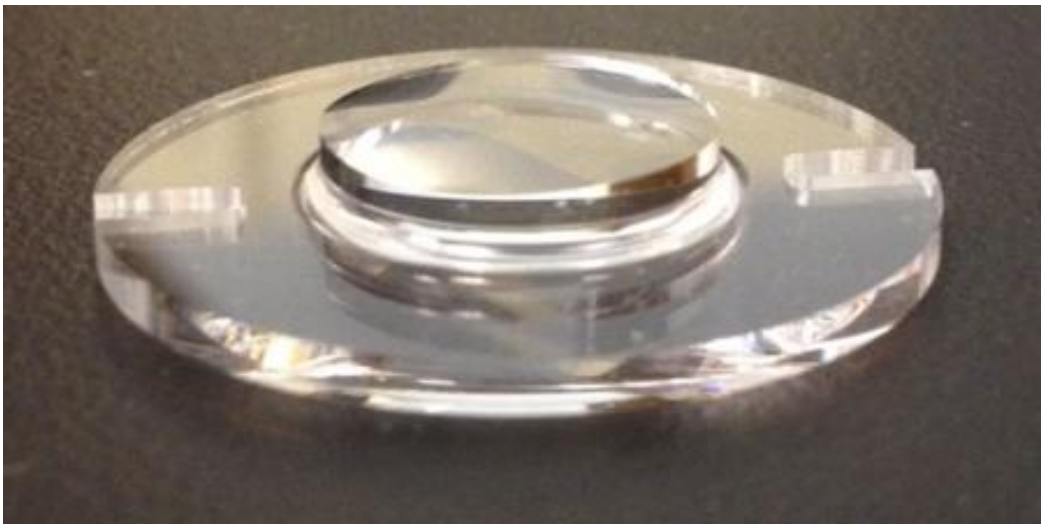

Fig. 3.1: One of the two freeform elements for the first variable beam shaper, fabricated using diamond milled approach on the Moore Nanotech® 350 FG.

The beam shaper surfaces were measured using a Zygo® scanning white light interferometer (SWLI) and MetroPro® software. *These measurements were performed by Dr. Matthew Davies, Professor at the UNC Charlotte Center for Precision Metrology*. Fig. 3.2 shows the results, where throughout the surface it can be seen that there is a significant amount of residual noise on the surface from the diamond milling process. The majority of this residual noise is believed to be a product of an interpolation error between data points in the MasterCam© software when generating the toolpath. This noise resulted in a peak-to-valley (P-V) error of 0.542 μm, and an RMS surface error of 0.093 μm.

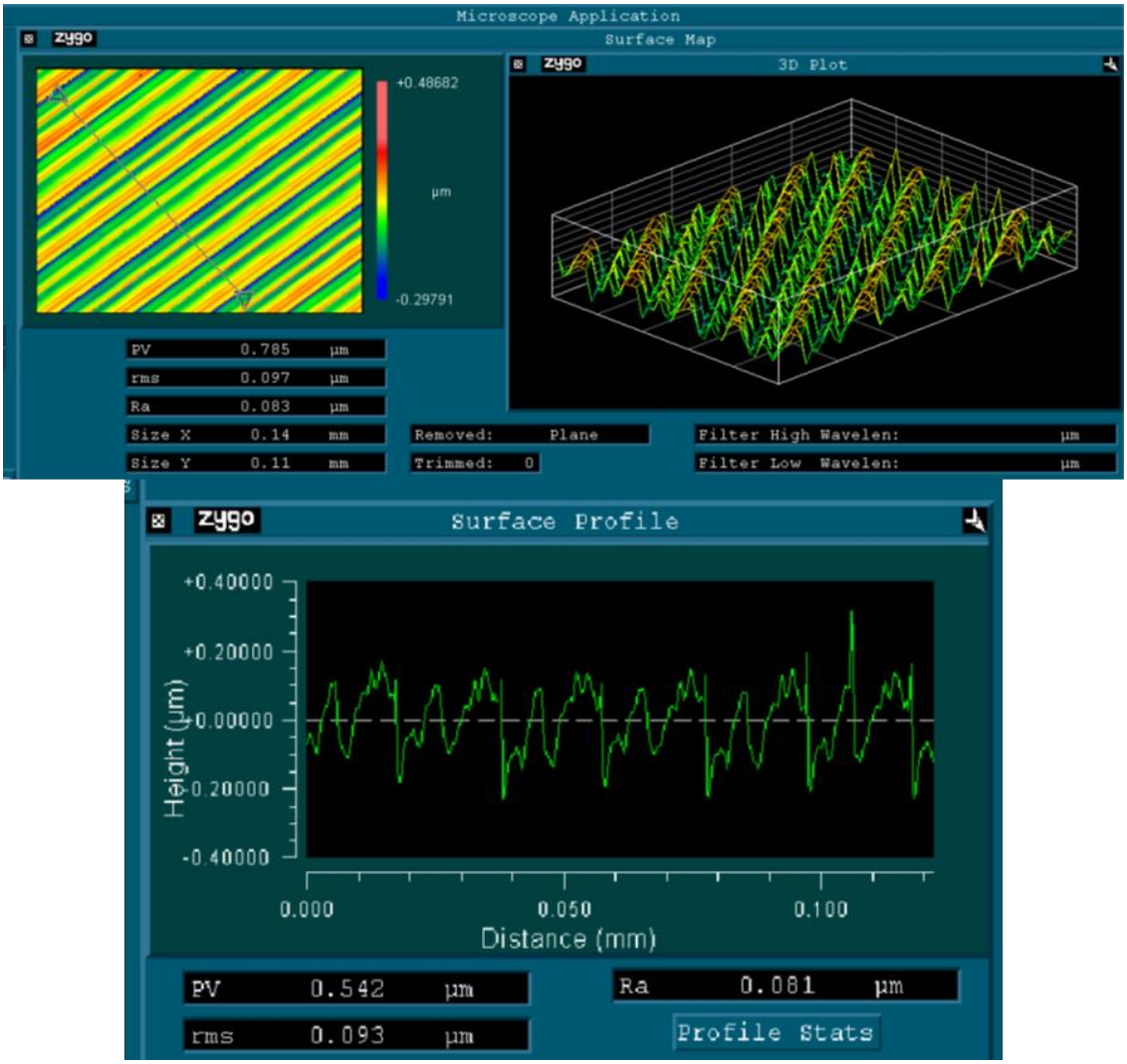

Fig. 3.2: SWLI measurements showing the surface finish of the diamond milled freeform surface.

3.2 Experimental test results of a step function beam shaper

This device was tested using the optomechanical assembly discussed in Chapter 2. Fig. 3.3 shows a schematic of the test setup, where a HeNe laser source with nominal wavelength of 632.8 nm was used as the Gaussian input. The nominal waist diameter of the HeNe laser source was 1.0 mm; therefore, because the beam shaper was designed for an input waist diameter of 6 mm, a Galilean beam expander [119] was designed and implemented. This beam expander consisted of a 12.7 mm diameter spherical lens with a

-25 mm focal length, followed by a 25 mm diameter spherical lens with a 150 mm focal length. A separation of 125 mm between the two lenses facilitates the required 6x magnification needed for the appropriate input waist diameter. A Uni-q™ digital CCD camera with a 4.785 mm x 4.757 mm detector was placed at the target location following the beam shaper to capture the output spot profile.

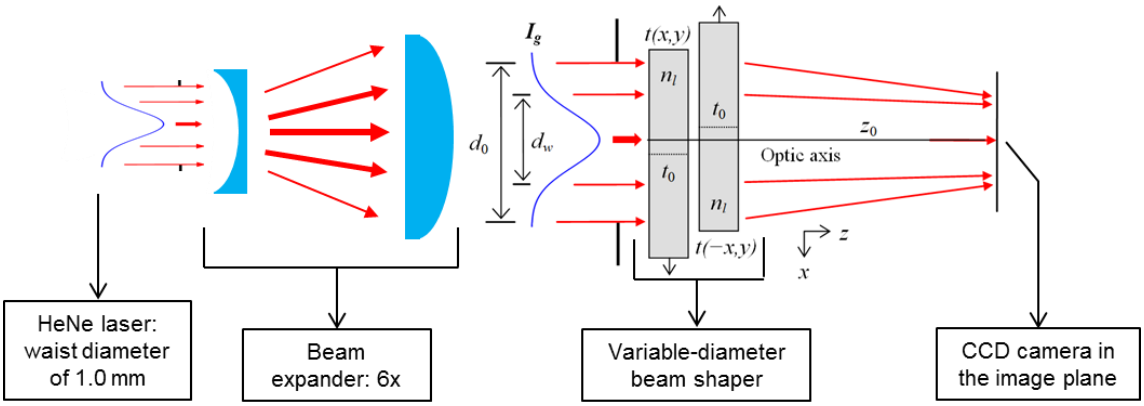

Fig. 3.3: General schematic of the variable output beam shaper experimental test setup.

Using translation stages, several different amounts of lateral shift *d* were introduced to the system, where images of and output spot were captured using Spiricon™ imaging software. These results are shown in Fig. 3.4 along with images of the input Gaussian beam before and after expansion. Additionally, for each case of lateral shift, output spot diameter was measured and summarized in Table 3.1.

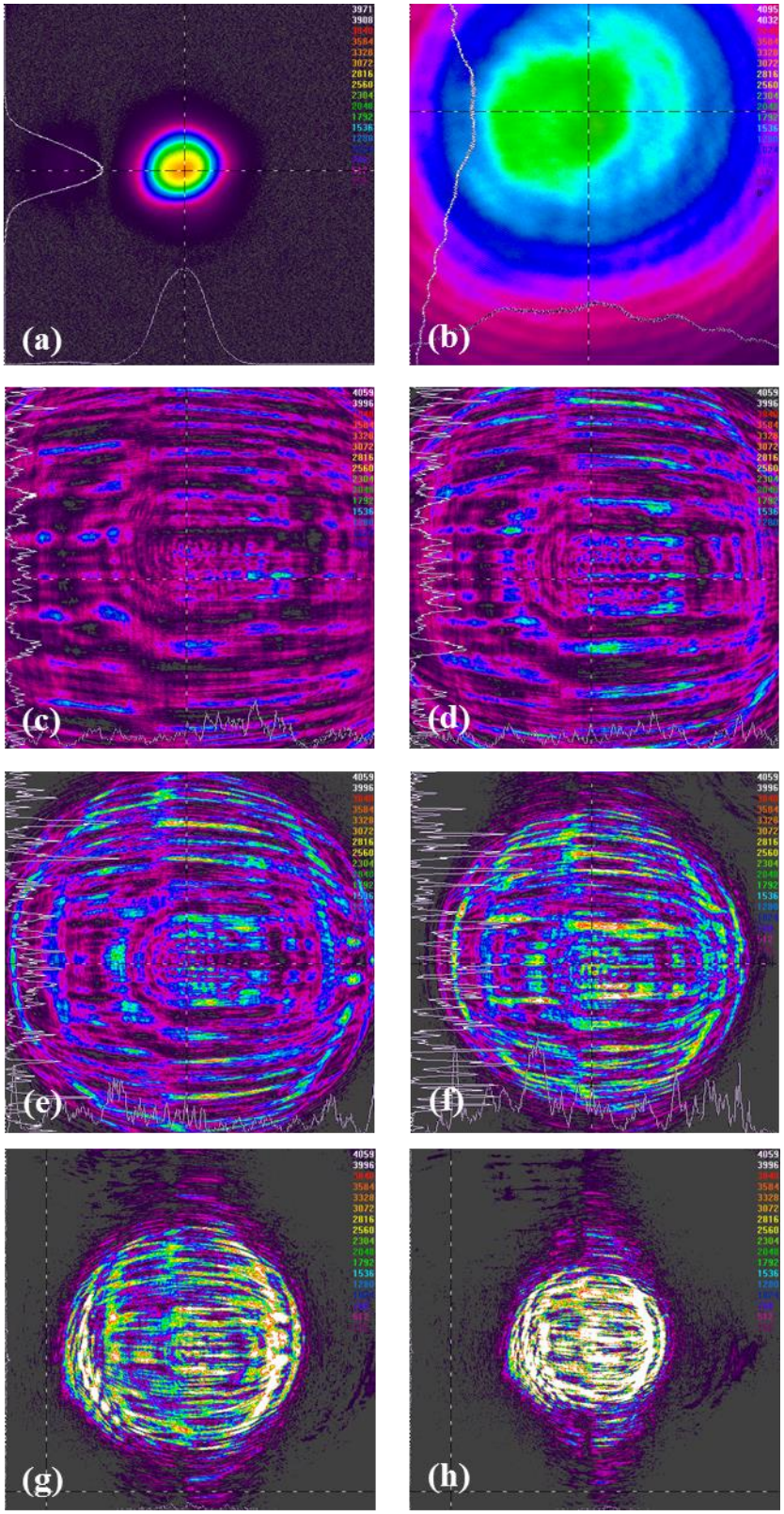

Fig. 3.4: Experimental images of (a) the 632.8 nm Gaussian input, (b) the expanded input beam waist, and output irradiance spot profiles for lateral shifts of (c) -300 µm, (d) -150 µm, (e) 0 µm, (f) 150 µm, (g) 300 µm, and (h) 450 µm.

Table 3.1: Predicted, modeled, and measured output spot diameters for several amounts of lateral shift for first beam shaper.

Lateral Shift d (mm)	Predicted Diameter (mm)	Modeled Diameter (mm)	Measured Diameter (mm)
-0.15	6.000	5.988	6.05
0	5.000	4.988	4.97
0.15	4.000	3.982	4.07
0.3	3.000	2.968	2.96
0.45	2.000	1.950	1.99

Overall, the initial experimental testing showed mixed results. The variable beam shaping functionality was confirmed through the output spot images in Fig. 3.4 and, as seen in Table 3.1, the output spot diameters compared well with the predicted diameters. However, the output spot quality and overall uniformity was poor, with a significant amount of 'noise' in the spot. The reason for this noise is investigated in the next section. Considering this undesired noise, we note there is an undefined degree of uncertainty in the measurement of the output diameters. We also note that in some cases the detector was smaller than the size of the output spot, resulting in clipping at the edges of the spots.

3.3 Spot quality investigation

There are several potential contributors to the poor output spot quality of the beam shaper. First, during experimental testing the input waist diameter was measured to be 1.15 mm (magnifying to 6.9 mm) which differs from the previously assumed diameter of 6.0 mm. Next, the previous optical modeling assumed an ideal input beam, and did not include the beam expanding lenses in the simulations. Due to the sizes of these lenses, there could potentially be diffraction effects from the edges that would have a negative impact on the performance. In an attempt to investigate these effects, we modeled the complete experimental set up in VirtualLab™, expanding on previous models by

including the corrected input beam diameter and beam expansion lenses. Fig. 3.5 shows the results of this simulation and compares it to the ideal case. We see that the performance is negatively impacted by the changes, but these results do not suggest that these changes are the main contributors to the 'noise' seen in the experimental measurements.

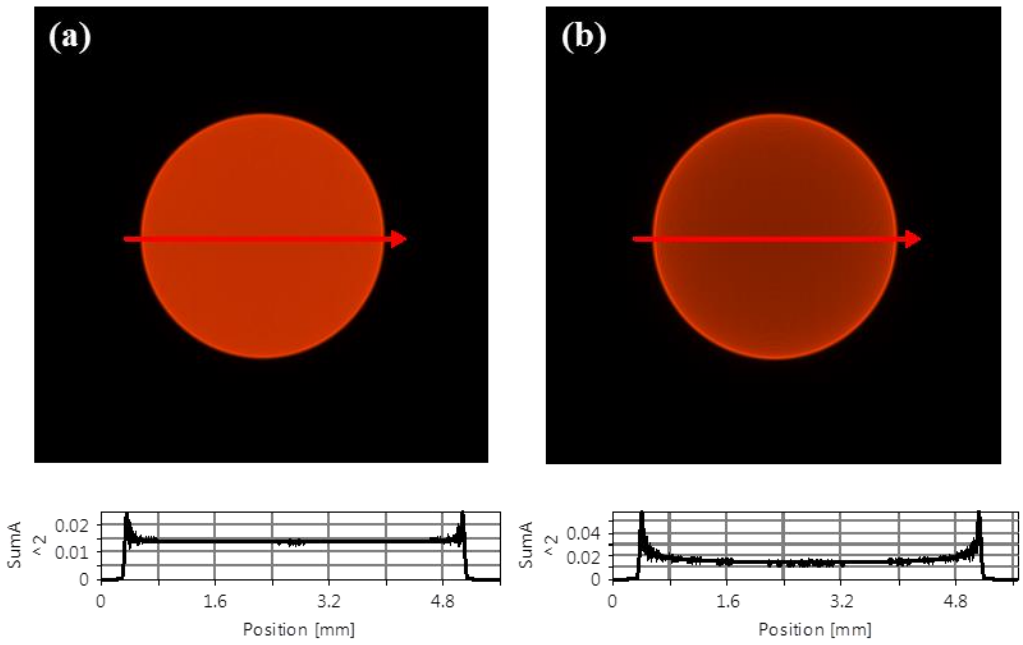

Fig. 3.5: Output irradiance profiles for the beam shaper with (a) the ideal input and (b) the experimental input diameter and beam expansion lenses.

The surface finish of the freeform surfaces was thought to be a main driver in the poor spot quality. As seen earlier in Fig. 3.4, there was a significant amount of residual noise on the surface from the diamond milling process believed to be the result of a tool path generation error. While it is possible to import the measured surface texture into VirtualLab™ and impose it onto the freeform surfaces, this simulation was found to be impractical due to computational requirements. Instead, we approximated the SWLI surface structure with a grating structure, shown in Fig. 3.6.

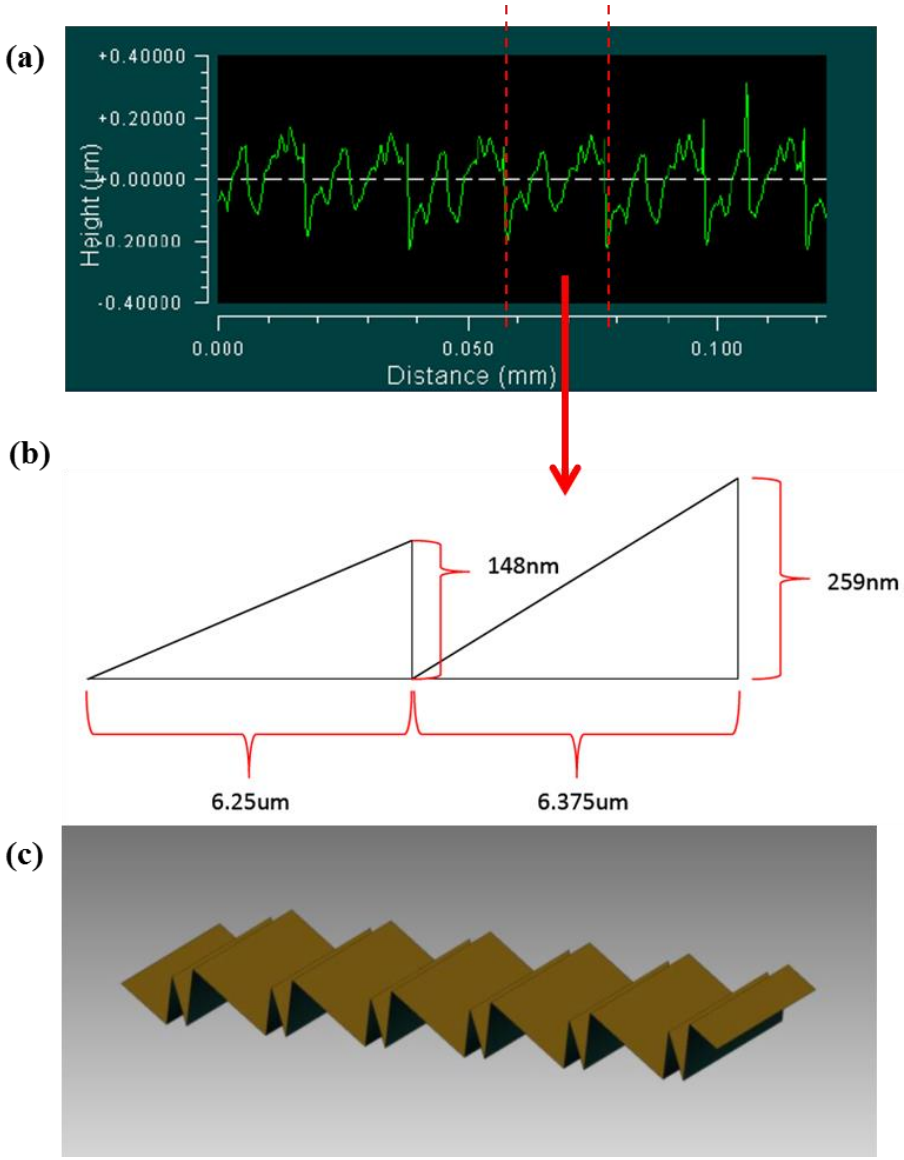

Fig. 3.6: (a) Sample surface profile cross-section from the SWLI data for first beam shaper, (b) the approximation of this surface, and (c) the modeled surface imposed on the beam shaping surfaces in VirtualLab™.

Due to the relative sizes of the surface textures; diffraction effects must be accounted for in order to achieve accurate results, therefore physical optics models are needed to accurately analyze the effects. This grating structure from Fig. 3.6c was defined in VirtualLab™ and imposed onto the freeform surfaces. With this surface imposed on the freeform surfaces, the simulation was performed again, using the same simulation parameters as in Fig. 3.5. While still not a model of the actual surface, the simulation

results shown in Fig. 3.7 display a more drastic impact on the output spot quality, and qualitatively match the poor spot quality seen in the experimental results.

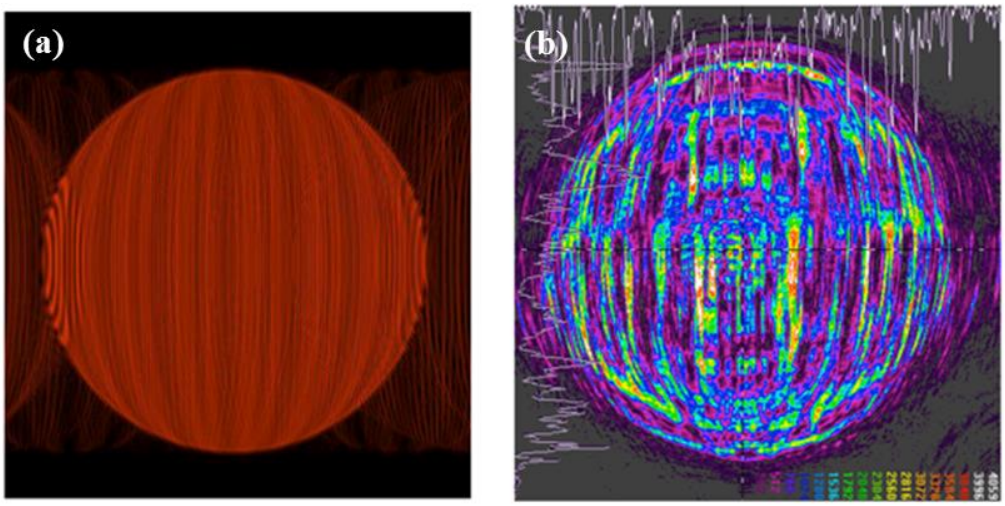

Fig. 3.7: (a) Output irradiance spot for the approximated SWLI data simulation, and (b) experimental output spot.

3.4 Optical design of a super Gaussian variable diameter beam shaper

Using information learned from the step function variable beam shaper discussed, a second variable diameter beam shaper was designed in an attempt to achieve higher quality output spots. As mentioned before, the previous beam shaper had an output irradiance distribution that was defined to be a step-function. As a consequence, there were undesirable spikes of energy at the edges of the output spot, known as the Gibb's phenomenon [57, 58]. A solution to this problem is to implement an output irradiance profile described by a continuous distribution that contains edges that are less steep, such as the super-Gaussian form presented by Shealy and Hoffnagle [59]. The super-Gaussian irradiance distribution, I_{SG}, is described by,

$$I_{SG}(R) = I_o \exp\left(-2\left(\frac{R}{R_{SG}}\right)^p\right), \tag{3.1}$$

where R is the output radial coordinate, R_{SG} is the waist radius of the output spot, p is the parameter which controls the edge steepness, and I_o is the constant output irradiance for which the energy conservation condition is met. Fig. 3.8 displays sample distributions with varying p parameters. Here, it can be see how the edge steepness increases as p increases, and performs essentially as a step-function as p approaches infinity.

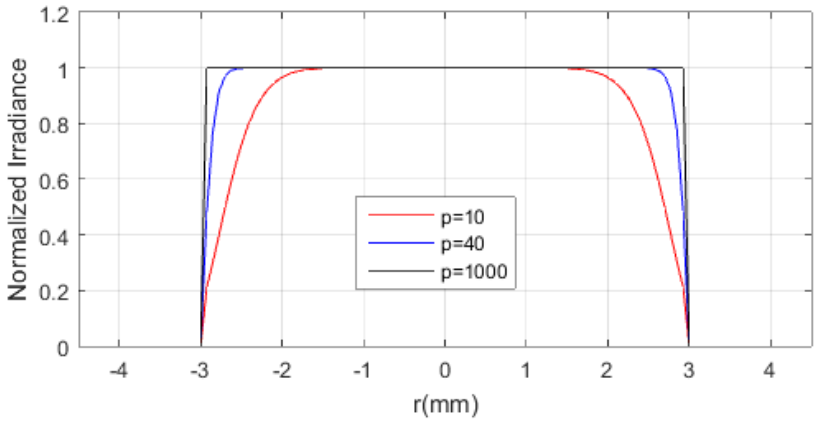

Fig. 3.8: Super-Gaussian irradiance distributions for several different edge steepness p values.

In addition to altering the output irradiance distribution, there were several other design and fabrication issues addressed for this design. We implemented smaller output spot diameters to better fit the detector, and we adjusted the design to match the experimental input waist diameter. A custom tool path was also generated (by Dr. Joseph Owen) to improve the surface finish of the fabricated freeform surfaces [120].

The design process for this device follows very closely to the process Smilie *et al.* used (in Chapter 2) when designing the step-function beam shaper [35], with one key difference. Recall the ray mapping technique, where complex integrals were implemented using energy conservation in combination with Snell's law to derive the required composite surface en route to ultimately defining the freeform surface. Previously, this

part of the design process was purely analytical. However, there are no simple analytical solutions to those complex integrals for distributions such as the super-Gaussian function. In an effort to further generalize this design process and enable the implementation of different irradiance distributions, a custom MATLAB® code (Appendix A.1.1) was created to numerically determine the ray mapping function. This custom code determines the constant output irradiance I_0 such that the conservation of energy is achieved, and then numerically equates the input and output radial coordinates using a series of 'for' loops and the 'fit' function in MATLAB®, ultimately providing the ray mapping function. This process is illustrated in Fig. 3.9; where Fig. 3.9(a) and Fig. 3.9(b) show the integral of the input and output irradiance distributions as a function of the respective radial coordinates, and Fig. 3.9(c) shows the output radial coordinate R versus input radial coordinate r where the corresponding integral values were equal. Using this coordinate relationship, the remainder of this design procedure follows the procedure used for the step function beam shaper. This numerical aspect to the design process ultimately provides more flexibility in design, resulting in improved performance as well as the potential development of novel optical functions.

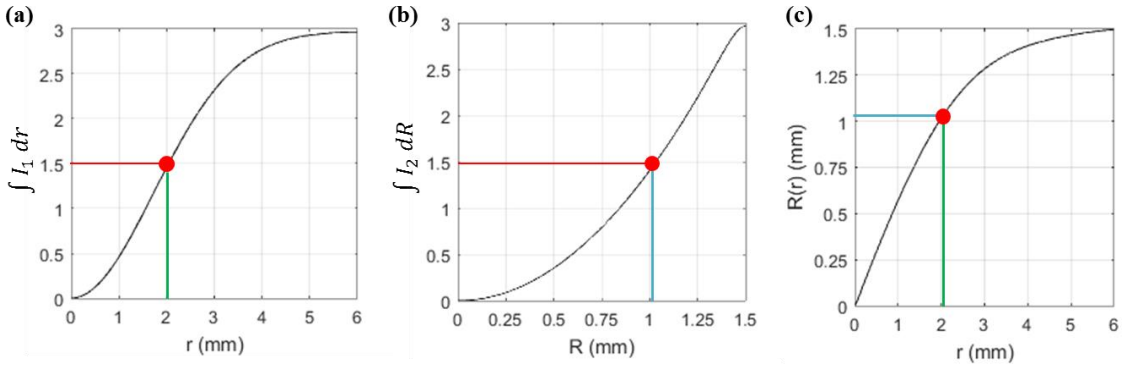

Fig. 3.9: Integral of (a) the input Gaussian beam and (b) the output super-Gaussian beam as a function of their respective radial coordinate. (c) The output radial coordinate R versus input radial coordinate r where the corresponding integral values were equal (ray mapping function).

For this specific example, we define the output irradiance distribution to be super-Gaussian with a *p* value of 40 across the range of output diameters. Some key design parameter changes included the input waist diameter of the Gaussian input, defined to be 6.9 mm with a wavelength of 632.8 nm, which is equivalent to the experimental diameter measured in the previous tests. The output spot diameter was defined to be 3 mm for the specific case where there is no relative shift in the system (d = 0), and defined to have a range from 1 mm to 5 mm over the lateral shift range of d = +/-300 μm meaning that with every lateral shift of Δd =150 μm, there will be a 1 mm change in output diameter. These spots were defined to be slightly smaller than the previous example in order to avoid the previous clipping of the output spot by the detector. All other parameters were kept the same with the 12mm aperture diameter, 150 mm target distance, and PMMA material.

Multiple beam shapers with output spot diameters ranging from 1-5 mm were designed using the numerical ray mapping procedure. Fig. 3.10 shows each surface profile on the same scale across the 12 mm aperture.

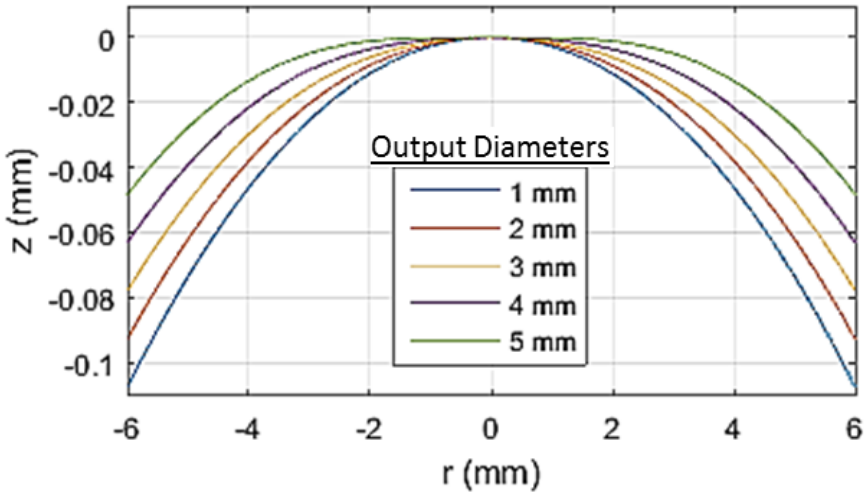

Fig. 3.10: Surface height profiles for multiple beam shapers with various output spot diameters.

For each surface height profile, the "polyfit" function was used in MATLAB® [121] to fit a set of polynomial coefficients to Eq. (2.7). Each set of coefficients are listed in Table 3.2 along with the average change, Δa_{2k}. Because this beam shaper is designed to have a 3 mm output diameter when there is no lateral shift in the system, those corresponding polynomial coefficients will inherently be defined as the base component coefficients (a_{2k}).

Table 3.2: Surface coefficients for five output spot diameters and the associated changes.

a_{2k} values (mm^{-2k+1})	**Output Diameter**					**Avg. Δa_{2k} (mm^{-2k+1})**
	1mm (*d*=300µm)	**2mm (*d*=150µm)**	**3mm (*d*=0)**	**4mm (*d*=-150µm)**	**5mm (*d*=-300µm)**	
a_2	-5.46E-03	-4.11E-03	-2.76E-03	-1.41E-03	-6.48E-05	-1.35E-03
a_4	-2.70E-05	-5.42E-05	-8.14E-05	-1.09E-04	-1.36E-04	2.72E-05
a_6	4.90E-07	9.79E-07	1.47E-06	1.96E-06	2.44E-06	-4.88E-07
a_8	-6.27E-10	-1.24E-09	-1.84E-09	-2.42E-09	-2.99E-09	5.90E-10
a_{10}	-2.24E-10	-4.49E-10	-6.73E-10	-8.98E-10	-1.12E-09	2.25E-10
a_{12}	5.13E-12	1.03E-11	1.54E-11	2.05E-11	2.57E-11	-5.14E-12
a_{14}	-3.89E-14	-7.78E-14	-1.17E-13	-1.56E-13	-1.95E-13	3.90E-14

Now that the average changes in coefficients Δa_{2k} per unit change in lateral shift Δd have been defined, Eq. (2.14) is used to determine the variability coefficients b_{2k}, displayed in Table 3.3 along with the base coefficients a_{2k}. Similar to before, a performance sweep was then performed on the tilt term to find the point at which the sag of the freeform surface was at a minimum. The resulting tilt term of 0.053 decreased the sag from 670 µm to 290 µm over the 12 mm aperture diameter. As before, the reduction in sag is beneficial both for fabrication as well as allowing the two surfaces to be closer together, ultimately minimizing the potential error caused by the stand-off distance.

Table 3.3: Freeform surface coefficients for the super-Gaussian variable diameter beam shaper.

Order (k)	a_{2k} Values (mm^{-2k+1})	b_{2k} values (mm^{-2k})
1	-2.7600E-03	-4.4919E-03
2	-8.1356E-05	9.0507E-05
3	1.4671E-06	-1.6276E-06
4	-1.8361E-09	1.9656E-09
5	-6.7326E-10	7.4954E-10
6	1.5407E-11	-1.7136E-11
7	-1.1679E-13	1.2986E-13

These coefficients are then used with Eq. (2.9) and Eq. (2.10) to define the base and variability components, and combined to create the desired freeform surface. Fig. 3.11 displays the resulting base, variability, and freeform surfaces.

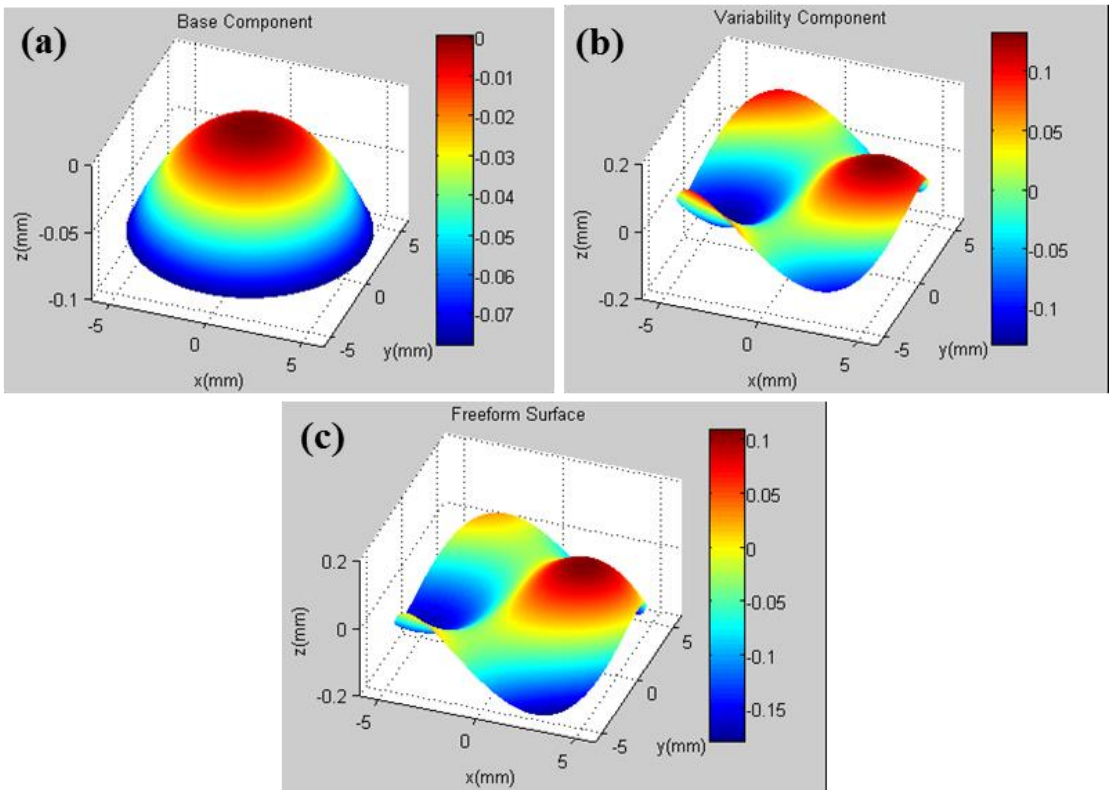

Fig. 3.11: Surface plots showing the (a) base component, (b) variability component, and (c) one of the two freeform surfaces.

3.5 Optical modeling of a super-Gaussian variable diameter beam shaper

Using the same approach as before, VirtualLab™ was used to simulate the performance of this optical device. The only simulation parameter changed was the sampling distance of the output light field, which was now set to 6 x 6 μm over a 6 x 6 mm window due to the smaller output spot sizes. The "Beam Parameters" function was again used to determine the diameter of the output spot where the irradiance fell to zero. Table 3.4 shows the constant input diameter with the expected output diameters and simulated output diameters relative to the corresponding lateral shift. The predicted results were in good agreement with the simulated results in VirtualLab™.

Table 3.4: Predicted and modeled input and output spot diameters for several amounts of lateral shift.

Lateral Shift d (μm)	Input Diameter (mm)	Predicted Output Diameter (mm)	VirtualLab™ Output Diameter (mm)
-300	6.9	5.0	4.997
-150	6.9	4.0	3.992
0	6.9	3.0	2.988
150	6.9	2.0	1.962
300	6.9	1.0	0.953

Fig. 3.12 shows images of the simulated input and output spots for lateral shifts of d = 0 μm, +/-150 μm, and +/-300 μm. The output spots in Fig. 3.12 clearly display the variability function, as well as the desired uniform super Gaussian irradiance distribution where the aforementioned Gibb's phenomenon is no longer observed.

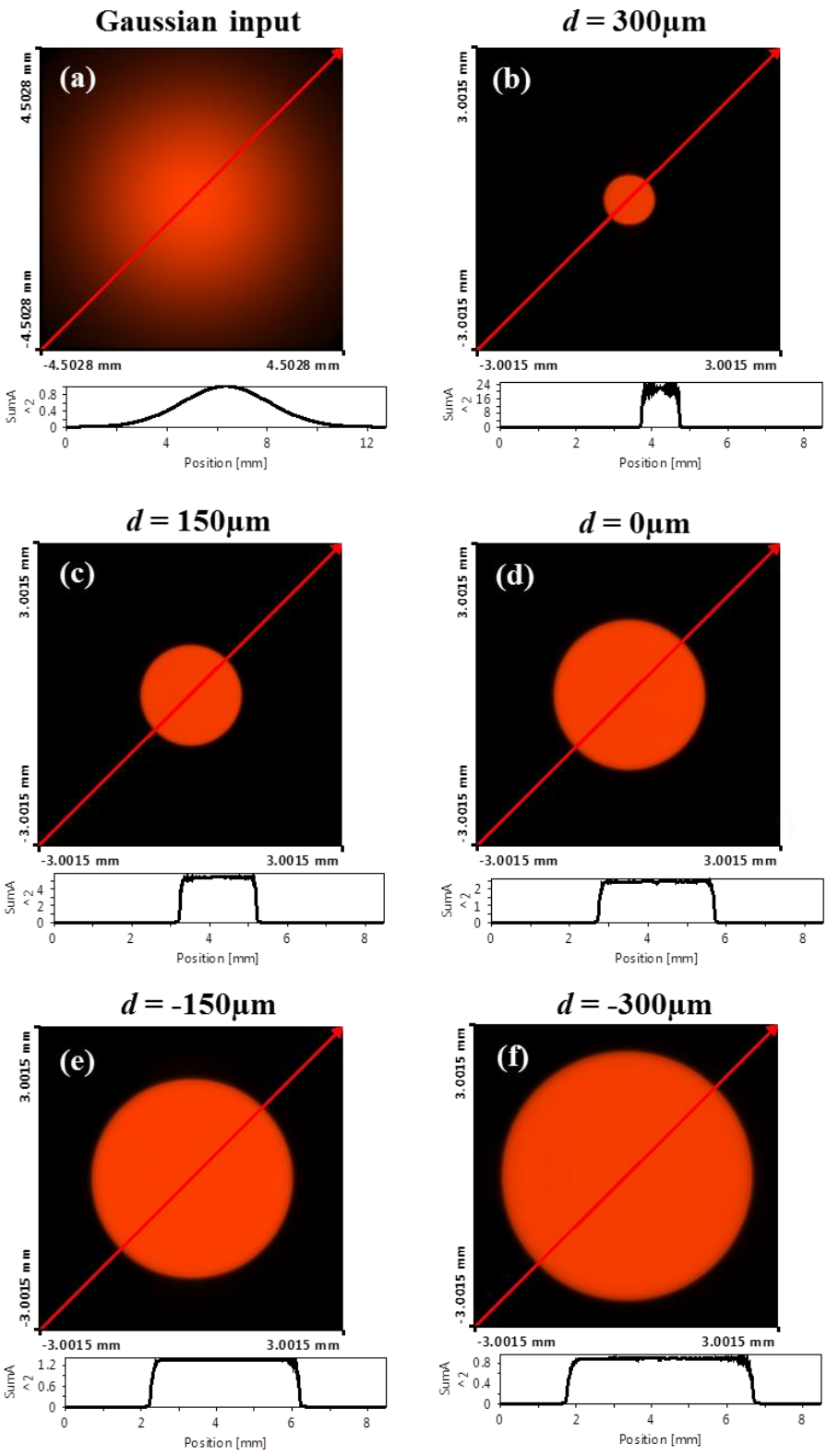

Fig. 3.12: Six VirtualLab™ images and 1-D profiles, (a) Gaussian input, (b) d = 300 µm, (c) d = 150 µm, (d) d = 0.0 mm, (e) d = –150 µm, and (f) d = –300 µm. Note: the input in (a) is set to a different lateral scale.

3.6 Fabrication results of the super-Gaussian variable diameter beam shaper

The freeform elements were again fabricated using a diamond milling approach with nearly the same procedure as the previous step function beam shaper. *Fabrication was performed using a Moore Nanotech® 350 FG by Brian Dutterer, machinist at the UNC Charlotte Center for Precision Metrology*. The diamond endmill used for fabrication had the same tool radius of 1.0 mm; however, a smaller milling step-over of 10 μm was used opposed to the larger step-over of 20 μm used in the previous case. The reason for this change was to achieve a better surface finish in an attempt to avoid undesired optical artifacts. Another key change in the fabrication was the method used for generating the milling toolpath. After fabrication of the step-function beam shaper, it was found that there was an interpolation error when using MasterCAM®, causing significant surface finish errors. Dr. Joseph Owen *et al.* addressed this through extensive research on generating a custom toolpath in order to achieve optimum results by compensating for different machining errors, such as tool edge waviness, tool offset error, and machine axis misalignment [120]. Additionally, a new spindle head was acquired that could be balanced to minimize vibrations, further increasing the surface finish quality. The effects of the surface finish quality will be discussed later in Chapter 8 with more detail. The resulting diamond milled PMMA freeform surfaces are shown in Fig. 3.13.

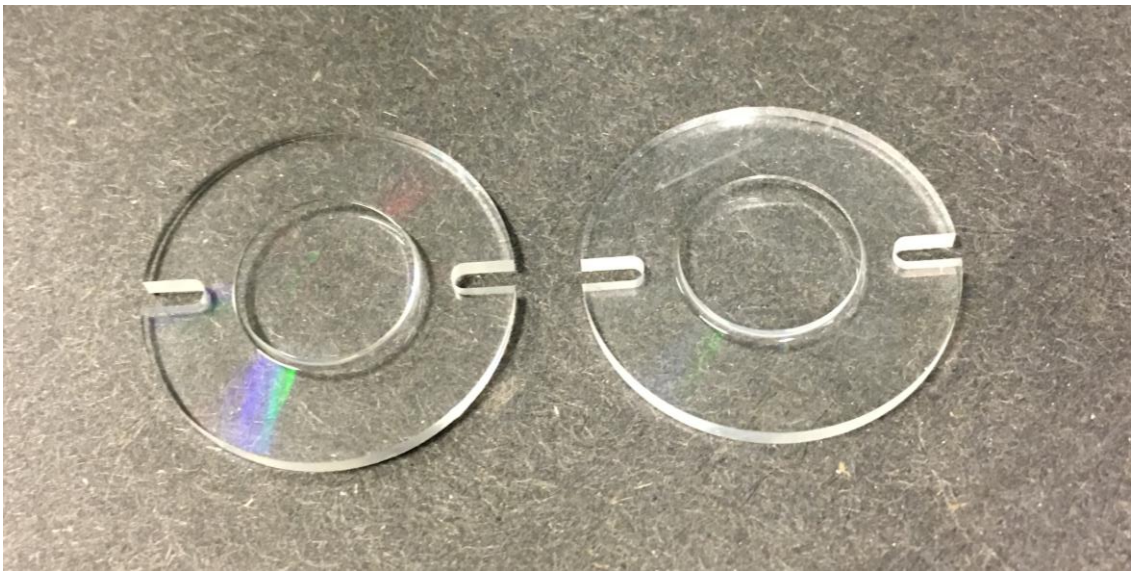

Fig. 3.13: Image of the two freeform elements diamond milled in PMMA for the super-Gaussian variable diameter beam shaper.

The super-Gaussian beam shaper surfaces were measured again using a Zygo® scanning white light interferometer (SWLI) and MetroPro® software. *These measurements were performed by Dr. Matthew Davies, Professor at the UNC Charlotte Center for Precision Metrology*. Fig. 3.14 shows a cross-sectional slice of the measured surface data. As expected, through the number of improvements made throughout the fabrication process, there is much less residual noise on the surface on the freeform surfaces from the diamond milling process. This resulted in a 0.012 μm RMS and a 0.060 μm P-V, which is significantly less than the previous example which had a 0.093 μm RMS and a 0.542 μm P-V. This suggests that the changes made were successful in their attempt to improve the surface finish quality.

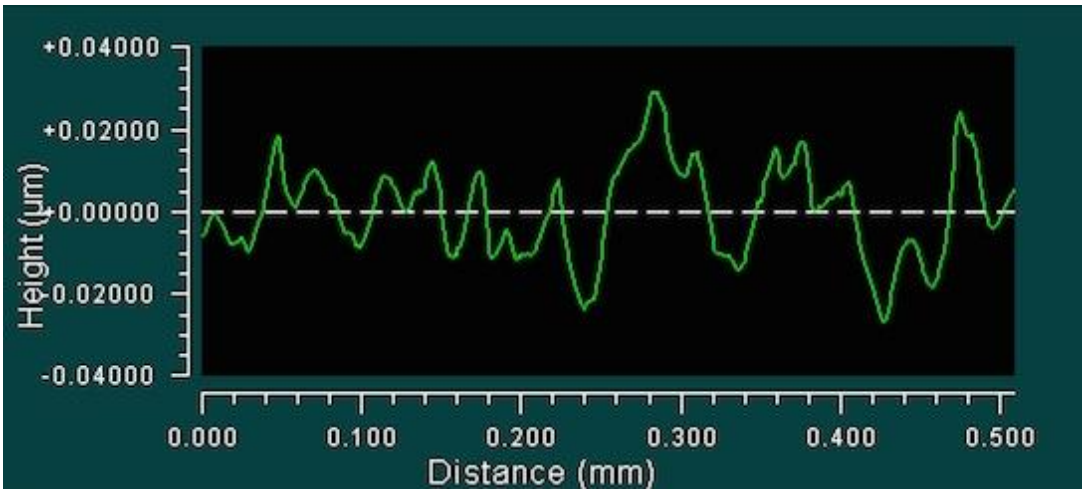

Fig. 3.14: Sample surface profile cross section for super-Gaussian beam shaper from SWLI data. Note that the vertical scale in this measurement is an order of magnitude smaller than the measurement of the step-function beam shaper.

3.7 Experimental testing of the super-Gaussian variable diameter beam shaper

Experimental testing of this device was performed using the same setup described in earlier in this Chapter. Fig. 3.15 displays the Gaussian input before and after the beam expander as well as the experimental output spots for different values of lateral shift *d*. Table 3.5 shows the measured experimental output spot diameters. These results show a dramatic improvement in the output spot quality. This improvement is thought to be a direct product of the much improved surface finish. While the performance is much improved, there still remains some undesired noise in the output spot. This is still thought to be a product of additional surface finish errors (e.g., vibrations, thermal cycling, tool misalignment, tool chatter, etc.). Methods for further improvement of surface finish are currently being explored.

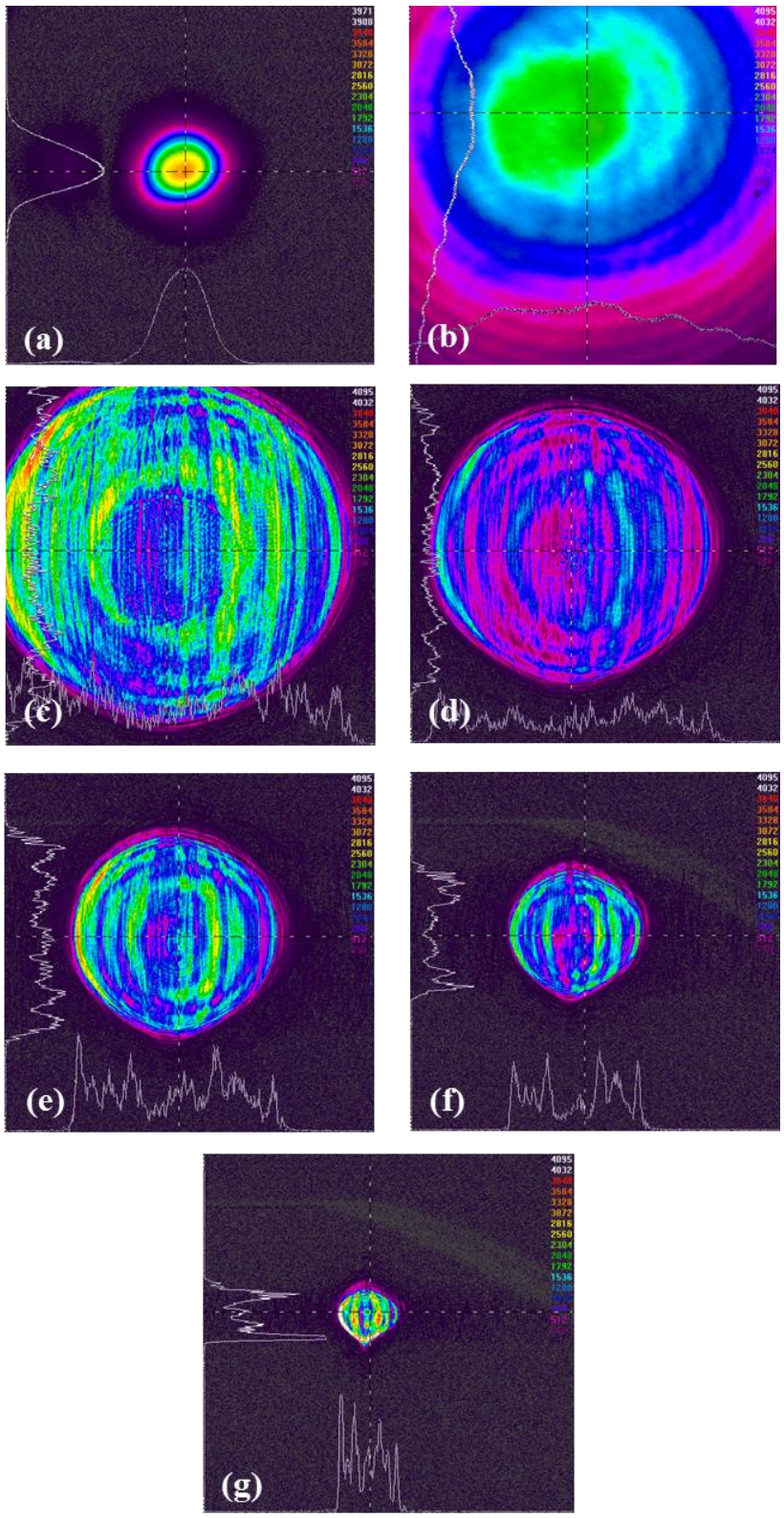

Fig. 3.15: Experimental results for (a) the 632.8 nm Gaussian input, (b) the expanded input beam waist, and output irradiance spot profiles for lateral shifts of (c) -300 µm, (d) -150 µm, (e) 0 µm, (f) 150 µm, and (g) 300 µm.

Table 3.5: Predicted, modeled, and measured output spot diameters for several amounts of lateral shift for second beam shaper.

Lateral Shift d (mm)	Predicted Diameter (mm)	Simulated Diameter (mm)	Experimental Diameter (mm)
-0.3	5.00	4.978	5.09
-0.15	4.00	3.985	3.91
0	3.00	2.991	2.93
0.15	2.00	1.953	2.07
0.3	1.00	0.947	1.05

3.8 Discussion

The results from both of these variable output diameter beam shaper were extremely encouraging, leaving several takeaways. Through the first set of experimental tests, the general functionality of the dynamic freeform system was confirmed. However, the uniformity was less than ideal with a significant amount of undesired noise observed in the output spots. While there are several contributing factors to this noise, the majority of the error was found to result from residual surface finish errors on the fabricated freeform surfaces, confirmed through SWLI tests and approximated simulations in VirtualLab™. Following this, a second beam shaper was designed, fabricated, and tested. Several improvements were made for this second iteration of a variable output diameter beam shaper. Design changes included smaller spot sizes, adjustments for the experimental input diameter, and implementation of a continuous super Gaussian irradiance distribution. Additionally, the ability to numerically define freeform surfaces based on a continuous output irradiance distribution was demonstrated in this chapter. The simulation results suggest that this design process could be applied to different semi-

arbitrary irradiance distributions that would otherwise be impossible using an analytical approach. These irradiance distributions could include both imaging and non-imaging applications. Fabrication improvements included a smaller step-over distance during milling, tool path corrections, and a balancing spindle head. With these changes, the surface finishes of the fabricated freeforms were improved by close to an order of magnitude. Experimental testing of this beam shaper showed significantly better output spot uniformity, but remaining noise in the output spot suggests the need for additional studies on surface finish.

CHAPTER 4: ALVAREZ LENS WITH A SHIFTED FOCAL RANGE

4.1 Introduction

As mentioned in Chapter 1, the Alvarez lens and Lohmann varifocal lens are classic examples in which two superimposed freeforms with cubic phase profiles create a composite lens of whose focal length can vary simply by changing the relative lateral position of the surfaces [28-30]. Before explaining the advantages and novelty of the shifted focus Alvarez lens, it is important to understand the basic functionality of the 'standard' Alvarez lens. To do this, we revisit the design process used in previous work done by Smilie *et al.* [34, 35], where the design, fabrication, and testing of a diamond micro-milled germanium Alvarez lens pair was first presented. In this example, the 'standard' definition of the Alvarez lens pair was used, where the freeforms were described by,

$$z = A\left(\frac{1}{3}x^3 + xy^2\right). \tag{4.1}$$

Here, the amplitude coefficient A controls the amount of surface depth modulation (sag) and essentially determines how the system's optical power. Similar to before, the z-axis corresponds to the direction of light propagation, and the x-axis corresponds to the axis which the surfaces are inverted as well as the direction the lateral shifts are designed to take place. It was shown in detail that by following the first order analysis approach outlined by Alvarez and Humphrey [28, 29], the focal length f of the composite lens is

dependent on the amplitude coefficient A, the index of refraction n_l, and the lateral shift d. The resulting relationship between these parameters is given by,

$$f = \frac{1}{4Ad(n_l - 1)}. \tag{4.2}$$

In order to determine the amplitude coefficient, Eq. (4.2) can be reworked using simple algebra and assuming a minimum focal length at a maximum allowable lateral shift, resulting in the relationship given by,

$$A = \frac{1}{4fd(n_l - 1)}. \tag{4.3}$$

This analytical procedure was used to create an example design to demonstrate and compare the functionality and performance of this device. The material of choice for the examples in this chapter was IRG26 (n_l = 2.79 at 4 μm wavelength) [118] due to collaborative research efforts with UNC Charlotte's Center for Precision Metrology on ultraprecision manufacturing methods, specifically on chalcogenide glasses [60, 122-125]. We define the minimum focal length to be 38.5 mm at the defined lateral shift limit of 1.8 mm. These considerations were input into Eq. (4.3) where the amplitude coefficient was determined to be A = 0.00201 mm^{-2}, which resulted in a surface depth modulation of 669 μm over the 14.14 mm diameter. Similar to the previous variable beam shaper examples, a tilt term of 0.0443 was added, decreasing the height modulation to 279 μm. The resulting surface was decomposed into the equivalent base and variability components, as shown in Fig. 4.1. It can be seen that the base component has no surface curvature, meaning the freeform surface is essentially the same as the variability component. This is inherent given that the base component is defined as the composite surface when d = 0 mm, and for this 'standard' Alvarez example there is no optical power

present when there is no lateral shift present in the system. Fig. 4.2 shows a plot of the composite lens focal length as a function lateral shift, produced using Eq. (4.2) with the assumed design parameters for a lateral shift range of d = +/- 2 mm, further exemplifying the dynamic focal range of this optical system.

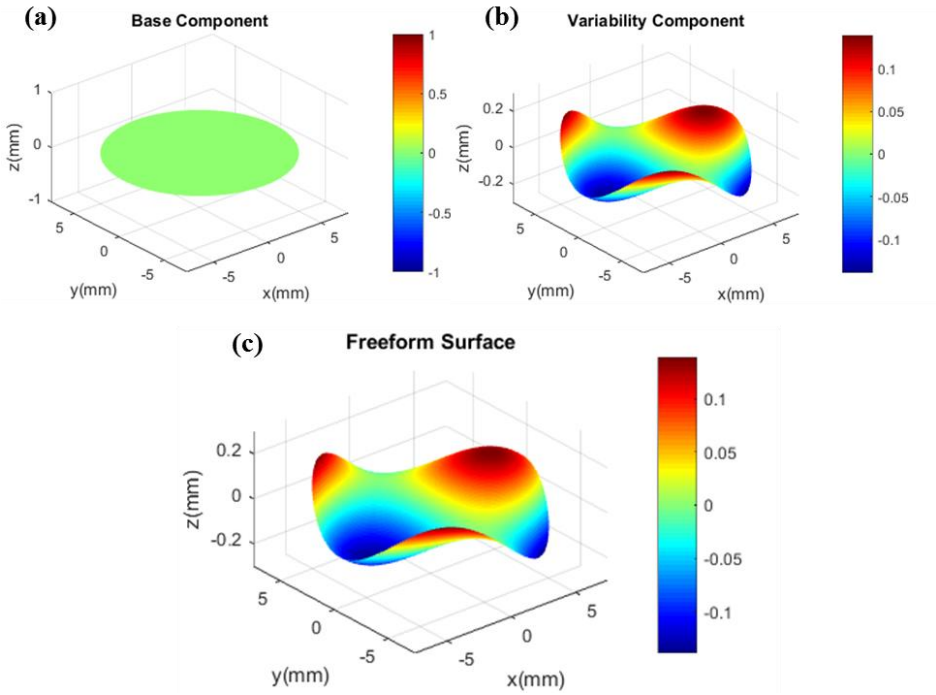

Fig. 4.1: 3-D plots of the (a) base component, (b) variability component, and (c) freeform surface for the IRG26 standard Alvarez lens design.

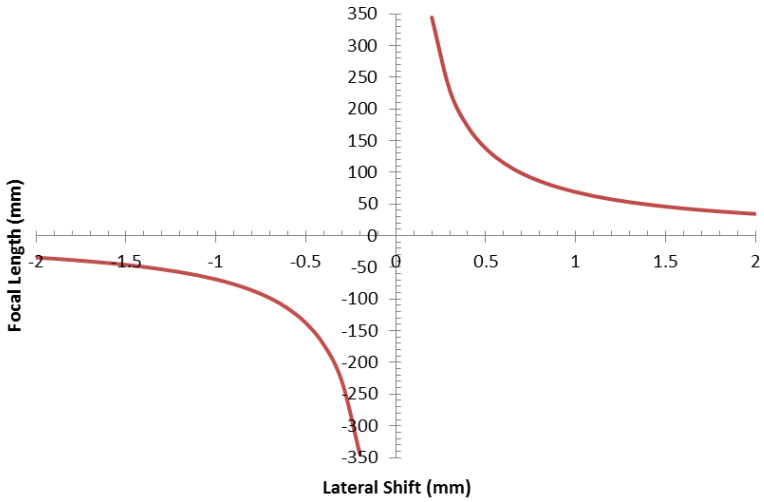

Fig. 4.2: Predicted focal length vs. lateral shift of the 'standard' Alvarez lens system.

As seen from this example; one limitation, when using the 'standard' definition of the Alvarez lens, is that the composite lens has no optical power with no lateral shift present. The composite lens acts as a converging lens with a negative shift $-d$, and as a diverging lens with a positive shift $+d$. Researchers have previously reported an approach to have the lens converge across the entire lateral shift range $+/-d$ [53-55] by presetting a lateral offset while employing the first order analysis. This approach is effective, but requires an empirical selection of the assumed lateral offset. In addition to this, other work has been done to achieve this effect [56] through optimization in optical software for a specific system. As a result, the freeforms elements were no longer identical ($z_{f1} \neq z_{f2}$), and they were no longer plano-freeform. Again, this approach is effective, but does not provide a general procedure for future designs and curvature on both sides of each element could potentially add complexity to the fabrication process.

In this chapter, we present a more general design approach for defining and implementing the shifted focal range. We utilize a 14^{th} order polynomial surface with the same design approach used for the super-Gaussian variable beam shaper (discussed in Chapter 3) to realize an Alvarez lens with a shifted focal range. The motivation for this approach is to add more flexibility throughout the design process by enabling the selectivity of a specific focal range that would otherwise not be possible using the standard analytical approach.

4.2 Design of an Alvarez lens with a shifted focal range

Recall from Chapter 2 that the composite lens was defined as the combination of two identical freeforms flipped 180^{o} relative to each other. We begin by designing the

composite lenses (MATLAB® code shown in Appendix A.1.2), which in this case are spherical lenses of varying focal lengths (surface curvature). It is important to note that the induced lateral shift varies the composite surface curvature linearly with respect to the polynomial coefficients. From the well-known Lensmaker's equation [126], the focal length of a spherical lens is inversely proportional to the surface curvature, which means the focal length will also be inversely proportional to lateral shift. To be consistent with the design process used previously, five different composite lenses with varying focal lengths were designed. Each focal length was determined using the following relationship;

$$\frac{1}{f_5}-\frac{1}{f_4} = \frac{1}{f_4}-\frac{1}{f_3} = \frac{1}{f_3}-\frac{1}{f_2} = \frac{1}{f_2}-\frac{1}{f_1}, \tag{4.4}$$

where the index on the focal lengths correspond to its respective lateral shift increment. With considerations to the mid-IR imaging system geometry and optomechanics which will be used for experimental testing, the focal length range was defined to be $\infty \geq f \geq$ 38.5 mm across the lateral shift range of d = +/-1.8 mm. The intermediate focal lengths, determined using Eq. (4.4), are listed in Table 4.1 with their corresponding lateral shift.

Table 4.1: Focal lengths and corresponding lateral shifts for the multiple composite surfaces designed.

Index	Lateral Shift (mm)	Focal Length (mm)
1	-1.8	∞
2	-0.9	154
3	0	77
4	0.9	51.33
5	1.8	38.5

Using IRG26 again as the lens material, the necessary surface height profiles of several composite lenses were determined using the numerical ray mapping procedure (discussed in Chapter 3). To put this into terms of the ray mapping function developed for the variable beam shaper, the target spot size (focal spot) for this device was essentially set to zero at a varying target location (focal length). The resulting composite surfaces are shown in Fig. 4.3.

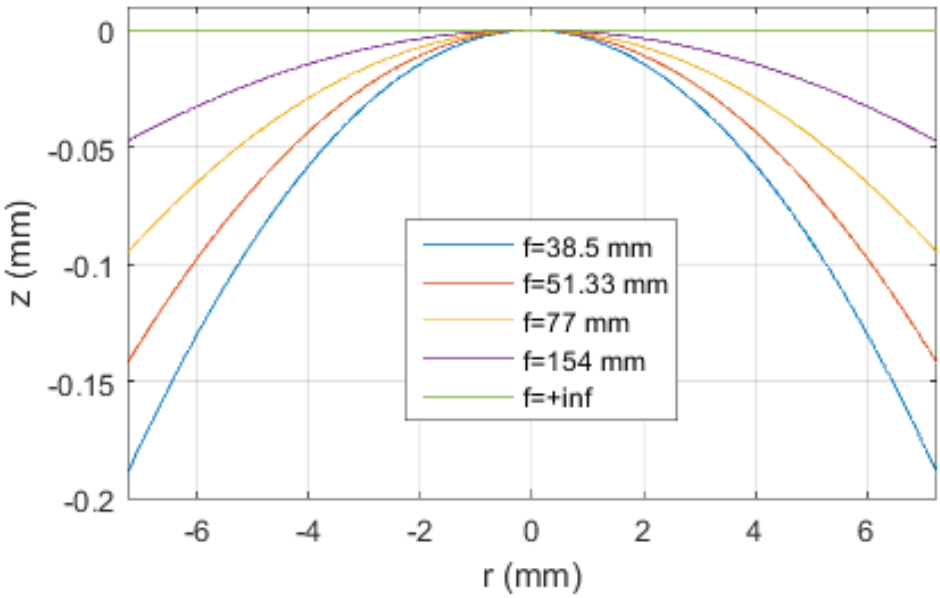

Fig. 4.3: Surface height profiles for multiple composite lenses of varying focal lengths.

Following the same design procedure as in Chapter 3, a set of polynomial coefficients for each height profile was numerically assigned to fit the polynomial equation, Eq. (2.7). Each set of coefficients are listed in Table 4.2 along with the average change, Δa_{2k}. Again, this system is defined to have a focal length of 77 mm when d = 0 mm, meaning the corresponding polynomial coefficients is inherently defined as the base component coefficients a_{2k}.

Table 4.2: Surface coefficients for multiple spherical lenses of varying focal lengths, along with the associated changes

a_{2k} values (mm^{-2k+1})	Focal Length					Avg. Δa_{2k} (mm^{-2k+1})
	38.5 mm (*d*=1.8mm)	**51.33 mm (*d*=0.9mm)**	**77 mm (*d*=0)**	**154 mm (*d*=-0.9mm)**	**inf (*d*=-1.8mm)**	
a_2	-7.24E-03	-5.43E-03	-3.62E-03	-1.81E-03	0.00E+00	-1.81E-03
a_4	6.80E-07	2.87E-07	8.50E-08	1.06E-08	0.00E+00	1.70E-07
a_6	-1.28E-10	-3.04E-11	-4.00E-12	-1.25E-13	0.00E+00	-3.20E-11
a_8	3.16E-14	4.40E-15	2.89E-16	3.56E-18	0.00E+00	7.91E-15
a_{10}	-5.48E-17	-1.23E-17	-1.61E-18	-5.11E-20	0.00E+00	-1.37E-17
a_{12}	6.84E-19	1.70E-19	2.31E-20	7.42E-22	0.00E+00	1.71E-19
a_{14}	-3.85E-21	-9.57E-22	-1.31E-22	-4.19E-24	0.00E+00	-9.61E-22

The variability coefficients b_{2k} were determined using Eq. (2.14), and are displayed in Table 4.3, along with the base coefficients a_{2k}. As before, the tilt term was determined by performing a parameter sweep to find the point at which the sag of the freeform surface was at a minimum. The resulting tilt term of 0.0262 decreased the sag from 360 μm to 214 μm over the 14.5 mm aperture diameter. Again, the reduction in sag is beneficial both for fabrication as well as allowing the two surfaces to be closer together, ultimately minimizing the potential error caused by the stand-off distance.

Table 4.3: Freeform surface coefficients for the Alvarez lens with a shifted focal range

Order (k)	a_{2k} Values (mm^{-2k+1})	b_{2k} values (mm^{-2k})
1	-3.6190E-03	-1.0051E-03
2	8.5045E-08	9.4472E-08
3	-3.9980E-12	-1.7762E-11
4	2.8850E-16	4.3921E-15
5	-1.6077E-18	-7.6125E-18
6	2.3135E-20	9.4941E-20
7	-1.3056E-22	-5.3408E-22

Fig. 4.4 displays the resulting base, variability, and freeform surfaces. In this case, the base component has noticeable surface curvature, as compare to the standard Alvarez lens (Fig. 4.1) which has no surface curvature for the base surface. This difference is a result of the system being designed to have optical power when there is no lateral shift in the system. Fig. 4.5 shows the comparison between this new design and the corresponding ‘standard’ Alvarez lens.

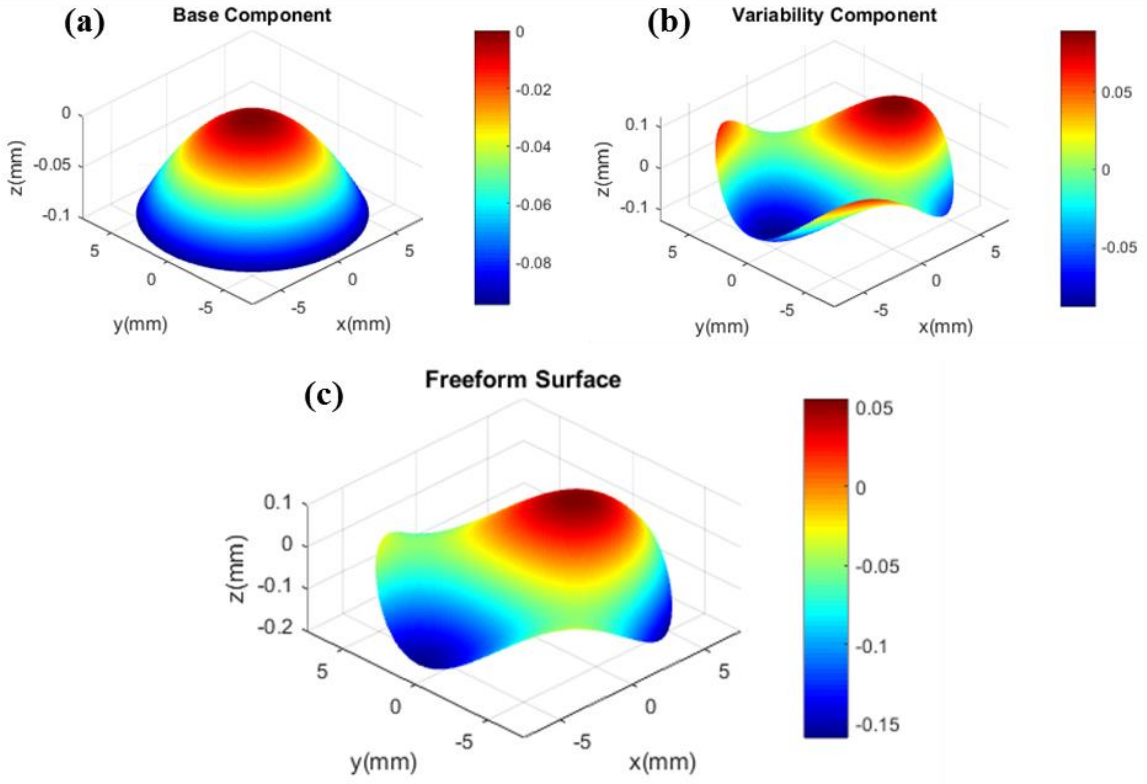

Fig. 4.4: Surface plots showing the (a) base component, (b) variability component, and (c) one of the two freeform surfaces for the IRG26 shifted focus Alvarez lens.

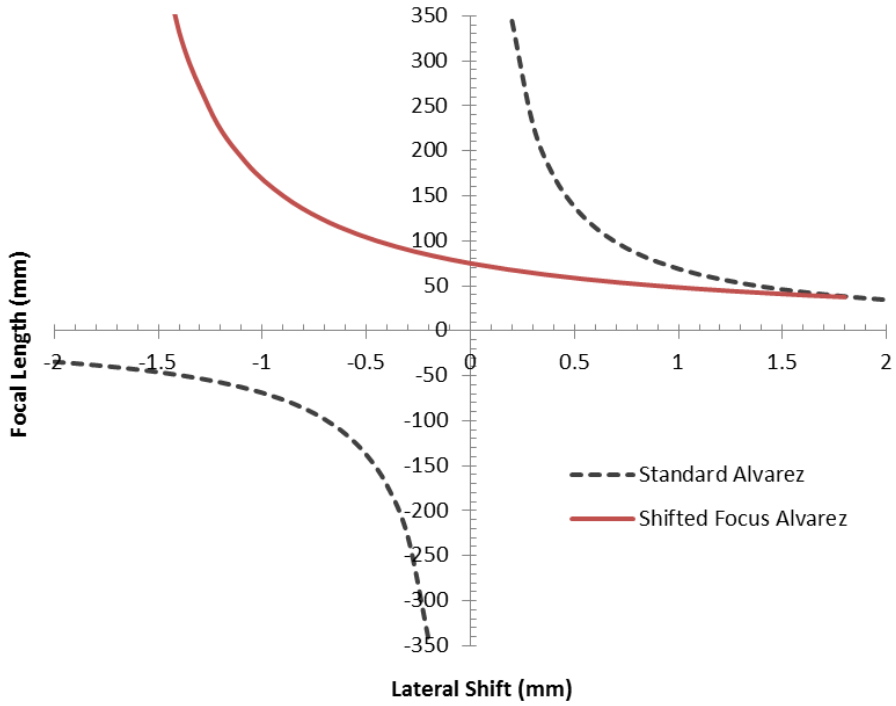

Fig. 4.5: Predicted focal length vs. lateral shift for the shifted focus Alvarez lens system compared to an equivalent standard Alvarez lens.

4.3 Optical modeling of the shifted focus Alvarez lens

Ray-based optical simulations were performed using ZEMAX® to better understand the performance of this device. These simulations assume a normally incident collimated input with a 4 μm wavelength and an 8 mm diameter aperture directly in front of the first element. As mentioned earlier, the design approach assumes a negligible air gap between the two freeform surfaces; however; a 400 μm standoff was added in the simulation setup. The center thickness of each freeform was set to 2.5 mm.

To characterize the focal length of the system, rays were traced through both freeform elements for several different amount of lateral shift *d*. The 'back distance', defined as the distance between the second element and the image plane, was recorded for each case. In order to find the image plane, the back distance was set as a variable and

ZEMAX's default RMS optimization algorithm was used to determine the location of the smallest RMS spot. Fig. 4.6 shows the results of geometrical ray-trace simulations for lateral shifts of d = -1.8 mm, d = 0 mm, and d = 1.8 mm.

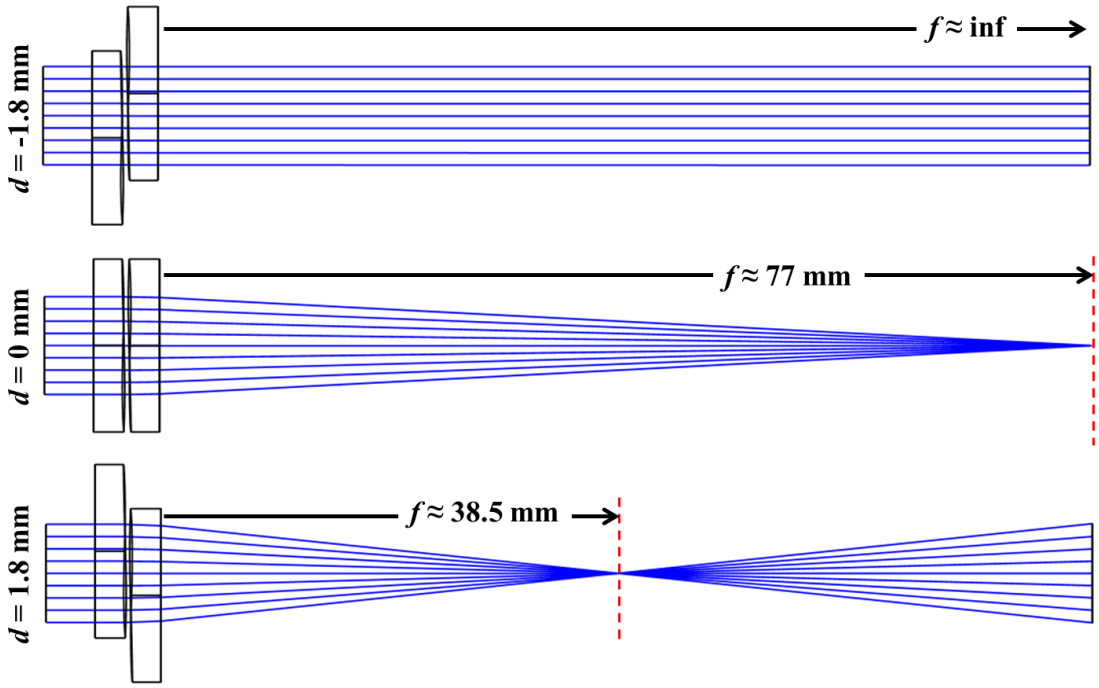

Fig. 4.6: Geometrical ray trace simulations of the shifted focus Alvarez lens for lateral shifts of d = -1.8 mm, d = 0 mm, and d = 1.8 mm.

It is important to note, as it was presented in [34, 35], that the back distance is not equivalent to the system focal length due to the thickness of each freeform element. To determine an accurate value for the focal length, the second principal plane location h_2 was calculated using the equation for a thick lens [126] given by,

$$h_2 = -\frac{f(n_l - 1)d_1}{ROC * n_l}, \tag{4.5}$$

where d_1 is the thickness of the lens, and ROC is the composite radius of curvature. The wavefront is only affected by the thickness of the second element, therefore d_1 = 2.5 mm.

From the Lensmaker's equation [126] the radius of curvature for a spherical lens is given by

$$ROC = f(n_l - 1). \tag{4.6}$$

By substituting *ROC* from Eq. (4.6) into Eq. (4.5), the location of the second principal plane is calculated as

$$h_2 = -\frac{d_1}{n_l} = -\frac{2.5}{2.79} = -0.896\ mm, \tag{4.7}$$

where the negative sign denotes the direction of which the plane is located with respect to the back surface of the second element. This means that the principal plane is located 0.896 mm to the left of the back surface, illustrated in Fig. 4.7. The system focal lengths were then calculated by adding 0.896 mm to the back distance values previously determined in the ZEMAX® simulations. Table 4.4 compares the resulting modeled focal lengths for this system to predicted values.

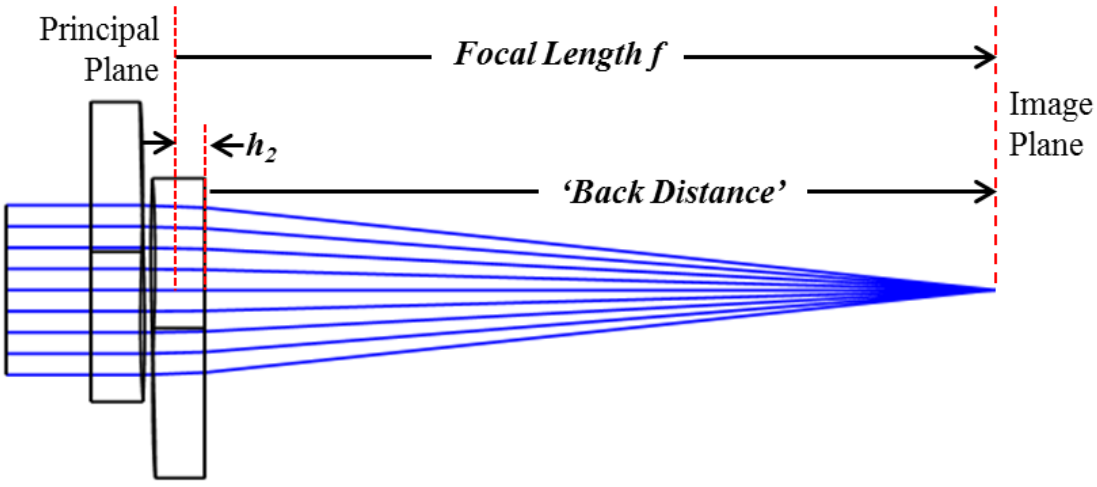

Fig. 4.7: Illustration of the second principal plane location h_2, added to the back distance to determine the effective focal length of this system.

Table 4.4: Focal lengths determined using ZEMAX® simulation models compared to theoretical values for different lateral shift increments.

Lateral Shift *d* (mm)	Theoretical Focal Length *f* (mm)	Simulated Focal Length *f* (mm)
-1.8	inf	inf
-1.35	308.00	310.29
-0.9	154.00	154.53
-0.45	102.67	102.82
0	77.00	77.01
0.45	61.60	61.53
0.9	51.33	51.21
1.35	44.00	43.85
1.8	38.50	38.32

As observed in Table 4.4, the focal lengths from the ZEMAX® simulations are in good agreement with predicted values. The slight differences between the two results are thought to result from geometrical aberrations introduced by the error terms (discussed in Chapter 2) that were assumed negligible for relatively small lateral shifts. These error terms are inherently dependent on lateral shift *d* which is why the difference between theoretical and simulated focal lengths increases as the magnitude of the lateral shift increases. Additional aberrations (relatively smaller) are caused by the inevitable air gap between the two freeform elements in the simulations.

Focal spot diagrams in ZEMAX® were also produced in to view the geometrical aberrations present in this system. Fig. 4.8 shows the spot diagrams in the image plane for lateral shifts d = -0.9 mm, d = 0 mm, and d = 1.8 mm. In each case, to assess the performance relative to the diffraction limit, the RMS spot radius was compared to the Airy disk radius, defined in ZEMAX® using the definition found in [127].

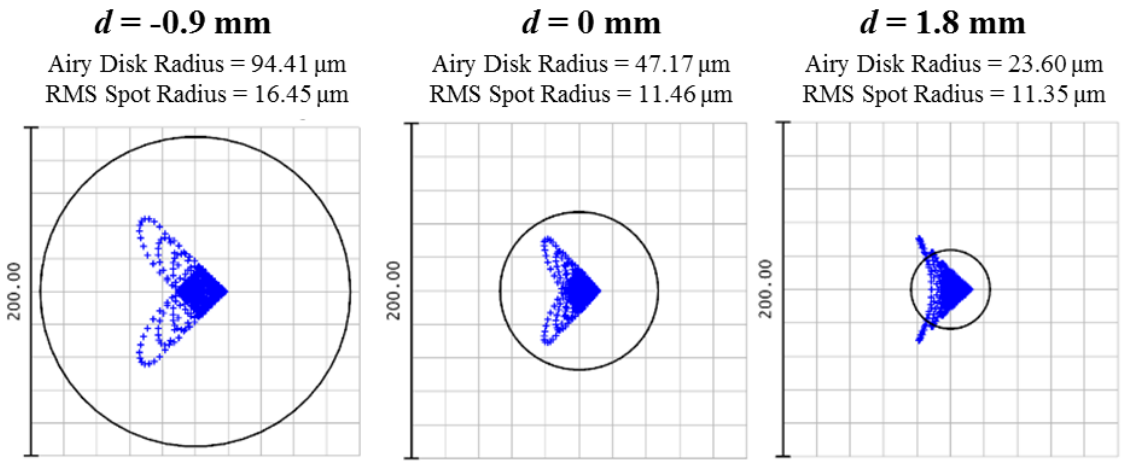

Fig. 4.8: Spot diagrams generated in ZEMAX® compared to the diffraction limited Airy disk for lateral shifts of d = -0.9 mm, d = 0 mm, and d = 1.8 mm.

The RMS spot radius and the Strehl ratio both provide quantitative metrics for the output image quality. The Airy disk radius defined as 1.22 times the wavelength times the system f-number, and the Strehl ratio S is defined as the ratio of the peak aberrated on-axis image intensity and peak on-axis non-aberrated image intensity [126]. A perfect system has a $Strehl = 1$ and a system is generally considered to be diffraction limited with $Strehl \geq 0.8$. Using these metrics, performance summary plots are presented in Fig. 4.9 across the defined range of focal lengths, comparing this design with the equivalent standard Alvarez lens design mentioned earlier. Though both systems would be considered diffraction limited based on the RMS spot size, the shifted focus Alvarez lens has significantly smaller spot sizes and better Strehl ratios. This improvement is largely due to the decrease in the surface height modulation; a byproduct of defining the focal range over the entire lateral shift range (+/d). A possible advantage, as a result of this improvement, could be the use of a larger aperture size, allowing for more light to be captured while remaining diffraction limited.

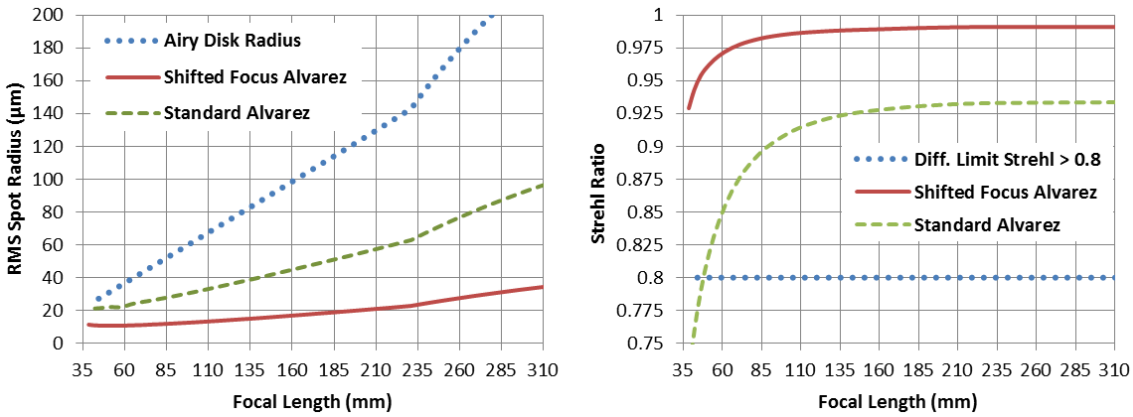

Fig. 4.9: Performance summary plots for the shifted focus Alvarez lens across the range of lateral shifts with regards to (left) RMS spot radius and (right) Strehl ratio.

To examine impacts of aperture diameter on performance, this system was simulated for a variety of aperture diameters ranging from 5 mm to 11 mm. For each simulation, the 'worst case' scenario was modeled (focal length at its minimum of f = 38.5 mm and the lateral shift at its maximum of d = 1.8 mm). Additionally, for each aperture diameter, the system was re-optimized to find the back focal distance location where the RMS spot radius was at its minimum. Fig. 4.10 shows spot diagrams in the image plane for aperture diameters of 6 mm, 8 mm, and 10 mm.

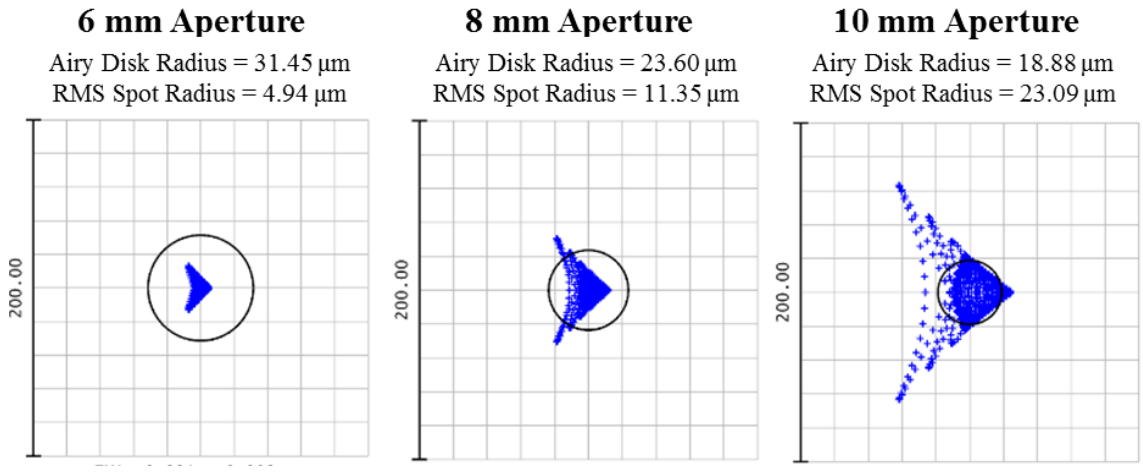

Fig. 4.10: Spot diagrams generated in ZEMAX® compared to the diffraction limited Airy disk for different aperture diameters of 6 mm, 8 mm, and 10 mm.

Performance summary plots for RMS spot radii and Strehl ratio of this device across the defined lateral shift range are presented in Fig. 4.11, where this system was again compared to the equivalent standard Alvarez lens design. As expected, we note that aberrations increase for both systems as the aperture diameter increases. For the shifted focus Alvarez, the Strehl ratio decreases below the diffraction limit at an aperture diameter of ~9.25 mm. This is notably better than the standard Alvarez design where the Strehl ratio decreases below the diffraction limit at an aperture diameter of ~7.5 mm. Furthermore, these results suggest that an 8 mm aperture diameter is an adequate choice for the experimental tests with regards to power throughput while remaining diffraction limited.

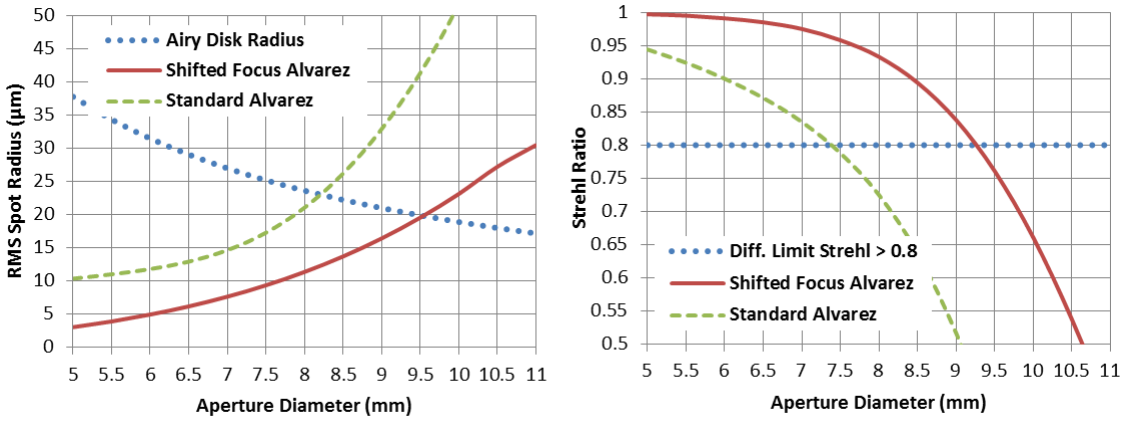

Fig. 4.11: Performance summary plots for the shifted focus Alvarez lens across a range of aperture diameters with regards to (left) RMS spot radius and (right) Strehl ratio.

4.4 Fabrication of the shifted focus Alvarez lens

The shifted focus Alvarez freeforms were fabricated in IRG26 chalcogenide glass [60, 122, 125], using a slow tool servo (STS) diamond turning machining process along with a toolpath generated by the same custom code employed in the previous example [122].

Fabrication was performed using a Moore Nanotech® 350 FG by Dr. John Troutman, Graduate Student at the UNC Charlotte Center for Precision Metrology. A controlled-waviness tool with nose radius of 1.5 mm, 7^o clearance, and 0^o top rake was selected for this machining process where the finishing path had a 7.5 µm depth of cut, 2.0 µm step-over per revolution, and a rotational rate of 16.66 rpm [125]. Similar to the previous examples in Chapter 3, monolithic slots were machined into the pedestal of the freeform surfaces to ensure proper rotational alignment in the optomechanical custom mounting assembly. The resulting IRG26 freeform elements are shown in Fig. 4.12.

Fig.4.12: Image of the two fabricated IRG26 freeform elements for the shifted focus Alvarez lens.

The fabricated surfaces were examined using a Zygo ZeGage Plus scanning white light interferometer (SWLI) where the test results indicated a surface roughness of 2 nm Ra, and a peak to valley form error of 1.726 µm with an RMS deviation of 100 nm [125]. Fig. 4.13 shows a cross-sectional slice of the measured surface data. *These measurements were performed by Daniel Barnhardt, Graduate Student at the UNC Charlotte Center for Precision Metrology*.

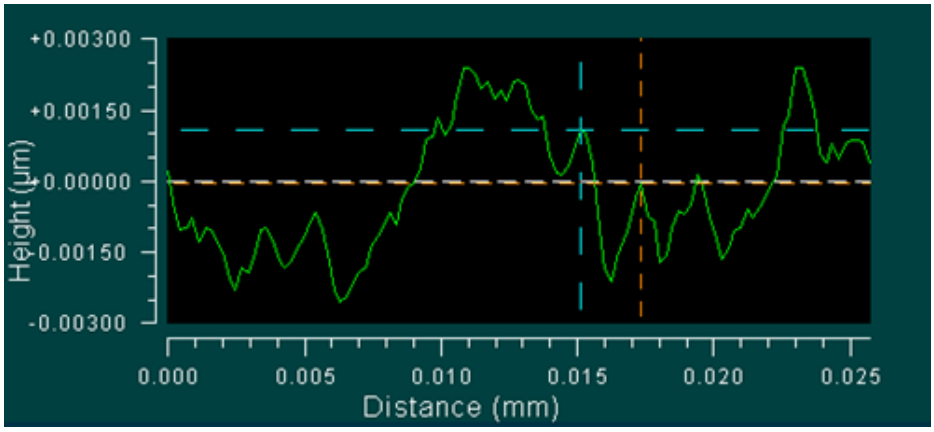

Fig. 4.13: Sample surface profile cross section from the SWLI data of the shifted focus Alvarez lens.

4.5 Experimental testing of the shifted focus Alvarez lens

Experimental testing began with installing the fabricated surfaces into the same custom mounting assembly discussed in Chapter 2. The experimental test used for this device followed the same setup and procedure used by Smilie *et al.* in previous work testing a standard IR Alvarez lens [34, 35], where the setup is explained in more detail. To review, this setup included a hot plate mounted normal to the table approximately 2.54 m away from a liquid nitrogen-cooled Indigo Phoenix™ thermal imaging camera along its optic axis. The hot plate, which emits at wavelengths throughout the near to mid-IR range, doubles as a light source and imaging object due to its pattern of coils being detectable. The freeform assembly was mounted onto a Newport ILS linear motion stage, which was then mounted in front of the IR camera such that the linear motion was along the *z* axis (optic axis). This motion stage was equipped with a digital controller, enabling control of the stage along the *z* axis with measurement accuracy of 100 nm over a 200 mm range. Fig. 4.14 shows a schematic from [35] of the experimental test setup.

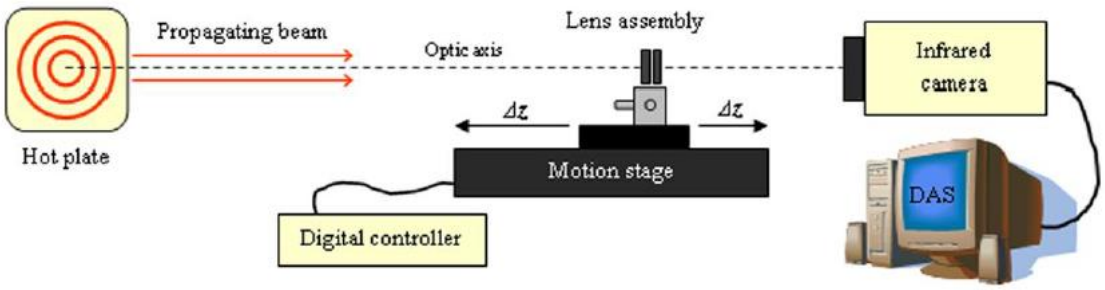

Fig. 4.14: Schematic of the experimental IR imaging test setup, where the lens assembly was moved along the *z* axis to form a clear image for each amount of lateral shift.

The optic was translated until the best focus position (image distance) was determined at several different amounts of lateral shifts, ranging from d = -0.8 mm to d = 1.1 mm in 0.1 mm increments. Each focus position was recorded three separate times, and the "near" and "far" blur locations were also recorded to provide a rough measurement of experimental error. This device was characterized by comparing the experimental focal length to the theoretical focal length. The focal length is related to the object (s_o) and image (s_i) distances by the well-known equation [126]

$$\frac{1}{f} = \frac{1}{s_o} + \frac{1}{s_i}. \tag{4.8}$$

By keeping the distance between the hot plate and detector at a constant value, the image distance can be equated to $s_i = 2540 - s_o$. Applying this to Eq. (4.8), we can solve for the focal length as a function of the measured image distance. This relationship is given in mm by,

$$f = \frac{s_i(2{,}540 - s_i)}{2{,}540}. \tag{4.9}$$

The experimental focal lengths for the corresponding lateral shifts were calculated using Eq. (4.9), and compared to the theoretical values calculated earlier. Fig. 4.15 displays

these results as well as the “near” and “far” blur values discussed previously, which are displayed as error bars in this plot.

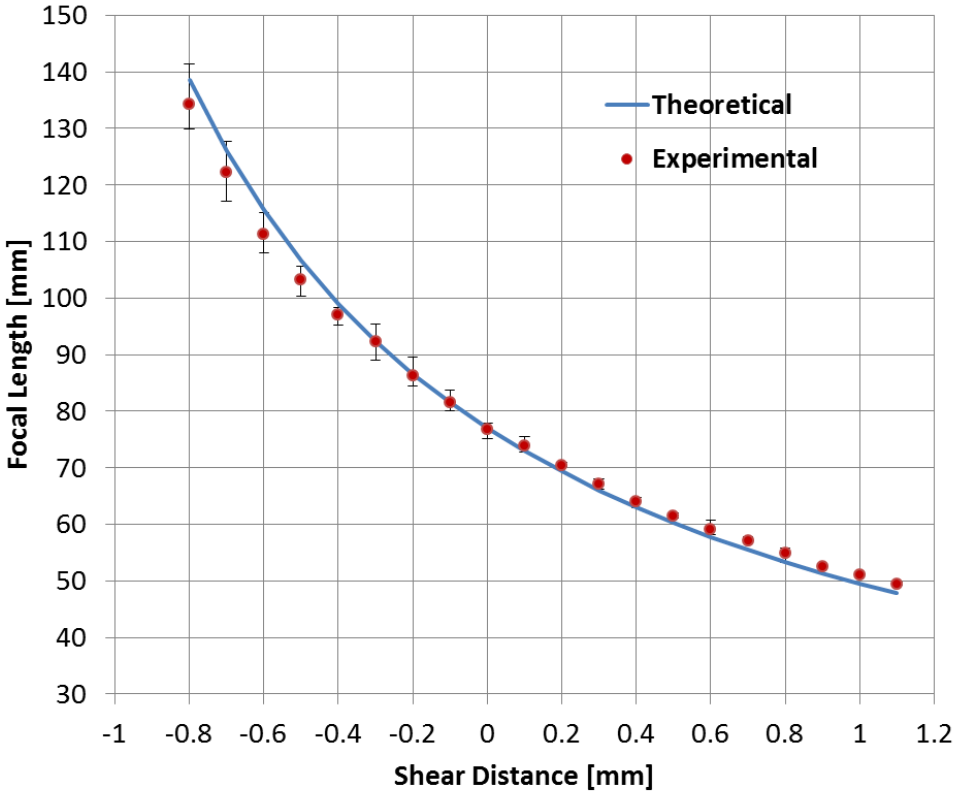

Fig. 4.15: Experimental focal length data for the shifted focus Alvarez lens, compared to the theoretical values along with the experimental error estimates.

The experimental results shown in Fig. 4.15 demonstrate a clear variation of focal length per lateral shift. There are slight differences between the experimental and theoretical focal lengths, but the results are generally in good agreement. These differences are thought to be a result of inaccurate recordings of the ‘best’ focus location due to the inherent depth of focus. We also note that there are likely small uncertainties in the object distance, detector array distance in the camera, and lateral shift increments.

Several images of the hot plate were obtained using the IR camera for several different lateral shifts with an 8 mm diameter aperture placed directly in front of the lens assembly. Fig. 4.16 shows images for lateral shifts of d = -0.8 mm, d = 0 mm, and d = 1.0 mm. The magnification changes seen in Fig. 4.16 are expected due to the inherent changing of focal length and changes in the object and image distances. The slight aberrations observed in the optical modeling appear to be insignificant in these images for the d = -0.8 mm and d = 0 mm cases. However, for the case where d = 1.0 mm, the image is noticeably worse. Some features on the optical table are now visible, while the features at the edge of the hot plate appear to be much brighter in comparison to the other images. This suggests that the IR camera was oversaturated at the point when this image was captured. This oversaturation is thought to be a direct product of imaging on the 'hotter' end of the heat cycle undergone by the hot plate, compared to the 'cooler' end of the heat cycle where the gain/offset of the IR camera was originally set for the images taken in Fig. 4.16(a) and Fig. 4.16(b).

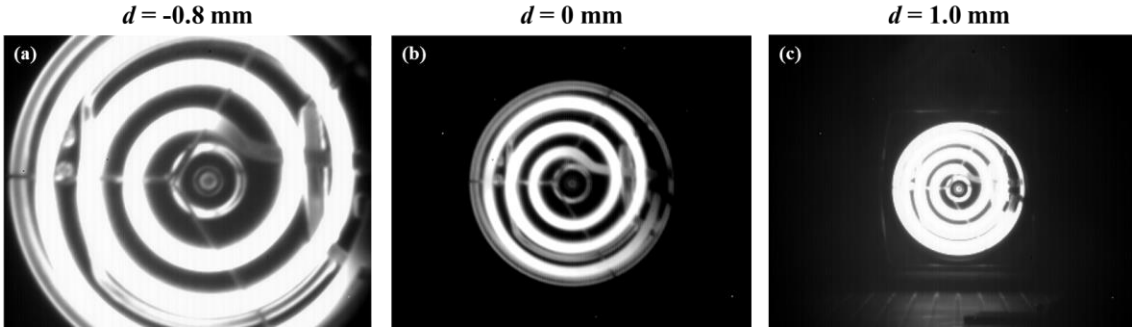

Fig. 4.16: Obtained images of the hot plate through for lateral shifts (a) d = -0.8 mm, (b) d = 0 mm, and (c) d = 1.0 mm.

4.6 Discussion

The standard Alvarez lens prescription inherently assumes that the system has no optical power (f = inf) at lateral shift d = 0. By implementing the design process used in the earlier examples, this device was expanded upon by shifting the focal range such that the system had a positive focal length across the entire lateral shift range +/-d, including when d = 0. This alteration in design resulted in a surface height modulation of 214 μm, which was 65 μm smaller than equivalent standard Alvarez lens. As a result, the performance was much improved, as the respective spot sizes were significantly smaller and the Srehl ratio was increased. Experimental tests of the STS diamond turned freeform elements were performed where the results were in good agreement with the theoretical results, further verifying the variable functionality of this optical system. Future work using this design procedure could include, for example different composite surfaces to realize aspheric lenses to further improve the system performance and capabilities. Additionally, this design process serves as an excellent *starting place* for designing dynamic freeform systems, where simulation software packages could later be used for optimization to further improve overall system performance.

CHAPTER 5: ADDITIONAL NOVEL DYNAMIC FREEFORM OPTICAL SYSTEMS

5.1 Introduction

Novel dynamic freeform optical systems were presented in previous chapters where the output functions (composite surfaces) were radially symmetric and the lateral shifts were constrained to one dimension along a single axis (x). The corresponding dynamic changes of the output functions were equal along the x and y directions, maintaining rotational symmetry in the outputs. In an effort to further expand on the design process for dynamic freeform optics, we now consider cases where the output is no longer radially symmetric. Additionally, we explore using lateral shifts along both the x and y axes, where the corresponding x and y dimensions of the optical output are varied independently of each other. In this chapter, three novel devices are presented; a variable square output beam shaper from 1-dimensional lateral shifts, a variable rectangular output beam shaper from 2-dimensional lateral shifts, and a variable toric lens from 2-dimensional lateral shifts.

5.2 Design of a square output beam shaper

Consider a component in which a circular Gaussian input irradiance is redistributed into a square uniform step function rather than the circular step function discussed in Chapter 2. We begin by defining a single optical element using a non-radially symmetric polynomial equation to define the composite surface which is representative of the optical function to be performed. This is where this work begins to differ from the radially

symmetric composite surface described by Eq. (2.2). The general non-radially symmetric polynomial equation is defined as,

$$z(x,y) = \sum_{k=1}^{n} (a_{2kx} * x^{2k} + a_{2ky} * y^{2k}) \tag{5.1}$$

where a_{2kx} and a_{2ky} represents the polynomial coefficients, dependent on index *k*, which control the overall shape or curvature of the surface in the *x* and *y* directions respectively. We note that this can again be used for any optical function, as long as it that can be accurately described accurately using this general polynomial equation.

As in the previous design process (originally derived in [35]) a ray mapping technique is used using radial coordinates to generate the required radially symmetric surface needed to perform the desired optical function. For this new non-symmetric case we follow the same basic steps as in [35] but in separable *x* and *y* coordinates. We begin by defining the Gaussian input beam irradiance as

$$I_1(x,y) = \exp\left[-2\left(\frac{x^2}{{w_{0x}}^2} + \frac{y^2}{{w_{0y}}^2}\right)\right], \tag{5.2}$$

where w_{ox} and w_{oy} are the beam waist radii, defined as the radius for which the irradiance has fallen to $1/e^2$ times its value at the *x* and *y* axes, respectfully [128, 129]. Because radial symmetry is no longer a constraint, the mathematical framework can be separated into two different components. More specifically, the input irradiance is separated into an *x* and *y* term, given by,

$$I_{1x} = I_1(x,0), I_{1y} = I_1(0,y). \tag{5.3}$$

It is important to note that the separation of the x and y components will continue for the remainder of this particular section, and for brevity, only the solution for the x term is shown here. The exact same procedure is employed using the y term.

After separating the input irradiance, conservation of energy is implemented to equate the energy contained within a defined input radius to the energy contained within the defined output spot area. This energy conservation condition is defined as,

$$\int_0^{x_0} I_{1x}(x)dx = \int_0^{X_0} I_{2x}(X)dX, \tag{5.4}$$

where I_{1x} and I_{2x} are the irradiance distributions for the input and output spot, and the spot side lengths along the specified axis for the input and output spot are labeled as x_0 and X_0, respectively. Expanding the integral on the left side of Eq. (5.4) yields,

$$\int_0^{x_0} I_{1x}(x)dx = \int_0^{x_0} \exp[-2\left(\frac{x}{w_{0x}}\right)^2]dx = \frac{{w_{0x}}^2}{4}\{1 - \exp\,[-2\left(\frac{x_0}{w_{0x}}\right)^2]\}. \tag{5.5}$$

The output irradiance distribution is defined to be a step function with a constant output irradiance given by I_{0x}, for $0 \leq X \leq X_0$. Integrating the right side of Eq. (5.4) yields,

$$\int_0^{X_0} I_{2x}(X)dX = I_{0x}\int_0^{X_0} XdX = \frac{1}{2}I_{0x}X_0^2. \tag{5.6}$$

I_{0x} can now be solved for by setting Eq. (5.5) to Eq. (5.6), providing the constant output irradiance for which the energy conservation condition is met:

$$I_{0x} = \frac{{w_{0x}}^2}{2{X_0}^2}\left\{1 - \exp\left[-2\left(\frac{x_0}{w_{0x}}\right)^2\right]\right\}. \tag{5.7}$$

Next, several rays are mapped from the input to the output to determine the corresponding input and output axial coordinate relationship. Using Eq. (5.4), x and X are left as variables and again inserted into Eq. (5.5) and Eq. (5.6). These two equations are

set equal to each other. Solving for output spot coordinate X as a function of input coordinate x, yields the ray mapping function, given by

$$X(x) = \frac{{w_{0x}}^2}{2I_{0x}}\{1 - \exp[-2\left(\frac{x}{w_{0x}}\right)^2]\}^{1/2}. \tag{5.8}$$

Following the detailed derivations from [2, 13], Snell's law and other geometric considerations are used to derive a differential equation. This differential equation was then used in combination with Eq. (5.8) to solve for a nominal surface height profile z_x which represents the composite surface required to perform the desired optical function. The differential equation is given by

$$\frac{dz_x}{dx} = \frac{X - x}{(n_l - 1)[z_0 - z_x(x)]}, \tag{5.9}$$

where z_x is the surface height profile, n_l is the refractive index, and z_0 is the target location where the light output will be in the desired form. This height profile is then fit to the polynomial equation, numerically defining the a_{2kx} coefficients. As before, the base component is symmetric across the x-axis, so $z_b(x,y) + z_b(-x,y) = 2z_b(x,y)$. Because this handles the specific case where there is no lateral shift, the base component z_b can be defined using Eq. (5.1). The component is halved due to the eventual combination of the two freeforms. The base component along the x direction of the lens is therefore defined as,

$$z_x(x) = \sum_{k=1}^{n} \frac{1}{2}(a_{2kx} * x^{2k}). \tag{5.10}$$

As mentioned at the beginning of this section, the x and y components were treated separately, where Eq. (5.10) is the x component. The same process is followed in order to define z_y, with the option of changing different parameters based on the desired output,

i.e. square or rectangular shape. After going through the process again to determine the a_{2ky} coefficients, the resulting base component is defined as,

$$z_b(x,y) = z_x(x) + z_y(y) = \sum_{k=1}^{n} \frac{1}{2}(a_{2kx} * x^{2k} + a_{2ky} * y^{2k}). \tag{5.11}$$

The next step is to define multiple beam shapers of varying output parameters which will be used when determining the variability components. For the two variable square output beam shaper examples presented in the following sections, the base component will have the same form, while the variability components will differ based on the lateral shift functionality (1-dimensional and 2-dimensional).

5.3 Variable square output beam shaper from a 1D lateral shift

5.3.1 General analysis defining the variability component

The first example presented is a variable square output beam shaper in which the output spot side lengths are varied in both the *x* and *y* directions *simultaneously* when the freeform surfaces are laterally shifted along the *x*-axis. We previously noted that the base component will take the form of Eq. (5.11); however, the variability component must still be defined. To this end, we utilize the result from Palusinski [44] that shows the desired composite surface *z(x,y)* is the derivative of the freeform surface z_f. This implies that the variability component can be defined as the integral of the composite surface with respect to the *x*-axis (lateral shift axis). With this in mind, the variability component (ignoring the constant) is given by

$$z_v(x,y) = \sum_{k=1}^{n} b_{2k} \int (x^{2k} + y^{2k})dx = \sum_{k=1}^{n} b_{2k} \left(\frac{x^{2k+1}}{(2k+1)} + y^{2k}x \right), \tag{5.12}$$

where b_{2k} represents the polynomial coefficients for the variability component. The integral in Eq. (5.12) is performed with respect to *x* because the only lateral shift is along the *x*-axis. Furthermore, the integral is performed on the *x* terms as well as the *y* terms because we want simultaneous variability of the output in the *x* and *y* direction per the lateral shift along the *x*-axis. With this in mind, we combine Eq. (5.11) with Eq. (5.12) to mathematically define the freeform surface as,

$$z_f(x,y) = \sum_{k=1}^{n} [\frac{1}{2}(a_{2kx} * x^{2k} + a_{2ky} * y^{2k}) + b_{2k}(\frac{x^{2k+1}}{(2k+1)}) + y^{2k} * x] + c_0 x, \tag{5.13}$$

where c_0 is the tilt term which is used to minimize the overall sag of the surface without affecting the optical properties.

The next step is to determine the b_{2k} coefficients found in Eq. (5.13). We complete this by calling on Eq. (2.1) and Eq. (5.13), while introducing a lateral shift *d* along the *x*-axis. The combined composite surface with the introduced lateral shifts in the appropriate direction is given by,

$$\begin{aligned} Z_c(x,y,d) &= z_b(x+d,y) + z_b(-(x-d),y) \\ &\quad + z_v(x+d,y) + z_v(-(x-d),y) \\ &= \sum_{k=1}^{n} [a_{2kx} * x^{2k} + a_{2ky} * y^{2k} + 2db_{2k}(x^{2k} + y^{2k}) + \varepsilon(x,y,d)], \end{aligned} \tag{5.14}$$

where $\varepsilon(x,y,d)$ represents the combined error terms that come out of the integration which were determined to be negligible if the lateral shift *d* is small. In an attempt to simplify the equation for brevity purposes, we let $a_{2kx} = a_{2ky} = a_{2k}$, which means the curvature will

be the same in both the *x* and *y* directions, resulting in a square output shape. With this simplification we can define the combined composite surface as,

$$Z_c(x,y,d) = \sum_{k=1}^{n} (a_{2k} + 2db_{2k}) * (x^{2k} + y^{2k}) = \sum_{k=1}^{n} a_{2k}'(d) * (x^{2k} + y^{2k}). \tag{5.15}$$

Here the lateral shift *d* again represents the amount of displacement for one freeform lens, meaning the total displacement between both freeform lenses is $2d$. This is very similar to the previous radially symmetric examples, where the only subtle difference is seen in the root polynomial equation, as desired. Similar to before, we see that the curvature/power of the composite surface is, as expected, a function of lateral shift. This means the same linear relationship exists between a_{2k}' and lateral shift *d* as in the radially symmetric examples. Hence, the same approach given by Eq. (2.14) was used to determine the b_{2k} coefficients, stated again as,

$$b_{2k} = \frac{\Delta a_{2k}}{2\Delta d}. \tag{5.16}$$

As stated previously in Chapter 2, Δa_{2k} is the average change per unit Δd, meaning that with every unit of lateral shift introduced in the system, there will be a change in the overall combined composite surface coefficient.

5.3.2 Optical design

To stay consistent with the previous examples, we keep much of the same design parameters as the previous beam shaping examples. The design parameters are summarized in Table 5.1. Multiple beam shapers with different output spot side lengths

were designed using the ray mapping procedure detailed in the previous section. Fig. 5.1 shows each composite surface profile on the same scale across the 12 mm aperture.

Table 5.1: Design parameter summary for the variable square beam shaper.

Design Parameters	
Wavelength:	632.8 nm
Input Waist Diameter	6 mm
Material/index:	PMMA/n_l=1.49
Aperture Diameter:	12 mm
Target Distance:	150 mm
Output Side Length Range:	2x2 $\leq X_0$x$Y_0 \leq$ 6x6 mm
Lateral Shift Range:	$-300 \leq d \leq 300$ μm

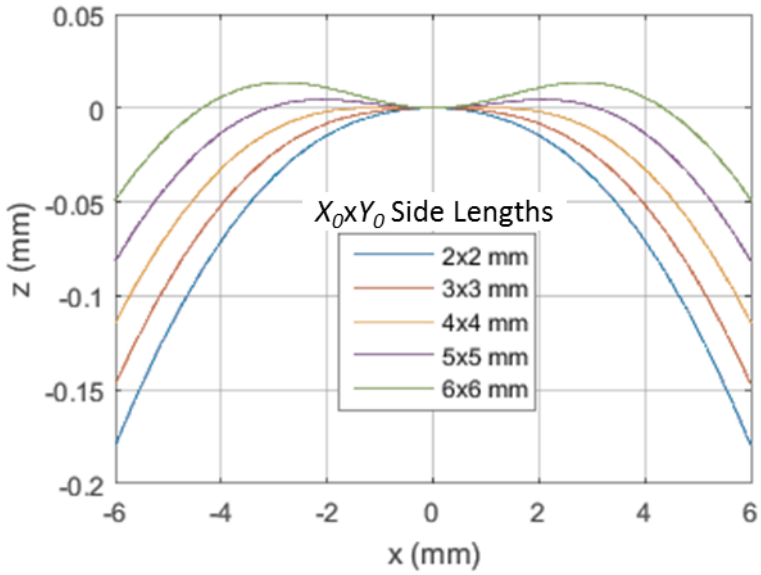

Fig. 5.1: Surface height profiles for multiple beam shapers with various output spot side lengths.

Following the same procedure as before, a set of polynomial coefficients was fit to Eq. (5.1) for each surface height profile. The resulting coefficients are listed in Table 5.2 along with the average change, Δa_{2k}. Because this beam shaper is designed to have a 4 mm output side length with no lateral shift in the system, the corresponding polynomial

coefficients (a_{2kx} and a_{2ky}) for that output are the base component coefficients for the *x* and *y* directions. Eq. (5.16) was then used to determine the variability coefficients (b_{2k}) displayed in Table 5.3 along with the base coefficients, a_{2k}.

Table 5.2: Surface coefficients for a square beam shaper with five different output spot side lengths and the associated changes.

a_{2k} values (x&y) (mm^{-2k+1})	Output X & Y Side Length					Avg. Δa_{2k} (mm^{-2k+1})
	2x2 mm (*d*=300µm)	3x3 mm (*d*=150µm)	4x4 mm (*d*=0)	5x5 mm (*d*=-150µm)	6x6 mm (*d*=-300µm)	
a_2	-3.19E-03	-1.38E-03	4.30E-04	2.24E-03	4.05E-03	-1.81E-03
a_4	-1.33E-04	-1.99E-04	-2.65E-04	-3.31E-04	-3.97E-04	6.62E-05
a_6	5.57E-06	8.35E-06	1.11E-05	1.39E-05	1.67E-05	-2.78E-06
a_8	-1.85E-07	-2.77E-07	-3.69E-07	-4.61E-07	-5.53E-07	9.21E-08
a_{10}	4.25E-09	6.36E-09	8.48E-09	1.06E-08	1.27E-08	-2.11E-09
a_{12}	-5.81E-11	-8.71E-11	-1.16E-10	-1.45E-10	-1.74E-10	2.89E-11
a_{14}	3.50E-13	5.25E-13	6.99E-13	8.73E-13	1.05E-12	-1.74E-13

Table 5.3: Freeform surface coefficients for variable square output beam shaper.

Order (k)	a_{2kx} (mm^{-2k+1})	a_{2ky} (mm^{-2k+1})	b_{2k} (mm^{-2k})
1	4.3021E-04	4.3021E-04	-6.0315E-03
2	-2.6511E-04	-2.6511E-04	2.2072E-04
3	1.1124E-05	1.1124E-05	-9.2525E-06
4	-3.6927E-07	-3.6927E-07	3.0703E-07
5	8.4816E-09	8.4816E-09	-7.0494E-09
6	-1.1601E-10	-1.1601E-10	9.6390E-11
7	6.9909E-13	6.9909E-13	-5.8068E-13

The tilt term was determined by performing a parameter sweep to find the point at which the sag of the freeform surface was at a minimum. The resulting tilt term of 0.06 decreased the sag from 837 µm to 326 µm over the 12 mm aperture diameter. Eq. (5.13) was then used with these coefficients to define the freeform surface. The resulting base, variability, and freeform surfaces are displayed in Fig. 5.2.

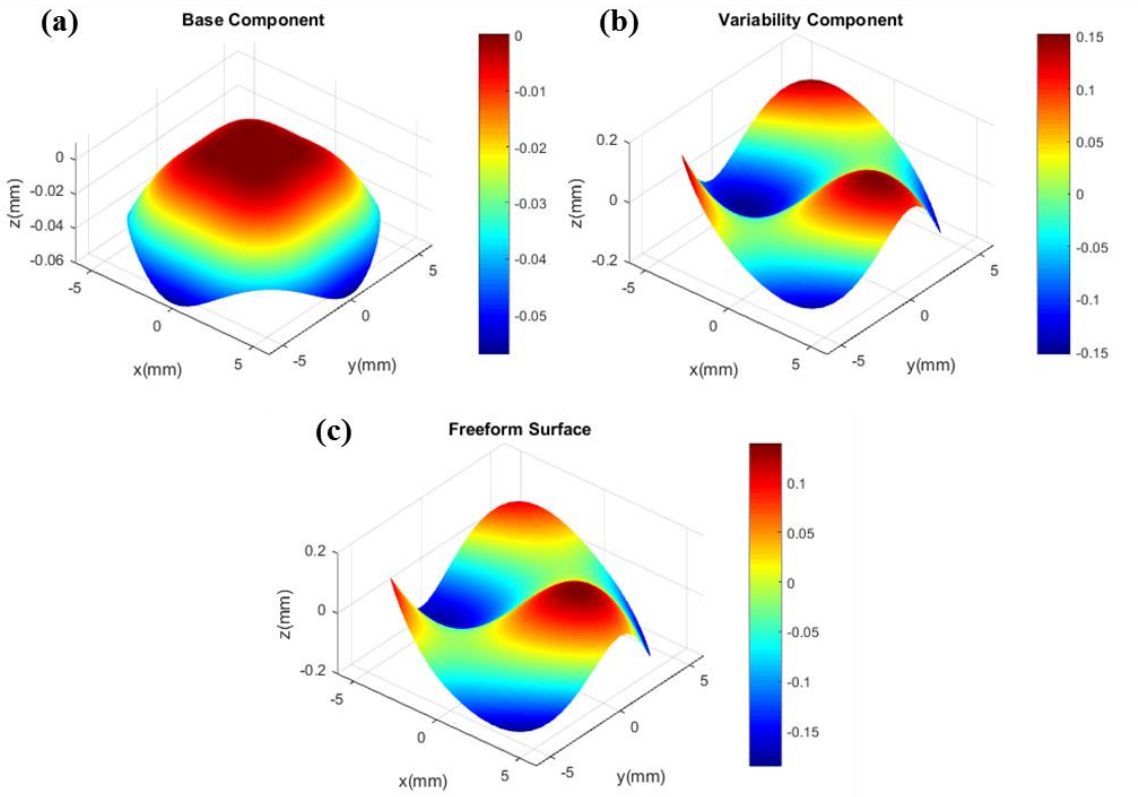

Fig. 5.2: Surface plots showing the (a) base component, (b) variability component, and (c) one of the two freeform surfaces for the variable square beam shapers

5.3.3 Optical modeling

As before, we used VirtualLab™ to simulate this dynamic optical system. The surface coefficients defined in Table 5.3 were imported into the software as plano-freeform surfaces with 400 µm standoff distance between the freeform surfaces. The propagation method used for all simulations was the combined SPW/Fresnel propagation operator [111]. The sampling distance of the output light field was set to 4.5 x 4.5 µm over a 9 x 9 mm window. The "Beam Parameters" function was used to determine the diameter of the output spot relative to the centroid at the target distance (150 mm).Table 5.4 shows the input diameter with the expected output side lengths X_0 and Y_0 and simulated output side

lengths X_0 and Y_0 for the corresponding lateral shifts. The predicted results were in good agreement with simulated results from VirtualLab™.

Table 5.4: Predicted and modeled input and output spot side lengths for several amounts of lateral shift.

Lateral Shift d (μm)	Input Diameter (mm)	Predicted Output X_0 x Y_0 (mm)	VirtualLab™ Output X_0 x Y_0 (mm)
-300	6.0	6.0 x 6.0	5.950 x 5.950
-150	6.0	5.0 x 5.0	4.982 x 4.982
0	6.0	4.0 x 4.0	3.988 x 3.988
150	6.0	3.0 x 3.0	2.988 x 2.988
300	6.0	2.0 x 2.0	1.991 x 1.991

Fig. 5.3 shows VirtualLab™ simulation results for output spots with lateral shifts of 0 μm, +/-150 μm, and +/-300 μm, as well as the round, Gaussian input. The redistribution of energy can be seen where the output spots are highly uniform. We note that the output irradiance profiles have an undesired spike of energy along the edges (Gibb's phenomenon) as a consequence of defining the output as a step-function. These spikes could be eliminated using the super-Gaussian output irradiance profile, as discussed in Chapter 3. Additionally, the shape of the output spot is now a square with varying side lengths which was assumed when we let $a_{2kx} = a_{2ky} = a_{2k}$. It should be noted that, if desired, the output shape could be a rectangle with equally varying side lengths, depending on the freeform surface coefficients a_{2kx}, a_{2ky}, and b_{2k}.

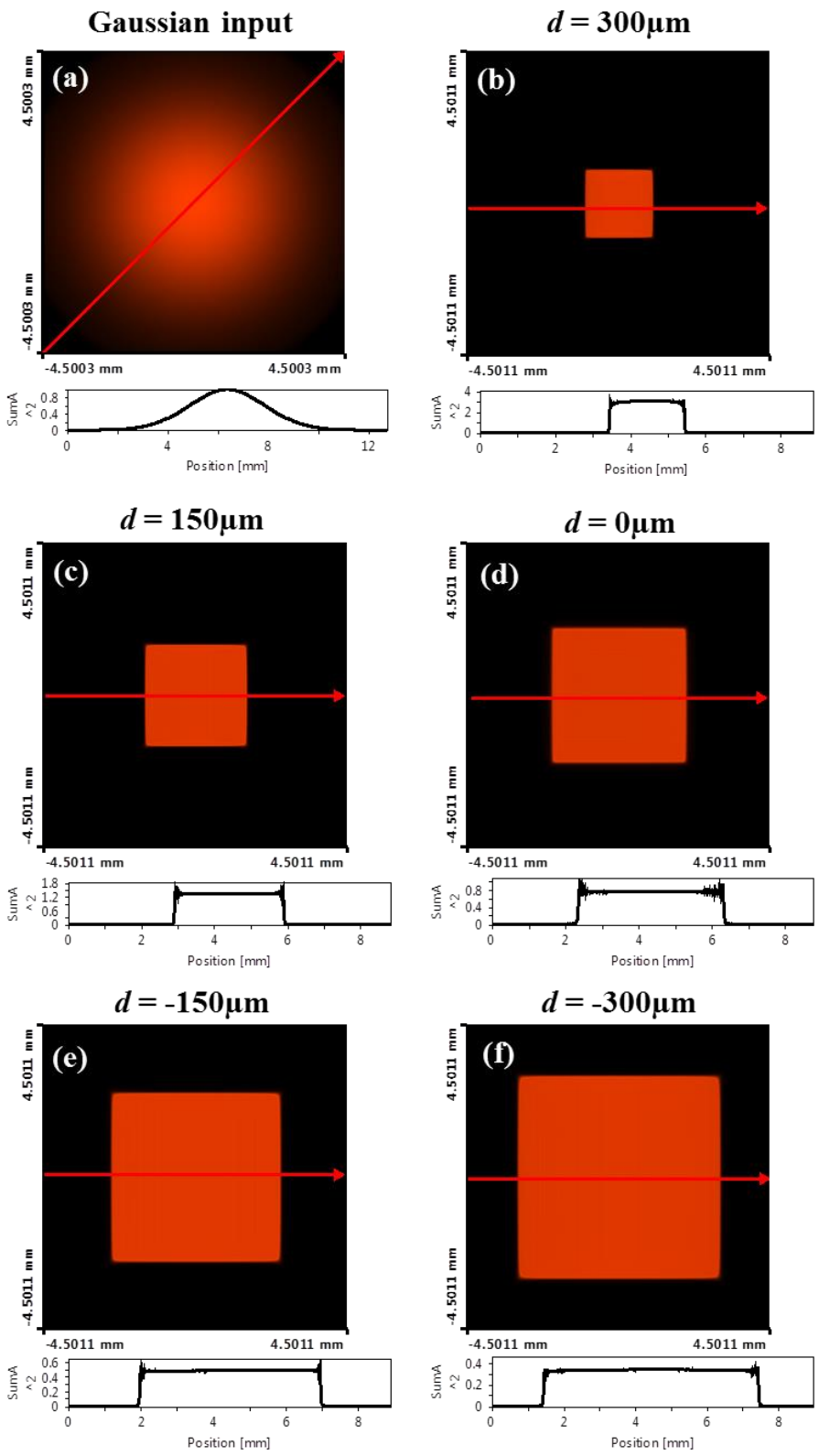

Fig. 5.3: Six VirtualLab™ images and 1-D profiles, (a) Gaussian input, (b) d = 300 µm, (c) d = 150 µm, (d) d = 0.0 mm, (e) d = –150 µm, and (f) d = –300 µm.

5.4 Variable rectangular output beam shaper from 2D lateral shifts

5.4.1 General analysis defining the variability component

For the next example, we consider a similar beam shaper in which we independently vary the dimensions of a rectangular flat-top (step-function) output spot using 2-dimensional lateral shifts; the output size varies in the *y*-direction when the freeform surfaces are laterally shifted parallel to the *y*-axis, and the output size varies in the *x*-direction when the freeform surfaces are laterally shifted parallel to the *x*-axis. We assume the same base optical function as the previous example; the base component is thus defined using Eq. (5.11).

We define the variability component using the approach from Section 5.3.1 in which the desired composite surface is the derivative of the freeform surface. The desired composite surface in this example must be separable along the *x* and *y* axes because we want independent output variations along *x* and *y* directions with corresponding lateral shifts d_x and d_y. Thus, we separate the *x* and *y* components of the composite surface and integrate the *x* terms with respect to the *x*-axis, and integrate the *y* terms with respect to the *y*-axis. The resulting variability component is given by

$$\begin{aligned} z_v(x,y) &= \sum_{k=1}^{n} [\ (b_{2kx} \int x^{2k} dx) + (b_{2ky} \int y^{2k} dy)\ ] \\ &= \sum_{k=1}^{n} [\ b_{2kx} * \frac{x^{2k+1}}{(2k+1)} + b_{2ky} * \frac{y^{2k+1}}{(2k+1)}\ ], \end{aligned} \tag{5.17}$$

where b_{2kx} and b_{2ky} represent the variability coefficients for the *x* and *y* directions, respectively. The base component, defined in Eq. (5.11), is then combined with Eq. (5.17) to mathematically describe the freeform surface as

$$z_f(x,y) = \sum_k^n [\frac{1}{2}(a_{2kx} * x^{2k} + a_{2ky} * y^{2k}) + b_{2kx} * \frac{x^{2k+1}}{(2k+1)} + b_{2ky} * \frac{y^{2k+1}}{(2k+1)}] + c_{0x} * x + c_{0y} * y, \tag{5.18}$$

where c_{0x} and c_{0y} are the tilt terms for the x and y axes, respectively, used to minimize the overall sag of the surface without affecting the optical properties.

In order to view the relationship between lateral shift and composite surface profile, we again combine the freeforms, while introducing a lateral shift d_x along the x-axis and lateral shift d_y along the y-axis. The combined composite surface with the introduced lateral shifts in the appropriate direction is given by,

$$\begin{aligned} Z_c(x,y,d_x,d_y) &= z_b(x+d_x, y+d_y) + z_b(-(x-d_x), -(y-d_y)) \\ &\quad + z_v(x+d_x, y+d_y) + z_v(-(x-d_x), -(y-d_y)) \\ &= \sum_{k=1}^{n} (a_{2kx} + 2d_x b_{2kx}) * x^{2k} + (a_{2ky} + 2d_y b_{2ky}) * y^{2k} \\ &\quad + \varepsilon(x,y,d_x,d_y), \end{aligned} \tag{5.19}$$

where $\varepsilon(x,y,d_x,d_y)$ represents the combined error terms, deemed negligible when d_x and d_y are small. We see that the surface curvature in the x direction is linear with respect to the lateral shift along the x-axis, independent of the lateral shift along the y-axis. Similarly, the surface curvature in the y direction is independent of the lateral shift along the x-axis. With this in mind, we define the variability coefficients in a similar fashion as in Eq. (5.16), now defined as,

$$b_{2kx} = \frac{\Delta a_{2kx}}{2\Delta d_x}, b_{2ky} = \frac{\Delta a_{2ky}}{2\Delta d_y}, \tag{5.20}$$

where Δa_{2kx} and Δa_{2ky} represent the average change in surface curvature per unit Δd_x and Δd_y, respectively.

5.4.2 Optical design

In order to draw direct comparisons to the previous example in section 5.3, all of the same base input parameters were used. The output spot was designed to be a uniform 4 x 4 mm square when there is no lateral shift in the system in either direction, which means $a_{2kx} = a_{2ky}$, as before. The output spot side lengths were defined to have the same range from 2 mm to 6 mm over lateral shift range d = +/-300 μm in both the x and y directions; with every lateral shift of Δd_x =150 μm, there will be a 1 mm change in output side length in the x direction. Similarly, with every lateral shift of Δd_y =150 μm, there will be a 1 mm change in output side length in the y direction.

Multiple beam shapers with different output spot side length configurations were designed using the ray mapping procedure defined previously. Fig. 5.4 shows a grid of composite surfaces for several different configurations of lateral shift, all of which are on the same scale across the 12 mm aperture.

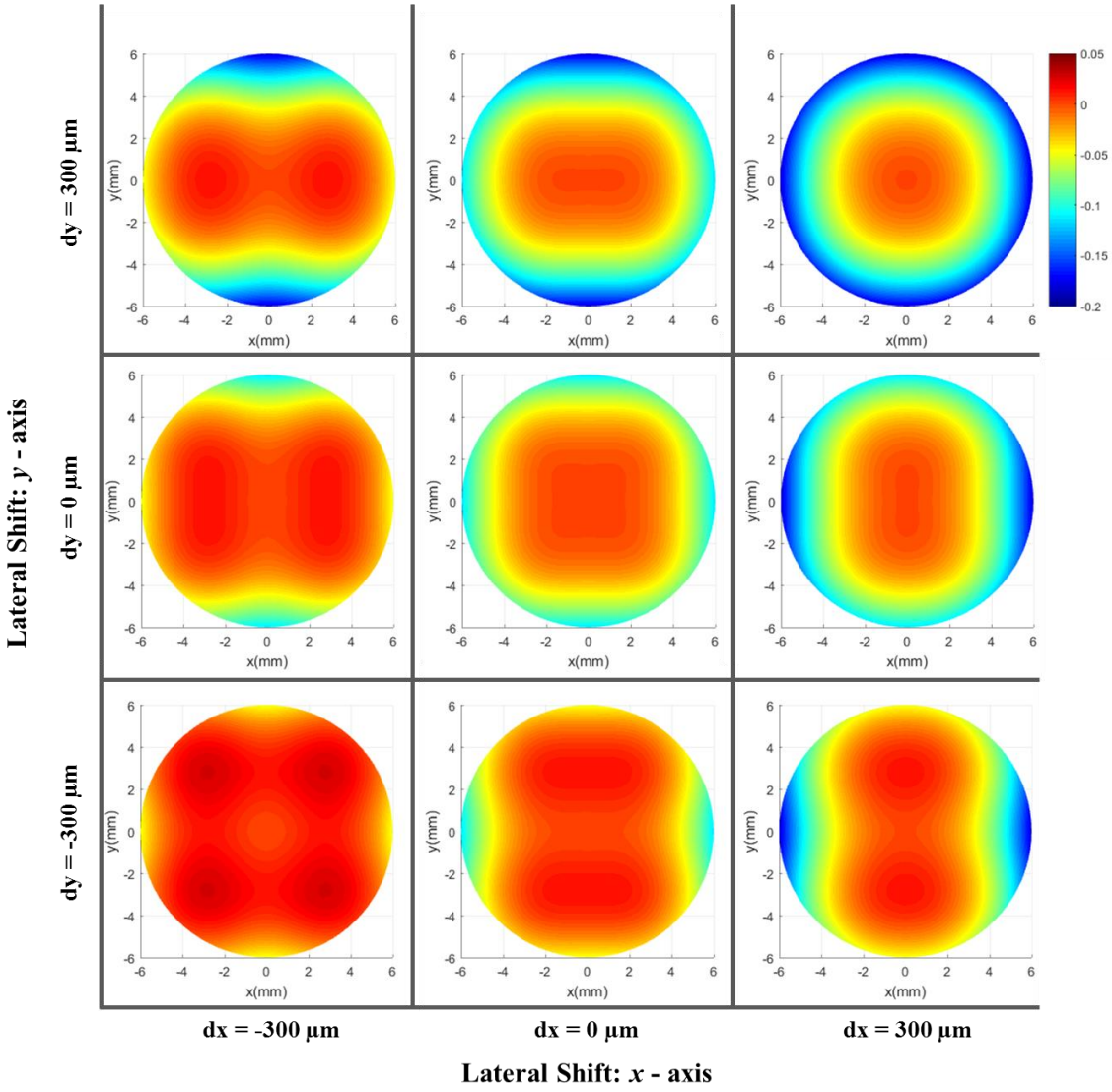

Fig. 5.4: Composite rectangular beam shaping surface profiles for several different configurations of *x* and *y* lateral shifts, all of which are on the same color scale.

A set of polynomial coefficients was then fit to Eq. (5.1) for each surface height profile. Since the same base parameters and side length ranges were chosen, the cross-sectional profiles for each of the composite surfaces are the same as in Section 5.3, listed in Table 5.1. This means that this device has the same a_{2k} and b_{2k} coefficients for the *x* and *y* directions; the main difference ends up being in the mathematical description of the

freeform lens. The surface coefficients for the base component and variability component are listed in Table 5.5.

Table 5.5: Freeform surface coefficients for the variable rectangular output beam shaper.

Order (k)	**a_{2kx} (mm^{-2k+1})**	**a_{2ky} (mm^{-2k+1})**	**b_{2kx} (mm^{-2k})**	**b_{2ky} (mm^{-2k})**
1	4.3021E-04	4.3021E-04	-6.0315E-03	-6.0315E-03
2	-2.6511E-04	-2.6511E-04	2.2072E-04	2.2072E-04
3	1.1124E-05	1.1124E-05	-9.2525E-06	-9.2525E-06
4	-3.6927E-07	-3.6927E-07	3.0703E-07	3.0703E-07
5	8.4816E-09	8.4816E-09	-7.0494E-09	-7.0494E-09
6	-1.1601E-10	-1.1601E-10	9.6390E-11	9.6390E-11
7	6.9909E-13	6.9909E-13	-5.8068E-13	-5.8068E-13

The tilt terms c_{0x} and c_{0y} were both determined by performing parameter sweeps to find the point at which the sag of the freeform surface was at a minimum. The resulting tilt term of 0.0304 decreased the sag from 542 μm to 258 μm over the 12 mm aperture diameter with respect to the un-tilted surface. Eq. (5.18) was then used with these coefficients to define the freeform surfaces. Fig. 5.5 displays the resulting base, variability, and freeform surfaces. Similar to the first square beam shaper example, the output spot was designed to be a 4 x 4 mm square with no lateral shifts. It should be noted that this is not a constraint, and was only done this way for brevity in the presentation with $a_{2kx} = a_{2ky}$. If it were desired to have a rectangular output at the zero-shift point, a_{2kx} would no longer be the same as a_{2ky}, which is acceptable because the freeform equation treats x and y independently. The equality of the b_{2kx} and b_{2ky} coefficients is likewise not a constraint; it is possible to have different rates of side length change along the x and y directions per the respective units of lateral shift.

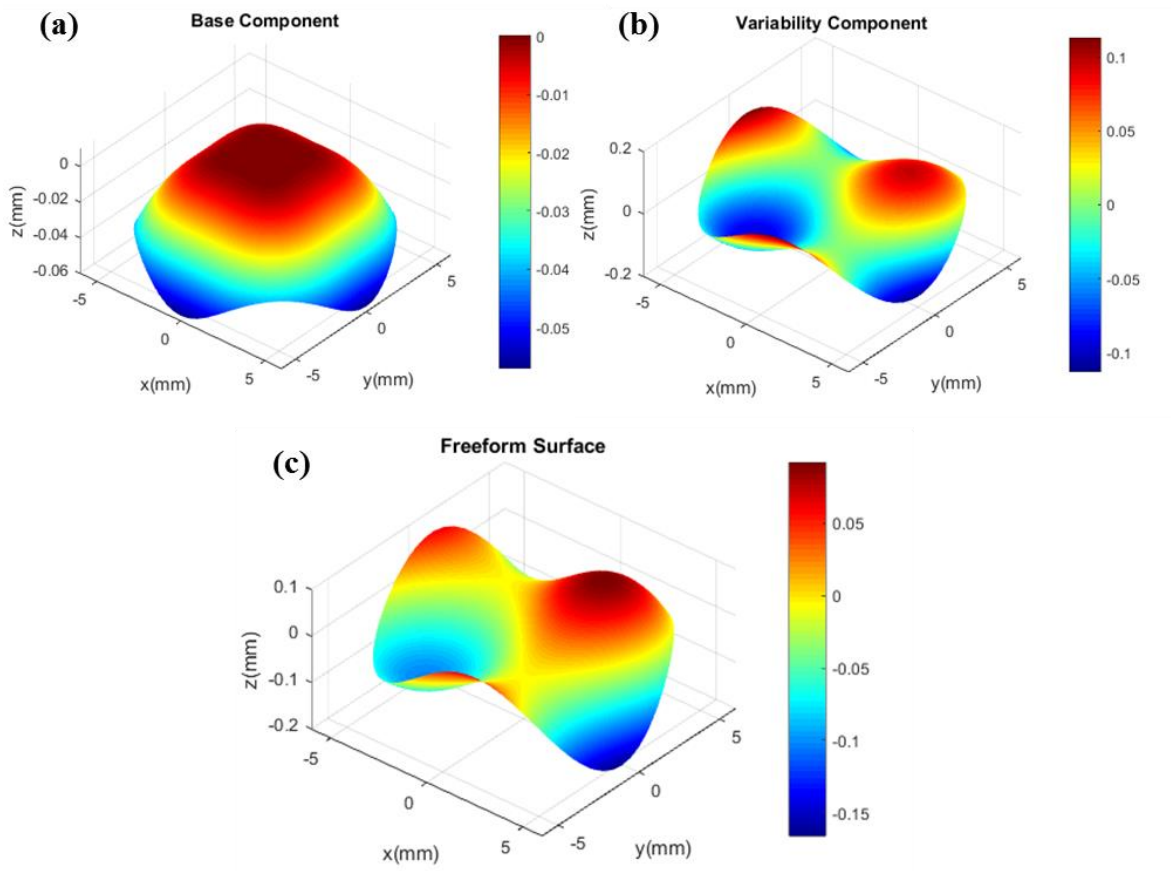

Fig. 5.5: Surface plots of the variable rectangular output beam shaper, showing the (a) base component, (b) variability component, and (c) one of the two freeform surfaces.

5.4.3 Optical modeling

The resulting system was again modeled in VirtualLab™ using the same parameters and methods as in Section 5.3.3. Table 5.6 shows the constant input diameter with the expected output side lengths X_0 and Y_0 and simulated output side lengths X_0 and Y_0 for the corresponding lateral shift and axis orientation. The predicted results are again in good agreement with simulated results in VirtualLab™.

Table 5.6: Predicted and modeled input and output spot side lengths for several different lateral shift configurations.

Shift d_x (μm)	Shift d_y (μm)	Input D_o (mm)	Predicted Output X_0 x Y_0 (mm)	VirtualLab™ Output X_0 x Y_0 (mm)
-300	-300	6.0	6.0 x 6.0	5.948 x 5.948
-300	0	6.0	6.0 x 4.0	5.948 x 3.961
-300	300	6.0	6.0 x 2.0	5.948 x 1.989
0	-300	6.0	4.0 x 6.0	3.961 x 5.948
0	0	6.0	4.0 x 4.0	3.961 x 3.961
0	300	6.0	4.0 x 2.0	3.961 x 1.989
300	-300	6.0	2.0 x 6.0	1.989 x 5.948
300	0	6.0	2.0 x 4.0	1.989 x 3.961
300	300	6.0	2.0 x 2.0	1.989 x 1.989

Fig. 5.6 shows a grid of simulation results for output spots with multiple lateral shift configurations of 0 μm and +/-300 μm for d_x and d_y. The redistribution of energy can be seen with uniform irradiance distributions and the output size varied independently in the *x* and *y* directions. Similar to the previous results, the Gibb's phenomenon was present in the output spots due as a product of using a step-function, and could be eliminated using the super-Gaussian irradiance distribution. Overall, the success of this design and additional flexibility to independently vary the output field in two directions opens up new classes of optical devices and possibilities that lie within this idea of freeform optics and general mathematical approach.

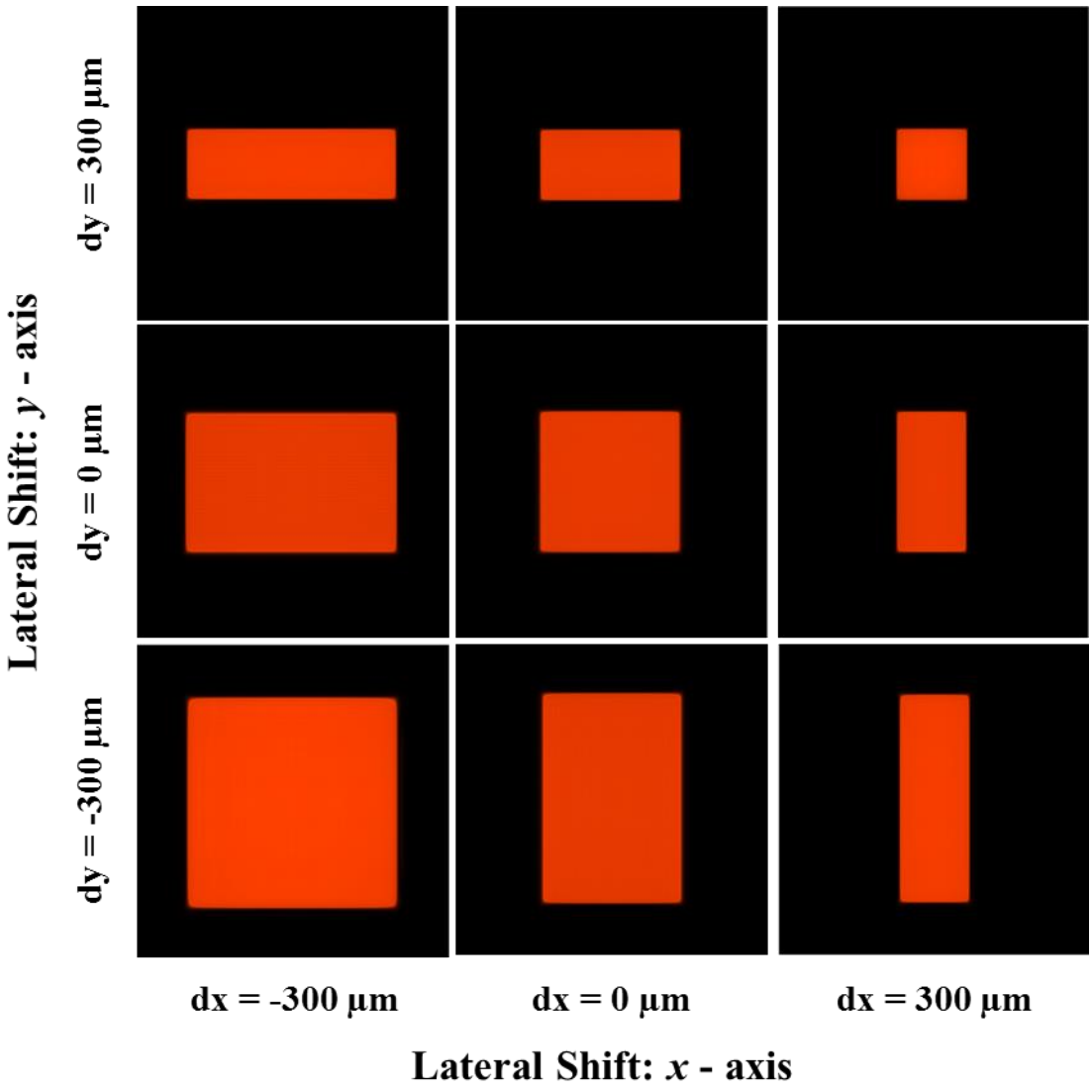

Fig. 5.6: Physical optics simulations of spot irradiance at 150 mm target distance for different relative shifts along x- and y-axes for a Gaussian to variable rectangular flat-top (step-function) beam shaper.

5.5 Variable toric lens from 2D lateral shifts

5.5.1 Introduction

Up to this point in this Chapter we have only considered non-imaging applications. For a final example, we expand the design approach of implementing lateral shifts in two dimensions to create a variable toric lens. Similar to the variable rectangular beam shaper with lateral shifts along the *x* and *y* axes; the focal length varies in the *x*-direction when the freeform surfaces are shifted along the *x*-axis, and the focal length varies independently in the *y*-direction when the freeform surfaces are shifted along the *y*-axis. Researchers [42, 61-65] have previously demonstrated that shifting the Alvarez lens in the adjacent direction inherently creates a toric function, *but the variability in the x and y focal lengths are not independent of each other and the respective shifts.* It was mentioned by Lohmann [30] that two crossed variable cylindrical lens pairs creates a varifocal lens with appropriate lateral shifts. This was later demonstrated by Barbero [42], where the performance of a varifocal Lohmann lens was compared to a standard Alvarez lens. However, in those cases, the independent *x* and *y* output functions were not realized, nor did the presented designs include optical power when no lateral shift was in the system. Additional work was done involving a diffractive varifocal lens where a variable toric function was realized [66]; however, similar to other work, the system was designed using optimization, where the procedure was not reported. Furthermore, there has not been any work reported (to the knowledge of the author) which included a variable toric lens with independently varied x and y focal lengths, while also having optical power when no lateral shift is present.

5.5.2 Optical design

Due to the fact that the base optical function is now a spherical lens, use of Eq. (5.1) is not required to represent the composite surface. However, the implementation of a second lateral shift to achieve the variable toric effect necessitates the separate treatment of the *x* and *y* terms for the base function. With this consideration in mind, Eq. (5.18) was again used to represent the freeform surfaces of this lens pair.

In order to draw direct comparisons to the shifted Alvarez lens example in Chapter 4, all of the same base input parameters were used. In this case, the focal lengths in the *x* and *y* directions (f_x and f_y) were both centered at 77 mm, and both ranged from infinity to 38.5 mm for the same lateral shift range of $\Delta d_x = \Delta d_y$ = +/-1.8 mm. Fig. 5.7 shows individual plots of the independent focal ranges for each axis corresponding to the respective lateral shift axis.

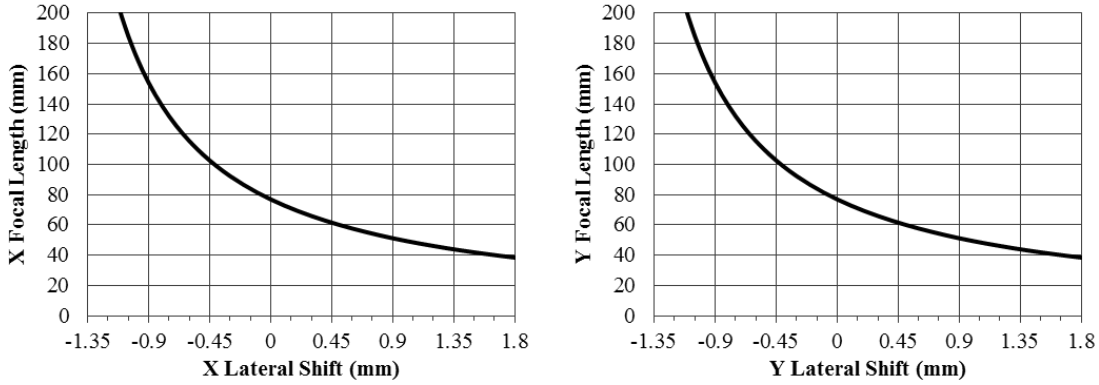

Fig. 5.7: Independent variable lens focal lengths vs. lateral shift relationships along the (left) *x*- and (right) *y*- axes for a variable toric lens.

As before, multiple toric lenses with different *x* and *y* focal length configurations were designed using a ray mapping procedure. Fig. 5.8 shows a grid of composite surfaces for several different configurations of lateral shift, all with the same scale across the 14.5 mm

aperture. These results clearly show how the composite curvature changes in the *x* direction independently of the *y* direction with their corresponding lateral shifts.

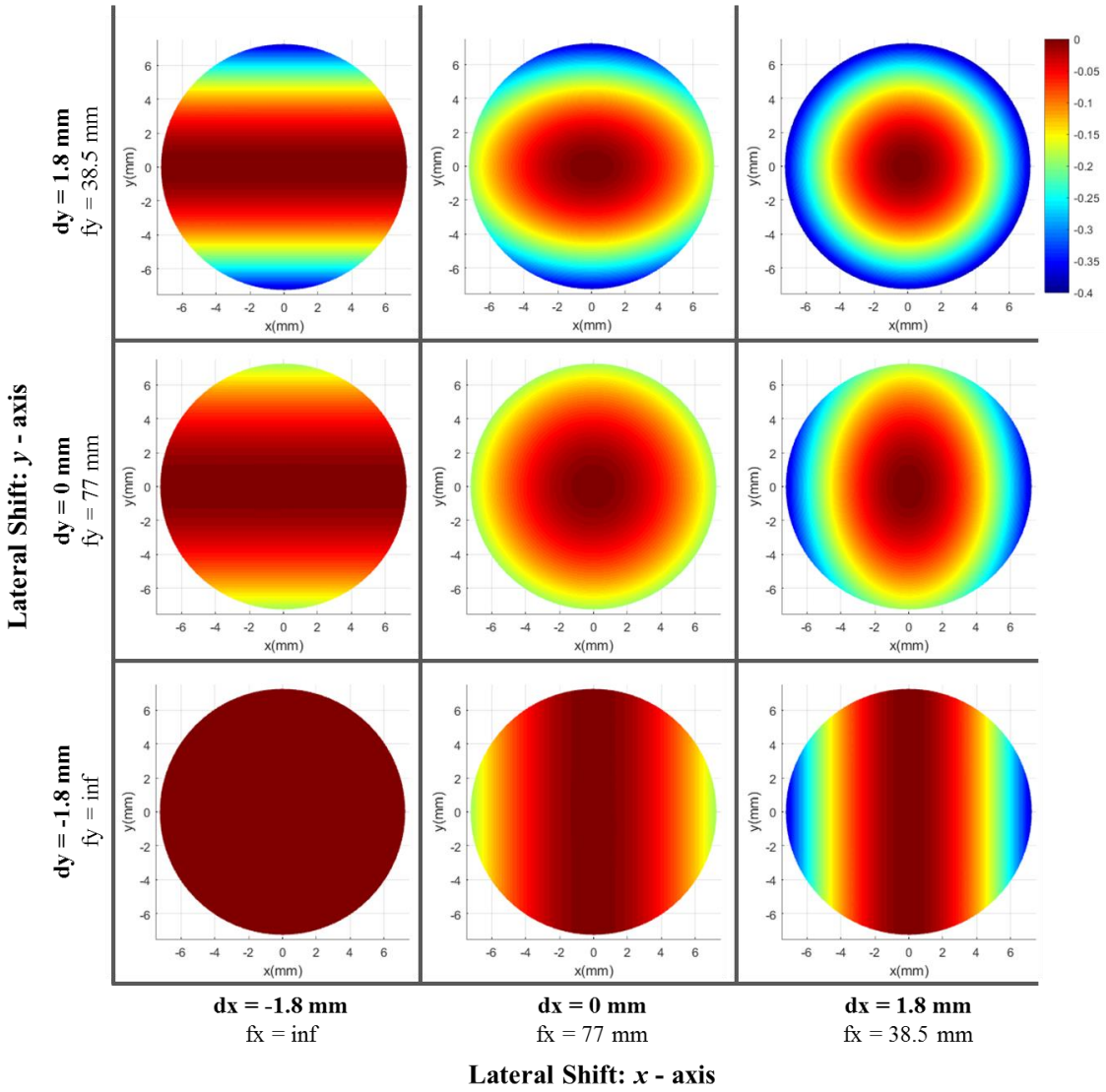

Fig. 5.8: Composite toric lens surface profiles for several different configurations of *x* and *y* lateral shifts. All images are on the same color scale.

A set of polynomial coefficients was then fit to Eq. (5.1) for each surface height profile. Since the base parameters and focal length range are the same as in the Chapter 4 example, the cross-sectional profile for each of the composite surfaces are also the same (Table 4.2). Additionally, because f_x and f_y have the same change per lateral shift range

and are centered at the same value, the polynomial coefficients for the x terms will be the same as the y terms, ($a_{2kx} = a_{2ky}$ and $b_{2kx} = b_{2ky}$) as in the previous beam shaping example. The resulting surface coefficients for the base and variability components are listed in Table 5.7.

Table 5.7: Freeform surface coefficients for the variable toric lens pair.

Order (k)	a_{2kx} (mm^{-2k+1})	a_{2ky} (mm^{-2k+1})	b_{2kx} (mm^{-2k})	b_{2ky} (mm^{-2k})
1	-3.6190E-03	-3.6190E-03	-1.0051E-03	-1.0051E-03
2	8.5045E-08	8.5045E-08	9.4472E-08	9.4472E-08
3	-3.9980E-12	-3.9980E-12	-1.7762E-11	-1.7762E-11
4	2.8848E-16	2.8848E-16	4.3921E-15	4.3921E-15
5	-1.6072E-18	-1.6072E-18	-7.6125E-18	-7.6125E-18
6	2.3128E-20	2.3128E-20	9.4940E-20	9.4940E-20
7	-1.3052E-22	-1.3052E-22	-5.3407E-22	-5.3407E-22

As before, the tilt terms c_{0x} and c_{0y} were both determined by performing parameter sweeps to find the point at which the sag of the freeform surface was at a minimum. The resulting tilt term of 0.013 decreased the sag from 254 μm to 173 μm over the 14.5 mm aperture diameter with respect to the untilted surface. Eq. (5.18) was then used to define the freeform surfaces. The resulting base, variability, and freeform surfaces are shown in Fig. 5.9. Again, we note that the equality of the x and y coefficients is not a constraint because x and y are separable in the freeform prescription; the focal length ranges and center focal lengths can be different for the x- and y- axes.

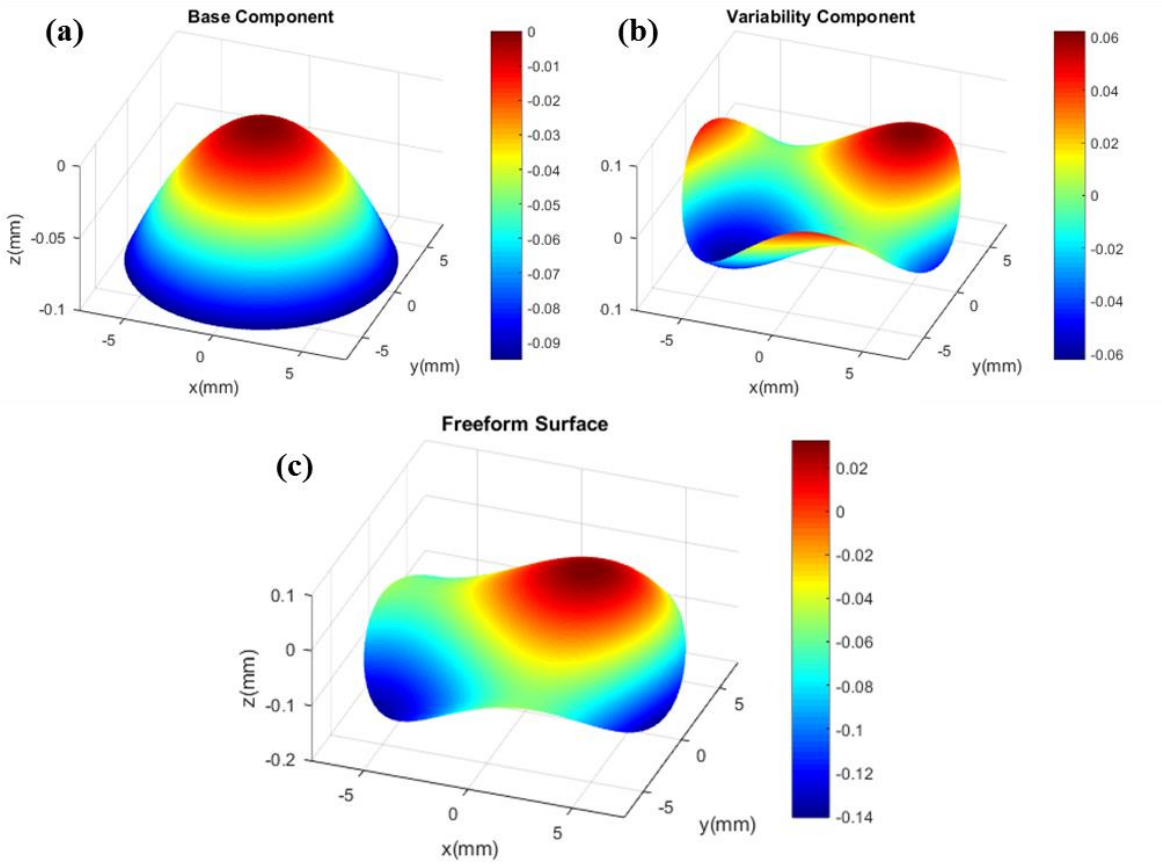

Fig. 5.9: Surface plots of the variable toric lens, showing the (a) base component, (b) variability component, and (c) one of the two freeform surfaces.

5.5.3 Optical modeling

Ray-trace simulations were performed using ZEMAX® to verify the independent variable functionality of this device. As in the shifted Alvarez example in Chapter 4, these simulations assumed a normally incident collimated input with 4 μm wavelength and 8 mm diameter aperture directly in front of the first element. The center thickness of each freeform element was set to 2.5 mm, with a 400 μm standoff gap between the lens pair. Fig. 5.10 displays a grid of multiple ray-trace simulation results with several different configurations of x and y lateral shifts ranging from d_x = +/-1.8 mm and d_y = +/-1.8 mm.

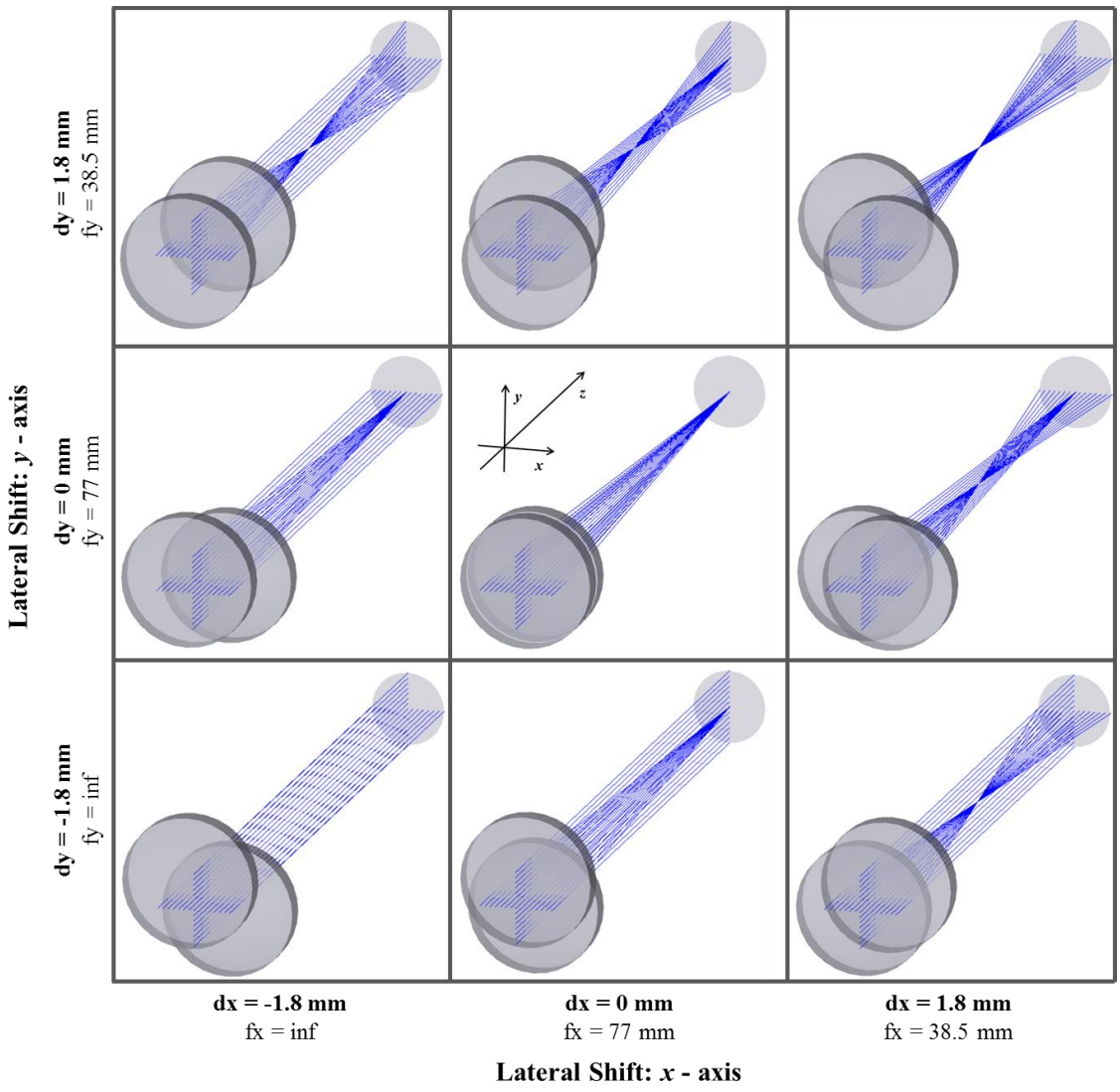

Fig. 5.10: Geometric ray-trace simulations of the variable toric lens for several different configurations of *x* and *y* lateral shifts. All simulations are on the same axial scale.

Two ray-trace simulations were also performed for each lateral shift configuration to characterize the independence of the *x* and *y* focal lengths of the system. The distances between the second element and the corresponding focal plane (the back distance) along the *x* or *y* axis were recorded for each configuration. In order to find the focal plane, the back distance was set as a variable and ZEMAX's default RMS optimization algorithm was used to determine the location of the smallest RMS spot size for each of the respective axes. Recall from the discussion in Chapter 4, the back distance is not

necessarily equivalent to the system focal length due to the thickness of each freeform element. The focal length was determined by adding the location of the second principal plane to the back distance recorded in the ZEMAX® simulations. The location of the principal plane was determined in Chapter 4 to be 0.896 mm. Table 5.8 compares predicted values to modeled results of the *x* and *y* focal lengths for this system for several different lateral shift configurations.

Table 5.8: Focal lengths in the *x* and *y* direction determined using ZEMAX® simulation models compared to theoretical values for different lateral shift configurations.

Lateral Shift		**Predicted Focal Length**		**ZEMAX® Focal Length**	
d_x (mm)	d_y (mm)	f_x (mm)	f_y (mm)	f_x (mm)	f_y (mm)
-0.9	-0.9	154	154	154.22	154.23
-0.9	0	154	77	154.18	76.94
-0.9	0.9	154	51.3	154.14	51.19
-0.9	1.8	154	38.5	154.08	38.32
0	-0.9	77	154	76.93	154.18
0	0	77	77	76.92	76.92
0	0.9	77	51.3	76.90	51.19
0	1.8	77	38.5	76.88	38.32
0.9	-0.9	51.3	154	51.19	154.13
0.9	0	51.3	77	51.18	76.90
0.9	0.9	51.3	51.3	51.17	51.18
0.9	1.8	51.3	38.5	51.16	38.31
1.8	-0.9	38.5	154	38.32	154.07
1.8	0	38.5	77	38.31	76.88
1.8	0.9	38.5	51.3	38.31	51.16
1.8	1.8	38.5	38.5	38.29	38.30

The focal lengths from the ZEMAX® simulations are in good agreement with the predicted values. The slight difference between the two results is thought to be a consequence of geometrical aberrations caused by the air gap between the two freeform

elements. Similarly, as a lateral shift is varied along a single axis, there is minimal change in the focal length for the orthogonal axis, which further verifies the independent variable functionality of this device.

For the specific configurations where the *x* and *y* focal lengths are equal ($f_x = f_y$), *x*-*y* spot diagrams in ZEMAX® were produced in order to assess the geometrical aberrations present in this system. Fig. 5.11 shows the spot diagrams in the image plane for lateral shifts d = -0.9 mm, d = 0 mm, and d = 1.8 mm [$d_x = d_y = d$], compared to the Airy disk radius to assess the performance relative to the diffraction limit. Compared to the previous shifted focus Alvarez lens (Chapter 4), this device has a slightly better performance regarding spot size. This improvement is thought to result from the use of bilateral shifts versus a unilateral shift. Though the effective focal range is the same, the lateral shift takes place along a diagonal for the variable toric lens, which is inherently a larger shift compared to shifting along one axis. For example, the shifted focus Alvarez was laterally shifted 1.8 mm along the *x* axis, whereas the variable toric lens was shifted $\sqrt{2}$*1.8 mm along the diagonal between the *x* and *y* axes. As a result, noted in [42], this inherently decreases the required surface curvature (surface depth modulation), resulting in a better performance.

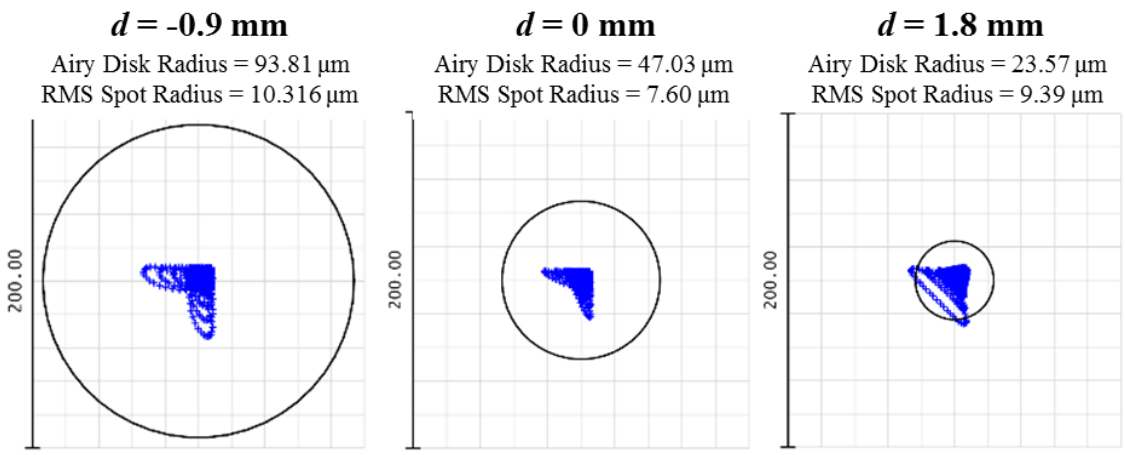

Fig. 5.11: Spot diagrams generated in ZEMAX® compared to the diffraction limited Airy disk for lateral shifts of d = -0.9 mm, d = 0 mm, and d = 1.8 mm

Fig. 5.12 shows performance summary plots of this device across the defined lateral shift range [when $d_x = d_y = d$] for RMS spot radii and Strehl ratio. Recall that a system is generally considered to be diffraction limited for Strehl ratio $Strehl \geq 0.8$. The aberrations found in the image plane are below the diffraction limit for the range of lateral shifts, suggesting that the image would be of high quality.

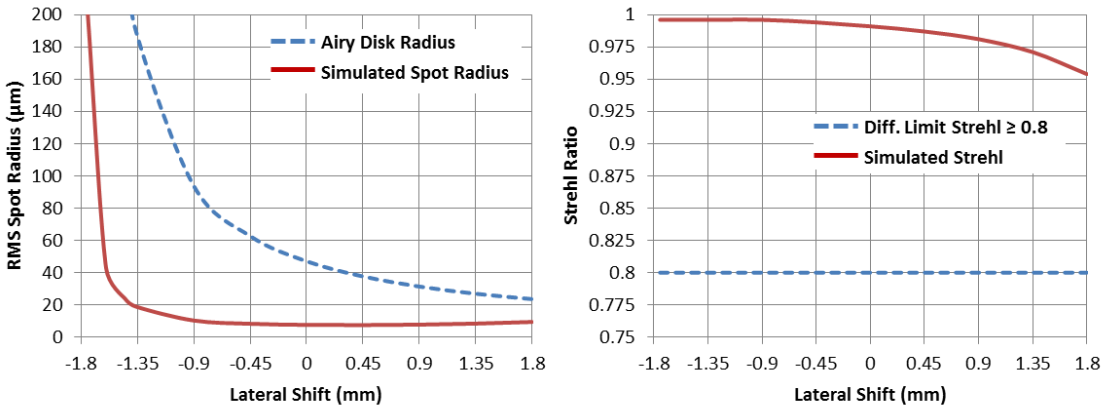

Fig. 5.12: Performance summary plots for the variable toric lens across the range of lateral shifts (for $d_x = d_y = d$) with regards to (left) RMS spot radius and (right) Strehl ratio.

5.6 Discussion

Three novel dynamic freeform optical systems were presented in this chapter; a variable square output beam shaper from 1-dimensional lateral shifts, a variable rectangular output beam shaper from 2-dimensional lateral shifts, and a variable toric lens from 2-dimensional lateral shifts. These examples all expanded on earlier design processes by enabling non-radially symmetric variable outputs. Furthermore, the design process was expanded by enabling independent control of x and y dimensions of the optical outputs through independent lateral shifts along the x and y axes. The performance of each of these designs shows that the general design process works as intended and also suggests other applications are possible in this genre of optical systems with arbitrary irradiance distributions or imaging properties. Similarly, it is important to note that the demonstrated design approaches were analytic, with no numerical optimization performed to achieve the freeform lens prescription. As in conventional lens design in which analytic methods are used to provide promising initial design forms prior to numerical optimization, this process provides a starting point for numerical optimization of future freeform designs using optical simulation software for enhanced performance.

CHAPTER 6: OPTOMECHANICAL TOLERANCING OF DYNAMIC FREEFORM OPTICAL SYSTEMS

6.1 Introduction

To this point, a significant amount of research has been demonstrated on general design processes within the genre of dynamic optical systems. However, there has been no consideration of performance sensitivity to potential system errors. For example, since there are two elements in the dynamic optical systems we consider, tolerances on relative spacing, displacement, rotation, and tilt (illustrated schematically in Figure 6.1) between the surfaces must be understood as part of the design process. Having an optical system that requires a substantial amount of optomechanics could be costly, bulky, and prone to additional error [130-132]. Performing a tolerance analysis provides a necessary insight into the impacts that specific system errors have on optical performance. Furthermore, the ability to determine specific tolerance specifications precludes the over-tolerancing of the system, where overly tight tolerances could unnecessarily increase system costs.

The computational time and accuracy needed for determining tolerance values are very important. To put the need for a well-established tolerance procedure in perspective, first consider a straight-forward approach in which every possible permutation of different errors between the two freeform surfaces is simulated. If we consider displacement and rotational (tilt) errors on all three axes (x, y, & z) (Fig. 6.1) for both freeform elements individually, then there would be a total of 12 independent variables of error (six for each lens). Assuming each variable can take one of five predetermined deviation values, there

would need to be 5^12 = 24,4140,625 simulations to simulate every possible permutation. Assuming 10 seconds for each simulation, this would take approximately ~77 years for one individual system.

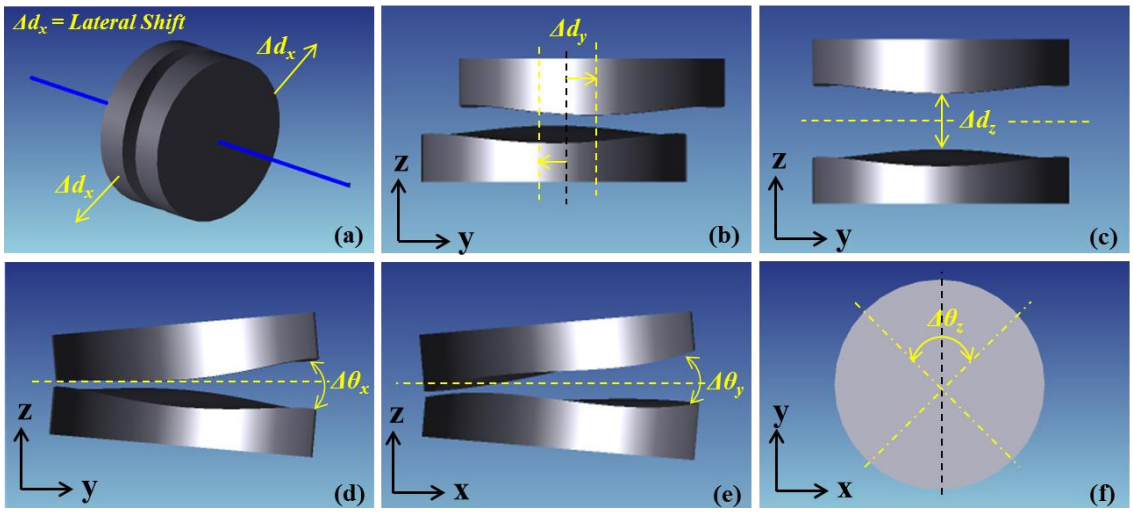

Fig. 6.1: Illustration of the direction of the (a) controlled lateral shift, and the potential (b) lateral, (c) axial, and (d-f) rotational misalignment errors along their respective axes.

Many different methods and approaches have been taken to develop standard tolerancing procedures for different optical systems and to reduce computational effort. These methods range from connecting design performance to production costs to achieve the most cost-effective design [133-135], to incorporating different statistical approaches to drive down computational efforts while still maintaining the required accuracy [68-71, 136-140]. The majority of previous approaches [68-71] utilize a Monte Carlo analysis. Monte Carlo analyses enable cross-communication between error sources by randomly deviating the system a predetermined number of times while viewing the performance trends. This approach eventually provides statistically relevant tolerance results based on a specified performance metric. This is a relatively standard approach for tolerancing

systems with multiple rotationally symmetric optical components, where alignment errors can be described in terms of tilt and decenter (fewer variables).

In our case, many of the assumptions made in Monte Carlo procedures are not valid due to the lack of rotational symmetry in the freeform components, thereby increasing the computational requirements. Additionally, Monte Carlo analyses are inherently based around statistical measures, meaning the procedure is not entirely deterministic. To this end, we consider a simplified deterministic procedure for defining optomechanical tolerances for dynamic freeform optical systems. *This procedure is aimed towards decreasing the computational effort by making several assumptions that are based on 'worst-case' scenarios*.

6.2 Performance metric study

Tolerance analyses require a performance metric in order to provide the desired tolerance specification. Though we are using the same methods and procedure for our two dynamic freeform examples, the different functionalities achieved (imaging vs non-imaging) require different performance metrics. We now consider the chosen performance metrics for the imaging and non-imaging examples in more detail.

6.2.1 Imaging performance metrics

Well-known standards exist within the classical optics regime for imaging devices. In the case of the Alvarez lens, we consider the RMS spot radius and the Strehl ratio. The RMS spot radius is simply a measure of the output spot size in the focal plane of the system [126]. As mentioned earlier, the Strehl ratio is defined as the ratio between the peak aberrated on-axis image intensity and peak non-aberrated image intensity [126],

providing a measure of the quality of optical image formation. Both metrics can easily be related to a diffraction limited system which can be used as a basis for tolerance allowances.

6.2.2 Non-imaging performance metrics

Non-imagining devices have various measures of performance that depend on application. For the variable output beam shaper, the performance can be segmented into three separate categories; size, shape, and uniformity of the output irradiance pattern. Each of these metrics can be qualitatively analyzed while viewing the simulated output. Conversely, there are not many known standards to *quantitatively* evaluate each of these metrics. In each of the tolerance analyses, there needs to be a quantitative metric in order to determine the necessary specifications. For this reason, a significant amount of research was performed to enable and define quantitative measures of the size, shape, and uniformity of the output spots. Multiple custom codes (presented in Appendix A.2) were created in MATLAB® to enable these analyses. We now consider this work in more detail.

Spot size and shape determination

To measure the size and shape of the output irradiance, a custom edge finding algorithm (EFA) was created in MATLAB® to find the outer edge of the spot irradiance. This algorithm begins with import of the simulated output spot into MATLAB® as a 2D array, where the contrast of the spot is then enhanced using the “nthroot” command [141]. Enhancing the contrast creates a sharper transition at the edge of the spot, and improves the accuracy and consistency of the end result. Next, a numerical derivative is

performed on the data along both the *x* and *y* axes separately and then added together. Calculating the derivative on the data maps the change of irradiance within the spot, and highlights the areas where there are large changes in irradiance – i.e. along the edge of the spot. Fig. 6.2 shows an example of a simulated output spot as originally imported, as contrast enhanced, and the resulting *x* and *y* derivatives added together to highlight the edges.

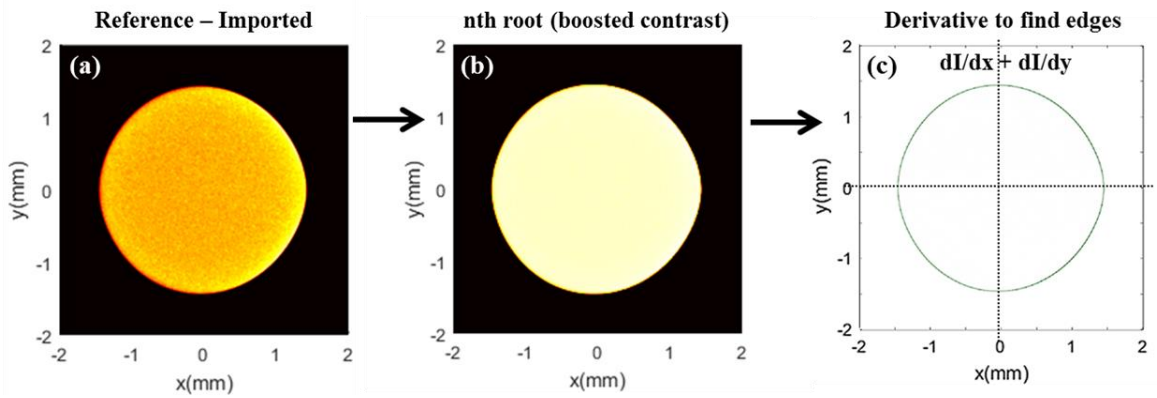

Fig. 6.2: Example of a simulated output spot as (a) originally imported, (b) contrast enhanced, and (c) the resulting *x* and *y* derivatives added together to highlight the edges.

The next step in the EFA is to trace the outer edge to create a 'radius-map' that plots the radius as a function of theta. To do this, code was written in MATLAB® to find the *x* and *y* location of the maximum value as a function of the azimuthal angle θ, as demonstrated in Fig. 6.3. Once these locations are found they are translated into a radial component using $R^2 = x^2 + y^2$. A numerical curve fit algorithm was then implemented in MATLAB®, using the 'fit' command [142], to create a continuous spot radius function as a function of θ. The results for the example output spot shown in Fig. 6.2 are shown in Fig. 6.3.

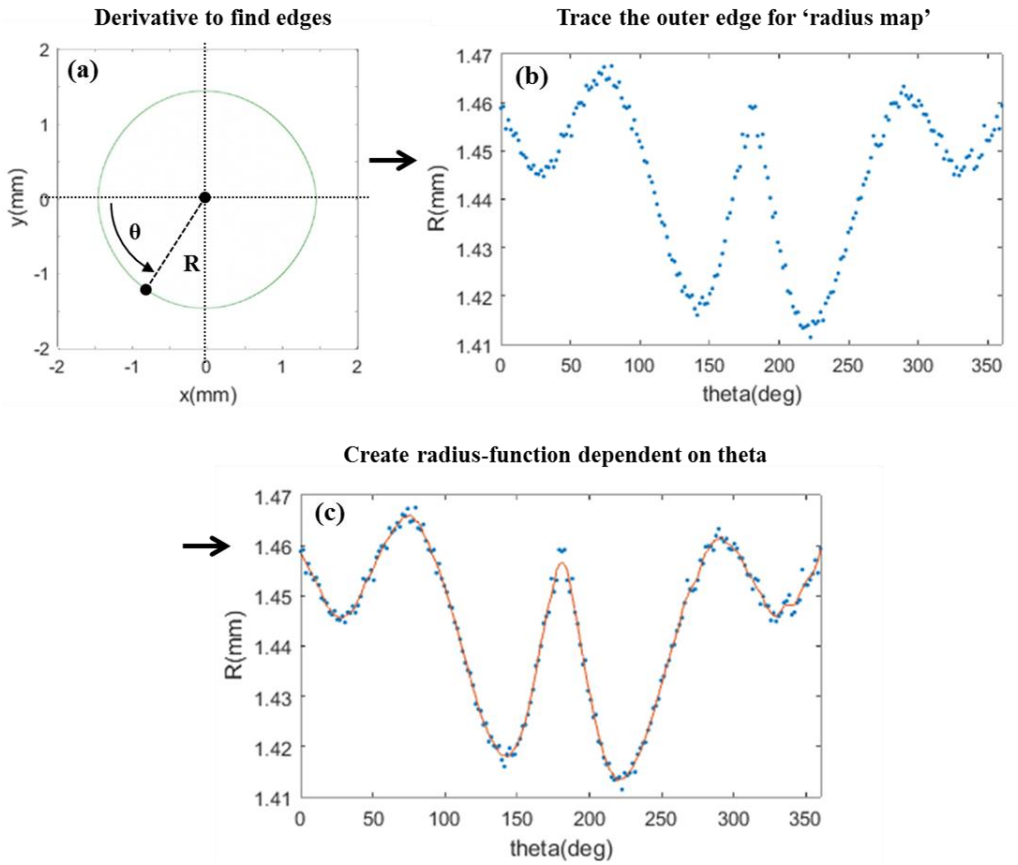

Fig. 6.3: Demonstration of the EFA using the (a) derivative of the output spot to create a (b) radius map by tracing the edges and then generating a (c) spot radius function dependent on θ.

To further demonstrate this algorithm and its usefulness, another example output spot was created, in which an alignment error was introduced that skewed the shape of the spot. Fig. 6.4 shows the deviated output spot along with the highlighted edge and spot radius function compared to the reference spot. Figure 6.4(d) shows how much the shape deviates from the reference.

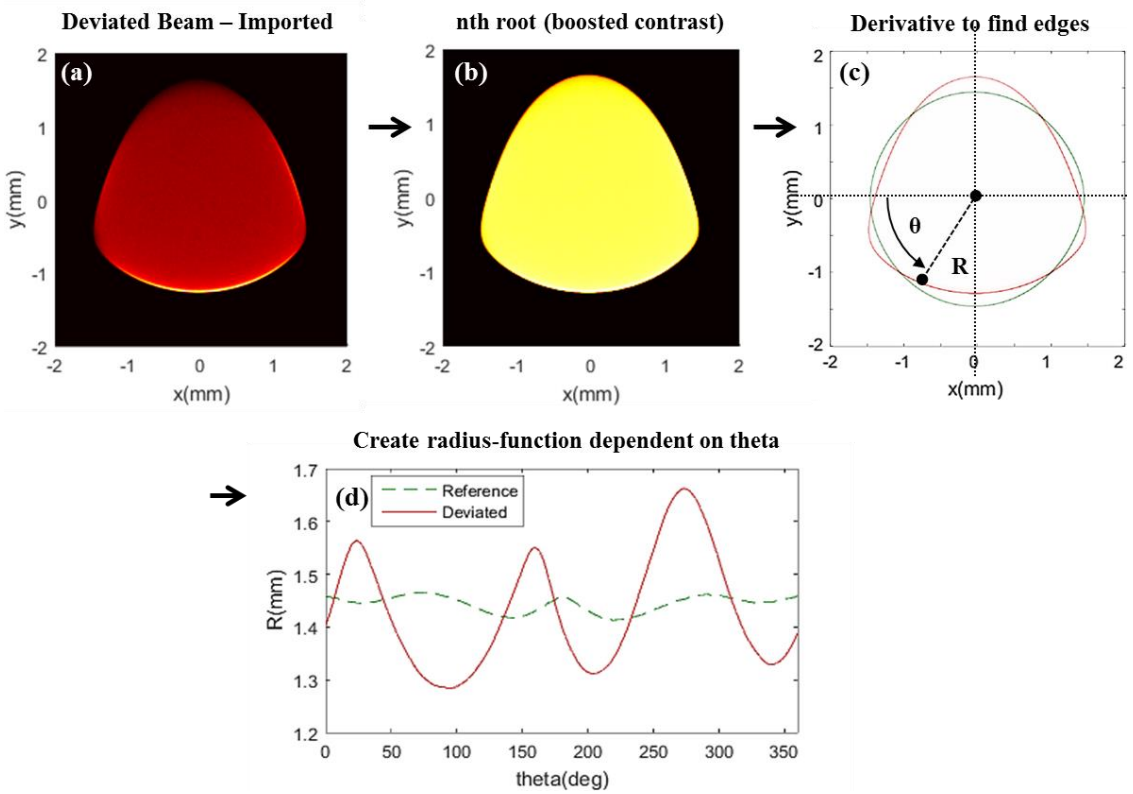

Fig. 6.4: Further demonstration of the EFA; purposely deviated output spot (a) as imported and (b) contrast enhanced, along with the (c) derivative of the output spot and (d) the spot radius function, both compared to the reference.

Though, it is clear that the algorithm works as intended, a quantitative measure of shape is still required. To this end, we apply a standard deviation root mean square error (RMS) approach given by,

$$R_{rms} = \sqrt{\sum_{i=1}^{N} \left(R_i(\theta_i) - R_{ref\_avg}\right)^2 / N} \tag{6.1}$$

where $R_i(\theta_i)$ is the spot radius function, R_{ref_avg} is the average radius of the reference output spot, and N is the number of data points used in the analysis. Since this application is a dynamic system with multiple output spots of varying diameter, there are multiple data sets with different output parameters that must be compared. A shape error

coefficient of variation R_{CV} is used to avoid any potential confusion when quantitatively comparing the magnitude of shape error for output spots with different diameters. R_{CV} is a unit-less measure of variability relative to the reference mean, enabling a comparison of dissimilar data sets. The shape error coefficient of variation [143] is defined as

$$R_{CV} = \frac{R_{rms}}{R_{ref\_avg}}. \tag{6.2}$$

This provides a good quantitative metric for both size and shape; however, there are no known *standards* for this particular unit of measure. With this in mind, a pass-fail threshold must be determined during the tolerancing procedure. The important takeaway is the ability to quantitatively evaluate the shape and size of the output spot.

Spot uniformity determination

The second measure of performance is the uniformity error of the output spot. Uniformity, otherwise described as lack of variance, is a standard mathematical term used in a variety of different applications. Despite this being the most common of all the metrics used, there are subtleties that must be addressed. The unclear edge of the output spot has potential to cause confusion and inconsistencies when comparing results; therefore, only a certain percentage of the spot window is analyzed [107, 144]. This spot window will herein be referred to as the *clear aperture (CA) window*. Figure 6.5 shows an example output spot with its corresponding cross-sectional irradiance, where the clear aperture window is shown.

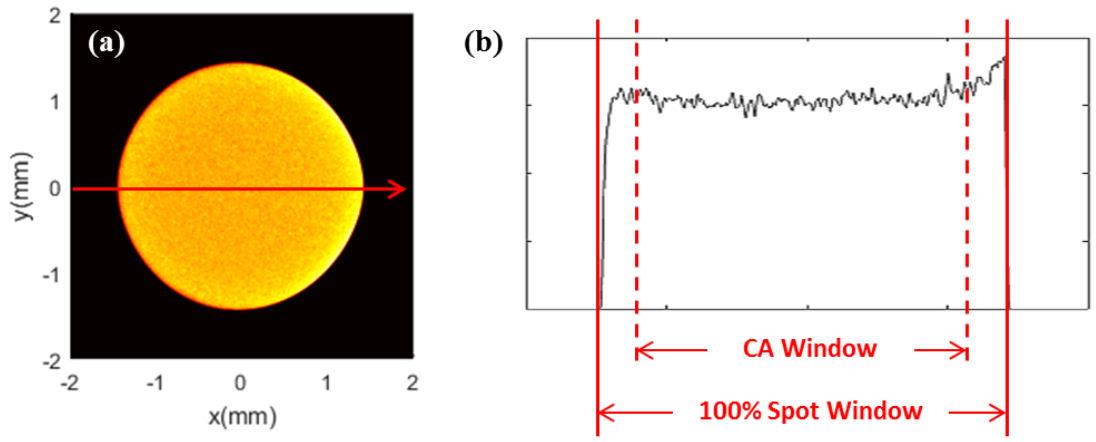

Fig. 6.5: (a) Example of a simulated output spot with its (b) corresponding cross-sectional irradiance where the clear aperture (CA) window is shown as a percentage of the entire spot window.

For a non-deviated system, the output spot is circular, which makes it relatively easy to distinguish a clear aperture window with a smaller diameter. However, once error has been introduced to the system, the shape and size can change to something more random. To combat this potential issue, a MATLAB® code was written which employs the EFA again to create a spot radius function. This function is then decreased to the clear aperture window percentage, which in this case was set to 95%. Fig. 6.6 shows an example of the decreased radius function used to create the clear aperture window.

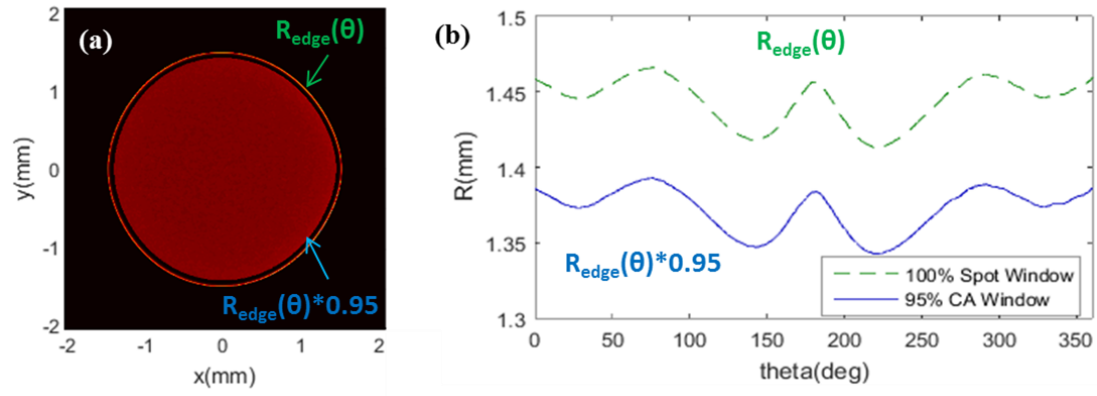

Fig. 6.6: (a) Example of a simulated output spot showing the outer edge as well as the inner clear aperture window. (b) Demonstration of the radius map decreased to the clear aperture window percentage.

Now that the clear aperture window of the output spot has been distinguished, we use a similar root mean square error approach as a quantitative measure for uniformity error. This is given by,

$$U_{rms} = \sqrt{\sum_{i=1}^{N} \left(I(i) - I_{avg}\right)^2 / N} \tag{6.3}$$

where *I(i)* is the irradiance distribution of the output spot within the clear aperture window, I_{avg} is the average spot irradiance, and *N* is the number of data points used in the analysis. We note that this metric is compared to the mean of its individual data set, since the overall uniformity error of the output spot is of primary concern, rather than the average magnitude of irradiance of the target output spot. Much like the shape error, the standard deviation for uniformity error is an adequate measure for an individual system, but this is a dynamic system and there are multiple data sets with different parameters that must be compared. Thus, we employ a coefficient of variation again, defined as,

$$U_{CV} = \frac{U_{rms}}{I_{avg}}. \tag{6.4}$$

There are no well-established standards for beam shaper uniformities, as most examples depend on the specific application. With this in mind, the pass-fail threshold must again be qualitatively determined during the tolerancing procedure.

Combination of spot size, shape, and uniformity

The previous two performance metrics measured the shape-size and uniformity separately. In order to have a *combined* quantitative measure of spot output quality, we implement a *correlation degree function* following the approach taken by Zwick and

Timinger [77, 78]. This approach evaluates the quality of the generated irradiance distribution by evaluating the similarity to an ideal target distribution by first using the cross-correlation integral described given by,

$$\Gamma_{12}(\tau,\eta) = \iint I_1(x,y)\, I_2(x+\tau, y+\eta)dxdy, \tag{6.5}$$

where I_1 describes the ideal irradiance distribution and I_2 describes the generated irradiance distribution with the error source included. This function provides the coordinates where the two distributions best match. Similarly, setting τ=0 and η=0, and normalizing this function allows a measurement of correlation between the two distributions. This correlation degree is defined as,

$$C_d(0,0) = \left| \frac{\Gamma_{12}(0,0)}{\sqrt{\Gamma_{11}(0,0)\,\Gamma_{22}(0,0)}} \right|. \tag{6.6}$$

The correlation degree lies within $0 \leq C_d \leq 1$, where $C_d = 1$ corresponds with a perfect match and $C_d = 0$ is non-conforming. Again, there are no known standards for this particular performance metric and the pass-fail threshold must be qualitatively determined during the tolerancing procedure.

6.3 Methods and assumptions

Several assumptions are made to reduce the number of system variables in the system and computational effort while maintaining an adequate level of accuracy. To start, we refer back to design examples in the earlier chapters where we noted that the standoff distance between the two freeforms had an insignificant effect on performance. With this in mind, the first assumption is to ignore the displacement along the *z* axis for both

lenses, reducing the number of variables from 12 to 10. Next, both elements are assumed to have equal *x*- and *y*-axis displacement tolerances and the same *x* and *y*-axis tilt tolerances. This assumes a worst-case scenario, and reduces the error variables from 10 to 6. Lastly, we assume both freeform elements to have equal tolerances for each alignment error by modeling the second freeform with alignment errors of equal magnitude in the opposite direction as the first freeform. Again, the worst-case scenario is inherent in this final assumption due to the relative positioning error between the two lenses always being at a maximum. To this end, the number of variables is reduced to 3: displacement S_{xy}, tilt T_{xy}, and rotation R_z. Fig. 6.7 illustrates the two assumptions regarding displacement error. It should be noted that these assumptions are made for the tilt and rotational errors as well, but are not illustrated in Fig. 6.7.

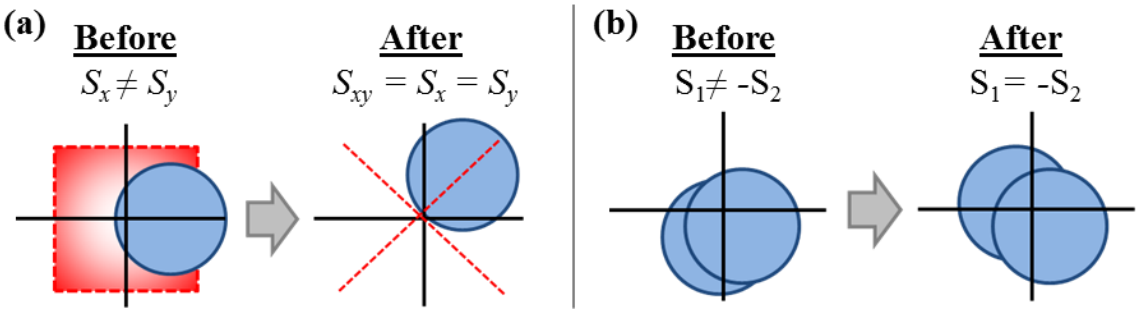

Fig. 6.7: Illustration of the displacement error before and after the assumptions made for the optomechanical tolerancing where both elements are (a) assumed to have equal *x* and *y*-axis tolerances ($S_{xy}=S_x=S_y$) and (b) assumed to have equal magnitude tolerance values in the opposite direction ($S_1=-S_2$). Note that these assumptions are also made for tilt and rotational errors despite not being shown.

Since the freeform surfaces are not rotationally symmetric, the performance impact is *not* assumed to be equivalent for positive and negative errors. Therefore, with the other assumptions in mind, the orientation of the first lens *must* be considered. In other words, the magnitude of the error will remain the same, while each case will include a series of different orientations of the error introduced. For the displacement and tilt errors, there

are four orientations each because they both have *x* and *y* components. The rotational error only has two orientations because it only has a *z*-axis component. This will be discussed in more detail later in this section. Fig. 6.8 demonstrates each of the different orientations for the displacement, tilt and rotational errors.

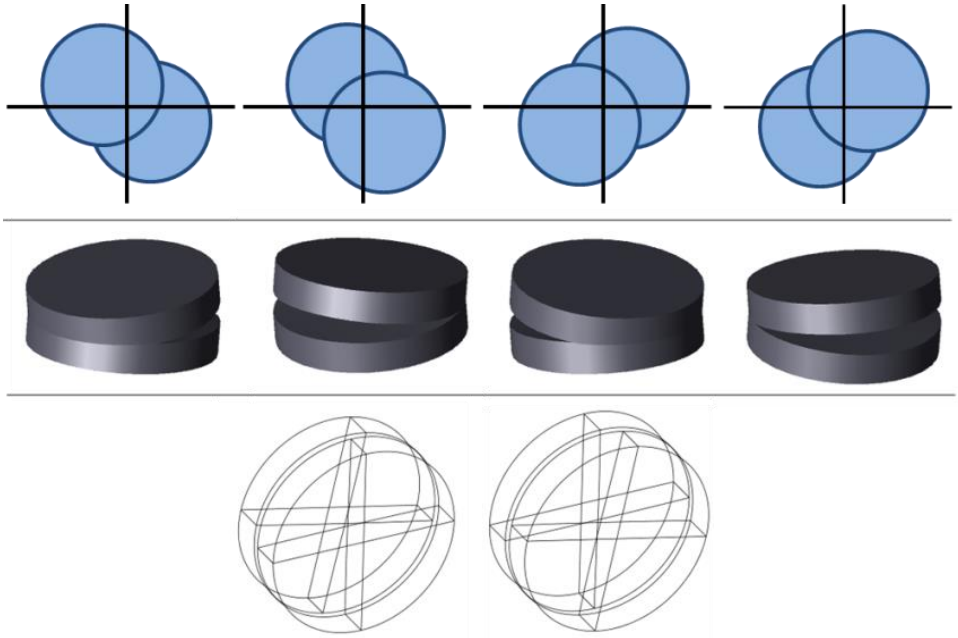

Fig. 6.8: Schematic of each different error source, demonstrating the worst-case scenario assumptions made, along with the different error orientations.

We have reduced complexity considerably with our assumptions, and now briefly outline the simplified optomechanical tolerancing procedure, as shown in Fig. 6.9. This process begins with a sensitivity analysis (SA) to provide an isolated measure of performance and initial tolerance bounds for each variable in the system. This is followed by a combined error analysis (CEA) that enables cross-communication between different errors in the system by implementing worst-case scenarios within a hierarchical progression model. These results are then used in combination with a curve-fitting algorithm in MATLAB® to create an empirical formula that is used as a design tool to

accurately predict the error budget (EB) and determine the worst-case performance of the system within the input tolerance ranges, based on the chosen performance metric.

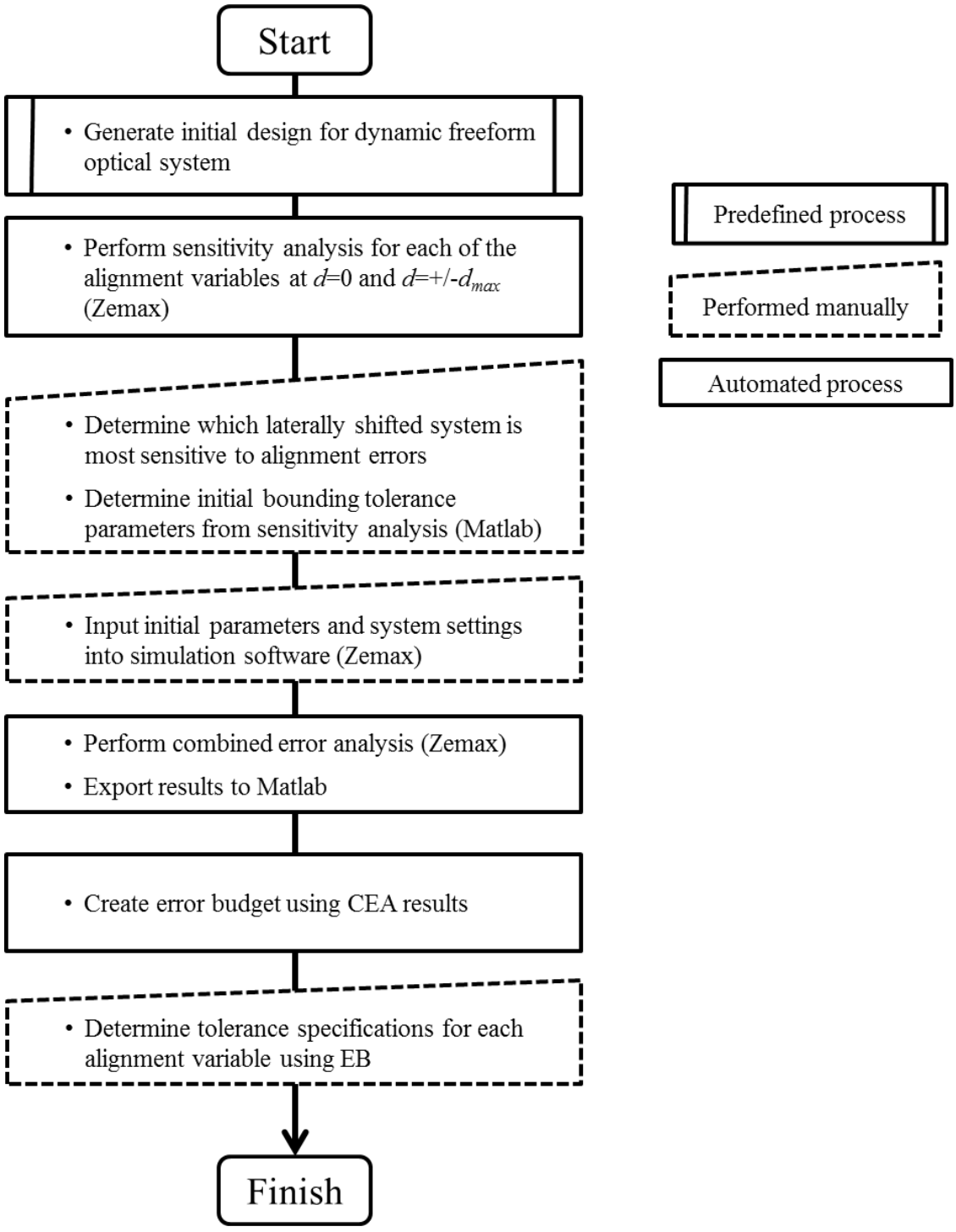

Fig. 6.9: Flow chart for the simplified optomechanical tolerancing procedure.

The sensitivity analysis procedure is relatively straight forward, and is performed by independently simulating a defined range for each of the three error variables. Analyzing each error of interest independently from the others allows us to determine the individual influence of each error on the optical system and determines the starting tolerance bounds for the combined error analysis. Considering the previous assumptions regarding *x* and *y* displacement and tilt errors, each parameter sweep will consist of all possible orientations, with the worst case scenario recorded. The end goal is to enable optomechanical tolerancing of the entire dynamic system. Since this tolerance analysis considers the entire system and its entire dynamic range, the sensitivity analysis is performed for the specific case (1) where no lateral shift is introduced ($d = 0$), and for the cases (2, 3) where the lateral shifts are at the design extremes ($d = +/-d_{max}$). Comparing the results from these analyses provides information on which specific lateral shift is most sensitive to the individual errors, for use in the combined error analysis. Using the results from the most sensitive case, the tolerance bound is determined as the minimum error value for which the performance is beyond the defined pass-fail threshold.

To begin the combined error analysis, each error variable is divided into five different 'tolerance classes'. The first class is defined such that no error is introduced and the last class has the maximum allowable error determined from the previous sensitivity analyses. The intermediate classes have errors evenly spaced between the first and last class. As a visual aid, Fig. 6.10 encapsulates all of the assumptions made to this point, displaying representative images for each of the error variables (displacement, tilt, and rotational). Each representative image consists of the different orientations (O1-O4) in the respective quadrants, as well as the different tolerance classes (S0-S4 for displacement, T0-T4 for

tilt, and R0-R4 for rotational). The tolerance classes are color coded on a green-to-red scale, ranging from a smaller to larger magnitude, where red represents the maximum allowable error for each respective alignment error.

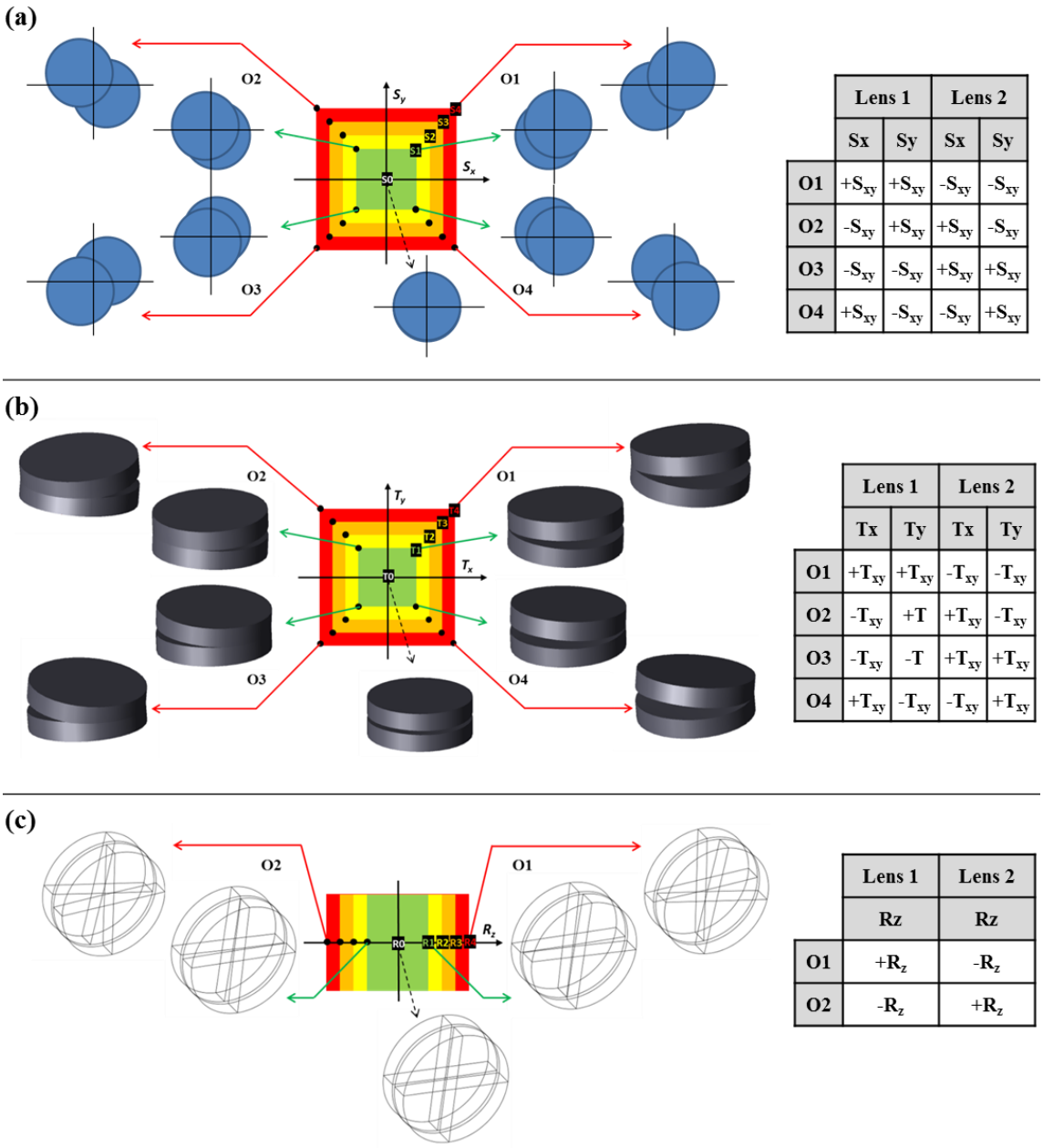

	Lens 1		Lens 2	
	Sx	Sy	Sx	Sy
O1	$+S_{xy}$	$+S_{xy}$	$-S_{xy}$	$-S_{xy}$
O2	$-S_{xy}$	$+S_{xy}$	$+S_{xy}$	$-S_{xy}$
O3	$-S_{xy}$	$-S_{xy}$	$+S_{xy}$	$+S_{xy}$
O4	$+S_{xy}$	$-S_{xy}$	$-S_{xy}$	$+S_{xy}$

	Lens 1		Lens 2	
	Tx	Ty	Tx	Ty
O1	$+T_{xy}$	$+T_{xy}$	$-T_{xy}$	$-T_{xy}$
O2	$-T_{xy}$	$+T$	$+T_{xy}$	$-T_{xy}$
O3	$-T_{xy}$	$-T$	$+T_{xy}$	$+T_{xy}$
O4	$+T_{xy}$	$-T_{xy}$	$-T_{xy}$	$+T_{xy}$

	Lens 1	Lens 2
	Rz	Rz
O1	$+R_z$	$-R_z$
O2	$-R_z$	$+R_z$

Fig. 6.10: Illustration of the different tolerance classes and the multiple orientations for the (a) displacement, (b) tilt, and (c) rotational errors.

Next, a hierarchical progression model is implemented, with each class from each error variable used to simulate all possible permutations of deviated systems, or ‘tolerance class variations’. There are five tolerance classes per error variable and three different error variables, resulting in 5^3 = 125 different tolerance class variations. For each class variation, the first class has no error introduced and thus only one orientation. For each of classes two through five, there are four orientations for the displacement and tilt and two orientations for rotational error. This means there is a total of 4x4+1 = 17 orientations to simulate for each of the displacement and tilt errors, and a total of 4x2+1 = 9 orientations to simulate for the rotational error. The hierarchical model thus require 17x17x9 = 2601 simulations to complete this procedure, which is considerably less than needed for the ‘brute-force’ method discussed previously. Fig. 6.11 illustrates the hierarchical progression model for all 125 tolerance class variations. The color code of each tolerance classes matches the color code from Fig. 6.10.

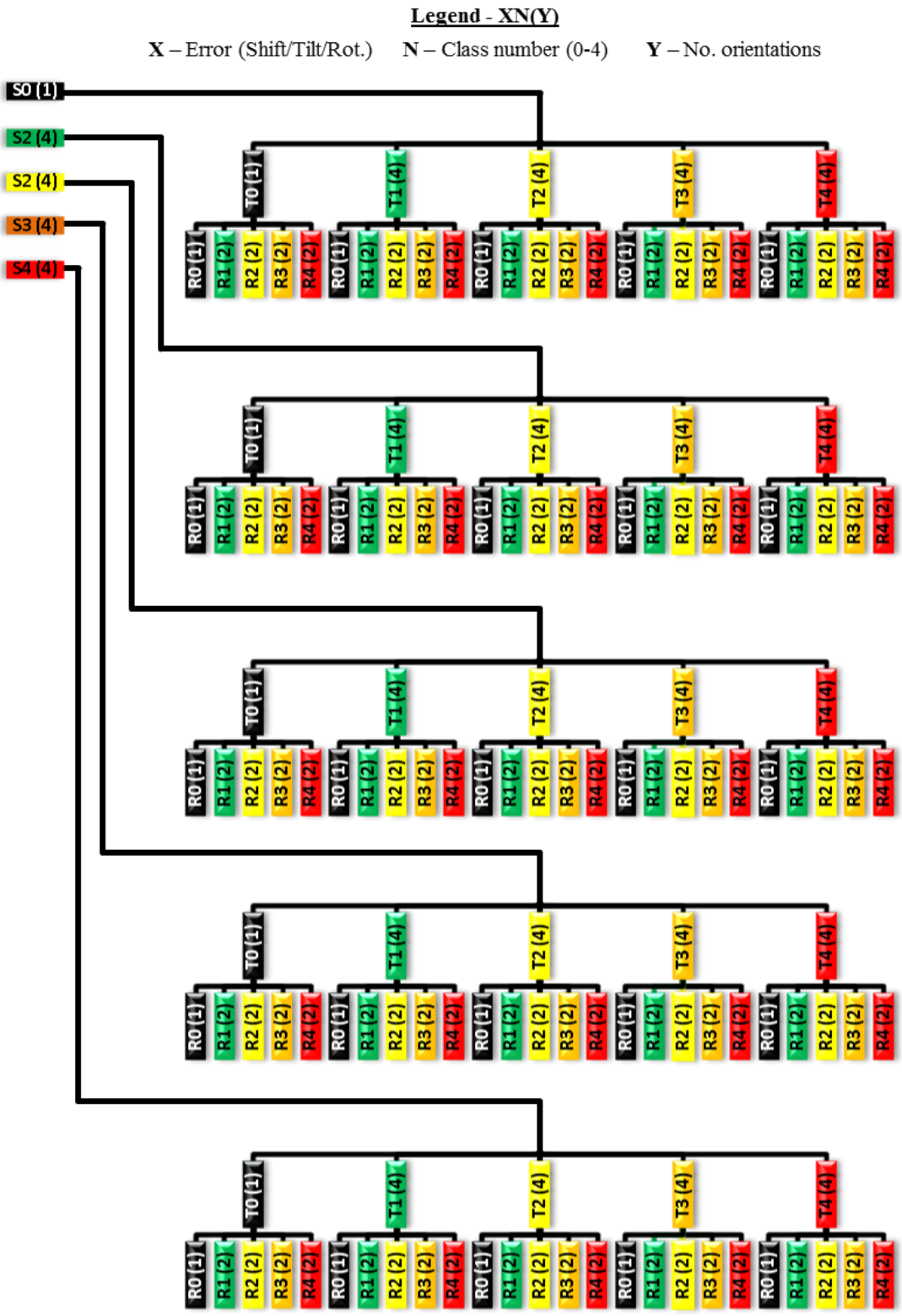

Fig. 6.11: Illustration of the hierarchical progression model showing all 125 tolerance class variations.

A custom MATLAB® code was created to generate a 2601 line text file containing all the possible error permutations (Appendix A.3). This this text file is imported into ZEMAX® using a custom macro to simulate and record the system performance for each error permutation. The results are then imported back into MATLAB® for further analysis. All possible orientations are evaluated for each class variation and the worst performing permutation is considered to be the worst-case scenario for the corresponding tolerance range.

For example, if we consider a hypothetical dynamic system with displacement, tilt, and rotational tolerance of classes 2 (S1), 3 (T2), and 5 (R4) respectively, are a total of 32 possible orientations within this class variation. Of these 32 simulations, the worst performance recorded amongst these simulations is then considered the worst-case scenario, ensuring the system within that specific tolerance range would never perform worse than that. Figure 6.12 shows an expanded version of the hierarchical progression for this specific example, with the worst performance highlighted. Note that the performance metric used in Fig. 6.12 is chosen arbitrarily for demonstration of the process.

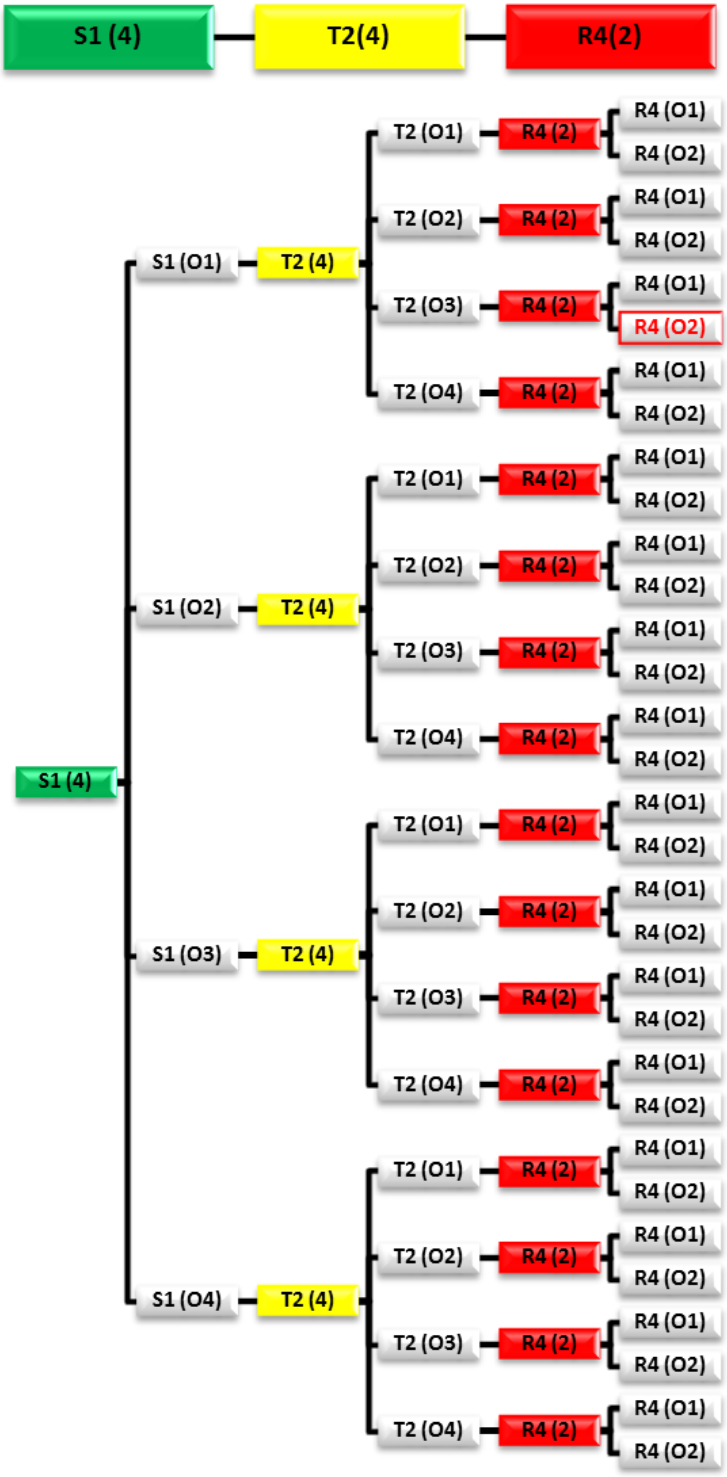

Sim No.	Metric
1	0.70
2	0.66
3	0.70
4	0.66
5	0.77
6	**0.51**
7	0.77
8	0.55
9	0.70
10	0.66
11	0.70
12	0.66
13	0.77
14	0.73
15	0.77
16	0.73
17	0.81
18	0.72
19	0.81
20	0.72
21	0.65
22	0.58
23	0.65
24	0.58
25	0.79
26	0.69
27	0.79
28	0.69
29	0.75
30	0.73
31	0.75
32	0.73

Fig. 6.12: Illustration of an expanded sub-segment of the hierarchical progression model, demonstrating the worst-case scenario performance for an example system with a tolerance class variation of S1, T2, and R4.

Once all 125 class variations have been analyzed, the next step is to apply the results to determination of meaningful specifications. The first approach present the results visually by creating a 4-dimensional scatter plot, where the *x*, *y*, and *z* plot axes respectively correspond to the displacement, tilt, and rotational errors, and the *c*-axis (color) is weighted based on the performance metric. These results are then interpolated between intermediate class variations to achieve a much finer sampling for a similar 4-dimensional surface plot. This plot can be viewed as a 'visual roadmap' for determining tolerance values for the system of interest. We note that interpolation assumes that the performance impact is linear between each of the classes.

While this visual representation provides a wealth of information, the resulting 4-D surface plot can be difficult to interpret, particularly if there is an interest in a specific tolerance value between tolerance classes. For this reason, we consider an approach used in [70, 145] where a quadratic equation was used to determine the correlation between performance impact and associated alignment errors. Rather than using this approach to determine the correlation, we utilize a similar method to create an empirical formula to quantitatively predict the performance impact based on the results from the combined error analysis with the associated alignment errors. This empirical formula is given by,

$$P\left(S_{xy}, T_{xy}, R_z\right) = \sum_{i=0}^{N} \sum_{j=0}^{N} \sum_{k=0}^{N} \left(a_{ijk} {S_{xy}}^{i} {T_{xy}}^{j} {R_z}^{k}\right). \tag{6.7}$$

A curve-fitting algorithm in MATLAB® is used to determine the a_{ijk} weighting coefficients. This formula determines the worst-case performance *P* of the system within the input tolerance ranges for displacement, tilt, and rotational errors (S_{xy}, T_{xy}, and R_z). This empirical formula can be used as a design tool to quantitatively determine the error

budget as well as the necessary optomechanical tolerance specifications that will ultimately result in a ‘pass-only’ system.

6.4 Optomechanical tolerancing example: imaging system

To demonstrate this tolerancing procedure, we consider the example presented in Chapter 4; an Alvarez lens with a shifted focal range of $\infty \geq f \geq 38.5$ mm across the lateral shift range of d = +/-1.8 mm. All simulations for this analysis were performed for a system with an 8-mm diameter aperture located in front of the first freeform lens. Additionally, the focal plane was set to the location where the RMS spot size was smallest for the ideal system (no error), determined using ZEMAX’s default optimization algorithm. It is worth noting that there was no re-optimization for the best focal spot after alignment errors were introduced. Since this is an imaging system, Strehl ratio and focal spot size where chosen as performance metrics.

The sensitivity analyses were performed for the specific systems where d = -0.9 mm (f = 154 mm), d = 0 mm (f = 77 mm), and d = 1.8 mm (f = 38.5 mm), all across error ranges of +/-50 μm (displacement), +/-5^{o} (tilt), and +/-1^{o} (rotation). Fig. 6.13 shows the results from the sensitivity analysis, where the Strehl ratio, RMS spot radius, and spot size/Airy Disk ratio are used as performance metrics. These results suggest that the system performance is more sensitive to rotational errors than tilt errors, and that the system is most sensitive to these alignment errors when d = 1.8 mm. This is not surprising since the effective focal length is shorter, meaning the composite lens has more surface curvature and thus steeper slope angles.

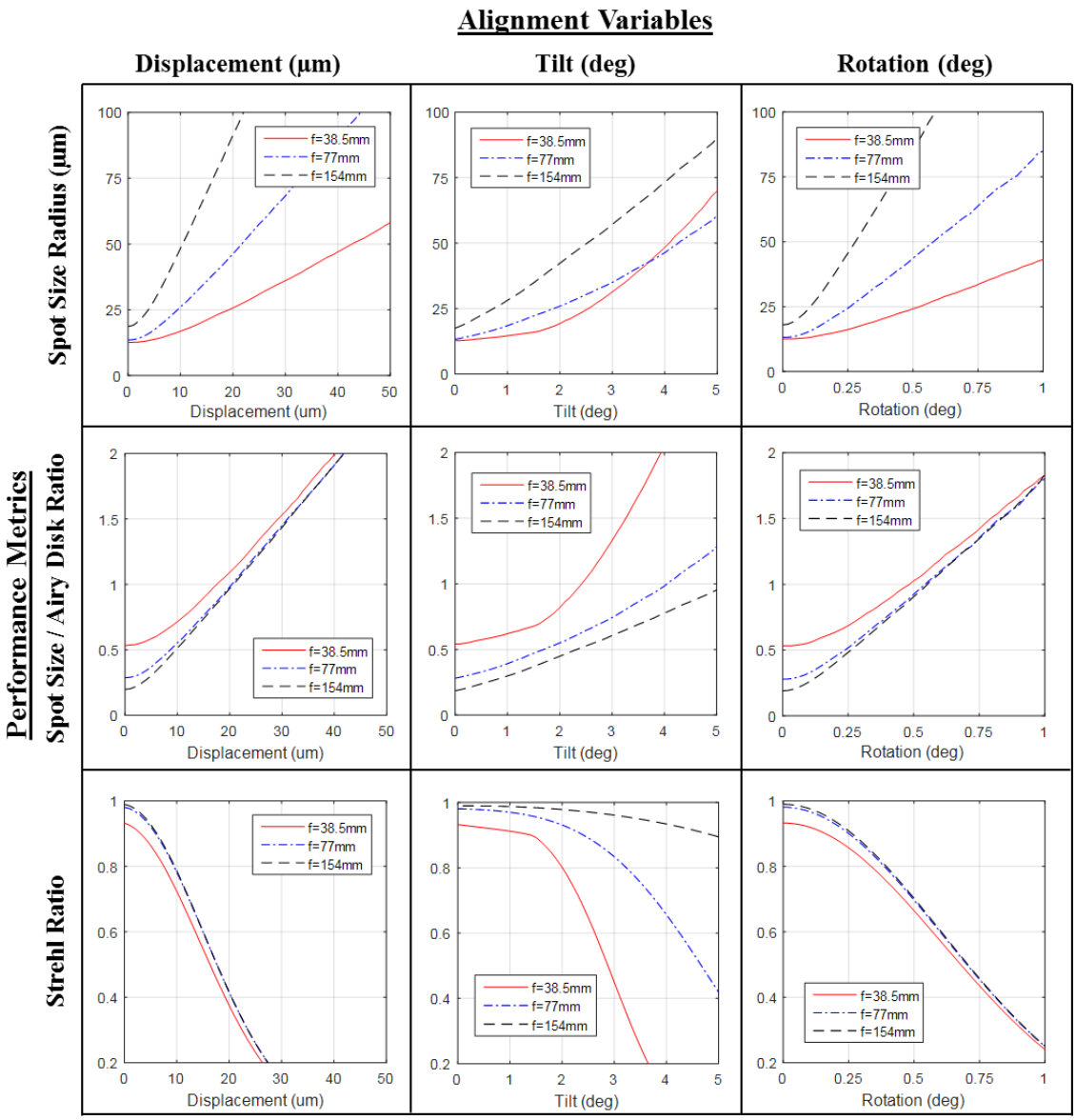

Fig. 6.13: Results from the Alvarez lens alignment sensitivity analysis for the cases where d = -0.9 mm (f = 154 mm), d = 0 mm (f = 77 mm), and d = 1.8 mm (f = 38.5 mm).

The initial tolerance bounds were then determined as the minimum error magnitudes for which the performance is equal to the pass-fail threshold, which in this example is defined as the diffraction limit. When using the Strehl ratio as the pass-fail threshold (*Strehl* = 0.8), the initial tolerance bounds were determined to be +/-8 µm (displacement), +/-2.0^{o} (tilt), and +/-0.35^{o} (rotational error). The initial tolerance bounds were imported into a custom macro created in ZEMAX®, for combined error analysis. As described

previously all 125 tolerance class variations and their respective orientations were simulated, and the worst-case scenarios for each class variation were determined in the custom MATALB® code. The results are displayed in Fig. 6.14, where the custom *c*-axis (color scale) of the 4-dimensional scatter plot is weighted based on the Strehl ratio.

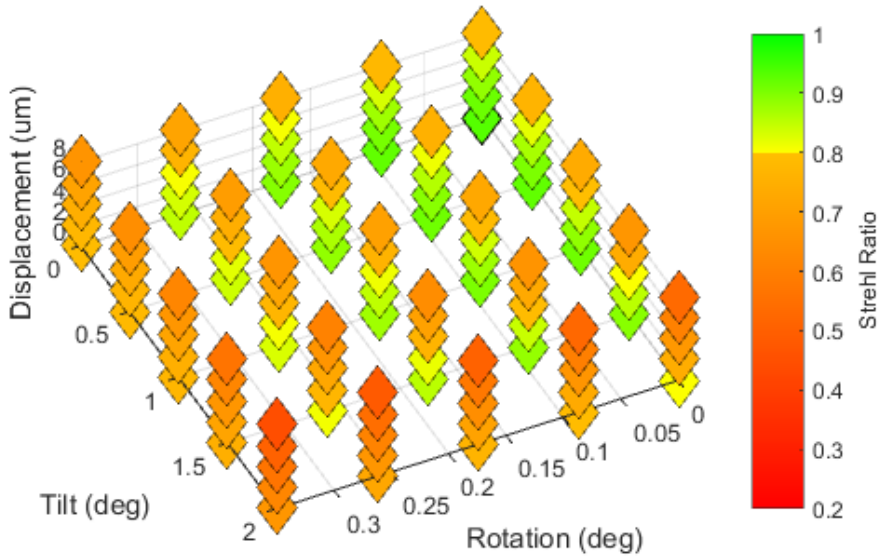

Fig. 6.14: A 4-dimensional scatter plot displaying the results from the combined error analysis where the minimum Strehl ratio is displayed through a custom color scale based on the alignment tolerance values.

These results were then interpolated in order to achieve a finer sampling between tolerance classes. Displaying a finely sampled 4-dimensional surface plot proved to be difficult. Instead, multiple 'slices' of the data were taken along the *x*, *y*, and *z* axes and the transparency of each data point was weighted to only be visible when above the pass-fail threshold ($Strehl \geq 0.8$); only the data points that qualify as a 'passing' system are visible, as demonstrated in Fig. 6.15. The final surface plot shows the performance impact of multiple alignment errors at different magnitudes and serves as a visual representation of the tolerancing specifications for this particular system.

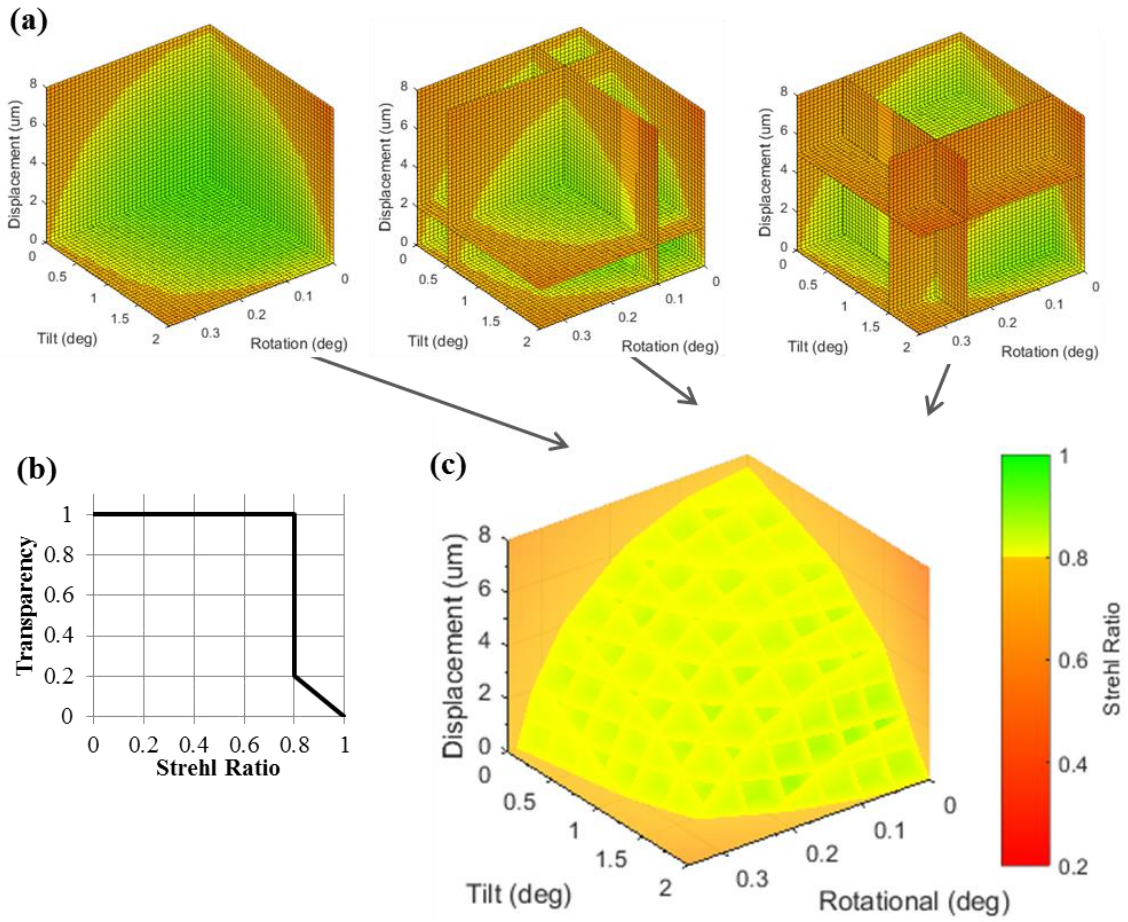

Fig. 6.15: Interpolated results from the Alvarez lens combined error analysis displayed using (a) multiple slices through a 4-dimensional surface plot, combined with (b) a custom transparency plot where only the tolerance class variations with passing Strehl ratios (*Strehl* ≥ 0.8) are visible in the (c) final surface plot.

The same analysis approach was applied using the Airy disk radius (23.6 μm) as the pass-fail metric. The initial tolerance bounds were determined to be +/-20 μm (displacement), +/-2.5^{o} (tilt), and +/-0.5^{o} (rotational error). The end results are shown in Fig. 6.16, where the transparency and custom *c*-axis (color scale) of the 4-dimensional scatter plot is weighted based on the RMS spot size.

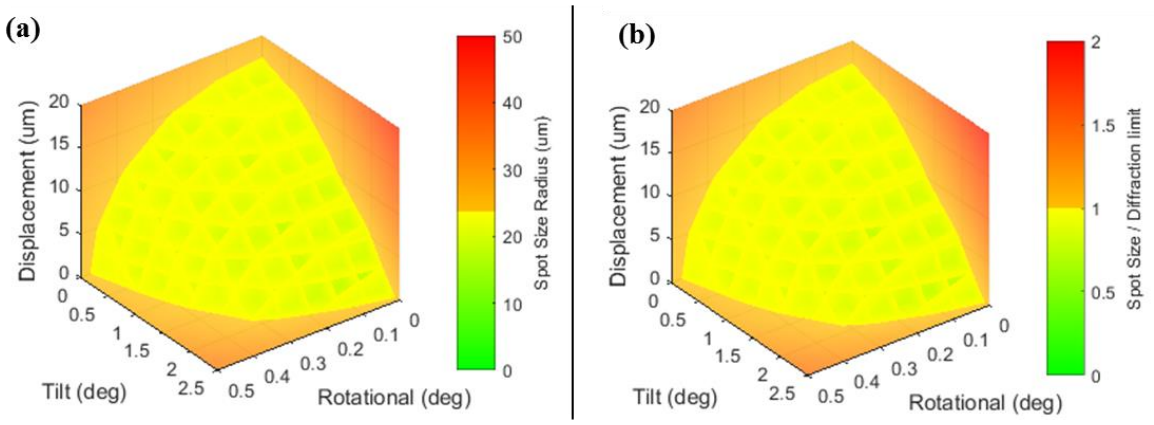

Fig. 6.16: Interpolated results from the Alvarez lens combined error analysis displayed through a 4-dimensional surface plot using a custom color and transparency scale based on (a) the RMS spot size radius and (b) the RMS spot size/diffraction limit ratio.

The surface plots from each of the CEA results suggest that the system would fail based on Strehl ratio before it would fail based on the spot size but are difficult to interpret together when quantitative tolerance specifications are required. Therefore, an empirical formula based on Eq. (6.7) was created to serve as a predictive model. A MATLAB® curve fitting algorithm was used to fit Eq. (6.7) to the CEA Strehl ratio results, with the resulting coefficients listed in Table 6.1. We note that this same empirical approach can be generated for any quantitative metric, including the RMS spot radius.

Table 6.1: Empirical formula coefficients for determining the system Strehl ratio as a function of the input tolerance specifications for displacement (S_{xy}), tilt (T_{xy}), and rotational (R_z) errors.

Empirical Formula Coefficients											
$Strehl = \sum\sum\sum a_{ijk} S_{xy}^{\ i} T_{xy}^{\ j} R_z^{\ k}$											
a000	0.0676	a100	0.0381	a200	0.1164	a300	0.0015	a400	-0.0102
a001	0.0000	a101	-0.0007	a201	0.0602	a301	-0.1729	a401	0.1162
a002	0.1533	a102	-0.0641	a202	0.2215	a302	-0.0953	a402	-0.0881
a003	0.0037	a103	0.0372	a203	-0.2810	a303	0.1444	a403	0.1001
a004	-0.0145	a104	0.0248	a204	-0.0207	a304	0.1254	a404	-0.1273
a010	0.0137	a110	0.0794	a210	0.0003	a310	-0.0050	a410	0.0174
a011	0.0038	a111	-0.1025	a211	0.0990	a311	0.0853	a411	-0.1025
a012	-0.0489	a112	0.2102	a212	-0.0536	a312	-0.0903	a412	0.1106
a013	0.0588	a113	-0.1957	a213	0.1866	a313	-0.2468	a413	-0.0116
a014	-0.0091	a114	0.0656	a214	-0.0930	a314	0.1028	a414	0.0228
a020	0.2299	a120	-0.1570	a220	-0.1151	a320	0.0231	a420	-0.0943
a021	0.0243	a121	0.0510	a221	-0.3981	a321	0.4154	a421	-0.0449
a022	0.1207	a122	-0.4171	a222	-0.1274	a322	0.1693	a422	-0.1972
a023	-0.2291	a123	0.3370	a223	0.1164	a323	-0.2355	a423	0.5058
a024	0.0228	a124	-0.2457	a224	0.3784	a324	-0.0594	a424	-0.2237
a030	-0.6102	a130	0.4204	a230	0.2886	a330	-0.1179	a430	0.1724
a031	-0.0428	a131	0.2527	a231	0.2299	a331	-0.3405	a431	-0.1143
a032	0.0367	a132	0.2435	a232	-0.2620	a332	0.0328	a432	0.3769
a033	0.0406	a133	0.2972	a233	-0.3000	a333	0.2391	a433	-0.4455
a034	0.1288	a134	-0.1125	a234	-0.2892	a334	0.2543	a434	-0.1315
a040	0.4976	a140	-0.1634	a240	-0.2099	a340	0.0652	a440	-0.0829
a041	0.0223	a141	-0.1465	a241	-0.1381	a341	0.1278	a441	0.1220
a042	-0.1234	a142	-0.2308	a242	0.5105	a342	0.1805	a442	-0.4809
a043	0.1158	a143	-0.1170	a243	-0.1496	a343	-0.3493	a443	0.3791
a044	-0.1334	a144	0.0758	a244	0.3092	a344	-0.3010	a444	0.2428

Several different tolerance class variations were analyzed to demonstrate the application of this empirical formula, as shown in Table 6.2.

Table 6.2: Example of several different tolerance class variations and their respective minimum system Strehl ratios predicted using the empirical approach and Eq. (6.7).

Example No.	**X-Y Disp. S_{xy} (μm)**	**X-Y Tilt T_{xy} (deg)**	**Z Rot. R_z (deg)**	**Predicted Strehl Ratio**
1	8	2	0.35	0.447
2	8	2	0.15	0.516
3	5	2	0.15	0.620
4	5	1	0.15	0.797
5	5	1	0.1	0.811

We note that the initial class variation chosen for this example did not produce a pass-only system. However, multiple pass-only systems can be achieved by tightening the input tolerance parameters. The demonstrated methods provide a useful approach for determining acceptable optomechanical tolerances.

6.5 Optomechanical tolerancing example: non-imaging system

To demonstrate this tolerancing procedure on a non-imaging system, we consider the super-Gaussian variable diameter beam shaper presented in Chapter 3. This example utilizes two laterally shifted PMMA freeform elements, resulting in uniform irradiance distributions of varying output radii R from 0.5 – 2.5 mm for a lateral shift range of d = +/-300 μm. We note that all simulations for this device were previously performed using VirtualLab™. However, for this tolerance analysis all simulations were performed using ZEMAX® due to its speed and capability to automate a large amount of simulations. Since this is a non-imaging system, uniformity error (U_{CV}), shape error (R_{CV}), and correlation degree (C_d) were used as performance metrics.

The sensitivity analyses were performed for the specific systems where d = -1.8 mm (R = 2.5 mm), d = 0 mm (R = 1.5 mm), and d = 1.8 mm (R = 0.5 mm), all across error ranges of +/-90 μm (displacement), +/-6^o (tilt) and +/-1^o (rotational). Fig. 6.17 shows the worst-case results from the sensitivity analysis for each of the performance metrics. These results suggest, again, that the system performance is more sensitive to rotational errors than tilt errors. Also, compared to the other alignment variables, the displacement error appears to have the most impact on the shape error R_{CV} while having minimal effect on the spot uniformity U_{CV}. This is largely due to the fact that this device is designed to

maintain uniformity with shifts in the *x* direction. Additionally, these results suggest that the system is most sensitive to these alignment errors when d = 1.8 mm (R = 0.5 mm). Similar to the imaging example, this is due to the fact that the composite lens at this point has more surface curvature and thus steeper slope angles.

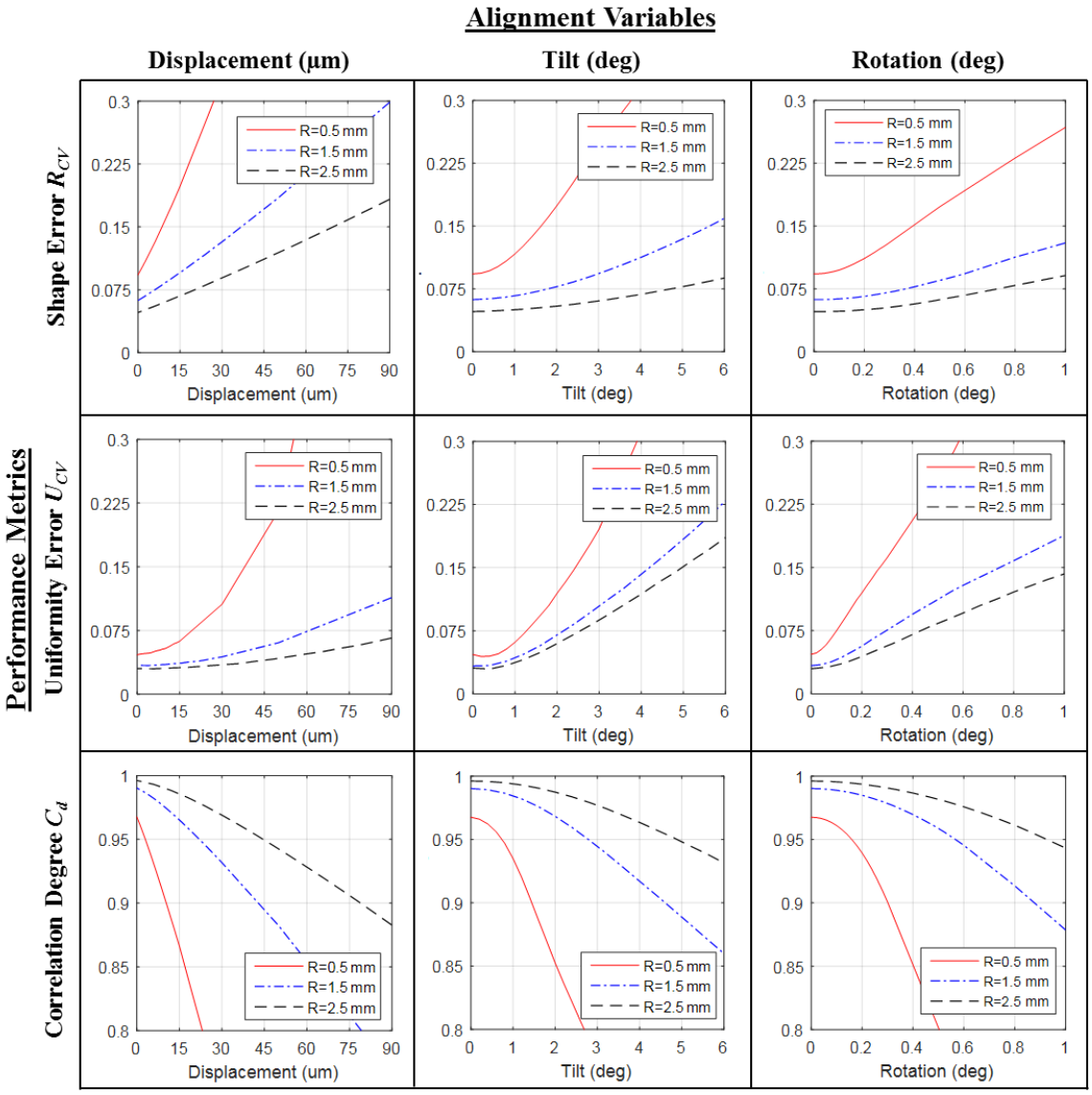

Fig. 6.17: Results from the beam shaper alignment sensitivity analyses for the cases where d = -1.8 mm (R = 2.5 mm), d = 0 mm (R = 1.5 mm), and d = -1.8 mm (R = 0.5 mm).

Pass-fail thresholds must be determined in order to determine the initial tolerance bounds. As discussed previously, performance metrics for these types of components are not standardized or well defined. For this reason, we subjectively determined acceptable thresholds by viewing the series of deviated spots. Comparing this qualitative assessment to quantitative metrics, the correlation degree C_d appears to be a good overall performance metric, accounting for shape, size, and uniformity. We therefore based the initial tolerance bounds off of this metric, with a pass-fail threshold of C_d >= 0.90. It should be noted that a specific application might demand a specific performance metric value which could then be used as a threshold. Fig. 6.18 displays the deviated output spots at the extremes of the initial tolerance bounds which were determined to be +/-30 μm (displacement), +/-2.5^o (tilt), and +/-0.55^o (rotational error).

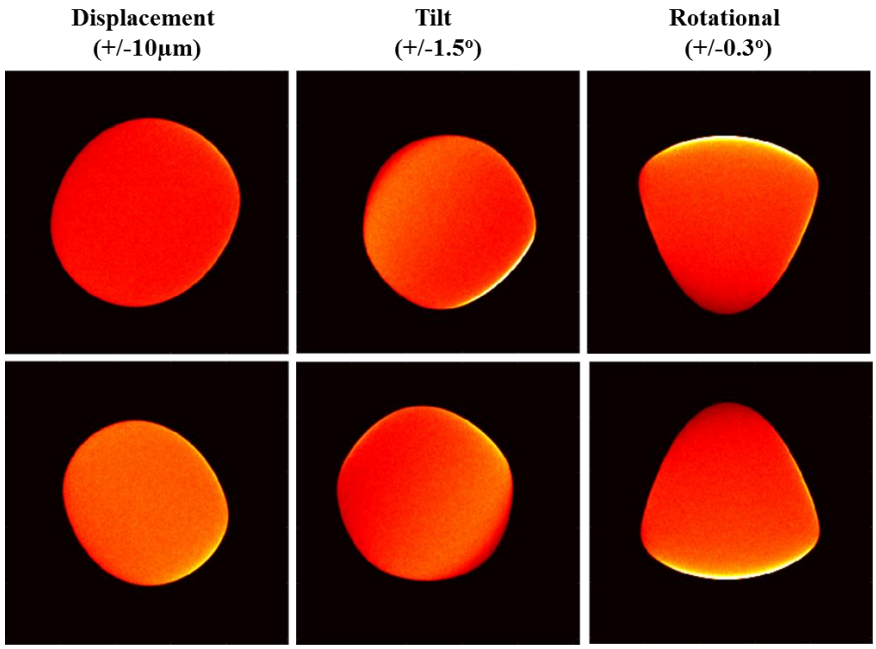

Fig. 6.18: Deviated output spots at the extremes of the initial tolerance bounds.

Once again, after importing the initial tolerance bounds into the custom macro created in ZEMAX®, the CEA was performed, simulating all 125 tolerance class variations and

their respective orientations. These results were interpolated to achieve a finer sampling between tolerance classes. The results from the interpolated CEA are displayed for each performance metric in a 4-dimensional surface plot in Fig. 6.19. Only the data points that qualify as a 'passing' system are visible. The pass-fail thresholds for shape error R_{CV} and uniformity error U_{CV} were both subjectively set to be 0.15. The same trends from the sensitivity analyses can be seen here, where the shape error is most impacted by displacement and the uniformity is most impacted by the tilt errors.

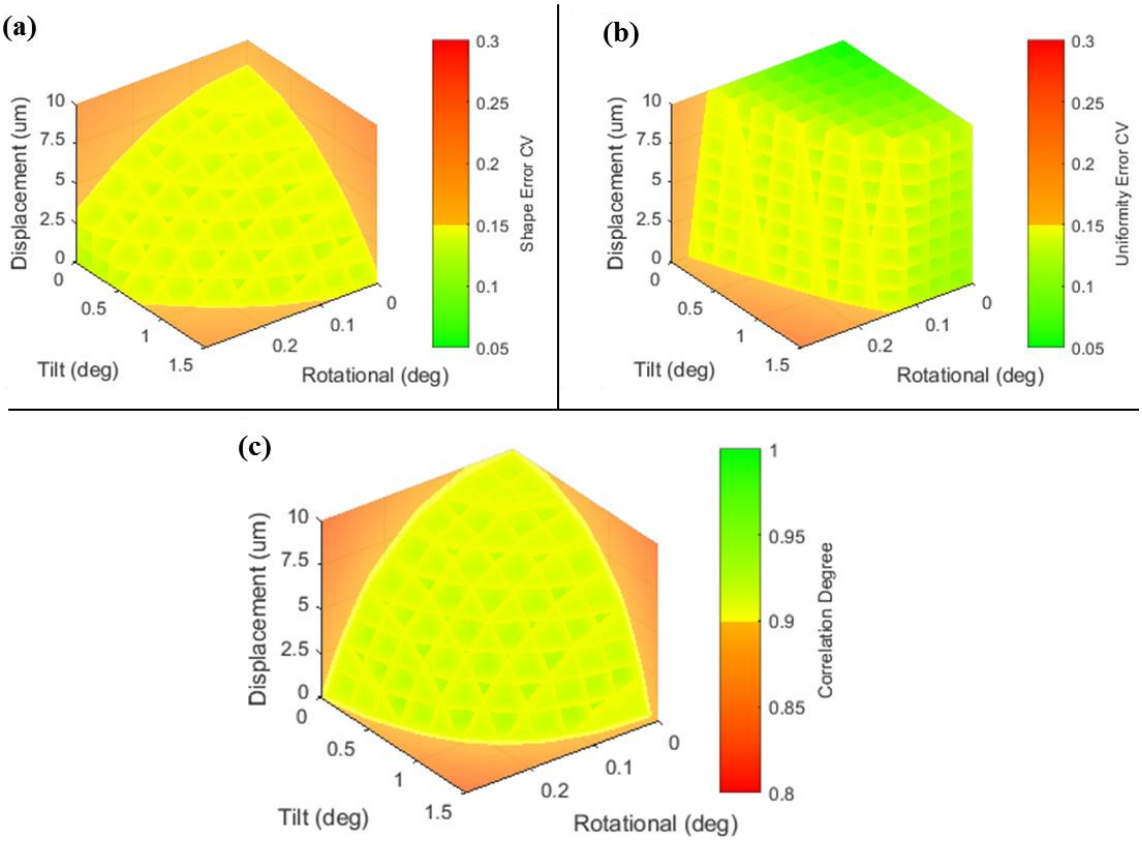

Fig. 6.19: Interpolated results from the beam shaper combined error analysis displayed through a 4-dimensional surface plot using a custom color and transparency scale based on (a) the shape error R_{CV}, (b) the uniformity error U_{CV}, and (c) the correlation degree C_d.

An empirical formula based on Eq. (6.7) was created for the correlation degree C_d to serve as a predictive model. This was performed for the worst case scenario by focusing on the case shown to be most sensitive to alignment errors (d = 300 μm and R = 0.5 mm).

For this specific case, a MATLAB® curve fitting algorithm was used to fit Eq. (6.7) to the CEA results for the correlation degree, with the resulting coefficients are listed in Table 6.3. We note again that this procedure can be implemented for any of the performance metrics, but the correlation degree was used since it incorporates measures of shape, size, and uniformity in a single metric.

Table 6.3: Empirical formula coefficients for determining the minimum system correlation degree C_d as a function of the input tolerance specifications for displacement (S_{xy}), tilt (T_{xy}), and rotational (R_z) alignment errors.

Empirical Formula Coefficients									
$C = \sum\sum\sum a_{ijk} S_{xy}^{\,i} T_{xy}^{\,j} R_z^{\,k}$									
a000	0.0322	a100	0.0543	a200	0.0188	a300	-0.0116	a400	0.0035
a001	0.0020	a101	-0.0076	a201	0.0656	a301	-0.2053	a401	0.1482
a002	0.0498	a102	-0.0802	a202	0.2741	a302	-0.0827	a402	-0.1351
a003	0.0201	a103	0.0135	a203	-0.2781	a303	0.1729	a403	0.1097
a004	-0.0048	a104	0.0550	a204	-0.0549	a304	0.1233	a404	-0.1283
a010	0.0172	a110	-0.0155	a210	0.0084	a310	0.0108	a410	-0.0072
a011	-0.0027	a111	-0.0773	a211	0.0379	a311	0.0746	a411	-0.0830
a012	-0.0453	a112	0.2467	a212	-0.1280	a312	-0.0745	a412	0.1518
a013	0.0756	a113	-0.1964	a213	0.1481	a313	-0.1997	a413	0.0221
a014	-0.0373	a114	0.0468	a214	-0.0907	a314	0.1467	a414	-0.0086
a020	-0.0106	a120	0.0038	a220	-0.0069	a320	0.0749	a420	-0.0706
a021	0.0325	a121	0.2461	a221	-0.2902	a321	0.4059	a421	-0.1317
a022	0.1656	a122	-0.3224	a222	-0.1082	a322	0.1301	a422	-0.2837
a023	-0.1821	a123	0.3433	a223	0.1070	a323	-0.2820	a423	0.4081
a024	0.0638	a124	-0.2450	a224	0.4112	a324	-0.0822	a424	-0.3318
a030	0.1307	a130	-0.0781	a230	0.0492	a330	-0.2123	a430	0.1813
a031	-0.0849	a131	-0.0389	a231	0.1948	a331	-0.3155	a431	-0.0409
a032	-0.0793	a132	0.0991	a232	-0.2566	a332	0.0950	a432	0.4948
a033	-0.0652	a133	0.1865	a233	-0.2823	a333	0.3097	a433	-0.3250
a034	0.0620	a134	-0.1774	a234	-0.2168	a334	0.3577	a434	-0.0047
a040	-0.0644	a140	0.0599	a240	-0.0426	a340	0.1226	a440	-0.1005
a041	0.0544	a141	-0.0751	a241	-0.0947	a341	0.1014	a441	0.0966
a042	-0.0607	a142	-0.1037	a242	0.5071	a342	0.1234	a442	-0.5052
a043	0.1699	a143	-0.0299	a243	-0.1989	a343	-0.4339	a443	0.3430
a044	-0.0865	a144	0.1279	a244	0.2635	a344	-0.3785	a444	0.2081

Several different tolerance class variations were analyzed to demonstrate the application of this empirical formula, as shown in Table 6.4.

Table 6.4: Example of several different tolerance class variations and their respective minimum system correlation degrees determined using empirical approach and Eq. (6.7).

Example No.	**X-Y Disp. S_{xy} (μm)**	**X-Y Tilt T_{xy} (deg)**	**Z Rot. R_z (deg)**	**Predicted Correlation Degree C_d**
1	10	1.5	0.3	0.794
2	10	1.5	0.15	0.833
3	5	1.5	0.15	0.862
4	5	1	0.15	0.893
5	5	1	0.1	0.902

We note that the initial class variation chosen for this example did not produce a pass-only system. However, multiple pass-only systems can be achieved by tightening the input tolerance parameters. The demonstrated methods provide a useful approach for determining acceptable optomechanical tolerances for non-imaging systems.

6.6 Discussion

A simplified tolerancing procedure has been developed and demonstrated for dynamic freeform optical systems with an eye towards efficiency and certainty. This procedure consisted of sensitivity analyses, a combined error analysis, and creation of an empirical formula for prediction of an error budget based on three individual tolerance parameters (displacement, tilt, and rotational). The ‘pass-fail’ approach applied ensures that the device will work properly within the determined tolerance parameters.

Multiple assumptions were made throughout this procedure, considering a sequence of worst-case scenarios in an attempt to have a deterministic end result while simplifying the entire process. The first assumption supposed equal tolerances for both elements by modeling the second freeform with an equal and opposite misalignment as the first. Both

elements were also assumed to have equal *x* and *y*-axis displacement and tilt tolerances. These assumptions significantly reduced the number of required simulations, though at a slight cost as they subtly increase the potential of over-tolerancing along the *x* or *y* direction. For example, tolerances for displacement in one direction could be set too tightly as a consequence of the system being more sensitive to displacement in the orthogonal direction. This subtlety was not considered in this dissertation. Future research could explore these assumptions to potentially produce more accurate tolerance specifications while maintaining simplicity and certainty.

This procedure was demonstrated using an Alvarez lens and a variable output beam shaper as case studies. In both cases, the results suggested that the system performance is less sensitive to tilt errors than to displacement and rotational errors. Also, comparing the performance sensitivity of the systems with different lateral shifts suggested that the sensitivity to alignment errors increases as the composite surface curvature increases. Lastly, we note the importance of the performance metric used when determining tolerances. The chosen performance metrics determines the pass/fail thresholds, which then ultimately determines the tolerance specifications. While the standards for imaging devices are well-established, the same cannot be said for non-imaging devices. In practice, several different performance metrics should be considered to ensure proper system performance.

CHAPTER 7: SURFACE FORM ERROR TOLERANCING OF DYNAMIC FREEFORM OPTICAL SYSTEMS

7.1 Introduction

In addition to the performance dependency on proper optomechanical alignment, dynamic freeform optical systems are also sensitive to the accuracy of the manufactured surface shape. Form error, often called figure error, is a low spatial-frequency deviation of a surface from a desired shape. Form errors can be caused by a number of different factors, including tool wear, tool shape error, tool alignment error, machine errors, thermal effects, and others. Understanding the impact of surface errors and the corresponding form tolerances is vital when considering the necessary balance between manufacturing costs and product performance. Overly tight tolerances on surface form unnecessarily increase manufacturing costs, while tolerances that are too loose can result in unusable optical components [130, 131].

Significant research has been performed on surface form error considerations for rotationally symmetric optical surfaces, including design methods for easier manufacturing [146-148], methods based on cost-versus-performance relationships [149, 150], and interpretations of tolerance specifications [151]. Rotationally symmetric surfaces generally follow specifications on power and irregularity error in the international ISO10110 standards [74, 75]. The power error specification is typically described by tolerances on the radius of curvature and conic constant based on the original lens prescription, while irregularity is described either by the P-V (peak to

valley) or root mean square RMS maximum of the residual surface error after a best fit sphere has been removed [152, 153]. In some cases power and irregularity errors are not sufficient, typically for complex aspheric surfaces. In such cases, a surface waviness tolerance is often implemented, where the maximum surface deviation and slope errors are specified relative to a surface that best fits the desired surface [79, 152].

Recent updates have been added to the ISO10110 standard which includes freeform surfaces in their tolerance standards [76, 154, 155]. Explained with greater detail in [154], these updates implement the specification of three coordinate systems corresponding to; (1) the origin of the freeform description, (2) a coordinate reference system at the intersection of a reference axis and surface, and (3) component reference points. Using these coordinate systems, a freeform surface can be specified through irregularity and slope tolerances at specific Cartesian coordinate points.

While surface form tolerance standards for freeform optical surfaces are now well-established, the same is not true for surface form tolerancing methods and procedures. This is partially due to the relative immaturity of freeform manufacturing processes, and largely due to the complexity and variety of freeform descriptions. The type of form error signature and required specification depends heavily on both the manufacturing method (diamond milled, diamond turned, polishing, etc.) and the mathematical description of the desired surface (toroidal, biconic, anamorphic, off-axis parabola, point clouds, Zernike polynomials, XY polynomials, etc.). Significant research has been performed on developing surface form error tolerancing methods for freeforms [77-81]. However, much of this work is application-specific and lacks a methodology for specifying tolerances on surface form accuracy for dynamic freeform systems such as the Alvarez

lens and variable diameter beam shaper. To this end, performance impacts of low frequency surface form errors were explored for dynamic freeform systems, with an eye towards developing meaningful manufacturing specifications.

7.2 Methods and assumptions

Modeling freeform surfaces with intentional form errors presents many challenges due to the complexity of the freeform surface definitions as well as their inherent rotational asymmetry. The shape of standard spherical and aspheric lenses is typically defined by two parameters; radius of curvature and a conic constant [126]. This small number of parameters enables straightforward ways to model a deviated surface and tolerance the system based on performance impacts through optical simulations. For aspheric lenses with additional aspheric terms, well-known Zernike polynomials have been used to model the deviated surface, which can be done using common optical design software [152, 156]. Additional methods have been implemented in order to tolerance complex aspheric lenses using rotationally symmetric surface slope deviations to represent the surface form error [157, 158]. Though effective, these methods do not directly apply to the freeform surfaces used in the examples presented in this dissertation. This is because the freeform surface prescriptions involve multiple terms that do not directly relate to meaningful form error tolerance specifications. Furthermore, in a general sense, signature form errors for freeforms are not accurately represented by Zernike polynomials and rotationally symmetric surface slope. Thus, a method for modeling deviated freeform surfaces is essential to enable meaningful specification of any form errors.

To begin the discussion, we note that surface form error characteristics are heavily dependent on the chosen fabrication method. For this analysis, the freeforms are assumed to be diamond raster-milled (discussed in Chapter 2), and each of the two freeforms in the dynamic system are assumed to have the same form error ($\varepsilon_{zf1} = \varepsilon_{zf2}$) for all subsequent simulations. Based on fabrication results from previous research and conversation with Dr. Joseph Owen from the Center of Precision Metrology at UNC Charlotte [159], there are two dominating characteristics of form error. The first is a surface deviation which is scaled relative to the local height of the prescribed surface Z_{ref}. The respective form error ε_{HS} is represented by,

$$\varepsilon_{HS}(x, y) = Z_{ref}(x, y) * HS, \tag{7.1}$$

where *HS* is the unitless height scale used to control the amount of deformation introduced to the lens. This type of error can be a product of several contributors such as thermal drift, position control errors from the machine, errors in the programmed tool path, etc. In essence, this is a straightforward way to vary the optical power of the system, conceptually illustrated in Fig. 7.1 for both a spherical lens and freeform surface.

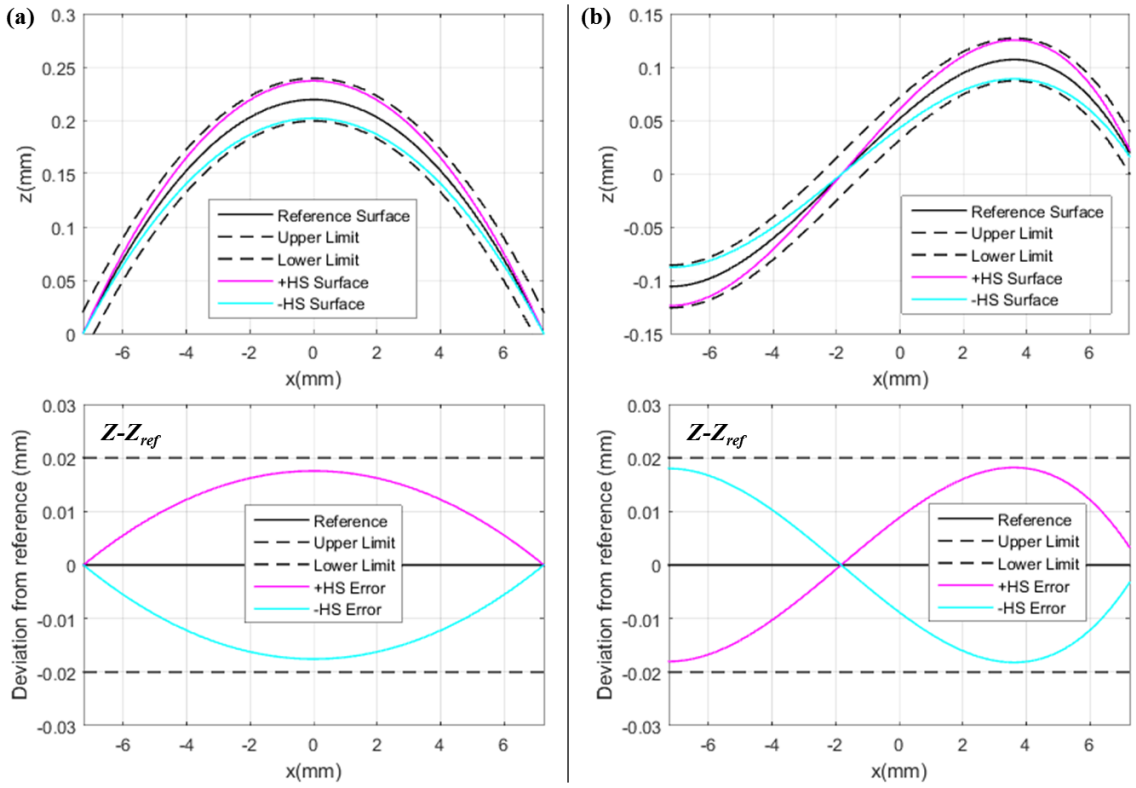

Fig. 7.1: Illustration of the height-scaled surface form error for (a) a spherical lens and (b) a freeform lens.

Performing a sensitivity analysis using *HS* as a variable enables a practical tolerance specification on this parameter. However, the height-scale specification by itself is not sufficient to represent the necessary surface accuracy, as there could be additional errors in the fabricated surface. Thus, we also incorporate the second dominating form error characteristic; a surface deviation based on the local slope angle of the prescribed surface. This characteristic can be attributed to multiple error sources, including machine errors due to cutting forces, errors in tool shape, tool path error, thermal drift, and others. In order to define this form error, the prescribed surface's slope angle dZ_{ref} must be determined. Referenced to the surface normal, this is given by,

$$dZ_{ref}(x,y) = \sqrt{\left(\frac{dZ_{ref}}{dx}\right)^2 + \left(\frac{dZ_{ref}}{dy}\right)^2}. \tag{7.2}$$

The surface error can then be defined as,

$$\varepsilon_{SS}(x,y) = dZ_{ref}(x,y)^2 * SS, \tag{7.3}$$

where *SS* is the unitless slope scale used to control the amount of deformation introduced to the surface. This form error is illustrated in Fig 7.2 for a spherical lens and freeform surface. The maximum amount of error is located where the prescribed surface angle is at its maximum.

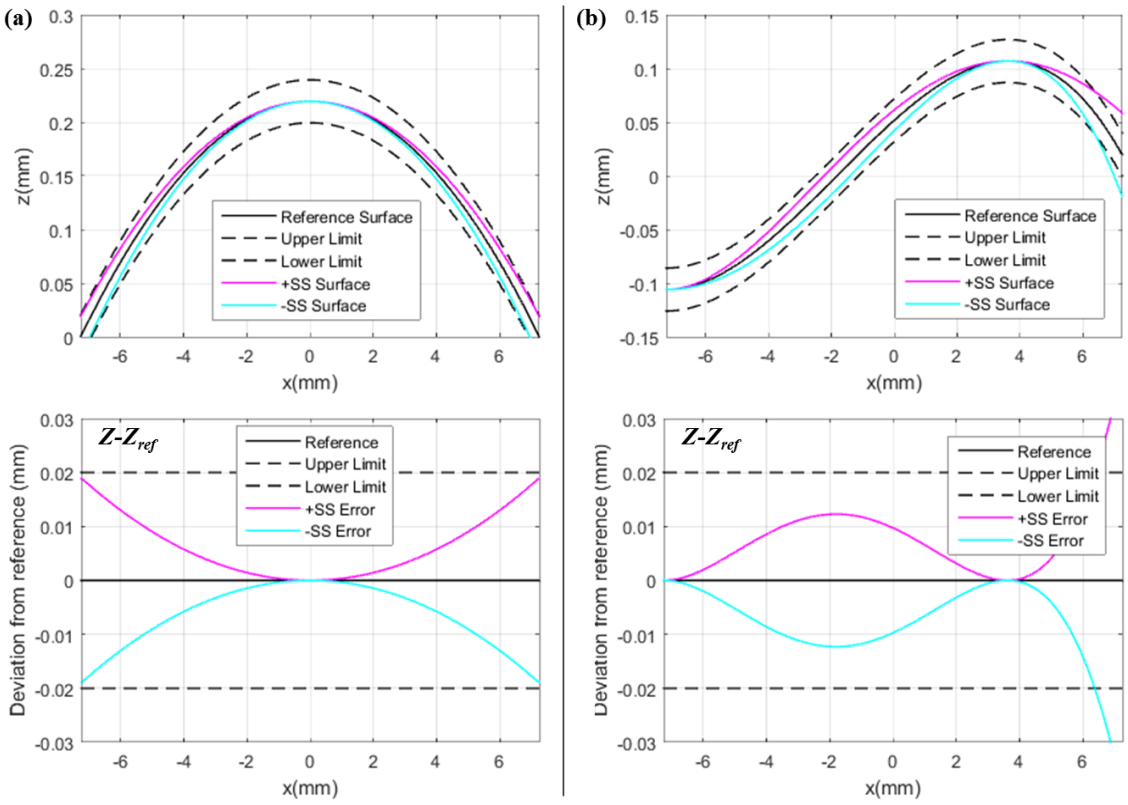

Fig. 7.2: Illustration of the slope-scaled surface form error added to (a) a spherical lens and (b) a freeform lens.

Performing a sensitivity analysis using *SS* as a variable enables a practical tolerance specification on this parameter. The resulting specification could be in the form of a maximum P-V value, RMS value, or slope error. As before, however, the slope-scale specification by itself is insufficient to represent the required surface accuracy

A straightforward way to tolerance freeform surface accuracy is to determine a specification on the maximum allowable P-V or RMS from the reference surface. This is determined using results gathered from simulations performed in the individual sensitivity analyses. Each sensitivity analysis provided a threshold for the maximum allowable height and slope scale. Maximum P-V and RMS values are embedded in these scale thresholds for both height scale *HS* and slope scale *SS*; the smaller of the height or scale P-V or RMS would serve as the threshold for the entire surface. This implies that as long as the fabricated surface is within a single tolerance range, the surface is considered acceptable. Although this is a deterministic way of tolerancing the surface, this approach can result in over-tolerancing. For example, assume the maximum acceptable P-V for a given surface was determined to be 0.5 μm for the height scale *HS* and 1 μm for the slope scale *SS*, and the overall P-V threshold would be set as the smaller of the two. With this in mind, assume a maximum measured P-V of 0.75 μm, above the threshold where the surface would be considered faulty. There is a possibility that the surface form error was almost entirely dependent on the slope angle of the surface, in which case the measured P-V would actually have been acceptable.

To avoid this potential issue, the two specifications must be modeled and simulated as a pair in order to view the performance impact that the entire surface form error has on the system. The total surface form error is defined as

$$\varepsilon_Z(x,y) = \varepsilon_{HS}(x,y) + \varepsilon_{SS}(x,y). \tag{7.4}$$

Combining the height scale and slope scaled errors helps ensure that all possibilities of low frequency form deviations are considered when determining the specifications, illustrated in Fig. 7.3 for a spherical lens and freeform surface.

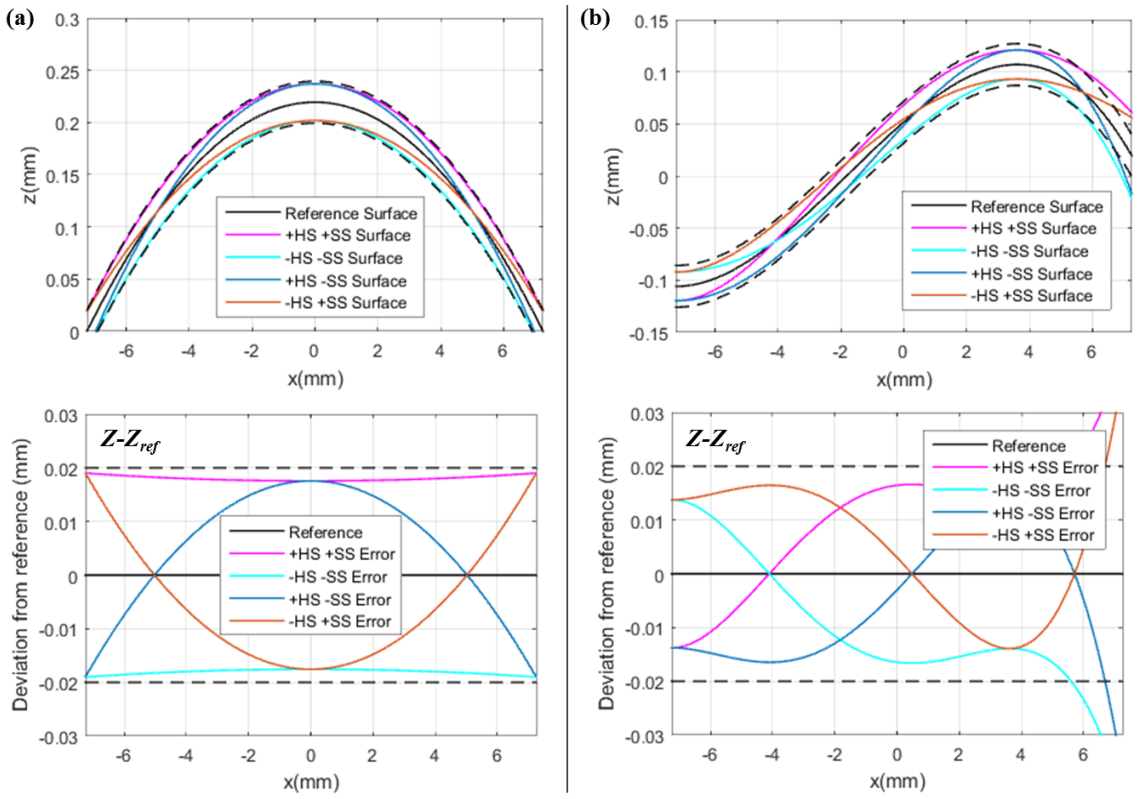

Fig. 7.3: Illustration of the combined height scale and slope-scaled surface form errors added to (a) a spherical lens and (b) a freeform surface.

With these factors in mind, the proposed method for tolerancing surface form error is to individually perform sensitivity analyses for each of the height scale and slope scale errors. Similar to the optomechanical tolerancing procedure discussed in Chapter 6, this approach must consider the entire dynamic range of the system. Therefore, the sensitivity analyses are performed for the case where no lateral shift is introduced (d = 0) and for the cases where the lateral shifts are at the design extremes (d = +/-d_{max}). Comparing the

results from these analyses provides information on which specific case of lateral shift is most sensitive to the individual form errors. Using the results from the most sensitive case, the initial tolerance bounds are determined where the system crosses the chosen performance metric threshold. These tolerance bounds are then used in the combined scale analysis where the height scales and slope scales are varied such that all possible scenarios are simulated for the specific laterally shifted system which was most sensitive to form error. This provides a grid of the system performance based on the respective error-scales that acts as a tolerance map for determining whether a fabricated surface passes or fails. We will demonstrate this approach in subsequent sections of this chapter.

7.3 Surface form error tolerancing example: imaging system

To demonstrate this tolerancing procedure, we again consider an Alvarez lens with a shifted focal range of $\infty \geq f \geq 38.5$ mm across the lateral shift range of d = +/-1.8 mm. A custom MATLAB® code was used to generate the freeform surfaces with the imposed surface form errors. These surfaces were exported from MATLAB® as DAT files, where the stored data included surface heights and slope angles for a grid of x and y coordinates. These surfaces were imported into ZEMAX® [127] as "grid sag" surface types, and an 8-mm diameter aperture was placed in front of the first freeform surface. Similar to the optomechanical tolerancing procedure (Chapter 6), the focal plane was set to the location where the RMS spot size was smallest for the ideal system (no error), and there was no re-optimization for the smallest focal spot after surface form errors were introduced.

The first sensitivity analysis was performed for the specific systems where d = -0.9 mm (f = 154 mm), d = 0 mm (f = 77 mm), and d = 1.8 mm (f = 38.5 mm), all across a height

scale *HS* range of +/-0.015. We note that only a portion of the freeform lens is being used, due to the smaller 8 mm aperture stop in front of the freeform elements. For a fixed system, it would be more accurate to measure the form error within the central 8 mm circular area of the freeform surface. However, considering the dynamic range of this device, the location of the aperture stop in reference to the freeform surface is dependent on the lateral shift *d* in the system, shown in Fig. 7.4. This means that the area of the freeform, from which the form error is measured and specified, is also a function of lateral shift *d*. Though possible, this adds a level of complexity that is considered beyond the scope of this work; however, it should be considered in future work for a more accurate specification. For now, the resulting form error, specified as maximum P-V and RMS values, were measured across the entire 14.5 mm lens diameter, shown in Fig. 7.5.

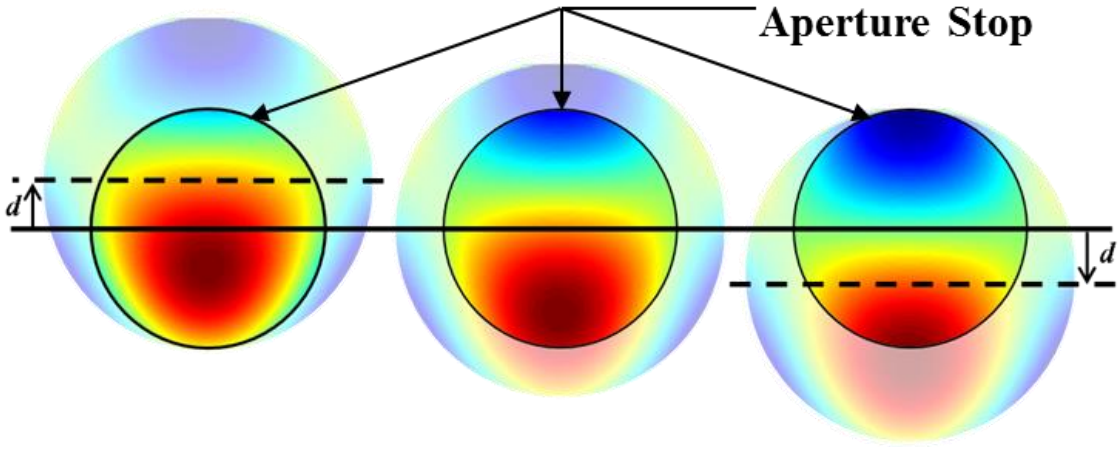

Fig. 7.4: Illustration of how lateral shift *d* changes the location of the aperture stop in reference to the freeform surface, implying that the area from which the form error is measured and specified is also a function of lateral shift *d*.

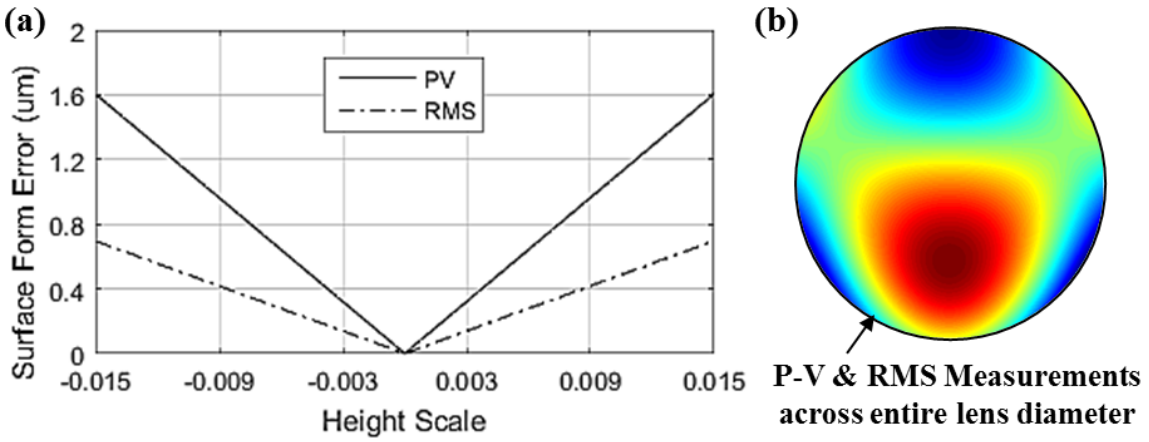

Fig. 7.5: (a) Resulting maximum P-V and RMS values of Alvarez freeform surfaces with the intentionally added height scale *HS* surface form errors, (b) measured across the entire 14.5 mm lens diameter.

The results from the sensitivity analyses are shown in Fig. 7.6. The Strehl ratio, spot size radius, and spot size/Airy disk radius ratio were used as performance metrics with respect to the height scale *HS* and the corresponding P-V and RMS measurement of the deformed surface. We note that the performance impact was not symmetric for positive and negative scales; therefore, the results shown in Fig. 7.5 represent the worst-case performance for the respective form error specification. These results suggest that the system performance is most sensitive to these form errors when d = 1.8 mm (f = 38.5 mm). This is due to the fact that the effective focal length is shorter at this specific lateral shift, meaning the composite lens has more surface curvature and is affected more strongly by the height scale form error.

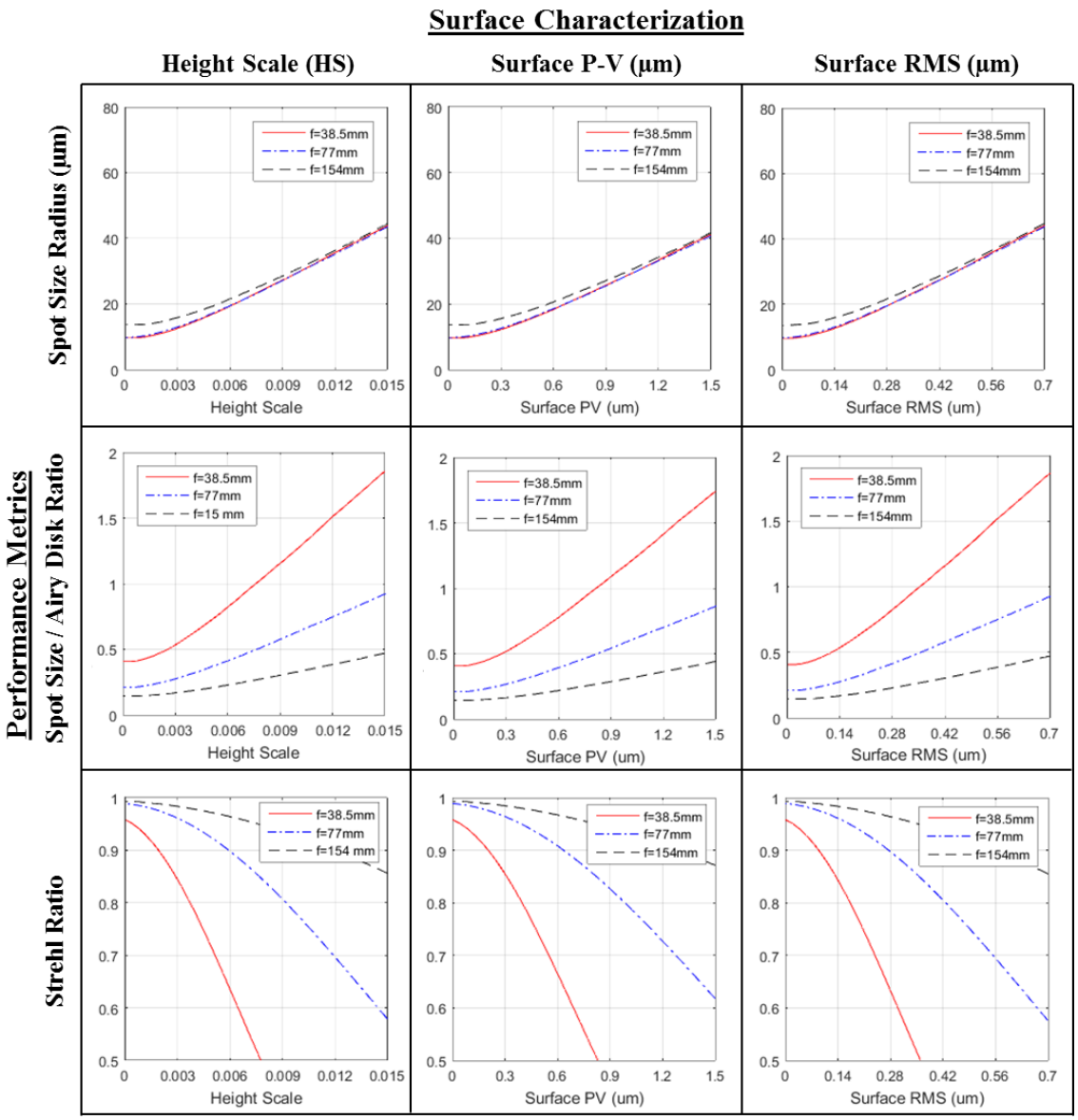

Fig. 7.6: Results from the Alvarez lens height scale *HS* form error sensitivity analyses for the cases where d = -0.9 mm (f = 154 mm), d = 0 mm (f = 77 mm), and d = 1.8 mm (f = 38.5 mm).

The same procedure was followed again; varying the slope scale *SS* rather than the height scale *HS*. Using another custom MATLAB® code, freeform surfaces were generated with imposed form errors with a slope scale *SS* range of +/-3.6E-05. For the same reasons discussed earlier regarding the area from which the form error is measured,

the resulting maximum P-V and RMS values were again measured across the entire 14.5 mm lens diameter, shown in Fig. 7.7.

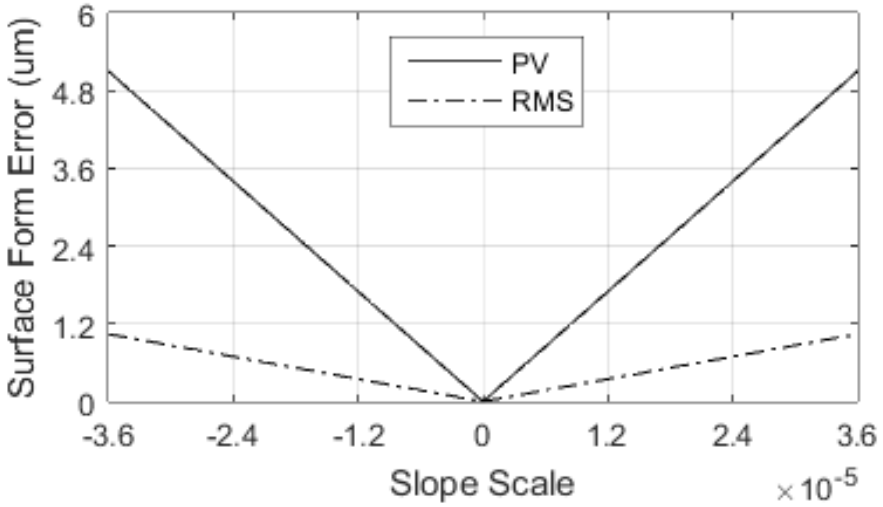

Fig. 7.7: Resulting maximum P-V and RMS values of the freeform surfaces with the intentionally added slope scale *SS* surface form errors.

The results from the sensitivity analyses are shown in Fig. 7.8 using the same performance metrics as before. Similar to the height scale analysis, the performance impact asymmetric for positive and negative scales; therefore, the results shown in Fig. 7.7 represent the worst-case performance for the respective form error specification. These results again suggest that the system performance is most sensitive to these particular form errors when d = 1.8 mm (f = 38.5 mm) where the composite lens has more surface curvature (larger slope angles) and is affected more strongly by the slope scale form error.

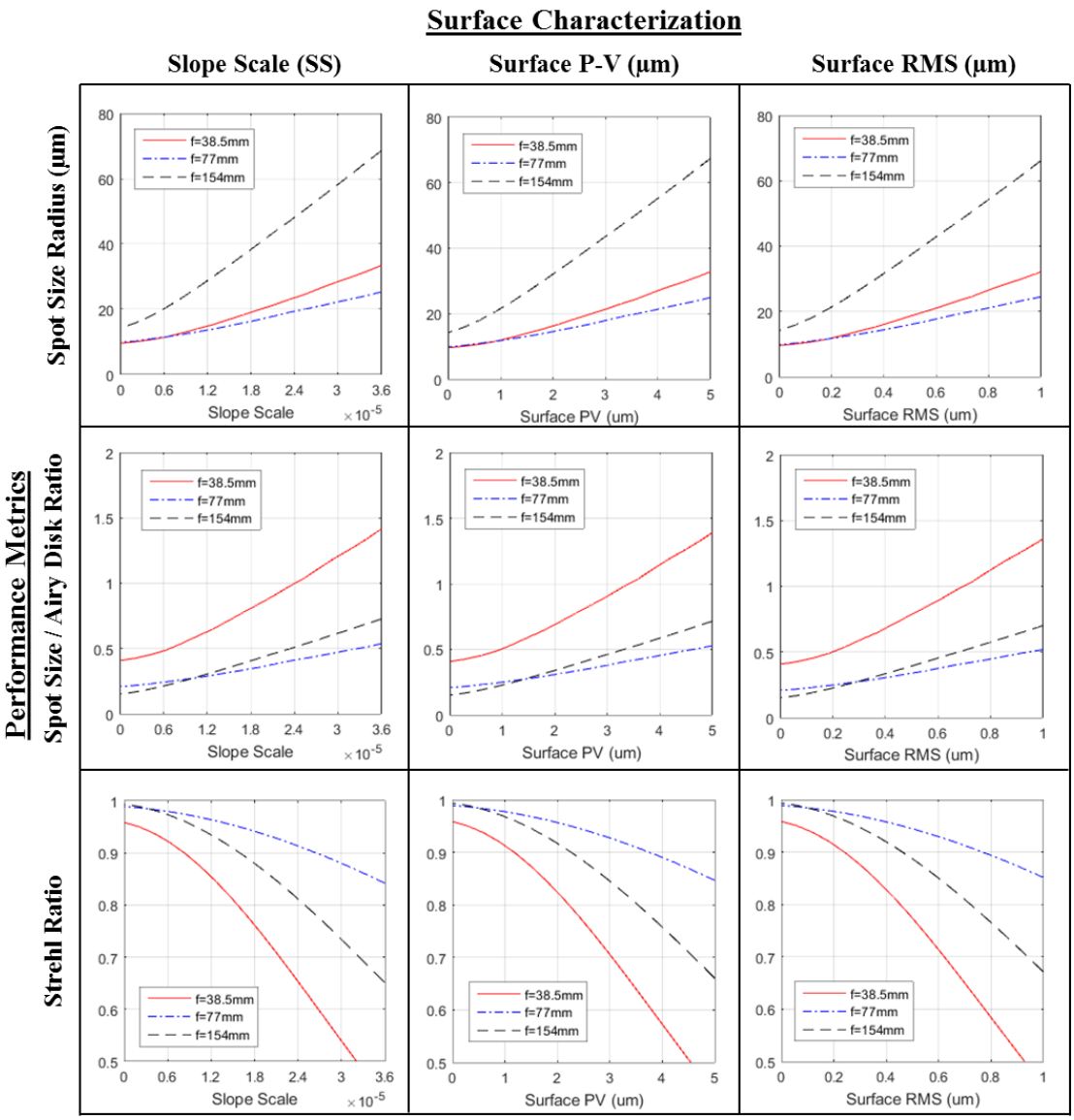

Fig. 7.8: Results from the Alvarez lens slope scale SS form error sensitivity analysis for the cases where d = -0.9 mm (f = 154 mm), d = 0 mm (f = 77 mm), and d = 1.8 mm (f = 38.5 mm).

Next, the initial tolerance bounds were determined as the minimum error magnitudes for which the performance equaled the pass-fail threshold, in this case the diffraction limit. When using the Strehl ratio as the pass-fail threshold ($Strehl$ = 0.8), the initial bounds were determined to be +/-0.004 for the height scale, and +/-1.75E-05 for the slope scale. The combined scale analysis was performed using these tolerance bounds, simulating all possible scenarios for positive and negative height scales and slope scales.

We note that there are four possible permutations of scale direction for each combination of *HS/SS* (+/+, +/-, -/+, and -/-). The worst performance of the permutations was recorded for each combination. The resulting Strehl ratios are shown in Fig. 7.9(a) with a custom color scale to show a distinct pass-fail cutoff line. The slope scale was also converted to the maximum allowable irregularity of the surface, with the results shown in Fig. 7.9(b). In this case the irregularity is the measured P-V value of the surface form error after removal of the reference and best-fit height scale.

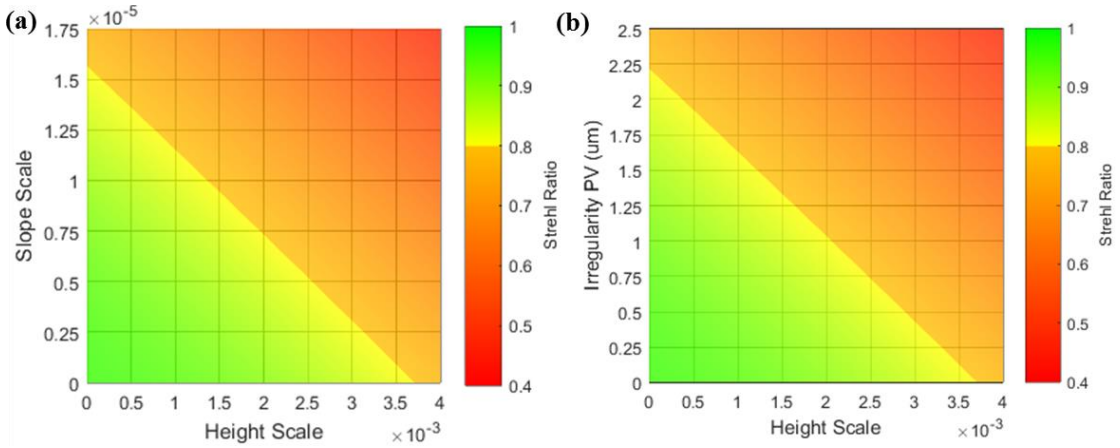

Fig. 7.9: Results from the combined height scale and slope scale analyses for the Alvarez lens, showing the Strehl ratio performance impact regarding (a) the height scale and slope scale and (b) the height scale and remaining irregularity P-V of the freeform.

As mentioned earlier, these results act as tolerance maps for determining pass-fail conditions for a fabricated surface. To demonstrate this procedure, we assume a fabricated Alvarez lens where the measured surface is shown in Fig. 7.10(a) and the surface form error (Z-Z_{ref}) is shown in Fig. 7.10(b). The height scale HS = 0.0035 was determined using a standard best-fit parameter sweep. This height scale is then removed from the form error, as shown in Fig. 7.10(c), leaving behind the residual surface error (irregularity) with a max P-V of 0.75 μm. The tolerance map is then used with both of these measurements to determine that the worst-case performance for that fabricated lens,

as shown in Fig. 7.10(d). For this particular example, the worst-case performance is a Strehl ratio of 0.7. This is unacceptable, suggesting that the fabricated surface is likewise unacceptable.

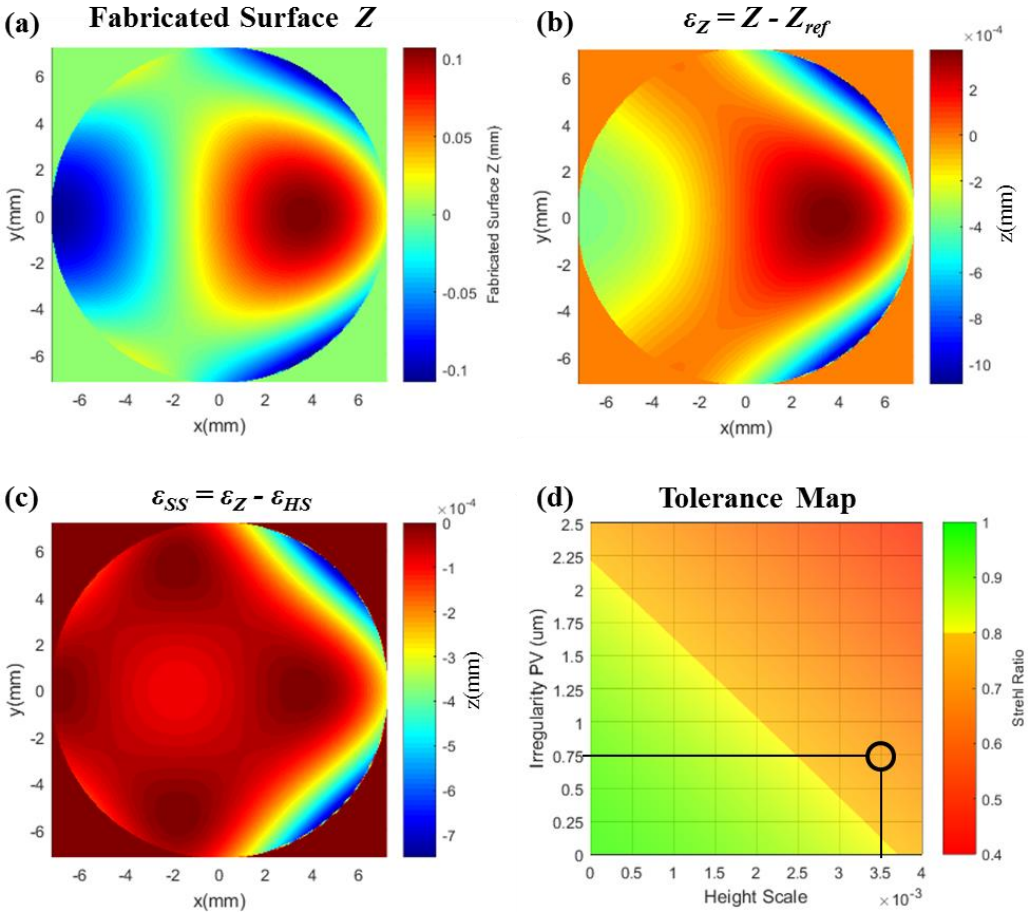

Fig. 7.10: Demonstration of the form error tolerance procedure, illustrating (a) an assumed fabricated Alvarez lens, (b) the total form error after removing the reference surface, (c) the irregularity after removing a best fit height scaled surface from the total form error, and (d) use of the tolerance map to determine the lens acceptability.

7.4 Surface form error tolerancing: non-imaging example

To further demonstrate this tolerancing procedure, we again consider the super-Gaussian variable diameter beam shaper presented in Chapter 3. This design consists of two laterally shifted freeform elements that produce varying uniform irradiance output

distributions with diameters from 1-5 mm for a lateral shift range of d = +/-300 μm., Freeform surfaces were generated with added form errors and exported as DAT files using the same custom MATLAB® code as the imaging example and imported into ZEMAX® as "grid sag" surface types as before. The target plane was located using the reference surfaces. No adjustments were made after the deviated surfaces were imported.

Following the procedure, sensitivity analyses were performed for the specific systems where d = -1.8 mm (R = 2.5 mm), d = 0 mm (R = 1.5 mm), and d = 1.8 mm (R = 0.5 mm), all across the height scale HS range +/-0.03. We note that for all the simulations in this section, a 10 mm diameter aperture stop was placed in front of the freeform elements. For the same reasons discussed in Section 7.3, he resulting maximum P-V and RMS values were measured across the 12 mm component diameter, as shown in Fig. 7.11.

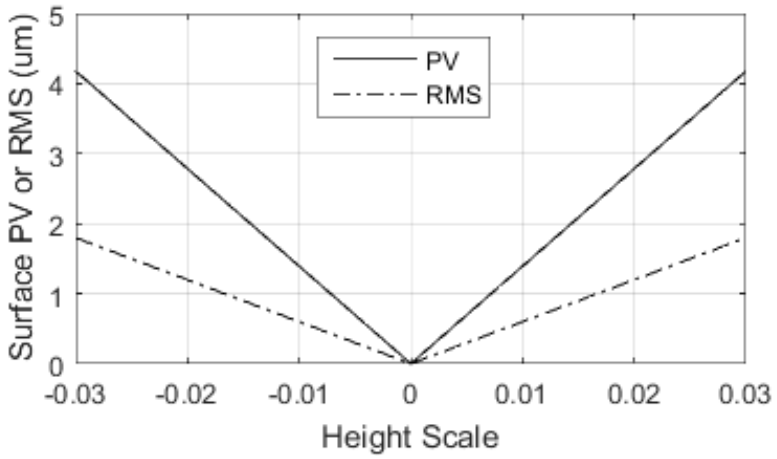

Fig. 7.11: Resulting maximum P-V and RMS values of the freeform beam shaper surfaces with intentionally added height scale surface form errors.

The results from the sensitivity analyses are shown in Fig. 7.12, where the shape deviation R_{CV}, uniformity U_{CV}, and correlation degree C_d are used as performance metrics with respect to the height scale and the corresponding P-V and RMS measurement of the deformed surfaces. We note that the performance impact was not symmetric for positive

and negative scales; therefore, the results shown in Fig. 7.12 represent the worst-case performance for the respective form error specification. These results suggest that the system performance is most sensitive to these particular form errors when d = 1.8 mm (R = 0.5 mm). This matches the observations made in the Alvarez example In this case; the spot diameter is smaller at this specific lateral shift, meaning the composite lens has more surface curvature and is affected more strongly by the height scale form error.

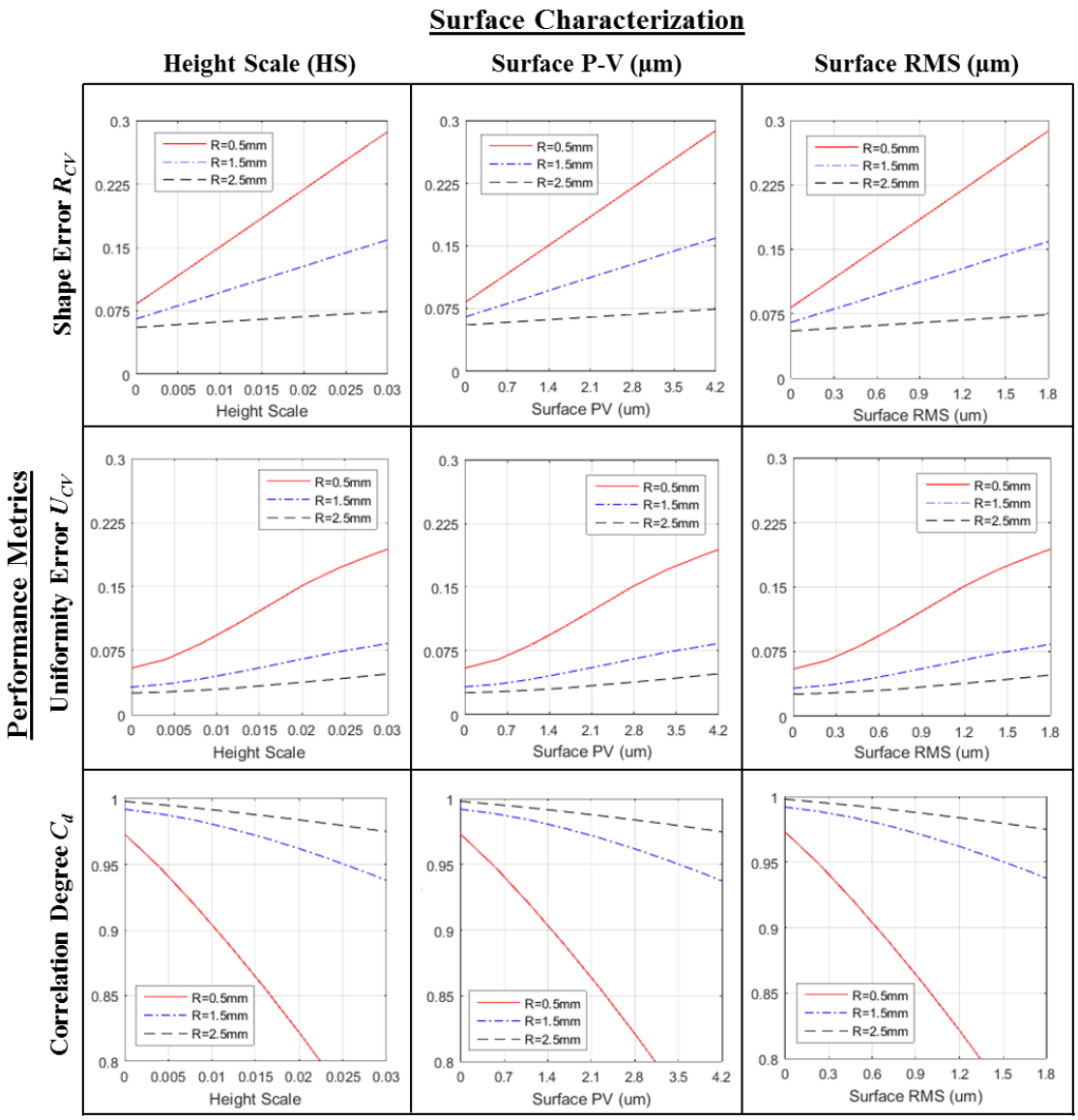

Fig. 7.12: Results from the beam shaper lens height scale *HS* form error sensitivity analysis for the cases where d = -1.8 mm (R = 2.5 mm), d = 0 mm (R = 1.5 mm), and d = 1.8 mm (R = 0.5 mm).

Next, the same procedure was followed for the slope scale *SS* range of +/-3.0E-05, where a custom MATLAB® code was again used to generate the freeform surfaces with the added form errors. Fig. 7.13 shows the resulting maximum P-V and RMS values measured across the entire 12 mm component diameter.

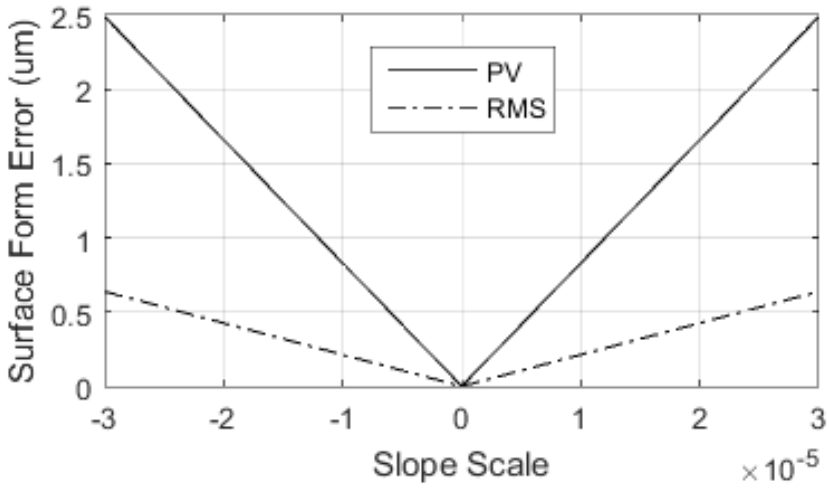

Fig. 7.13: Resulting maximum P-V and RMS values of the freeform beam shaper surfaces with the intentionally added slope scale surface form errors.

The results from the slope scale sensitivity analyses are shown in Fig. 7.14 using the same performance metrics as before, again representing the worst-case performance for the respective form error specification. These results further suggest that the system performance is most sensitive to these particular form errors when d = 1.8 mm (R = 0.5 mm). As expected, this matches the trends observed previously, as the spot diameter is smaller at this point, meaning the composite beam shaper has more surface curvature (larger slope angles) and is more strongly affected by the slope scale form error.

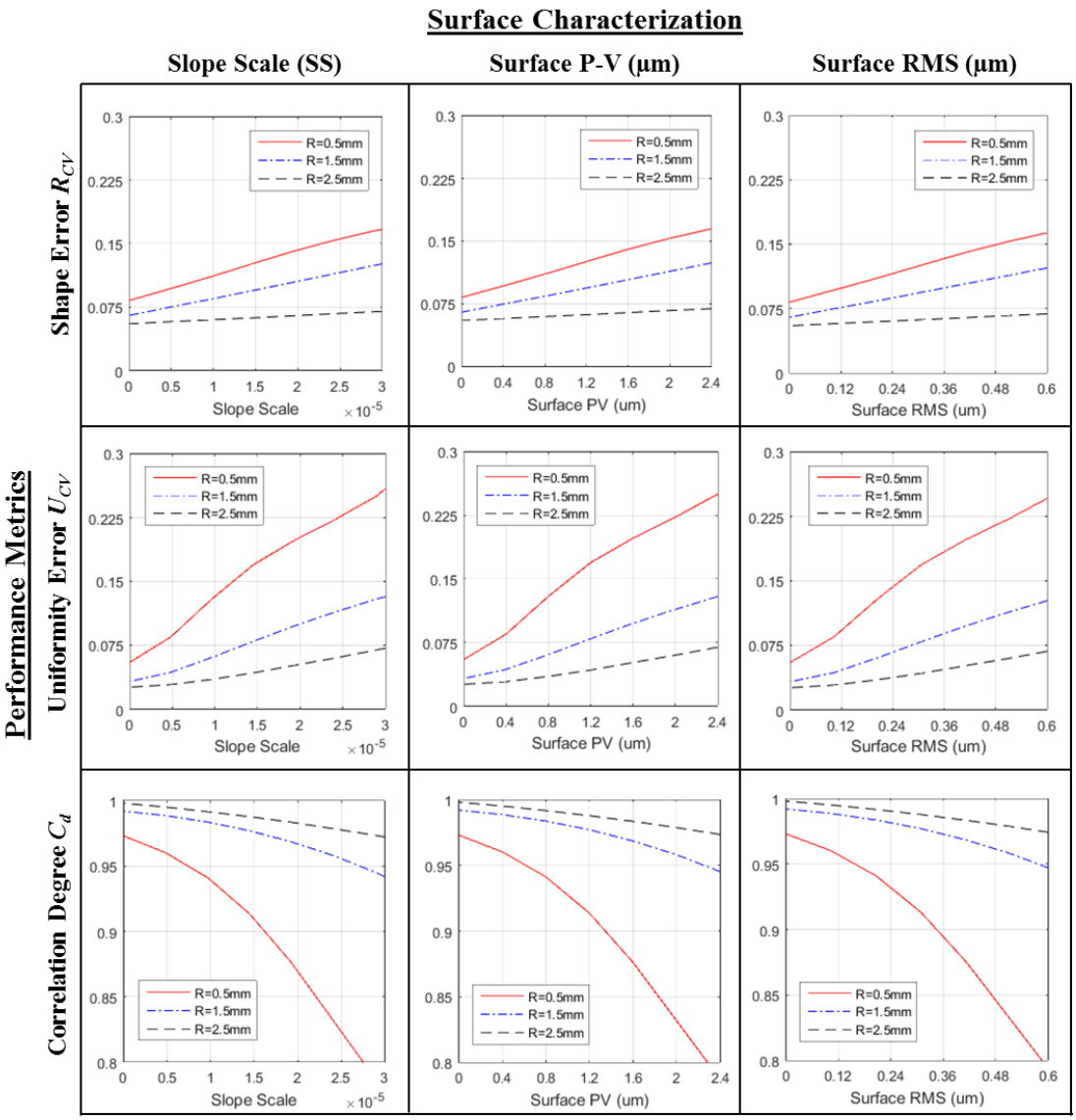

Fig. 7.14: Results from the beam shaping lens slope scale form error sensitivity analyses for the cases where d = -1.8 mm (R = 2.5 mm), d = 0 mm (R = 1.5 mm), and d = 1.8 mm (R = 0.5 mm).

Next, the initial tolerance bounds were determined as the minimum error magnitudes for which the performance equaled the pass-fail threshold. For brevity, we focus solely on the correlation degree C_d as a performance metric, as it was previously shown to represent a good balance between spot size, shape, and uniformity. However, it should be noted that a specific application might require a specific performance metric value which would then be used to set a pass-fail threshold. In order to define the C_d threshold, we

refer to the discussion on optomechanical tolerancing in Chapter 6.5, where we determined that a correlation degree above 0.9 would be acceptable. With this in mind, the initial bounds were determined to be +/-0.011 for the height scale *HS*, and +/-1.70E-05 for the slope scale *SS*. The combined scale analysis was performed using these tolerance bounds, simulating all possible scenarios for positive and negative height scales and slope scales. Considering the four possible cases of the *HS/SS* scale direction (+/+, +/-, -/+, and -/-), the worst-case performance results for the combined scale analsysis are shown in Fig. 7.15(a). These resulting worst-case correlation degrees are displayed using a custom color scale to show a distinct pass-fail cutoff line. The slope scale was again converted to the maximum allowable irregularity of the surface, as shown in Fig. 7.15(b). The irregularity in this case is the maximum P-V value of the surface form error after removing the reference and best-fit height scale.

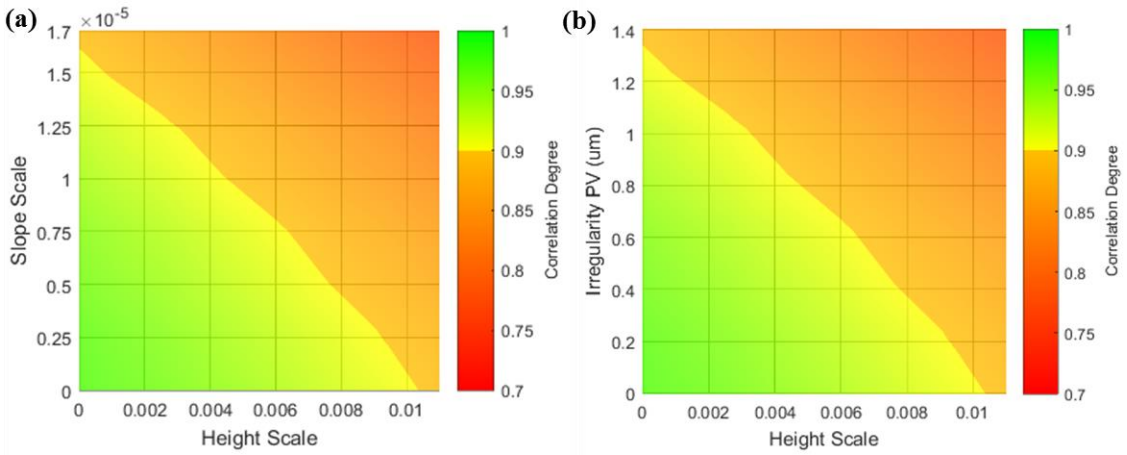

Fig. 7.15: Results from the combined height scale and slope scale analyses of the variable output beam shaper, showing the Correlation degree C_d performance impact regarding (a) the height scale and slope scale and (b) the height scale and remaining irregularity P-V of the freeform.

To demonstrate the implementation of this tolerance map, we assume a pair of fabricated freeform beam shaper surfaces where the measured surface is shown in Fig.

7.16(a) and the surface form error (Z-Z_{ref}) is shown in Fig. 7.16(b). The height scale HS = 0.004 was determined using a standard best-fit parameter sweep. This height scale is then removed from the form error, as shown in Fig. 7.16(c), leaving behind the residual surface error (irregularity) with a max P-V of 0.8 μm. The tolerance map is then used with both measurements to determine that the worst-case performance for that fabricated surface, as shown in Fig. 7.16(d). For this particular example, the worst-case performance gives a correlation degree of 0.91. This is acceptable, suggesting that the fabricated surface is likewise acceptable.

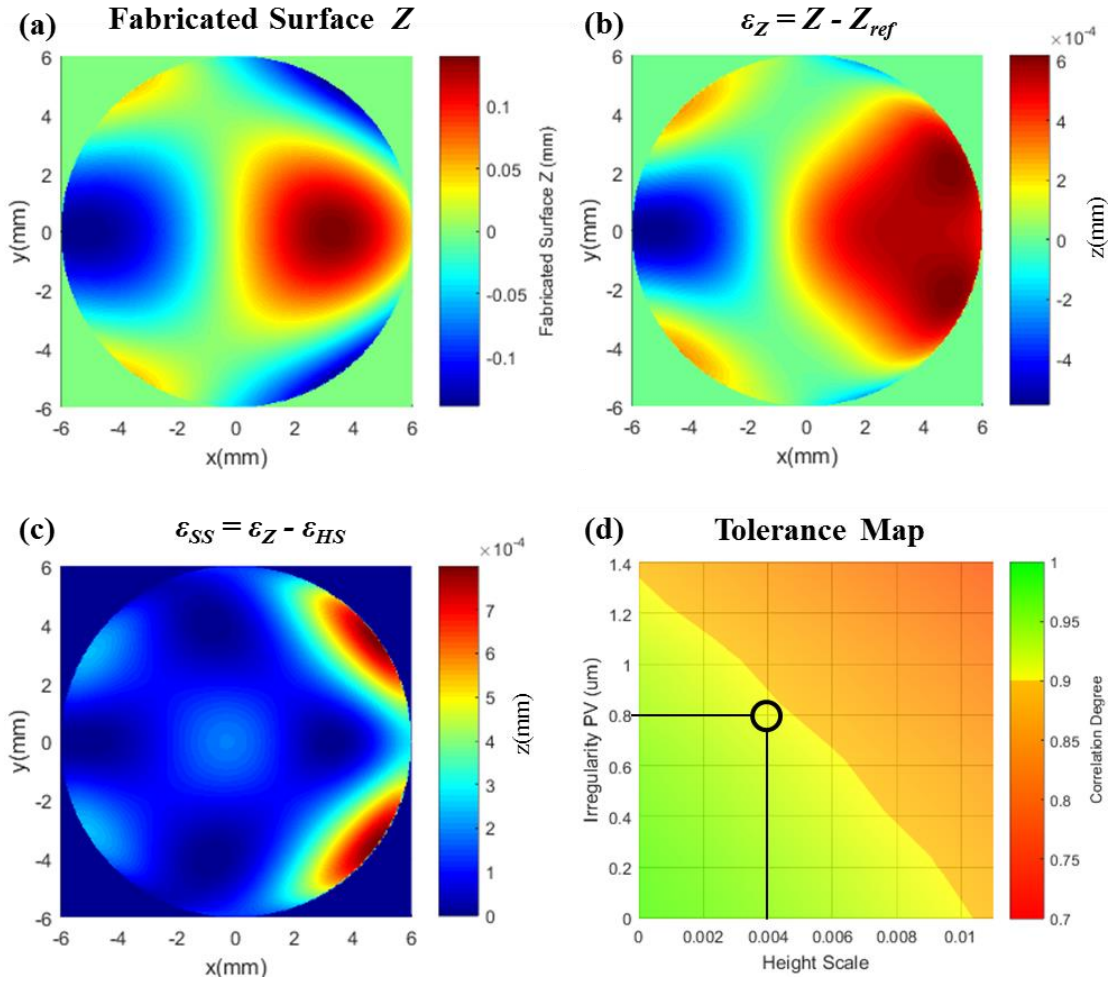

Fig. 7.16: Demonstration of the form error tolerance procedure, illustrating (a) an assumed fabricated beam shaping surface, (b) the total form error after removing the reference surface, (c) the irregularity after removing a best fit height scaled surface from the total form error, and (d) use of the tolerance map to determine surface acceptability.

7.5 Discussion

As demonstrated in this section, the performance of dynamic freeform systems is heavily dependent on surface accuracy. A deterministic approach was used to develop a procedure for specifying the surface accuracy of freeforms. This procedure considered two primary characteristics of low-frequency form error; height scale (*HS*) as a function of the surface height, and slope scale (*SS*) as a function of surface slope of the reference prescription.

This procedure, like the previous optomechanical tolerance procedure discussed in Chapter 6, is heavily dependent on the chosen performance metric. The performance metric determines the pass/fail threshold, which ultimately determines the tolerance specifications. In the examples presented in this chapter, the Strehl ratio was used as a performance metric for the Alvarez lens and the correlation degree C_d was used as a performance metric for the variable output beam shaper. However, it is possible to use a different metric (wavefront error, spot size, uniformity U_{CV}, shape deviation R_{CV}, etc.) if the application calls for it, with the only stipulation being that the metric must be quantitative. The performance metric must be chosen by the designer when generating the surface form specifications.

We note that there are different types of low-frequency form error that are not specifically represented by the height scale and slope scale (i.e. resulting from tilt, decenter, waviness, ogive errors, etc. [86]). However, these additional types of form error are specific to either a particular application or a particular fabrication method and not as straightforward to model, and are not considered in this dissertation. Investigating these additional form error signatures in the future would provide more insights into surface

accuracy requirements for dynamic freeform optical systems. Furthermore, it would be useful to expand this analysis to include errors that are a product of specific tool errors. Specifically for diamond machining methods, the tool path is based off of an assumed tool tip shape (curvature, symmetry, etc.); an error in this assumed shape would result in a loss of surface accuracy. Most diamond tools come with tolerance specifications on the tool shape. While there have been methods developed to account for some tool error when generating the final tool path [120, 122, 125, 160], it would be extremely useful for the manufacturer to be able to determine a pass-fail threshold based on the actual tool shape tolerance specification.

In addition to the enhancements suggested above, we note that specifying the surface irregularity as a maximum P-V value is deterministic for the form error characteristics simulated in this work. However, including more types of form errors will likely require a less-ambiguous irregularity specification. This is largely due to the fact that P-V values are single quantities that are generally not linked to any certain location on the surface, potentially subjecting the fabricated surface to a faulty pass/fail decision. With this in mind, an RMS specification for the irregularity could be implemented, where the error would be represented as the standard deviation of the entire surface rather than a single point. Similarly, a maximum or average surface slope error specification could also be implemented for the irregularity.

CHAPTER 8: ANALYZING SURFACE FINISH QUALITY – MID-SPATIAL FREQUENCY ERRORS

8.1 Introduction

Freeform optical surfaces can be manufactured using multiple techniques, ranging from coordinated-axis diamond turning and raster milling to grinding and magnetorheological finishing. Each of these techniques leaves residual mid-spatial frequency (MSF) surface errors that degrade the surface finish quality, ultimately degrading optical performance and introducing undesired optical artifacts that in many cases must be determined empirically. This genre of surface errors differs from the form errors discussed previously as MSF errors are typically periodic with smaller spatial frequencies, requiring different simulation methods to account for diffraction and interference artifacts. Understanding the impacts of MSF errors on optical performance is vital for freeform manufacturing, particularly when quantifying design specifications that affect performance, cost, and cycle times. Thus, optical models capable of simulating the effects from residual surface textures are highly desirable. Researchers have previously explored some effects of MSF errors on optical performance e.g. [82-86]. However, these studies have generally been limited to radially symmetric lenses in imaging systems. As discussed in Chapter 3, we have previously compared simulation models to experimental results from a diamond milled dynamic freeform beam shaper [51, 52]. The results from this previous work emphasized the need to investigate the effects that surface finish quality has on system performance. More specifically, specifications using parameters

relevant to the fabrication process, such that the machining parameters can be determined through optimization.

8.2 Methods and assumptions

As discussed previously in Chapter 2, diamond turning and diamond milling provide two key methods for fabrication of freeform surfaces. Diamond turning involves an optical workpiece on a rotating spindle relative to a diamond tool with synchronized modulation of tool depth. In contrast, diamond turning involves a non-rotating workpiece laterally translated relative to a rotating diamond tool (endmill) at varying depths. In both fabrication approaches, the diamond tool used for material removal has a nominally round tip. This results in characteristic 'cusp' grating patterns (radial for diamond turning and linear for diamond raster milling), as shown in Fig. 8.1. The grating period is determined by the increment distance (step-over) Λ_{cusp} of the diamond tool, and the grating amplitude h_{cusp} is determined by the step-over and diamond tool radius R.

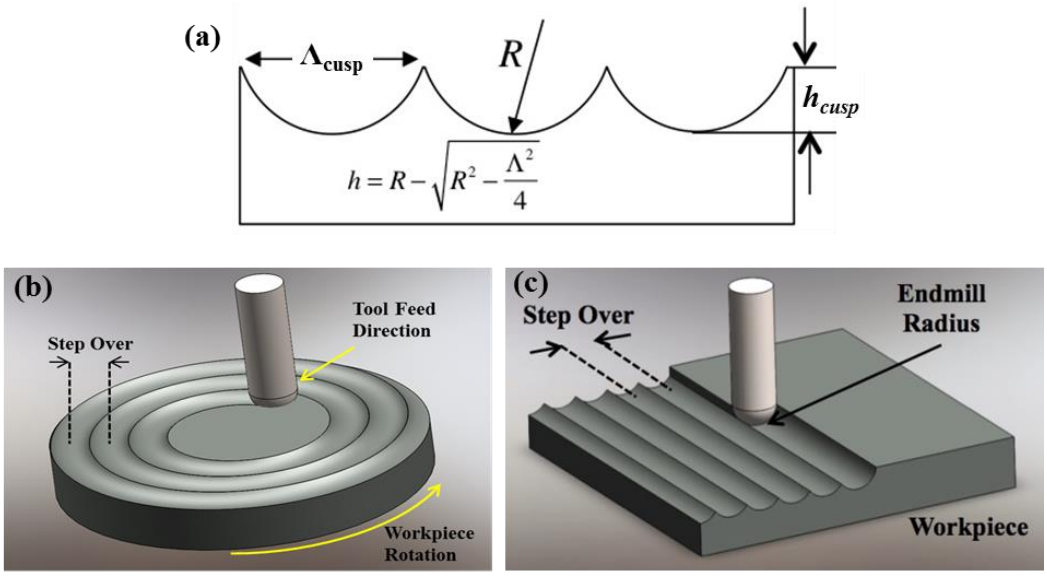

Fig. 8.1: (a) Cross-sectional profile of the 'cusp' grating along with illustrations of this error and its respective orientation for (b) diamond turning and (c) diamond milling.

As it was demonstrated in Chapter 3 regarding experimental results from the dynamic beam shaper, additional issues give rise to MSF errors that must also be considered. Researchers have previously have examined MSF errors and the impact of surface finish by decomposing the total error into known error sources [82, 85]. These sources can include, but are not limited to vibrations, thermal cycling, tool path error, and tool chatter. To investigate the impact of multiple MSF errors, we consider including the effects of thermal cycling, where the fluctuation of the temperature creates a characteristic sinusoidal grating pattern (radial for diamond turning and linear for diamond raster milling), as shown in Fig. 8.2. This grating period Λ_{sin} is of lower frequency than the 'cusp' grating, and is determined by the combination of the thermal cycle time and the tool feed rate during the machining process. The grating amplitude h_{sin} is determined by the temperature gradient. Fig. 8.2 shows the cross-sectional profile of the sinusoidal grating along with illustrations of this error and its directions for both machining methods.

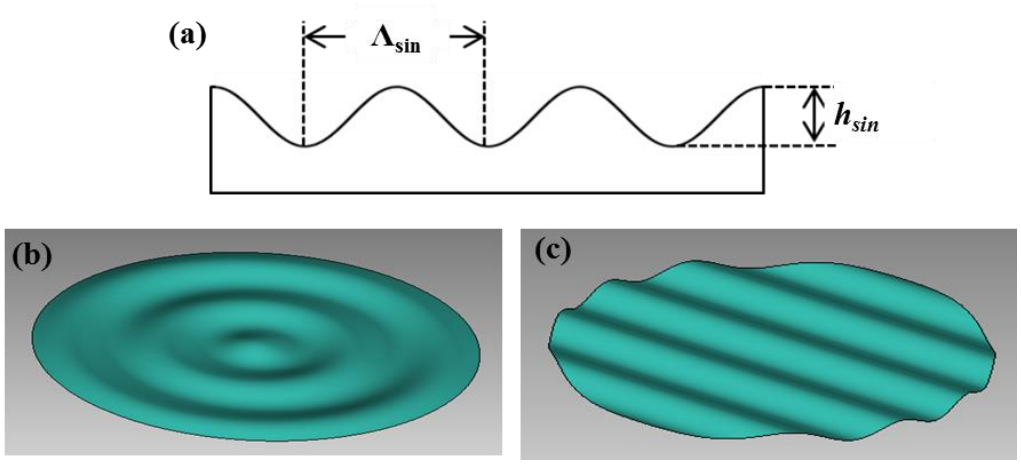

Fig. 8.2: (a) Cross-sectional profile of sinusoidal grating arising from thermal cycling effects. Illustrations of this error and its directions for (b) diamond turning and (c) diamond milling.

Due to the relative sizes of both surface textures, models based on geometrical ray tracing are generally insufficient; optical diffraction and interference effects must also be considered. To this end, wave-based physical optical models are implemented in LightTrans VirtualLab™, using a combined Fresnel/Spectrum of Plane Waves (SPW) propagator, to quantify optical performance impact of both MSF error types. Both profiles are added together directly, as demonstrated in Fig. 8.3, and are imposed onto the optical component to simulate the fabricated surface.

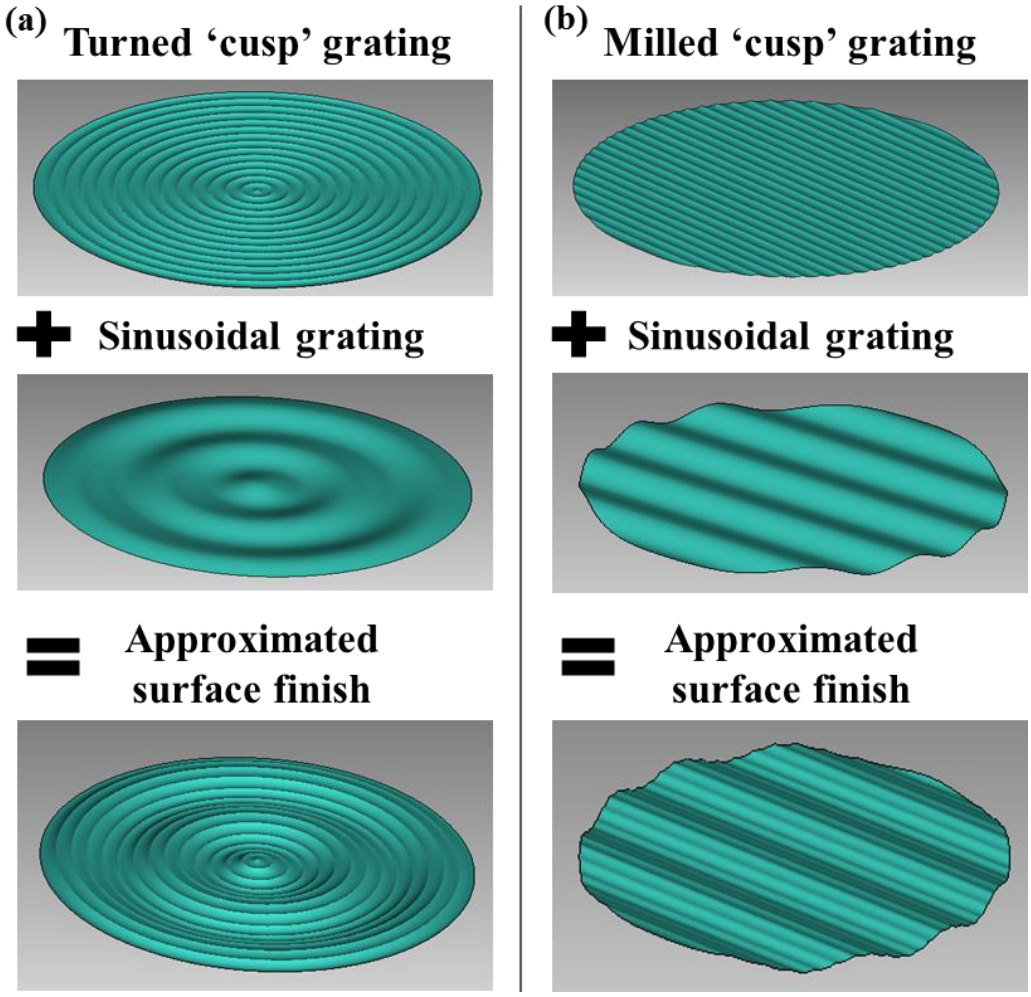

Fig. 8.3: Illustration of the cusp grating combined with the sinusoidal grating to approximate the (a) diamond turned and (b) diamond milled surface finishes.

We note that each MSF error parameter can be directly related to controllable machining parameters, which provides the ability to quantitatively determine meaningful tolerance specifications based on simulation performance. While ability is important for knowledge of system performance, it is also very useful for considering manufacturing costs (machine time, tool selection, etc.). Justifying specific machining parameters helps ensure that components are not 'over-toleranced' such that no gain is acquired for additional manufacturing time and cost.

8.3 Surface finish tolerancing: imaging example

As a representative example of an imaging system, we consider a simple spherical lens with a 4 mm aperture diameter and 100 mm focal length at 532 nm wavelength. Fig. 8.4 shows a geometrical ray trace of this system along with its corresponding spot diagram demonstrating that it is indeed diffraction limited.

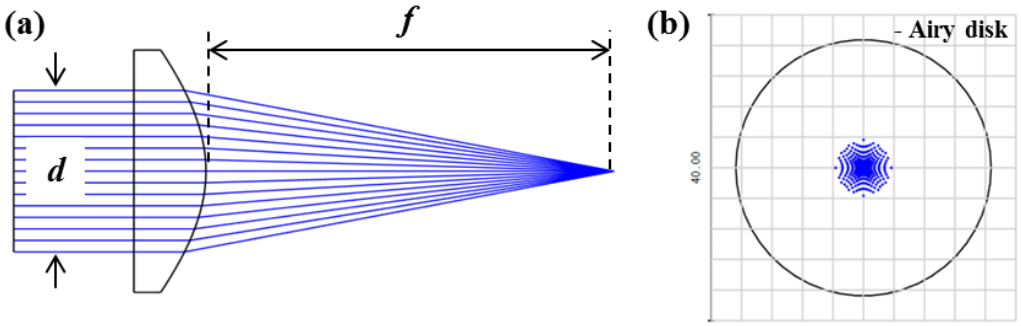

Fig. 8.4: (a) Geometrical ray trace of the spherical lens system along with the (b) spot diagram compared to the diffraction limited Airy disk (black circle).

The lens is assumed to be fabricated in poly (methyl methacrylate) PMMA (n_l = 1.49) using diamond tools with 1 mm radius and a 60 µm step-over for both diamond turning and diamond milling, resulting in a P-V height of h_{cusp}= 450 nm. Fig. 8.5 shows the cusp

gratings imposed on this spherical surface, with the features exaggerated in height for visual aid.

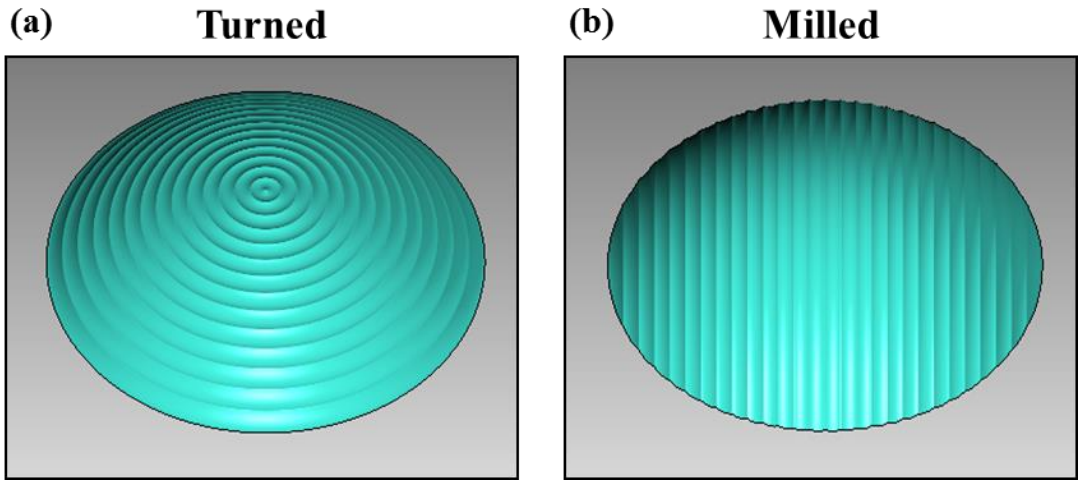

Fig. 8.5: (a) Diamond turned and (b) diamond milled cusp grating structures imposed on the example spherical surface.

Because this texture is a repeating structure, it is expected that there will diffraction effects. In general, for a grating, the separations of the diffraction order maxima y_m are given by

$$y_m = \frac{mf\lambda}{\Lambda} = \frac{1 * 100{,}000 * 0.532}{60}\ \mu\text{m} = 889.6\ \mu\text{m}, \tag{8.1}$$

where m is the diffraction order, f is the axial distance (focal length), and Λ is the period of the structure (step-over). To examine the impact these characteristic cusp gratings have on the imaging performance, we first consider the Point Spread Function (PSF) to describe the response of this system to a point source. This system was simulated using VirtualLab™ for both machining processes. Fig. 8.6 displays and compares the calculated PSF's from the two fabrication methods.

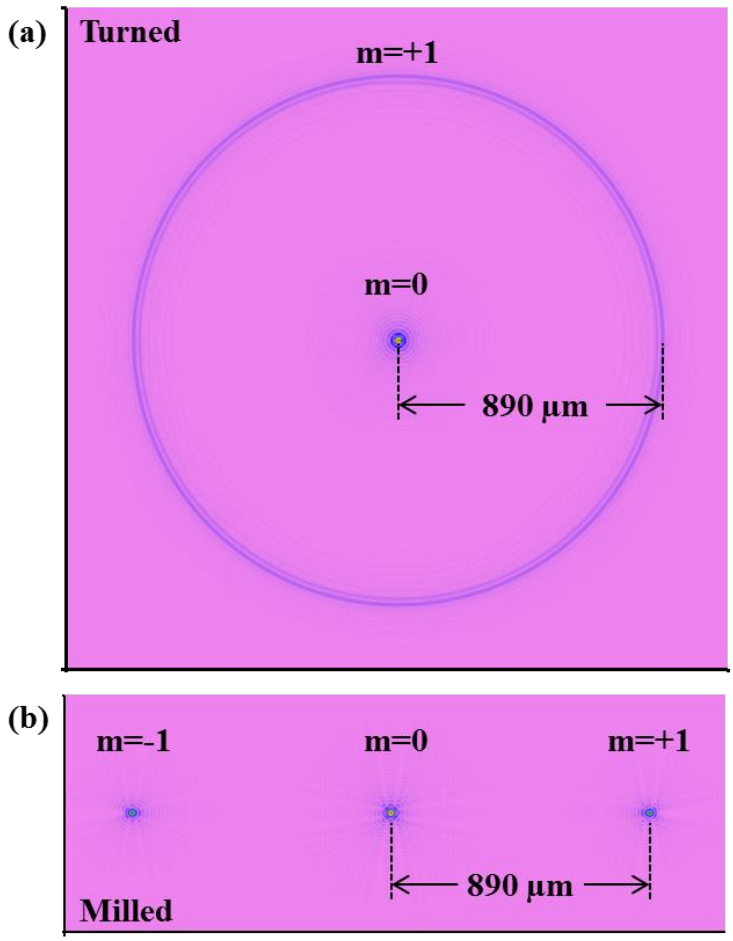

Fig. 8.6: Simulated point spread functions of the (a) diamond turned and (b) diamond milled spherical lens.

As expected, the PSF's show that the cusp grating casts undesired diffraction orders, radially for the diamond turned case and laterally for the diamond milled case. The locations of the maxima match the theoretical values. To investigate how an actual image would be impacted by this behavior, we consider the Fourier transform of the PSF, known as the Modulation Transfer Function (MTF), which is the normalized contrast of an image as a function of spatial frequency [161]. A diffraction limited imaging system will have a contrast of 1 where the spatial frequency is zero, dropping to a contrast of zero at some larger spatial frequency defined by the system. Fig. 8.7 shows the 2-dimensional MTF plots generated in VirtualLab™ for both fabrication methods.

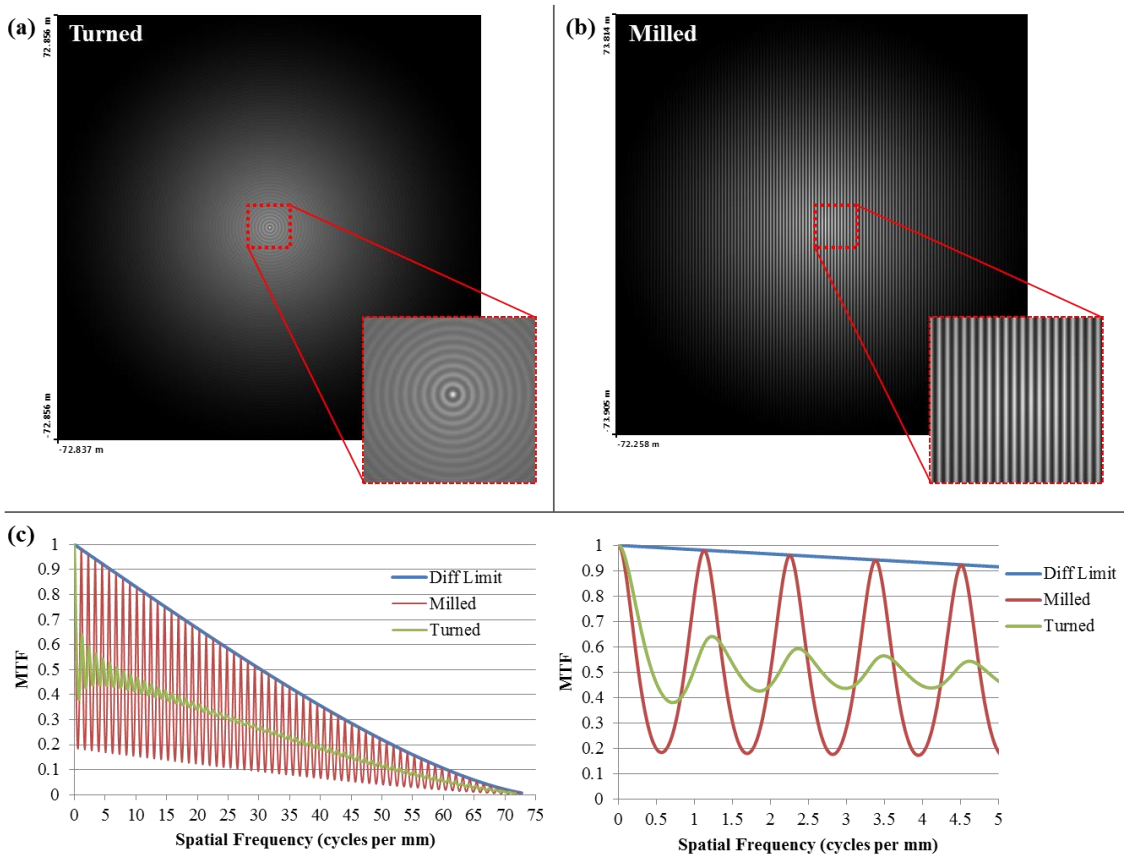

Fig. 8.7: Simulated 2-dimensional modulation transfer functions (MTF) for the (a) Diamond turned and (b) diamond milled spherical lens. (c) Comparison of the MTF along the x-axis for both fabrication methods.

Comparing these results to the diffraction limited MTF curve shows the drastic effect that MSF errors have on this system. Using the Strehl ratio again as a quantitative metric; the variation in the MTF curve decreases the system's Strehl ratio from ~1 to 0.52 for both cases. We simulate the same imaging system with varying step-overs (Λ = 10, 30, and 60 μm) to demonstrate how manufacturing parameters can be chosen to reduce the effects of MSF errors on the optical performance; results are shown in Fig. 8.8.

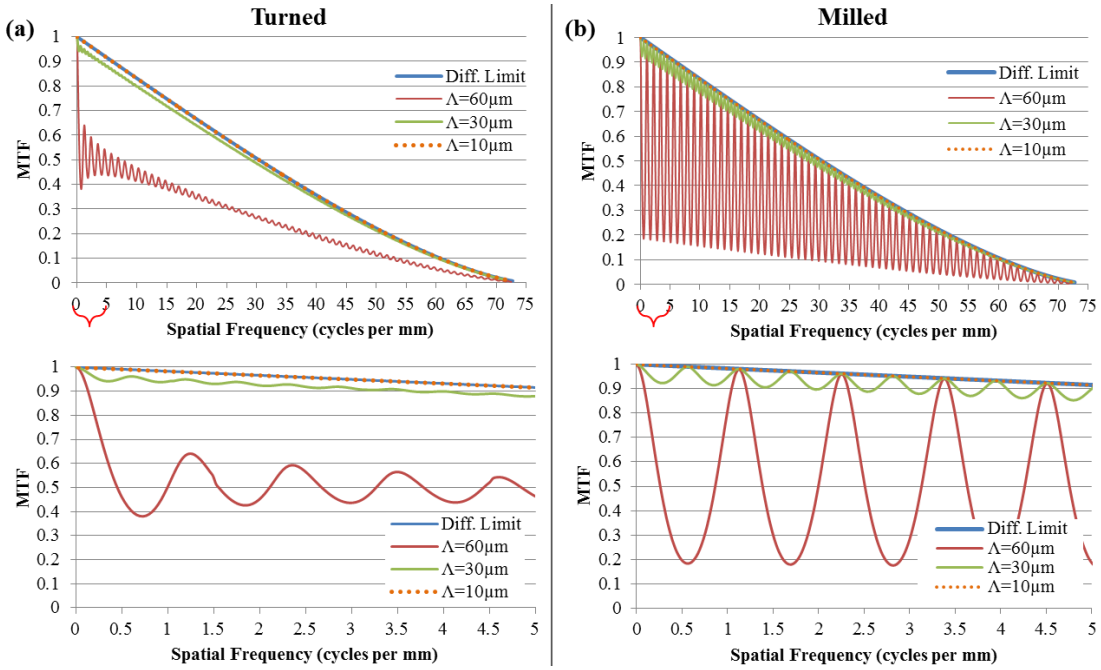

Fig. 8.8: Comparison of the MTF with varying step-overs for the (a) diamond turned and (b) diamond milled spherical lens.

As can be seen from these results, the choice of smaller step-over leads to a smoother surface texture and significantly improves the optical performance. This trend holds true for both fabrication methods. Decreasing the step-over to 10 μm results in a system MTF close to the diffraction limit for both fabrication methods; additional gains are unlikely if a smaller step-over (and thus longer cycle time) is used. Step-over is inversely related to manufacturing time which should be minimized if possible for cost purposes. With this in mind, the ability to simulate and choose an optimum step-over that will perform near or at the diffraction limit is very advantageous.

As discussed previously, the system can also experience a periodic thermal drift during the manufacturing process which introduces a lower frequency structure onto the final lens surface. This is represented here as a sinusoidal grating with period and amplitude which are a product of the thermal cycling time, tool feed rate, and temperature gradient.

Fig. 8.9 shows the cusp gratings combined with the added sinusoidal grating and imposed on a spherical surface with the features exaggerated vertically for visual aid.

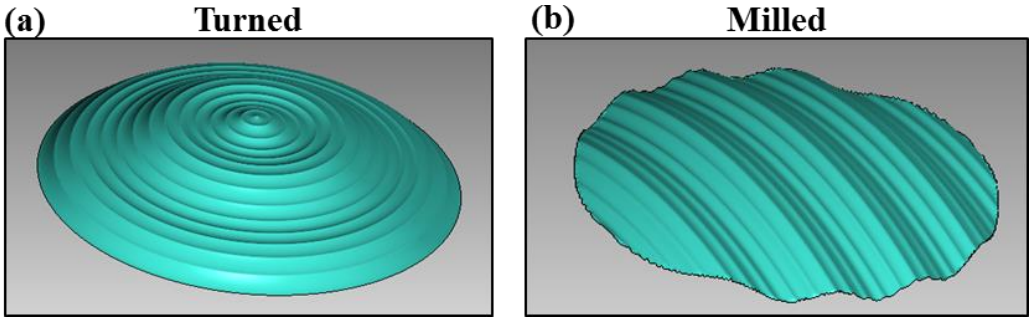

Fig. 8.9: (a) Diamond turned and (b) diamond milled spherical lens with the added cusp and sinusoidal grating structures.

To demonstrate the effects of adding another MSF error, we consider the same imaging system as before, fabricated using both diamond turning and diamond milling with a 30 µm step-over and 1 mm tool radius, along with a sinusoidal grating with a 1 mm period and 300 nm amplitude. The MTF's for each system were again generated in VirtualLab™ and the results are shown in Fig. 8.10.

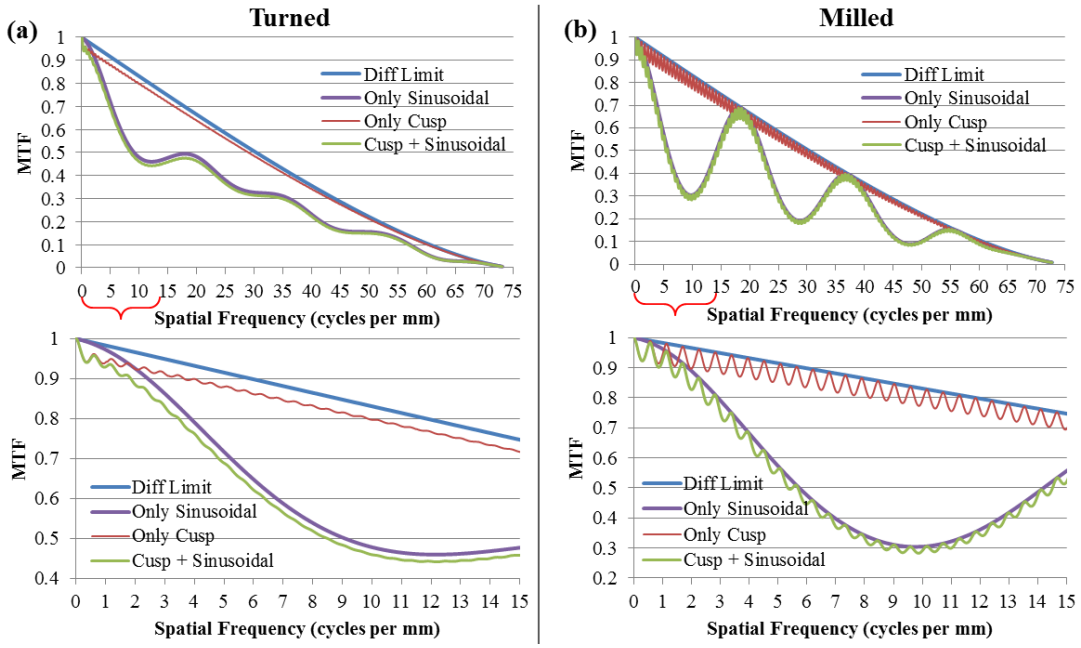

Fig. 8.10: Modulation transfer functions along the *x*-axis with the added sinusoidal grating structure for the (a) diamond turned and (b) diamond milled spherical lens.

As seen from the results, the addition of the sinusoidal grating has a significant negative impact on the system MTF curve. We note the shallow higher frequency oscillation from the cusp grating as well as a deeper MTF variation at lower frequency resulting from the thermal cycling error. This suggests that the impact of each MSF error adds linearly in this case, validating the idea of considering the total surface texture as a combination of multiple MSF errors that have their own individual impacts on the system performance. We note that the amplitude used to model thermal cycling effects is a relatively extreme value to illustrate the concept. While more difficult to control than the 'cusp' textures, reduction of MSF errors due to thermal cycling can result in significant performance improvements.

8.4 Surface finish tolerancing: non-imaging example

As a representative example of a non-imaging system, we consider a single freeform beam shaping element that converts a round Gaussian input to a square 'flat-top' irradiance distribution. This single element beam shaper was designed using the same techniques discussed in Chapter 5 [35, 51]. In this specific example, the component diameter is 14 mm, with an incident Gaussian waist diameter of 6 mm at a 632.8 nm wavelength, designed to produce a 3-mm square flat-top at target distance 100 mm. Fig. 8.11 shows a general schematic of this system along with its corresponding Gaussian input and reference output spot.

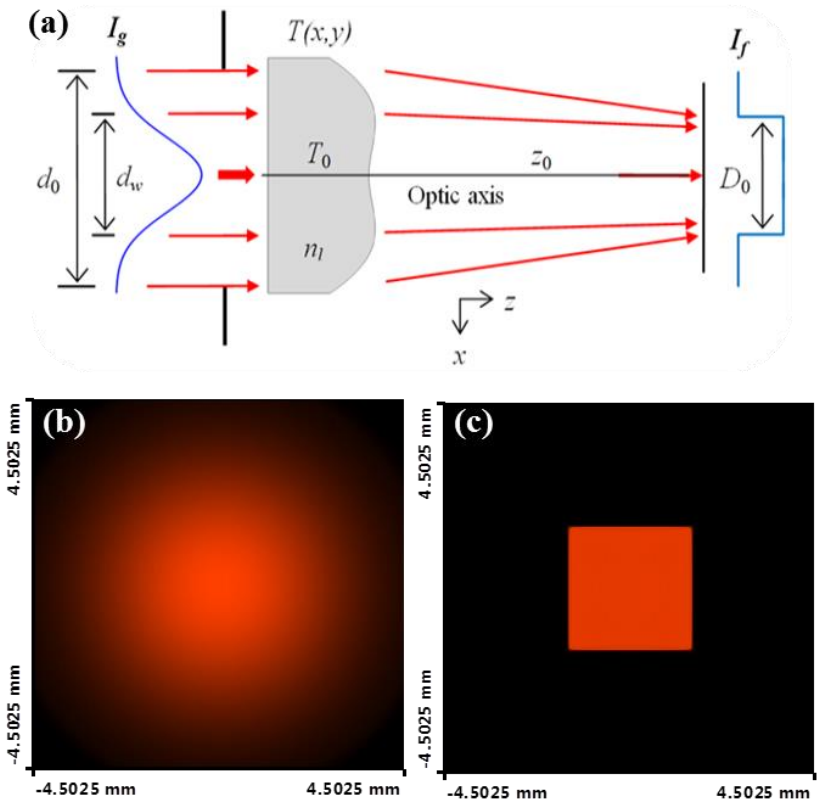

Fig. 8.11: (a) General schematic of the single element beam shaping system along with its corresponding (b) round Gaussian input (c) reference output spot.

We assume the beam shaper is fabricated in PMMA (n_l = 1.49) using diamond tools of 1 mm radius and a 60 µm step-over for both diamond turning and milling, resulting in a P-V height of h_{cusp}= 450 nm. Fig. 8.12 shows the cusp gratings imposed on this beam shaper surface, where the vertical features are exaggerated again for visual aid.

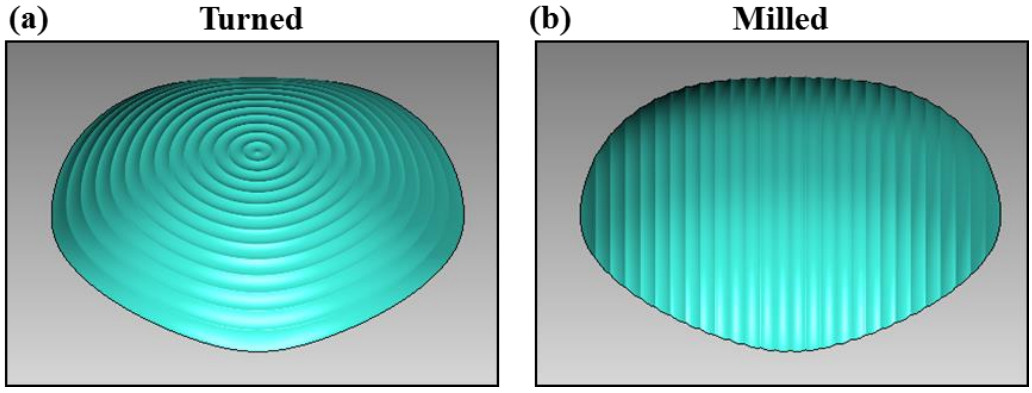

Fig. 8.12: (a) Diamond turned and (b) diamond milled cusp grating structures imposed on the example beam shaping surface.

VirtualLab™ was used to simulate this system for both machining processes to examine the impacts of these characteristic cusp gratings on beam shaping performance. Fig. 8.13 displays and compares the resulting output spots from these simulations along with cross-sections of their irradiance profiles.

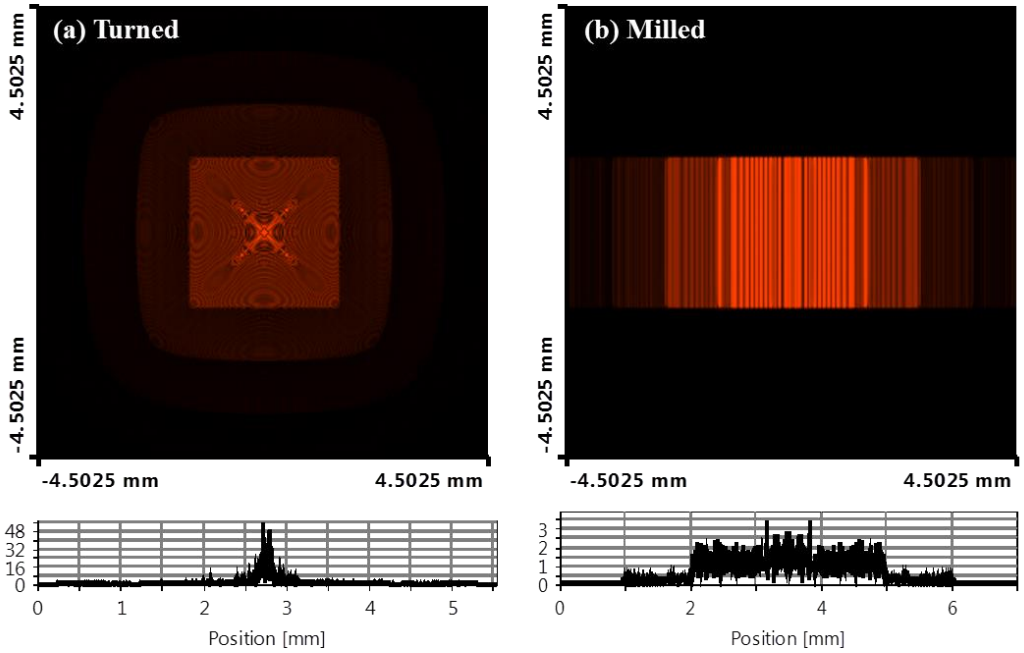

Fig. 8.13: Simulated beam shaper outputs fabricated through (a) diamond turning and (b) diamond milling, both with a 60 μm step-over and 1 mm tool radius.

Comparing these results to the reference output spot again shows the drastic effect that MSF errors can have on optical system performance. Similar to the imaging example, the cusp grating casts multiple undesired orders radially for the diamond turned case and laterally for the diamond milled case. These undesired diffraction orders overlap and interfere with one another, resulting in the high frequency variation of irradiance observed in the output spots. We simulate the same beam shaping system with smaller step-overs (Λ = 10 and 30 μm) to demonstrate how manufacturing parameters can be chosen to reduce the effects of MSF errors on optical performance. The results are shown in Fig. 8.14.

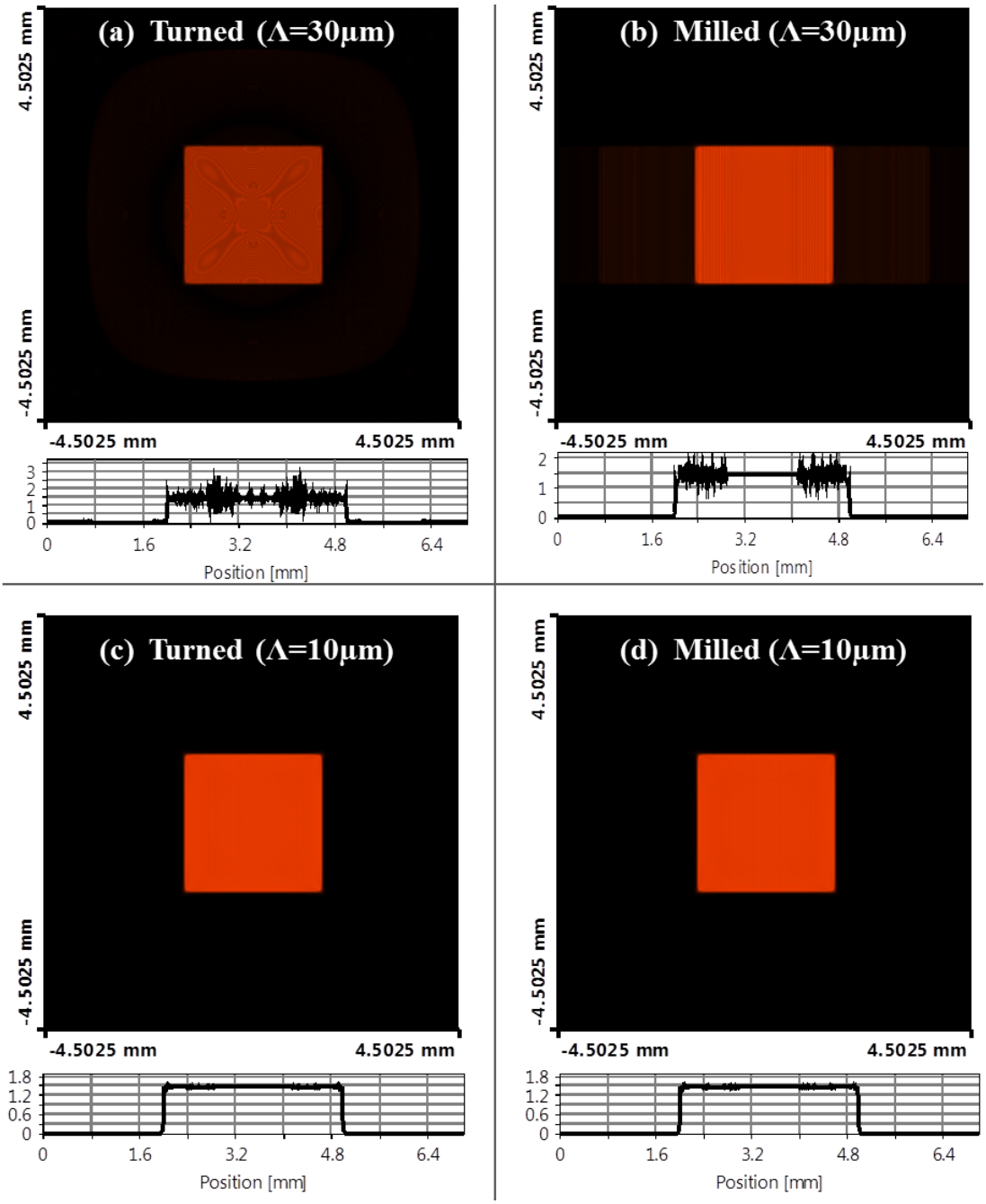

Fig. 8.14: Simulated outputs for beam shapers fabricated through diamond turning and diamond milling with various step-overs.

To quantify how much the output spot is impacted; we consider the uniformity of the irradiance distribution. This is determined using Eq. (6.3), where in this case the uniformity error U_{rms} is determined for a cross-sectional slice along the x-axis. It is

important to mention how the unclear edge of the output spot can cause confusion, therefore we implement a clear aperture (CA) window (discussed in Chapter 6). In this case, the CA window was set to 95% of the entire output spot window. Fig. 8.15 shows the approximate relationship between uniformity and step-over for both fabrication methods.

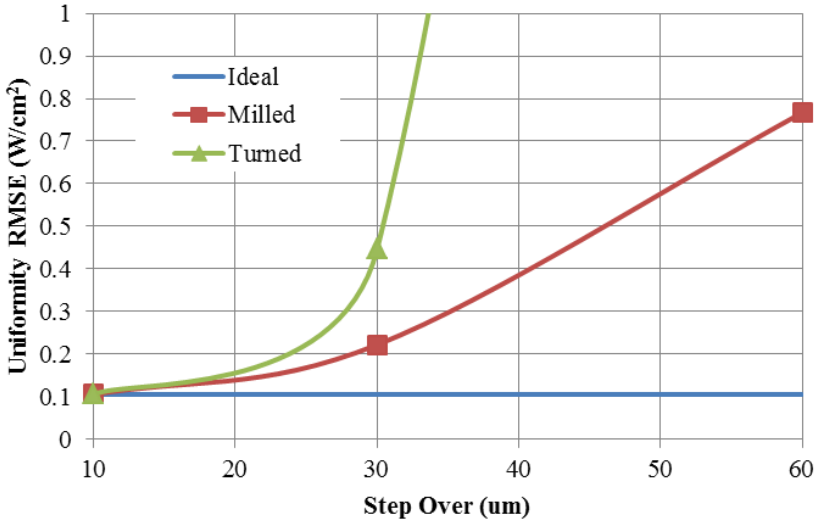

Fig. 8.15: Comparison of the uniformity error across the *x*-axis of the beam shaper output spot fabricated through diamond turning and diamond milling with various step-overs.

Intuitively, and as seen in the results in Fig. 8.14 and Fig. 8.15, smaller step-overs lead to smoother surface textures and significantly improve optical performance. This trend holds true for both fabrication methods. Decreasing the step-over to 10 μm results in irradiance uniformity equal to the reference output spot as a result of the undesired diffraction orders no longer overlapping one another. Additional gains are unlikely if smaller step-overs (and thus longer cycle times) are used, demonstrating the ability to simulate and choose an optimum step-over for manufacturing.

To demonstrate the effects of incorporating another MSF error, we again impose a low frequency sinusoidal grating on the optics to represent the effect of thermal cycling

during the fabrication processes. We consider beam shapers fabricated using both diamond turning and diamond milling with a 30 μm step-over and a 1 mm tool radius, along with a sinusoidal grating with 1mm period and 300 nm height. VirtualLab™ was again employed to simulate the respective output irradiance profiles. Fig. 8.16 shows the optical surfaces with the added structure for both fabrication methods, with the vertical features exaggerated for visual aid, along with the resulting output distributions.

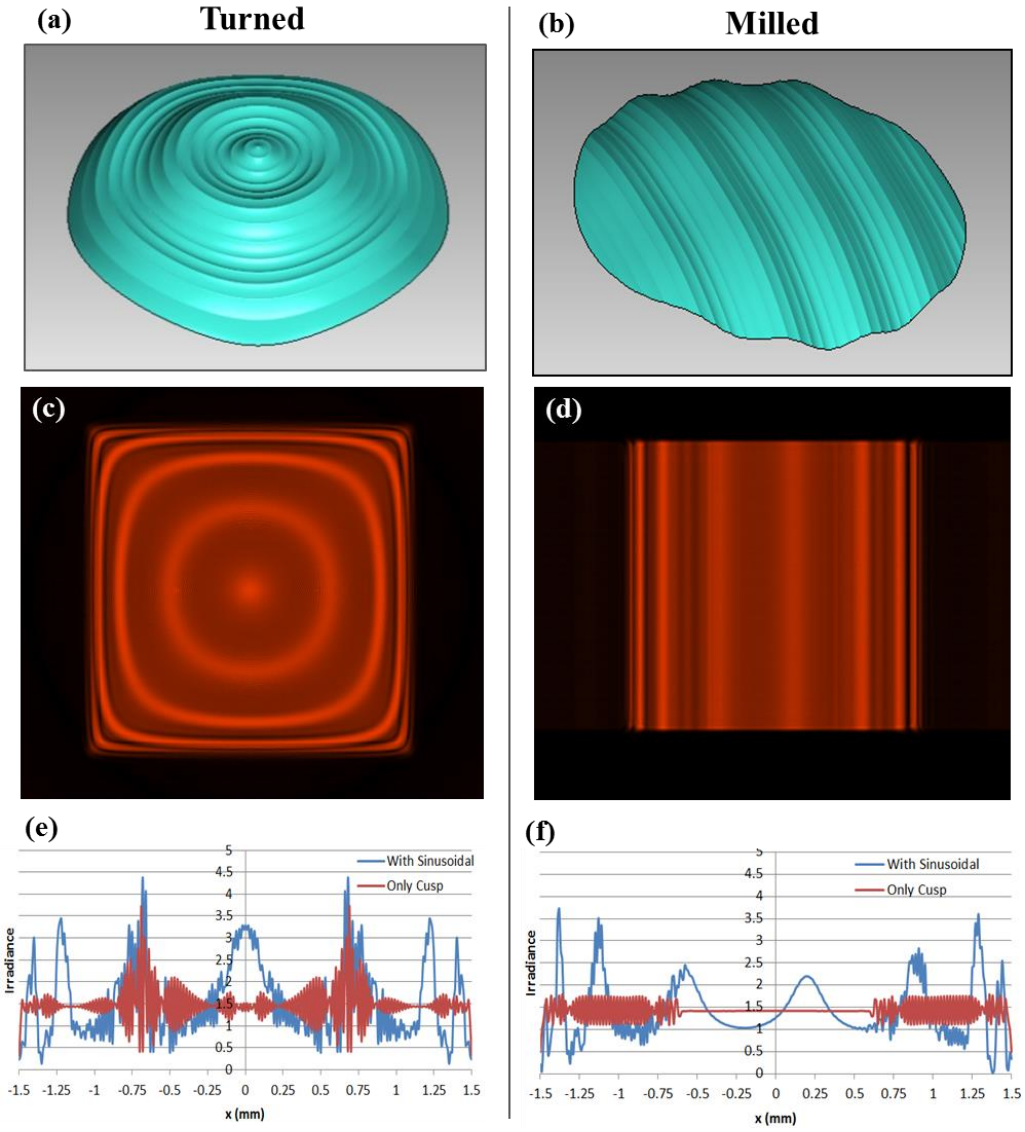

Fig. 8.16: (a) Diamond turned and (b) diamond milled beam shaping surface with cusp and sinusoidal grating structures. (c-d) Simulated output spots for both fabrication methods with the added sinusoidal grating. (e-f) Cross-sectional irradiance distribution of the output spots.

As with the imaging system example, the addition of the sinusoidal grating has a significant negative impact on system performance. For the diamond turned example, the cross-sectional uniformity error U_{rms} increased by 98% and for the diamond milled example, U_{rms} increased by 177%. Conceptually similar to the MTF results seen for the imaging example, we note shallow higher frequency oscillations in the irradiance profile from the cusp grating and a deeper variation at lower frequency resulting from the thermal cycling error. This further validates the idea of considering the total surface texture as a combination of multiple MSF errors that have their own individual impacts on system performance.

8.5 Manufacturing process optimization path

As demonstrated in the previous section, the ability to simulate system performance based on machining parameters offers promise for optimization of the manufacturing process. As a simple demonstration, we performed a series of parameter sweeps of the step-over and endmill radius to create a range of MSF textures on the dynamic beam shaper design from Chapter 3. VirtualLab™ simulations were performed to generate the corresponding collection of output spots. For each output spot, a cross-section of the irradiance along the *x*-axis was manually exported. Each irradiance profile was then analyzed in MATLAB®, where Eq. (6.3) was used to determine the uniformity error U_{rms} with a clear aperture window set to 90%. The results are shown in Fig. 8.17.

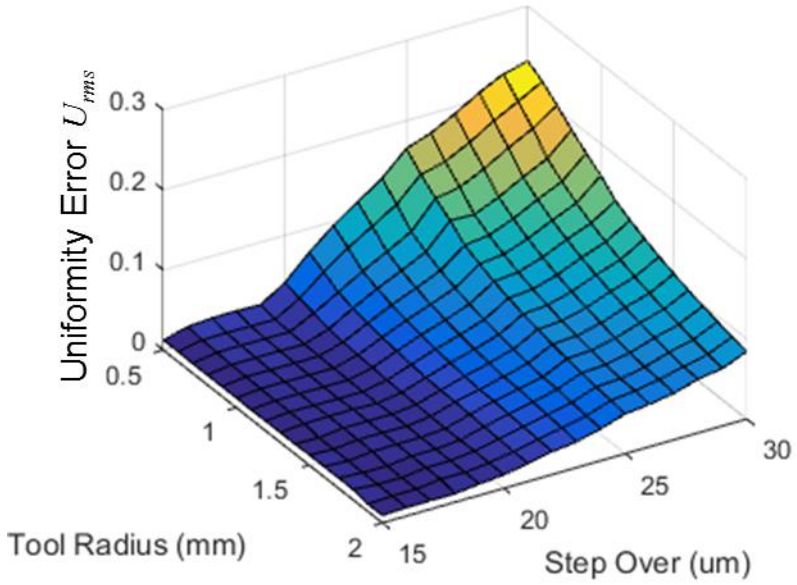

Fig. 8.17: Simulated uniformity error as a function of step over and endmill radius of curvature for the super-Gaussian beam shaper design from Chapter 3.

From these results, we note the increase in the uniformity error U_{rms} as the tool radius decreases and step-over increases. Also, the uniformity errors appear to plateau for step-overs less than 15 μm as a result of the diffraction orders no longer overlaying and interfering with each other. This approach enables determination of the minimum step-over needed for a required uniformity specification. Since manufacturing time and costs scale inversely with the step-over, determining this threshold is extremely useful for optimization of the manufacturing process.

8.6 Discussion

The performance impact of MSF errors resulting from diamond turning and diamond milling fabrication methods were investigated using a spherical lens and a fixed output beam shaper as case studies. The residual MSF structures were approximated as characteristic ‘cusp’ grating patterns and related to relevant manufacturing parameters

(step-over and tool radius). While varying these parameters, simulations were performed using wave-based optical models. Results from these simulations indicated that the step-over has a value for which the impact of the resulting MSF errors became negligible due to the undesired diffraction orders from the cusp grating no longer overlapping one another. Additionally, MSF errors due to thermal cycling were incorporated as a lower frequency sinusoidal structure and combined with the cusp structure for both fabrication methods. These simulation results suggested that the impacts from each MSF error could be considered separately. The results from these simulations are encouraging for future research. Defining additional MSF errors in terms of manufacturing parameters could enable development of a tolerance procedure in which the manufacturing parameters are optimized for minimal machine usage while maintaining a required optical performance.

CHAPTER 9: CONCLUSION

9.1 Summary

Many different aspects of dynamic freeform optics have been explored in this dissertation. Experimental tests were performed on a diamond raster-milled variable output diameter beam shaper, previously designed by Smilie *et al.* [45]. Initial experimental test results confirmed the general functionality of this device, but the uniformity was less than ideal with a significant amount of undesired noise observed in the output spots. The majority of this noise was found to result from residual surface finish errors on the fabricated freeform surfaces. An extended design approach was then used to create a second beam shaper with a super Gaussian irradiance distribution, rather than the previously-used step-function. Many fabrication improvements were also made which ultimately decreased the surface roughness by an order of magnitude, resulting in significantly better output spot uniformity. (Discussed in Chapter 3)

In Chapter 4, an Alvarez lens with a shifted focal range was designed using this extended design approach to have a positive focal length across the full range of lateral shifts. Compared to a equivalent ‘standard’ Alvarez lens, this new design resulted in decreased surface height modulation, which improved the overall performance which was realized through smaller spot sizes and increase in the Strehl ratio. Experimental tests of the STS diamond turned freeform elements were performed with the results in good agreement with the theoretical results, further verifying the variable functionality of this optical system.

In Chapter 5, we created three additional novel dynamic freeform optical systems with non-rotationally symmetric outputs using both one and two dimensional lateral shifts; a variable square output beam shaper with a 1-D shift, a variable rectangular output beam shaper with a 2-D shift, and a variable toric lens with a 2-D shift. These examples all expanded on earlier design procedures as they were limited to output functions with radial symmetry in which the *x* and *y* parameters are varied simultaneously through a lateral shift along a single axis. Simulations were performed for each of these designs, where the results indicated that the general design process worked as intended.

In addition to creating and characterizing novel optical systems, several different tolerance specifications were also investigated in this work. In Chapter 6, we developed a simplified optomechanical tolerancing procedure for dynamic freeform optical systems with an eye towards efficiency and certainty. This procedure consisted of sensitivity analyses, a combined error analysis, and creation of an empirical formula for prediction of an error budget based on three individual tolerance parameters (displacement, tilt, and rotation). In each of the analyses, a 'pass-fail' approach was implemented using worst case scenarios to ensure that the device would work properly within the determined tolerance parameters. The shifted focus Alvarez and the super Gaussian beam shaper were both used as case studies, and the importance of the chosen performance metric was discussed.

In Chapter 7, we developed a deterministic tolerancing procedure for specifying the surface form accuracy of freeforms using the same case studies and performance metrics as in the optomechanical tolerancing case. This procedure considered two primary characteristics of low-frequency form error; surface deformation of the reference

prescription as a function of surface height (*HS*), and surface slope (*SS*). These two characteristic errors were used in a combined error analysis to ensure that all possibilities of low frequency form deviations were considered. Resulting surface specifications consisted of two terms: (1) the maximum allowable height scale after removal of the reference and (2) the irregularity, which was the measured P-V value of the surface form error after removal of the reference and best-fit height scale.

In Chapter 8, we investigated the performance impact of mid-spatial frequency (MSF) errors resulting from diamond turning and diamond milling fabrication methods. The residual MSF structures were approximated as characteristic ‘cusp’ grating patterns and related to relevant manufacturing parameters (step-over and tool radius). A spherical lens and a fixed output beam shaper were used as case studies. For both cases, simulation results indicated that the step-over has a value for which the impact of the resulting MSF errors became negligible due to the undesired diffraction orders from the cusp grating no longer overlapping with one another. Additionally, MSF errors due to thermal cycling were incorporated as a lower frequency sinusoidal structure and combined with the cusp structure for both fabrication methods. These simulation results suggested that the impacts from each MSF error could be considered separately.

9.2 Future research

9.2.1 Optical design

A primary objective in this dissertation was expansion of analytical design procedures used in previous examples to overcome their inherent design constraints. Several novel designs were created through the development of an extended design procedure. The design advancements made in these designs can be summarized in four categories:

(1) Numerical definition of freeform surfaces based on a continuous output irradiance distribution.

(2) Varifocal system using laterally shifted freeform surfaces with optical power when lateral shift is zero.

(3) Definition of freeform surfaces based on non-rotationally symmetric irradiance distributions.

(4) Independent control of x and y dimensions of the optical outputs through independent lateral shifts along the x and y axes.

These advances are enabling and suggest that additional applications are possible in this genre of optical systems. Future work could include non-imaging applications with semi-arbitrary irradiance distributions, such as Gaussian beams with higher order modes [128]. Additional imaging applications could include, for example, different composite surfaces to realize variable aspheric lenses to further improve system performance and capabilities. Although these advancements are encouraging for future designs, the current design procedure is still limited in two ways; (1) the desired composite surfaces must be accurately represented by an XY polynomial with only even degree orders, and (2) the input dimensions are assumed to be fixed. Future work could focus on even further

expanding the design procedure to overcome these limitations, enabling the potential for additional novel designs.

Additionally, it is important to note that the demonstrated design approaches did not use numerical optimization in order to achieve the freeform lens prescriptions. As in conventional lens design, in which analytic methods are used to provide promising initial design forms prior to numerical optimization, our process provides a starting point for numerical optimization of future freeform designs using optical simulation software for enhanced performance.

9.2.2 Fabrication and experimental testing

Fabrication and experimental test results for the super Gaussian beam shaper discussed in Chapter 3 were much improved compared to the previous step-function beam shaper. However, remaining noise in the output spot suggested the need for better surface finish and for a thorough understanding of the performance impacts caused by different MSF errors. Additional research is being performed by others at UNC Charlotte on deeper understanding of the impact of MSF errors on optical performance and on methods to further improve and expand the capabilities of the fabrication process using diamond machining. With the continued advancement of fabrication capabilities, improved surface finish, and understanding of MSF error impacts, the experimental performance of current and future dynamic freeform designs could be significantly improved.

Experimental tests were performed on the shifted focus Alvarez lens, as discussed in Chapter 4. The system was characterized through experimental focal length measurements and captured images, using a hot plate as both a light source and imaging

object, with the experimental results in good agreement with theoretical predictions. Though encouraging, this system could be further expanded in order to more fully characterize the imaging properties. This could potentially involve a more complex experimental test setup to enable the measurement of the point spread function (PSF), as well as characterization of the system modulation transfer function (MTF).

9.2.3 Tolerancing methods and procedures

Tolerance analyses were performed with regards to three primary areas of potential error; optical alignment, surface form error, and surface finish quality. However, due to the vast number of variables within the system, this research was limited by separately performing a tolerance analysis for each error source. Though necessary to develop individual tolerance procedures, we realize that these errors can interact and have the potential to have compounded impacts on system performance. In order to properly tolerance these dynamic freeform systems, future research should work towards developing a global tolerancing procedure which encompasses the compounding performance impacts as multiple error sources are introduced.

Optomechanical tolerancing

Multiple assumptions were made throughout the optomechanical tolerancing procedure discussed in Chapter 6 in order to significantly reduce the number of required simulations. In particular there were two specific assumptions that could potentially be avoided; (1) equal displacement and tilt tolerances along the x and y axes, and (2) equal positive and negative tolerances. These assumptions came with a slight cost which subtly increased the potential of over-tolerancing along the x and y directions and in the positive

and negative directions. For example, tolerances for displacement in one direction could be set too tightly as a consequence of the system being more sensitive to displacement in the orthogonal direction. Future research on this procedure should focus on removing these assumptions to enable a more accurate tolerance specification, while still maintaining the primary advantages of being computationally efficient and deterministic.

Surface form error tolerancing

The tolerancing procedure used to specify the surface accuracy (discussed in Chapter 7) considered the combination of two primary characteristics of form error (*HS* and *SS*). This was assumed to generally capture the majority of possible form errors. However, there are different signatures that are not specifically represented by this assumption (i.e. resulting from tilt, decenter, waviness, ogive errors, etc. [86]). Investigating additional form error signatures in the future would provide more insights into general surface accuracy requirements. Furthermore, it would be useful to expand this analysis in future work to include errors that are products of specific tool errors. For example, an error in the assumed tool tip shape used in diamond machining methods would result in a loss of surface accuracy. Future work could include developing a procedure to determine a pass-fail threshold based on a tolerance specification of the actual tool shape. This would be an extremely useful capability to aid communication between designer and manufacturer.

Additionally, regarding surface error specifications, the resulting irregularity was specified as a maximum allowable P-V value. Though this is deterministic, including more types of form errors will likely require a less-ambiguous irregularity specification in order to avoid potentially subjecting the fabricated surface to a faulty pass/fail decision. With this in mind, a suggestion for future work is to specify the irregularity as an RMS

measurement of either the residual surface height error or surface slope error, where the error would be represented as the standard deviation of the entire surface rather than of a single point, as is the case with a P-V measurement.

Surface finish quality – MSF errors

The investigation on MSF errors and the corresponding performance impact (discussed in Chapter 8) provided results that are encouraging for future research. Defining additional MSF errors in terms of manufacturing parameters could enable development of a tolerance procedure in which the manufacturing parameters are optimized for minimal machine usage while maintaining a required optical performance. Additionally, this analysis on MSF errors was performed on single element devices, straying away from the dynamic freeform optical systems discussed throughout this dissertation. Future work should include similar analyses on dynamic freeform optical systems in which the addition of a second freeform and standoff distance between the two freeforms further increases the level of complexity.

REFERENCES

[1] H. Ries and J. Muschaweck, "Tailored freeform optical surfaces," JOSA A 19(3), 590-595 (2002).

[2] R. Jetter and H. Ries, "Optimized tailoring for lens design," Proc. SPIE 5875, 58750A, 1-8 (2005).

[3] J. Rubinstein and G. Wolansky, "Intensity control with a free-form lens," JOSA A 24(2), 463-469 (2007).

[4] L. Wang, K. Qian and Y. Luo, "Discontinuous free-form lens design for prescribed irradiance," Applied Optics 46(18), 3716-3723 (2007).

[5] T. A. Mitchell and J. M. Sasian, "Variable aberration correction using axially translating phase plates," Proc. SPIE 3705, 209-220 (1999).

[6] E. Acosta and S. Bará, "Variable aberration generators using rotated Zernike plates," JOSA A 22(9), 1993-1996 (2005).

[7] A. Y. Yi and T. W. Raasch, "Design and fabrication of a freeform phase plate for high-order ocular aberration correction," Applied Optics 44(32), 6869-6876 (2005).

[8] S. S. Sherif, W. T. Cathey and E. R. Dowski, "Phase plate to extend the depth of field of incoherent hybrid imaging systems," Applied Optics 43(13), 2709-2721 (2004).

[9] Y. Takahashi and S. Komatsu, "Optimized free-form phase mask for extension of depth of field in wavefront-coded imaging," Optics Letters 33(13), 1515-1517 (2008).

[10] U. Sander, "Optical device with increased depth of field," US 7,586,675 (September 8, 2009).

[11] M. Demenikov, G. Muyo and A. R. Harvey, "Experimental demonstration of continuously variable optical encoding in a hybrid imaging system," Optics Letters 35(12), 2100-2102 (2010).

[12] V. Oliker, "Optical design of freeform two-mirror beam-shaping systems," JOSA A 24(12), 3741-3752 (2007).

[13] D. Michaelis, S. Kudaev, R. Steinkopf, A. Gebhardt, P. Schreiber and A. Bräuer, "Incoherent beam shaping with freeform mirror," Proc. SPIE 7059, 705905, 1-6 (2008).

[14] V. Oliker, "On design of free-form refractive beam shapers, sensitivity to figure error, and convexity of lenses," JOSA A 25(12), 3067-3076 (2008).

[15] E. Marcellin-Dibon and F. Wielhege, "Projection system comprising a free form reflector and a free form lens," US 5,790,305 (August 4, 1998).

[16] T. Baba and C. Yamamoto, "Reflection type projection optical system," US 6,626,542 (September 30, 2003).

[17] A. L. Timinger, J. A. Muschaweck and H. Ries, "Designing tailored free-form surfaces for general illumination," Proc. SPIE 5186, 128-132 (2003).

[18] J. B. Jiang, C. E. Cheung, S. To, K. W. Cheng, K. Wang and W. B. Lee, "Design and fabrication of freeform reflector for automotive headlamp," Power Electronics Systems and Applications, 220-224 (2006).

[19] D. Vincenzi and G. Oliva, "Tailoring freeform lenses for barcode lighting," Automatic Identification Advanced Technologies, 134-139 (2007).

[20] A. A. Belousov, L. L. Doskolovich and S. I. Kharitonov, "A gradient method of designing optical elements for forming a specified irradiance on a curved surface," Journal of Optical Technology 75(3), 161-165 (2008).

[21] H. Xiang, Z. Zhenrong, L. Xu and G. Peifu, "Freeform surface lens design for uniform illumination," Journal of Optics A: Pure and Applied Optics 10, 075005 (2008).

[22] L. Sun, S. Jin and S. Cen, "Free-form microlens for illumination applications," Applied Optics 48(29), 5520-5527 (2009).

[23] Z. Zhenrong, H. Xiang and L. Xu, "Freeform surface lens for LED uniform illumination," Applied Optics 48(35), 6627-6634 (2009).

[24] A. Bäuerle, R. Wester, C. Schnitzler and P. Loosen, "Design of efficient freeform lenses for mass-market illumination applications using hybrid algorithms," Proc. SPIE 7788, 778807, 1-10 (2010).

[25] R. R. Shannon, "Overview of conformal optics," Proc. SPIE 3705, 180-188 (1999).

[26] J. L. Ruckman, E. M. Fess and H. M. Pollicove, "Deterministic processes for manufacturing conformal (freeform) optical surfaces," Proc. SPIE 4375, 108-113 (2001).

[27] R. R. Shannon, J. P. Mills, H. M. Pollicove, P. A. Trotta and L. N. Durvasula, "Optics that fit" (2001), http://wejump.ifac.cnr.it/pages/sw/programs/oslo/opticsthatfit.pdf.

[28] L. W. Alvarez, “Two-element variable-power spherical lens,” U. S. Patent No. 3,305,294 (1967).

[29] L. W. Alvarez and W. E. Humphrey, “Variable-power lens and system,” U. S. Patent No. 3,507,565 (1970).

[30] A. W. Lohmann, “A new class of varifocal lenses,” Appl. Opt. 9(7), 1669-1671 (1970).

[31] A. N. Simonov, G. Vdovin and M. C. Rombach, "Cubic optical elements for an accommodative intraocular lens," Optics Express 14, 7757-7775 (2006).

[32] C. Huang, L. Li and A. Y. Yi, "Design and fabrication of a micro Alvarez lens array with a variable focal length," Microsystem Technologies 15(4), 559-563 (2009).

[33] J. Schwiegerling and C. Paleta-Toxqui, "Minimal movement zoom lens," Applied Optics 48(10), 1932-1935 (2009).

[34] P. J. Smilie, B. S. Dutterer, J. L. Lineberger, M. A. Davies and T. J. Suleski, “Design and Characterization of an Infrared Alvarez Lens,” Opt. Engineering 51(1), 013006 (2012).

[35] P. J. Smilie, “Dynamic optical systems through laterally translated refractive freeform elements,” M.S. Thesis, Applied Physics, UNC Charlotte, Charlotte, (2011).

[36] J. G. Baker, "Variable-power, analytic function, optical component in the form of a pair of laterally adjustable plates having shaped surfaces, and optical systems including such components," US 3,583,790 (June 8, 1971).

[37] J. G. Baker and W. T. Plummer, "Analytic function optical component," US 4,650,292 (March 17, 1987).

[38] W. T. Plummer, J. G. Baker and J. V. Tassell, "Photographic optical systems with nonrotational aspheric surfaces," Applied Optics 38, 3572-3592 (1999).

[39] W. T. Plummer, "Free-form optical components in some early commercial products" (2004), http://www.wtpoptics.com/ASPEweb.htm.

[40] S. S. Rege, T. S. Tkaczyk and M. R. Descour, "Application of the Alvarez-Humphrey concept to the design of a miniaturized scanning microscope," Optics Express 12(12), 2574-2588 (2004).

[41] A. N. Simonov, M. Rombach, G. Vdovin and M. Loktev, "Varifocal optics for a novel accommodative intraocular lens," Proc. SPIE 6113, 61130B, 1 - 7 (2006).

[42] S. Barbero, "The Alvarez and Lohmann refractive lenses revisited," Optics Express 17(11), 9376-9390 (2009).

[43] A. Grewe, P. Fesser, and S. Sinzinger, "Diffractive array optics tuned by rotation," Appl. Opt. 56, A89-A96 (2017).

[44] I. A. Palusinski, J. M. Sasian and J. E. Greivenkamp, "Lateral-shift variable aberration generators," Applied Optics 38, 86-90 (1999).

[45] H. J. Caulfield, "The Alvarez-Lohmann lens as a do-nothing machine," Optics & Laser Technology 34(1), 1-5 (2002).

[46] K. N. LaFortune, "Generalized Alvarez lens for correction of laser aberrations," United States Dept. of Energy, Lawrence Livermore National Laboratory, UCRL-TR-208417 (2004).

[47] B. J. Bauman and S. Ebstein, "Concept for laser guide star dynamic refocusing using rotating phase plates," Proc. SPIE 7015, 70151M, 1-9 (2008).

[48] M. C. Rombach and A. N. Simonov, "Accommodating intraocular lens with variable correction," EP 1,932,492 (June 18, 2008).

[49] P. J. Smilie and T. J. Suleski, "Variable-diameter refractive beam shaping with freeform optical surfaces," Opt. Letters, 36 (21), 4170-4172 (2011).

[50] P. J. Smilie, J. Shultz, and T. J. Suleski, "Dynamic laser beam shaping methods and systems", U. S. Patent No. 9,238,577 (2015).

[51] T. J. Suleski, J. A. Shultz, and P. J. Smilie, "Dynamic beam shaping with freeform optics," Proc. SPIE 9194, 9194-19 (2014).

[52] J. A. Shultz, P. J. Smilie, B. S. Dutterer, M. A. Davies, and T. J. Suleski, "Experimental characterization of variable output refractive beam shapers using freeform elements," Proc. SPIE 9194, 91940M (2014).

[53] E. Acosta and J. Sasian, "Micro-Alvarez lenses for a variable dynamic range Shack–Hartmann wavefront sensor," Jpn. J. Appl. Phys. 53, 08MG04 (2014).

[54] S. Petsch, A. Grewe, L. Köbele, S. Sinzinger, and H. Zappe, "Ultrathin Alvarez lens system actuated by artificial muscles," Appl. Opt. 55, 2718-2723 (2016).

[55] G. Zhou, H. Yu, and F. S. Chau, "Microelectromechanically-driven miniature adaptive Alvarez lens," Opt. Express 21, 1226-1233 (2013).

[56] A. Grewe, M. Hillenbrand, and S. Sinzinger, "Aberration analysis of optimized Alvarez–Lohmann lenses," Appl. Opt. 53, 7498-7506 (2014).

[57] "Mathematical Illustration of the Gibbs Phenomenon" (2001), http://dpnc.unige.ch/tp/elect/doc/04-Gibbs-Phenomenon.pdf.

[58] G. B. Arfken, and H. J. Weber, "Gibbs Phenomenon," Chapter 14 in Mathematical Methods for Physicists, pp. 910-913, Elsevier Academic Press, Burlington, MA (2005).

[59] D. L. Shealy, and J. A. Hoffnagle, "Laser beam shaping profiles and propagation," Applied Optics 45, 5118-5131 (2006).

[60] J. Troutman, D. Barnhardt, J. Shultz, J. Owen, S. DeFisher, M. Davies and T. Suleski, "Machining and metrology of a chalcogenide glass freeform lens pair," Procedia Manufacturing, 2016.

[61] R. E. Gottschalk, "Variable anamorphic lens system," U. S. Patent No. 3,428,398 (1969).

[62] W. E. Humphrey, "Variable anamorphic lens and method for constructing lens," U. S. Patent No. 3,751,138 (1973).

[63] W. E. Humphrey, "Remote subjective refractor employing continuously variable sphere-cylinder corrections," Opt. Eng. 15(4), 286–291 (1976).

[64] I. Powell, "Variable anamorphic lens for a 35-mm SLR," Appl. Opt. 22, 3249-3257 (1983).

[65] S. Barbero, J. Rubinstein; Power-adjustable sphero-cylindrical refractor comprising two lenses," Opt. Eng. 52, 063002 (2013).

[66] I. M. Barton, S. N. Dixit, L. J. Summers, C. A. Thompson, K. Avicola, and J. Wilhelmsen, "Diffractive Alvarez lens," Opt. Lett. 25, 1-3 (2000).

[67] J. A. Shultz, and T. J. Suleski, "Design of a variable toric lens using laterally shifted freeform elements," in Optical Design and Fabrication 2017, paper JW2C.2, Optical Society of America, 2017.

[68] R. C. Juergens, H. J. Wood, "Random thoughts on Monte Carlo tolerancing," Proc. SPIE 6676; Optical System Alignment and Tolerancing;, 667605 (2007).

[69] E. Herman, J. Sasián, R. N. Youngworth, "Optomechanical considerations for realistic tolerancing," Proc. SPIE 8844, Optical System Alignment, Tolerancing, and Verification VII, 884402 (September 10, 2013).

[70] D. G. Koch, "A Statistical Approach To Lens Tolerancing," Proc. SPIE 0147, Computer-Aided Optical Design, 71 (December 1, 1978).

[71] R. N. Youngworth, "Twenty-first century optical tolerancing: a look at the past and improvements for the future," Proc. SPIE 6342, International Optical Design Conference 2006, 634203 (July 12, 2006).

[72] J. A. Shultz, M. A. Davies, and T. J. Suleski, “Simplified tolerancing of alignment errors in dynamic freeform optical systems,” in Optical Design and Fabrication 2017, paper JTh1C.3, Optical Society of America, 2017.

[73] J. A. Shultz, P. J. Smilie, M. A. Davies, and T. J. Suleski, “Optomechanical tolerancing of dynamic freeform optical systems,” Proc. ASPEN/ASPE Topical Meeting, Manufacture and Metrology of Structured and Freeform Surfaces for Functional Applications, 2017.

[74] International Standard ISO 10110-5:2015(E), Optics and optical instruments – Preparation of drawings for optical elements and systems, Part 5: Surface form, 2015.

[75] International Standard ISO 10110-12:2007(E), Optics and optical instruments – Preparation of drawings for optical elements and systems, Part 12: Aspheric surfaces, 2007.

[76] International Standard ISO 10110-19:2015(E), Optics and optical instruments – Preparation of drawings for optical elements and systems, Part 19: General description of surfaces and components, 2015.

[77] A. Timinger, J. Unterhinninghofen, S. Junginger, A. Hofmann, “Tolerancing free-form optics for illumination,” Proc. SPIE 8170; Illumination Optics II, 817006 (2011)

[78] S. Zwick, R. Knoth, R. Steinkopf, G. Notni, “Tolerancing of free form elements considering manufacturing characteristics,” Proc. SPIE 8550; Optical Systems Design, 855006 (2012).

[79] V. Oliker, "Sensitivity to figure error of a freeform refractive beam shaper," Proc. SPIE 7423, Nonimaging Optics: Efficient Design for Illumination and Solar Concentration VI, 742304 (August 20, 2009).

[80] J. D. Nelson, K. Medicus, G. Frisch, "Tolerancing an optical freeform surface: an optical fabricator's perspective," Proc. SPIE 9578, Current Developments in Lens Design and Optical Engineering XVI, 95780C (September 3, 2015).

[81] M. Maksimovic, “Optical design and tolerancing of freeform surfaces using anisotropic radial basis functions,” Opt. Eng. 55(7), 071203 (2016).

[82] J. M. Tamkin, T. D. Milster; “Effects of structured mid-spatial frequency errors on image performance,” Applied Optics 49 (33) 6522-6536 (2010).

[83] J. M. Tamkin, W. Dallas, T. D. Milster; “Theory of point-spread function artifacts due to structured mid-spatial frequency errors,” Applied Optics 49 (25) 4814-4824 (2010).

[84] J. E. Harvey, “Integrating optical fabrication and metrology into the optical design process,” Proc. SPIE 9293, 929328 (2014).

[85] R. N. Youngworth, B. D. Stone, “Simple estimates for the effects of mid-spatial frequency surface errors on image quality,” Applied Optics 39 (13) 2198-2209 (2000).

[86] H. G. Stillitto, "Analysis, Tolerancing And Diagnosis Of Diamond Machining Errors," Proc. SPIE 1013, Optical Design Methods, Applications and Large Optics, 105 (April 13, 1989).

[87] J. A. Shultz, H. Aryan, J. Owen, M. A. Davies, and T. J. Suleski, “Impacts of sub-aperture manufacturing techniques on the performance of freeform optics,” Proc. ASPEN/ASPE Topical Meeting, Manufacture and Metrology of Structured and Freeform Surfaces for Functional Applications, 2017.

[88] J. A. Shultz, M. A. Davies, and T. J. Suleski, "Effects of MSF errors on performance of freeform optics: Comparison of diamond turning and diamond milling," in Imaging and Applied Optics 2015, OSA Technical Digest (online), paper FT4B.3, Optical Society of America, 2015.

[89] O. Homburg and T. Mitra, "Gaussian-to-top-hat beam shaping: an overview of parameters, methods, and applications", Proc. SPIE 8236, Laser Resonators, Microresonators, and Beam Control XIV, 82360A (February 9, 2012).

[90] F. M. Dickey, and S. C. Holswade, "Laser Beam Shaping, Theory and Techniques," Marcel Dekker Inc, New York-2000.

[91] F. M. Dickey, and S. C. Holswade, “Beam shaping: a review,” in Laser Beam Shaping Applications, F. Dickey, S. Holswade, and D. Shealy, eds. (CRC Press, 2006), pp. 269–305.

[92] P. Calvet, C. Valentin, Y. Quiquempois, G. Bouwmans, L. Bigot, M. Douay, A. Mussot and E. Hugonnot, "Top-hat beam output from a large mode area microstructured fiber for beam delivery," Proc. SPIE 8433, Laser Sources and Applications, 84330K (June 1, 2012).

[93] O. Homburg, F. Toennissen, T. Mitra, and V. Lissotschenko, "Laser direct micro-machining with top-hat-convertedsingle mode lasers," Laser-based Micro- and Nanopackaging and Assembly II, Proceedings of SPIE, Vol. 6880, 68800R (2008).

[94] K. Jain, "Lithography and photoablation systems for microelectronics and optoelectronics: importance of laser beam shaping in system design," Proc. SPIE 4770, Laser Beam Shaping III, 1 (October 1, 2002).

[95] P. Gouriou, F. Scol, B. Sevigny, C. Valentin, Y. Quiquempois, L. Bigot, R. Habert, A. Cassez, O. Vanvincq, E. Hugonnot, and G. Bouwmans, "Top hat single-mode polarization maintaining fiber and polarizing numerical design," Proc. SPIE 9728, Fiber Lasers XIII: Technology, Systems, and Applications, 97281A (March 11, 2016).

[96] W. Zhao, J. H. Kim, and P. Palffy-Muhoray, "Z-scan measurement on liquid crystals using top-hat beams," Proc. SPIE 2229, Nonlinear Optical Materials for Switching and Limiting, 131 (July 6, 1994).

[97] W. C. Waes, "Advances in digital printing and quality considerations of digitally printed images," Proc. SPIE 2949, Imaging Sciences and Display Technologies, 383 (February 7, 1997).

[98] J. Mrazek, M. Pospisilova, V. Svozil, O. Cadek, and K. Nesporova, "Widefield imaging of upconverting nanoparticles on epifluorescence microscopes adapted for laser illumination with top-hat profile," J. Biomed. Opt. 21(5), 056007 (May 27, 2016).

[99] K. Kanzler, and A. Stockham, "Diffractive laser beam shaping for holography," Proc. SPIE 7430, Laser Beam Shaping X, 743006 (August 21, 2009).

[100] A. Laskin, and V. Laskin, "Beam shaping to improve holography techniques based on spatial light modulators," Proc. SPIE 8642, Emerging Liquid Crystal Technologies VIII, 86420I (March 5, 2013).

[101] B. R. Frieden, "Lossless conversion of a plane laser wave to a plane wave of uniform irradiance," Applied Optics 4(11), 1400-1403 (1965).

[102] J. L. Kreuzer, "Coherent light optical system yielding an output beam of desired intensity distribution at a desired equiphase surface," US 3,476,463 (November 4, 1969).

[103] P. W. Rhodes, and D. L. Shealy, "Refractive optical systems for irradiance redistribution of collimated radiation: their design and analysis," Applied Optics 19, 3545-3553 (1980).

[104] C. Y. Han, Y. Ishii, and K. Murata, "Reshaping collimated laser beams with Gaussian profile to uniform profiles," Applied Optics 22, 3644-3647 (1983).

[105] W. Jiang, D. L. Shealy, and J. C. Martin, "Design and testing of a refractive reshaping system," Proc. SPIE 2000, 64-75 (1993).

[106] J. A. Hoffnagle and C. M. Jefferson, "Design and performance of a refractive optical system that converts a Gaussian to a flattop beam," Applied Optics 39(30), 5488-5499 (2000).

[107] J. A. Hoffnagle and C. M. Jefferson, "Beam shaping with a plano-aspheric lens pair," Optical Engineering 42, 3090-3099 (2003).

[108] S. Zhang, G. Neil and M. Shinn, "Single-element laser beam shaper for uniform flat-top profiles," Optics Express 11, 1942-1948 (2003).

[109] M. Serkan and H. Kirkici, "Optical beam-shaping design based on ashperical lenses for circularization, collimation, and expansion of elliptical laser beams," Applied Optics 47, 230-241 (2008).

[110] A. Laskin, G. Williams and A. Demidovich, "Applying refractive beam shapers in creating spots of uniform intensity and various shapes," Proc. SPIE 7579, 75790N (2010).

[111] VirtualLab User's Manual (v. 5.0.0) (LightTrans GmbH, 2011).

[112] S. R. Patterson, and E. B. Magrab,"Design and testing of a fast tool servo for diamond turning," Precision Engineering, 7(3), 123-128 (1985).

[113] T. A. Dow, M. H. Miller, and P. J. Falter, "Application of a fast tool servo for diamond turning of non-rotationally symmetric surfaces," Precision Engineering, 13(4), 243-250 (1991).

[114] N. E. Clayor, D. M. Combs, O. M. Lechuga, J. J. Mader, and J. Udayasankaran, "An overview of freeform optics production," Proc. ASPE, Topical Meeting, Free-from Optics: Design, Metrology, Fabrication, Assembly (2004).

[115] G. M. Moorefield, K. P. Garrard, K. J. Falter, L. W. Taylor, and T. A. Dow, "Generation of rotationally asymmetric optical surfaces using a fast tool servo," Proc. ASPE 10, 45-48 (1994).

[116] Y. E. Tohme, and J. A. Lowe, "Machining of freeform optical surfaces by slow slide servo method," Proc. ASPE (2003).

[117] J. B. Bryan, "System and method for forming a non-rotationally symmetric portion of a workpiece," US 7,089,835 (August 15, 2006).

[118] Schott AG, "Infrared Chalcogenide Glass IRG 26," 17 October 2013. [Online]. Available:http://www.schott.com/advanced_optics/english/download/schottinfrared-chalcogenide-glasses-irg26-october-2013-eng.pdf. [Accessed 2 Feb. 2016].

[119] "Beam Expanders", http://www.edmundoptics.com/resources/application-notes/lasers/beam-expanders/.

[120] J. D. Owen, J. A. Shultz, T. J. Suleski, and M. A. Davies, "Error correction methodology for ultra-precision three-axis milling of freeform optics," 2017, CIRP Annals – Manufacturing Technology, 66(1), in press.

[121] “Polyfit”, https://www.mathworks.com/help/matlab/ref/polyfit.html?requestedDomain=www.mathworks.com.

[122] J. Troutman, D. Barnhardt, J. Shultz, J. Owen, M. Davies, and T. Suleski, "Pre-process error mapping and correction for ultraprecision manufacturing of freeform optics by slow tool servo," in 7th CIRP Conference on High Performance Cutting, Accepted, Chemnitz, Germany, 2016.

[123] J. Troutman, J. Owen, M. Davies, and T. Schmitz, "Cutting force measurement during diamond flycutting of chalcogenide glass," in 30th ASPE Annual Meeting, Austin, TX, 2015.

[124] J. Owen, M. Davies, D. Schmidt, and E. Urruti, "On the ultra-precision diamond machining of chalcogenide glass," CIRP Annals - Manufacturing Technology, vol. 64, pp. 113-116, 2015.

[125] J. Troutman, "Cutting mechanics and manufacture of optics for imaging applications," Ph.D. dissertation, UNC Charlotte, Charlotte, NC, 2016.

[126] E. Hecht, Optics, Addison Wesley, San Fransisco, CA (2002).

[127] ZEMAX® User's Guide (November 10, 2008).

[128] D. C. O'Shea, Elements of Modern Optical Design, Wiley-Interscience, New York (1985).

[129] P. Mouroulis and J. Macdonald, Geometrical Optics and Optical Design, Oxford University Press, Oxford (1997).

[130] R. R. Willey, "Economics in Optical Design, Analysis and Production," in Optical System Design, Analysis and Production,Rogers, and Fischer, eds. (SPIE, 1983), pp. 371-377.

[131] R. R. Willey, "The impact of tight tolerances and other factors on the cost of optical components," (SPIE, 1984), pp. 106-111.

[132] R. R. Willey, and R. E. Parks, eds., Handbook of Optomechanical Engineering (CRC Press, Boca Raton, FL, 1997).

[133] R. N. Youngworth, and B. D. Stone, "Cost-based tolerancing of optical systems," Applied Optics 39, 25, 4501-4512 (2000).

[134] R. N. Youngworth, and B. D. Stone, "Elements of cost-based tolerancing," Optical Review 8, 4, 276-280 (2001).

[135] J. D. Nelson, R. N. Youngworth, D. M. Aikens, "The cost of tolerancing," Proc. SPIE 7433, Optical System Alignment, Tolerancing, and Verification III, 74330E (August 28, 2009).

[136] D. Heshmaty-Manesh, and G. Y. Haig, "Lens tolerancing by desk-top computer," Appl. Opt. 25, 1268-1270 (1986).

[137] W. J. Smith, "Fundamentals of the optical tolerance budget," Proc. SPIE 1354, 1990 Intl Lens Design Conf, 474 (January 1, 1991).

[138] S. Magarill, "Optomechanical sensitivity and tolerancing," Proc. SPIE 3786, Optomechanical Engineering and Vibration Control, 220 (September 28, 1999).

[139] Synopsys, http://optics.synopsys.com/codev/pdfs/OpticalDesignTolerancing.pdf.

[140] Youngworth, R.N., "Statistical truths of tolerance assignment in optical design," Proc. SPIE 8131(Sep), 81310E (2011).

[141] "nthroot," https://www.mathworks.com/help/matlab/ref/nthroot.html.

[142] "fit," https://www.mathworks.com/help/curvefit/fit.html.

[143] E. W. Weisstein, "Variation Coefficient." From MathWorld--A Wolfram Web Resource. http://mathworld.wolfram.com/VariationCoefficient.html.

[144] C. Liu, and S. Zhang, "Study of singular radius and surface boundary constraints in refractive beam shaper design," Opt. Express 16, 6675-6682 (2008).

[145] M. Rimmer, "Analysis of Perturbed Lens Systems," Appl. Opt. 9, 533-537 (1970).

[146] R. R. Willey, "Optical design for manufacture," (SPIE, 1989), pp. 96-102.

[147] J. P. McGuire Jr., "Designing easily manufactured lenses using the global method," (SPIE, 2006), p. 63420O.

[148] R. E. Fischer, B. Tadic-Galeb, and P. R. Yoder, "Chapter 18: Optical Manufacturing Considerations," in Optical System Design, S. S. Chapman, ed. (McGraw-Hill Companies, Inc., 2008).

[149] G. Adams, "Selection of tolerances," (SPIE, 1988), pp. 173-185.

[150] J. L. Plummer, "Tolerancing for economies in mass production optics," in Contemporary Optical Systems and Components Specifications, R. E. Fischer, ed. (SPIE, 1979), pp. 181-183.

[151] R. Wilson, R. C. Brost, D. R. Strip, R. J. Sudol, R. N. Youngworth, and P. O. McLaughlin, "Considerations for tolerancing aspheric optical components," Applied Optics, 43 (2004) 10.

[152] G. Erdei, G. Szarvas, and E. Lorincz, "Tolerancing surface accuracy of aspheric lenses used for imaging purposes." Proc. SPIE 5249, Optical Design and Engineering, 718 (February 18, 2004).

[153] D. F. Figer, and I. S. McLean, "Wavefront error budget and optomechanical tolerancing for NIRSPEC," Proc. SPIE 3354, Infrared Astronomical Instrumentation, 1005 (August 21, 1998).

[154] S. R. Kiontke, D. M. Aikens, and R. N. Youngworth, "Freeform capability enabled by ISO 10110," Proc. SPIE 9582, Optical System Alignment, Tolerancing, and Verification IX, 958202 (September 3, 2015).

[155] R. N. Youngworth, S. R. Kiontke, and D. M. Aikens, "Implementing ISO standard-compliant freeform component drawings," Opt. Eng. 55(7), 071205 (Apr 07, 2016).

[156] U. Fuchs, "Tolerancing aspheric surfaces in optical design," Proc. SPIE 9582, Optical System Alignment, Tolerancing, and Verification IX, 958205 (September 3, 2015).

[157] C. Huang, R. Youngworth, and R. Liang, "Tolerancing sub-aperture regions of optical surfaces using circular and elliptical Zernike polynomials," Proc. SPIE 9195, Optical System Alignment, Tolerancing, and Verification VIII, 919506 (September 19, 2014).

[158] J. R. Rogers, "Orthogonal polynomials and tolerancing," Proc. SPIE 8131, Optical System Alignment, Tolerancing, and Verification V, 81310D (September 12, 2011).

[159] J. Owen, personal communication (2017).

[160] J. Owen, "Manufacture of infrared optics in brittle materials," Ph.D. dissertation, UNC Charlotte, Charlotte, NC, 2015.

[161] G. D. Boreman, Modulation Transfer Function in Optical and Electro-Optical Systems, Bellingham, WA: SPIE Press, 2001.

APPENDIX A: MATLAB CODES

A.1 Optical design

A.1.1 Super Guassian variable beam shaper: freeform surface coefficient generator

```
% SG_beamshaper_for_dissertation.m
% Beam shaper design in PMMA using a super gaussian approach
% Author: Jason Shultz
% Date: 05/04/15
clear all
%---------------all units in millimeters------------
%Base Parameters
z0=150;      %target length
nl=1.49;     %refractive index for PMMA
w0=3.45;     %waist radius for HeNe laser151
r0=6;        %lens radius
R0=1.5;      %output radius at d=0
change=.5;   %output radius change per unit shift increment (del)
p=40;        %super gaussian parameter
num=141;     %number of points in this analysis (keep odd)

%%%%%%%%--------develop composite surfaces------%%%%%%%%%%
%------Output diameter of 1mm--------
R_1=R0-2*change;
a2k_1=curvefit_sg_2(R_1,w0,r0,z0,nl,num,p);

%-------Output diameter of 2mm-------
R_2=R0-change;
a2k_2=curvefit_sg_2(R_2,w0,r0,z0,nl,num,p);

%-------Output diameter of 3mm-------
R_3=R0;
a2k_3=curvefit_sg_2(R_3,w0,r0,z0,nl,num,p);
a2k=a2k_3; %base component
%-------Output diameter of 4mm-------
R_4=R0+change;
a2k_4=curvefit_sg_2(R_4,w0,r0,z0,nl,num,p);

%-------Output diameter of 5mm-------
R_5=R0+2*change;
a2k_5=curvefit_sg_2(R_5,w0,r0,z0,nl,num,p);

%-----------------determine b2k coefficients---------------
                    %b2k=dela2k/(2deld)
del_d=.15; %amount of lateral shift for 1mm diam. increments

del_a2k_avg=((a2k_1-a2k_2)+(a2k_2-a2k_3)+(a2k_3-a2k_4)+(a2k_4-
a2k_5))./4;
flipud(del_a2k_avg);

b2k=del_a2k_avg./(2*del_d); %variability coefficients
```

```
%reorganize them for clearer display
a_surface_coeffs_2_14=flipud(a2k)
b_surface_coeffs_2_14=flipud(b2k)

%------------------generate freeform surfaces-----------------
%------------------circular plot for surface---------------------
pts=291;
r1 = linspace(0,r0,pts);    % radius array for plotting actual surface
th1 = linspace(0,2*pi,pts);  % theta array for plotting

%Define the r and th grids
[r,th] = meshgrid(r1,th1);
[x,y] = pol2cart(th,r);

%define a2k, and b2ks explicitly
a2=a2k(7); a4=a2k(6); a6=a2k(5); a8=a2k(4); a10=a2k(3); a12=a2k(2);
a14=a2k(1);
b2=b2k(7); b4=b2k(6); b6=b2k(5); b8=b2k(4); b10=b2k(3); b12=b2k(2);
b14=b2k(1);

%individual terms for variable component function
b2xy = (1/3)*(x.^3) + x.*(y.^2);
b4xy = (1/5)*(x.^5) + (2/3)*(x.^3).*(y.^2) + x.*(y.^4);
b6xy = (1/7)*(x.^7) + (3/5)*(x.^5).*(y.^2) + (x.^3).*(y.^4) +
x.*(y.^6);
b8xy = (1/9)*(x.^9) + (4/7)*(x.^7).*(y.^2) + (6/5)*(x.^5).*(y.^4) +
(4/3)*(x.^3).*(y.^6) + x.*(y.^8);
b10xy = (1/11)*(x.^11) + (5/9)*(x.^9).*(y.^2) + (10/7)*(x.^7).*(y.^4) +
2*(x.^5).*(y.^6) + (5/3)*(x.^3).*(y.^8) + x.*(y.^10);
b12xy = (1/13)*(x.^13) + (6/11)*(x.^11).*(y.^2) + (5/3)*(x.^9).*(y.^4)
+ (20/7)*(x.^7).*(y.^6) + 3*(x.^5).*(y.^8) + 2*(x.^3).*(y.^10) +
x.*(y.^12);
b14xy = (1/15)*(x.^15) + (7/13)*(x.^13).*(y.^2) +
(21/11)*(x.^11).*(y.^4) + (35/9)*(x.^9).*(y.^6) + (35/7)*(x.^7).*(y.^8)
+ (21/5)*(x.^5).*(y.^10) + (7/3)*(x.^3).*(y.^12) + x.*(y.^14);

r = sqrt((x.^2) + (y.^2)); %converting coordinates for brevity
fb=(a2*r.^2 + a4*r.^4 + a6*r.^6 + a8*r.^8 + a10*r.^10 + a12*r.^12 +
a14*r.^14)./2; %function for base component
fv=b2*b2xy + b4*b4xy + b6*b6xy + b8*b8xy + b10*b10xy + b12*b12xy +
b14*b14xy; %function for variable component

fs=fb+fv; %freeform surface without tilt

%---------------determine tilt for lowest sag on freeform surface------
----
c_limit=.5;
tilt=tilt_term(x,fs,c_limit)
fs=fs+tilt.*x; %add tilt term
sag_freeform=abs(max(max(fs))-min(min(fs))) %surface height modulation

figure(1)
surf(x,y,fb), shading interp, colorbar, view(20,45) %plot of base
component
```

```
xlabel('x(mm)'),ylabel('y(mm)'),zlabel('z(mm)'),title('Base
Component'),xlim([-6 6]),ylim([-6 6])

figure(2)
surf(x,y,fv+tilt*x), shading interp, colorbar, view(20,45) %plot of
variable component
xlabel('x(mm)'),ylabel('y(mm)'),zlabel('z(mm)'),title('Variability
Component'),xlim([-6 6]),ylim([-6 6])

figure(3)
surf(x,y,fs), shading interp, colorbar, view(20,45) %plot of freeform
surface
xlabel('x(mm)'),ylabel('y(mm)'),zlabel('z(mm)'),title('Freeform
Surface'),xlim([-6 6]),ylim([-6 6])

%curvefit_sg_2.m
function [a2k] = curvefit_sg_2(R0, w0, r0, z0, nl, num,p)
% composite surface design-Super gaussian approach
% Author: Jason Shultz
% Date: 05/04/15
%------this function will be called later in program-----

% develop equation relating r and R for ode45

RR=linspace(0,R0,4501)'; %output radius vector

num=141;                    %number of points in this analysis (keep
odd)
r_=linspace(-r0,r0,num)';   %radius vector from -r0 to +r0 (diameter)

I1=w0^2/4*(1-exp(-2*(r0/w0)^2)); %input gaussian integral
%from wolfram integral calc (see integral_attempt.m)
I2=(gammainc( (2/R0^p).*R0.^p , 2/p)).*(R0^2/(p*2^(2/p)));
I0=I1/I2;

%right hand side of the conservation of energy eq. (output)
rhs=I0.*(gammainc( (2/R0^p).*RR.^p , 2/p)).*(R0^2/(p*2^(2/p)));

%left hand side of the conservation of energy eq. (input)
lhs=w0^2/(4).*(1-exp(-2.*(r_./w0).^2));

%loop to create the output R vector relative to the input r vector
for k=1:length(lhs)
for i=1:length(rhs)
    A=lhs(k); B=rhs(i);
    if abs(A-B)<=0.001
        Rz(k)=RR(i);
        break
    end; end; end

%Rz is the output radius coordinates that would normally be a function
of
%the input radius coordinates
```

```
%%%%%----------------------------------------------------------------
%%%%%

  R_zfit= fit(r_,Rz','splineinterp');  %creating a fit function for Rz
and r

 R_z=@(rz) [R_zfit(rz)];
 dzdr= @(rz,z) [(R_z(rz)-rz)./((nl-1).*(z0-z))];

 Tspan=linspace(0,r0,num-floor(num/2))'; %Tspan see help ode45

 %differential eq function in matlab to solve for z(r) based on Snell's
law
 [rz,z]=ode45(dzdr, Tspan, 0);

 %%%%%%%%-----fitting the z(r) values to a polynomial function----
%%%%%%%%
  %creating a full length z vector from -r0 to +r0
 z_base_fit=[fliplr(z') z(2:round(num/2))']';

 N=14; %polynomial order in which we wish to fit
 %create function to fit data to polynomial of order n
 z_fit= @(z_bc) polyfit(r_,z_bc,N);
    zfit=z_fit(z_base_fit);

 a14=zfit(1); a12=zfit(3); a10=zfit(5); a8=zfit(7); a6=zfit(9);
a4=zfit(11); a2=zfit(13);
 a2k=[a14 a12 a10 a8 a6 a4 a2]'; %create vector for a2k coefficients
```

```
% tilt_term.m
% tilt term generator
% Author: Jason Shultz
% Date: 05/04/15

function [tilt]=tilt_term(x,zf,c_limit)
c0=[0:.0001:c_limit]'; %create tilt term array

k=1;

while 1
   sag_b=(max(max(zf+c0(k)*x)))-(min(min(zf+c0(k)*x)));
   sag_a=(max(max(zf+c0(k+1)*x)))-(min(min(zf+c0(k+1)*x)));
        if sag_b<sag_a
            break
        end
      k=k+1;
end

tilt=c0(max(k));
```

A.1.2 Shifted focus Alvarez: freeform surface coefficient generator

```
% shifted_focus_alvarez_for_dissertation.m
% Shifted focus Alvarez design in IR26
% Author: Jason Shultz
% Date: 03/14/16
clear all
%---------------all units in millimeters------------
%Base Parameters
z0=77;       %focal length
nl=2.7943;   %refractive index for IRG26
r0=7.25;     %lens radius
max_d=1.8;   %maximum lateral shift
min_f_at_max_d=38.26; %mininum focal length at maximum shift
num=81;      %number of points in this analysis (keep odd)

%%%%%%%%--------develop composite surfaces------%%%%%%%%%%
z05=500000; %close to infinte
z04=2*z05*z0/(z05+z0);
z03=z0;
z02=(z03*z04)/(2*z04-z03);
z01=(z02*z03)/(2*z03-z02);

%------focal length at d=1.8mm--------
a2k_1=curvefit_alvarez(r0,z01,nl,num);

%------focal length at d=0.9mm--------
a2k_2=curvefit_alvarez(r0,z02,nl,num);

%------focal length at d=0mm--------
a2k_3=curvefit_alvarez(r0,z03,nl,num);

%------focal length at d=-0.9mm--------
a2k_4=curvefit_alvarez(r0,z04,nl,num);

%------focal length at d=-1.8mm--------
a2k_5=curvefit_alvarez(r0,z05,nl,num);

%-----------------determine b2k coefficients---------------
                    %b2k=dela2k/(2deld)
del_a2k_avg=((a2k_1-a2k_2)+(a2k_2-a2k_3)+(a2k_3-a2k_4)+(a2k_4-
a2k_5))./4;

b2k=del_a2k_avg./(2*(max_d/2));

a2k=[a2k_3(1) a2k_3(2) a2k_3(3) a2k_3(4) a2k_3(5) a2k_3(6) a2k_3(7)]';

a_surface_coeffs_2_14=fliplr(a2k')'
b_surface_coeffs_2_14=fliplr(b2k')'
focal_range=[z01 z02 z03 z04 z05]'
```

```
%---------------determine tilt for lowest sag on freeform surface------
----
c_limit=.2;
tilt=tilt_term(a2k,b2k,c_limit,r0)


%-------------------generate freeform surfaces-----------------
%-------------------circular plot for surface----------------------
pts=291;
r1 = linspace(0,r0,pts);    % radius array for plotting actual surface
th1 = linspace(0,2*pi,pts);  % theta array for plotting

%Define the r and th grids
[r,th] = meshgrid(r1,th1);
[x,y] = pol2cart(th,r);

%define a2k, and b2ks explicitly
a2=a2k(7); a4=a2k(6); a6=a2k(5); a8=a2k(4); a10=a2k(3); a12=a2k(2);
a14=a2k(1);
b2=b2k(7); b4=b2k(6); b6=b2k(5); b8=b2k(4); b10=b2k(3); b12=b2k(2);
b14=b2k(1);

%individual terms for variable component function
b2xy = (1/3)*(x.^3) + x.*(y.^2);
b4xy = (1/5)*(x.^5) + (2/3)*(x.^3).*(y.^2) + x.*(y.^4);
b6xy = (1/7)*(x.^7) + (3/5)*(x.^5).*(y.^2) + (x.^3).*(y.^4) +
x.*(y.^6);
b8xy = (1/9)*(x.^9) + (4/7)*(x.^7).*(y.^2) + (6/5)*(x.^5).*(y.^4) +
(4/3)*(x.^3).*(y.^6) + x.*(y.^8);
b10xy = (1/11)*(x.^11) + (5/9)*(x.^9).*(y.^2) + (10/7)*(x.^7).*(y.^4) +
2*(x.^5).*(y.^6) + (5/3)*(x.^3).*(y.^8) + x.*(y.^10);
b12xy = (1/13)*(x.^13) + (6/11)*(x.^11).*(y.^2) + (5/3)*(x.^9).*(y.^4)
+ (20/7)*(x.^7).*(y.^6) + 3*(x.^5).*(y.^8) + 2*(x.^3).*(y.^10) +
x.*(y.^12);
b14xy = (1/15)*(x.^15) + (7/13)*(x.^13).*(y.^2) +
(21/11)*(x.^11).*(y.^4) + (35/9)*(x.^9).*(y.^6) + (35/7)*(x.^7).*(y.^8)
+ (21/5)*(x.^5).*(y.^10) + (7/3)*(x.^3).*(y.^12) + x.*(y.^14);

r = sqrt((x.^2) + (y.^2)); %converting coordinates for brevity
fb=(a2*r.^2 + a4*r.^4 + a6*r.^6 + a8*r.^8 + a10*r.^10 + a12*r.^12 +
a14*r.^14)./2; %function for base component
fv=b2*b2xy + b4*b4xy + b6*b6xy + b8*b8xy + b10*b10xy + b12*b12xy +
b14*b14xy+tilt*x; %function for variable component


fs=fb+fv; %freeform surface
sag_freeform=abs(max(max(fs))-min(min(fs)))
%%
figure(1)
surf(x,y,fb), shading interp, colorbar, view(-45,50) %plot of base
component
xlabel('x(mm)'),ylabel('y(mm)'),zlabel('z(mm)'), title('Base
Component'), xlim([-7.5 7.5]), ylim([-7.5 7.5])
colormap('jet')
figure(2)
```

```
surf(x,y,fv), shading interp, colorbar, view(-45,50) %plot of variable
component
xlabel('x(mm)'),ylabel('y(mm)'),zlabel('z(mm)'),title('Variability
Component'),xlim([-7.5 7.5]),ylim([-7.5 7.5]),zlim([-0.125 .125])
colormap('jet')
figure(3)
surf(x,y,fs), shading interp, colorbar, view(-45,50) %plot of freeform
surface
xlabel('x(mm)'),ylabel('y(mm)'),zlabel('z(mm)'),title('Freeform
Surface'),xlim([-7.5 7.5]),ylim([-7.5 7.5]), zlim([-0.2 .1])
colormap('jet')


% curvefit_alvarez.m
function [a2k] = curvefit_alvarez(r0,z0,nl,num)
% composite surface design-shifted focus Alvarez
% Author: Jason Shultz
% Date: 03/14/16
%------this function will be called later in program-----
r=linspace(-r0,r0,num)'; %input radius vector

%equation relating r and R for ode45
 R_z= @(rz) 0; %focusing lens

 dzdr= @(rz,z) (R_z(rz)-rz)./((nl-1).*(z0-z));
 [rz,z]=ode45(dzdr,[0 r0], 0);

%%%%%%%%-----fitting the z(r) values to a polynomial function----
%%%%%%%%
%creating a full length z vector from -r0 to +r0
 z_base_fit=[fliplr(z') z(2:round(num/2))']';

 N=14; %polynomial order in which we wish to fit
%create function to fit data to polynomial of order n
 z_fit= @(z_bc) polyfit(r,z_bc,N);
    zfit=z_fit(z_base_fit);

 a14=zfit(1); a12=zfit(3); a10=zfit(5); a8=zfit(7); a6=zfit(9);
a4=zfit(11); a2=zfit(13);
 a2k=[a14 a12 a10 a8 a6 a4 a2]'; %create vector for a2k coefficients


% tilt_term.m
% shifted focus alvarez tilt term
% Author: Jason Shultz
% Date: 03/14/16
%------this function will be called later in program-----
function [tilt]=tilt_term(a2k,b2k,c_limit,r0)
%------------------define x and y grid----------------------
%preferred method
pts=291;
r1 = linspace(0,r0,pts);    % radius array for plotting actual surface
th1 = linspace(0,2*pi,pts);  % theta array for plotting

%Define the r and th grids
```

```
[r,th] = meshgrid(r1,th1);
[x,y] = pol2cart(th,r);

%define a2k, and b2ks explicitly
a2=a2k(7); a4=a2k(6); a6=a2k(5); a8=a2k(4); a10=a2k(3); a12=a2k(2);
a14=a2k(1);
b2=b2k(7); b4=b2k(6); b6=b2k(5); b8=b2k(4); b10=b2k(3); b12=b2k(2);
b14=b2k(1);

%individual terms for variable component function
b2xy = (1/3)*(x.^3) + x.*(y.^2);
b4xy = (1/5)*(x.^5) + (2/3)*(x.^3).*(y.^2) + x.*(y.^4);
b6xy = (1/7)*(x.^7) + (3/5)*(x.^5).*(y.^2) + (x.^3).*(y.^4) +
x.*(y.^6);
b8xy = (1/9)*(x.^9) + (4/7)*(x.^7).*(y.^2) + (6/5)*(x.^5).*(y.^4) +
(4/3)*(x.^3).*(y.^6) + x.*(y.^8);
b10xy = (1/11)*(x.^11) + (5/9)*(x.^9).*(y.^2) + (10/7)*(x.^7).*(y.^4) +
2*(x.^5).*(y.^6) + (5/3)*(x.^3).*(y.^8) + x.*(y.^10);
b12xy = (1/13)*(x.^13) + (6/11)*(x.^11).*(y.^2) + (5/3)*(x.^9).*(y.^4)
+ (20/7)*(x.^7).*(y.^6) + 3*(x.^5).*(y.^8) + 2*(x.^3).*(y.^10) +
x.*(y.^12);
b14xy = (1/15)*(x.^15) + (7/13)*(x.^13).*(y.^2) +
(21/11)*(x.^11).*(y.^4) + (35/9)*(x.^9).*(y.^6) + (35/7)*(x.^7).*(y.^8)
+ (21/5)*(x.^5).*(y.^10) + (7/3)*(x.^3).*(y.^12) + x.*(y.^14);

c0=[-c_limit:.0001:c_limit]';

r = sqrt((x.^2) + (y.^2)); %converting coordinates for brevity
fb=(a2*r.^2 + a4*r.^4 + a6*r.^6 + a8*r.^8 + a10*r.^10 + a12*r.^12 +
a14*r.^14)./2; %function for base component
fv=b2*b2xy + b4*b4xy + b6*b6xy + b8*b8xy + b10*b10xy + b12*b12xy +
b14*b14xy; %function for variable component

fs=fb+fv; %freeform surface

k=1;
while 1
   sag_b=abs(max(max(fs+c0(k)*x)))+abs(min(min(fs+c0(k)*x)));
   sag_a=abs(max(max(fs+c0(k+1)*x)))+abs(min(min(fs+c0(k+1)*x)));
   if k==4000
      break
   end
   if sag_b<sag_a
      break
   end
   k=k+1;
end
    tilt=c0(max(k)-1);
```

A.2 Beam shaper performance metrics

```
% BSspot_metric_for_dissertation.m
% Beam shaper output spot performance analysis
% Author: Jason Shultz
% Date: 11/25/16
clear all
fclose('all');

x0=1.5/2; %window size
y0=1.5/2;
n=512; %data points in spot window
X=linspace(-x0,y0,n);
Y=linspace(-y0,y0,n);
[x,y]=meshgrid(X,Y); %coordinate system
th=(atan2d(y,x)+180);
R=sqrt(x.^2+y.^2);

%%%%%%%%%%%%%%%% Reference %%%%%%%%%%%%%%%
%target output spot txt file
 filename=sprintf('target_ref_D1mm_042017_X01.5.txt');
 I_ref=load(filename);

 h=1/12*ones(4);h(1,1)=0;h(1,4)=0;h(4,1)=0;h(4,4)=0;
 I_ref=filter2(h,I_ref); %smooth results

[R_ref,Idiffref]=edge_finder(I_ref,7,n,x0,y0); %EFA

rfref=fit(linspace(0,360,length(R_ref))',smooth(R_ref),'linearinterp');
Iref_CA=zeros(n);
for u=1:n
    for w=1:n
        if R(u,w)<=(0.95*rfref(th(u,w)))
             Iref_CA(u,w)=I_ref(u,w);
        end,end,end

 %%
%%%%%%%%%%%%%%%% Results %%%%%%%%%%%%%%%%
N=2601; %number of files/spots to analyze
for i=1:N
  %load output spot
  filename=sprintf('ME_BS_D1mm_042017_%d.0000.txt',i);
  I1=load(filename);
  I1=filter2(h,I1); %smooth

 %%%% Shape deviation
  [R_1,Idiff1]=edge_finder(I1,7,n,x0,y0);
  RU(i)=sqrt(sum((R_1-mean(R_ref)).^2)/length(R_1));
  RU_CV(i)=RU(i)/mean(R_ref);
  Rsig(i)=std(smooth(R_1),1);
  RCV(i)=std(smooth(R_1),1)/mean(smooth(R_1));

%%%%%%%%%%%%%%%% clear aperture window analysis %%%%%%%%%%%%%%%%
%output spot radius as a function of theta
```

```
rf=fit(linspace(0,360,length(R_1))',smooth(R_1),'linearinterp');
I_CA=zeros(n);
ivec=0;I_vec=0;
for u=1:n
    for w=1:n
        if R(u,w)<=(0.95*rf(th(u,w)))
            ivec=ivec+1;
            I_CA(u,w)=I1(u,w);
            I_vec(ivec)=I1(u,w);
     end,end,end

 %%%% Correlation degree
  C_11i=trapz(trapz(I_ref.*I_ref));
  C_12i=trapz(trapz(I_ref.*I1));
  C_22i=trapz(trapz(I1.*I1));
  Cdi=C_12i./(sqrt(C_11i.*C_22i));
  C(i)=Cdi;
%%%% Correlation degree of the CA
  C_11i_CA=trapz(trapz(Iref_CA.*Iref_CA));
  C_12i=trapz(trapz(Iref_CA.*I_CA));
  C_22i=trapz(trapz(I_CA.*I_CA));
  Cdi_CA=C_12i./(sqrt(C_11i.*C_22i));
  C_CA(i)=Cdi_CA;

%%%% Spot uniformity
  Usig(i)=std(I_vec,1);
  UCV(i)=std(I_vec,1)/mean(I_vec);

end
%%
  Results=[RU' RU_CV' Rsig' RCV' Usig' UCV' C' C_CA'];
  save('ME_BS_results_042017_RU_RUCV_Rsig_RCV_Usig_UCV_C_CCA_1-
1301.txt','Results','-ascii');

%%


% edge_finder.m
function [R_1,Idiff1]=edge_finder(I_1,nroot,n,x0,y0)
% edge finding algorithm for output spot
% Author: Jason Shultz
% Date: 11/25/16

fclose('all');

I_1=nthroot(I_1,nroot);
 xd=linspace(-x0,x0,n); yd=xd; [Xd,Yd]=meshgrid(xd,yd);

Idiffx1=zeros(n,n);Idiffy1=Idiffx1;
for i=1:n-1
Idiffx1(i,[2:n])=(abs(diff(I_1(i,:))));
Idiffy1([1:(n-1)],i)=(abs(diff(I_1(:,i))));
end

Idiff1_=Idiffx1+Idiffy1;
```

```
Idiff1=zeros(n,n);
for i=1:n
    j=i;
     if i==1
         j=n;
     end
    Idiff1(:,i)=Idiff1_(:,j-1);
end
Idiff1=nthroot(Idiff1,1);

%%%%%%%%%%%%%%%%%%%% Raidus algorithm%%%%%%%%%%%%%%%%%%%%
err=.01;
th=linspace(0,2*pi-2*pi/200,200);

R_1=zeros(length(th),1);
for g=1:length(th)
    TH=zeros(n,n);
    for i=1:n-1
        for k=1:n-1
            th_d=atan2(Yd(i,k),Xd(i,k))+pi;
            if (th_d >= th(g)-err && th_d <= th(g)+err)
            TH(i,k)=1;
            end
        end
    end
    [pk1,loc1]=max(nthroot(slice_check_1,3));
    [pkx1,locx1]=max(pk1);
    locy1=loc1(locx1);

    R_1(g)=sqrt(Xd(locy1,locx1).^2+Yd(locy1,locx1).^2);
end
end
```

A.3 Optomechanical tolerancing

A.3.1 Error generation – pre simulation

```
% CEA_dev_gen.m
% error generation - pre simulation
% Author: Jason Shultz
% Date: 11/25/16

clear all

Smax=.01; %maximum displacement
Tmax=1.5; %maximum tilt
Rmax=.3;  %maximum rotational

%different orientations
Sx=[0 Smax/4  Smax/4 -Smax/4 -Smax/4 Smax/2  Smax/2 -Smax/2 -Smax/2
Smax*3/4  Smax*3/4 -Smax*3/4 -Smax*3/4 Smax  Smax -Smax -Smax];
Sy=[0 Smax/4 -Smax/4  Smax/4 -Smax/4 Smax/2 -Smax/2  Smax/2 -Smax/2
Smax*3/4 -Smax*3/4  Smax*3/4 -Smax*3/4 Smax -Smax  Smax -Smax];
Tx=[0 Tmax/4  Tmax/4 -Tmax/4 -Tmax/4 Tmax/2  Tmax/2 -Tmax/2 -Tmax/2
Tmax*3/4  Tmax*3/4 -Tmax*3/4 -Tmax*3/4 Tmax  Tmax -Tmax -Tmax];
Ty=[0 Tmax/4 -Tmax/4  Tmax/4 -Tmax/4 Tmax/2 -Tmax/2  Tmax/2 -Tmax/2
Tmax*3/4 -Tmax*3/4  Tmax*3/4 -Tmax*3/4 Tmax -Tmax  Tmax -Tmax];
Rz=[0  Rmax/4 -Rmax/4  Rmax/2 -Rmax/2  Rmax*3/4 -Rmax*3/4  Rmax -Rmax];

n=1;
for s=1:17
   sx1=Sx(s); sx2=-Sx(s);
   sy1=Sy(s); sy2=-Sy(s);
for t=1:17
   tx1=Tx(t); tx2=-Tx(t);
   ty1=Ty(t); ty2=-Ty(t);
for r=1:9
   rz1=Rz(r); rz2=-Rz(r);

   devs_list(n,:)=[n sx1 sx2 sy1 sy2 tx1 tx2 ty1 ty2 rz1 rz2];

n=n+1;
end,end,end

save('ME_BS_D1mm_devs_042017.txt','devs_list','-ascii')
```

A.3.2 Combined error analysis – post simulation

```
% CEA_results_analysis_for_dissertation.m
% Combined error analysis - post simulation
% Author: Jason Shultz
% Date: 11/25/16

clear all

devs=load('ME_BS_D1mm_devs_042017.txt');
results=load('ME_BS_results_042017_RU_RUCV_Rsig_RCV_Usig_UCV_C_CCA.txt'
);%.txt');%
Smax=.01; %max displacement
Tmax=1.5; %max tilt
Rmax=.3;  %max rotational

sx1=devs(:,2);
tx1=devs(:,6);
rz1=devs(:,10);
cs=ones(2601,1);ct=cs;cr=cs;%tolerance classes
%index the different tolerance classes
for i=1:2601
    if abs(sx1(i))==Smax/4
        cs(i)=2;
    elseif abs(sx1(i))==Smax/2
        cs(i)=3;
    elseif abs(sx1(i))==(Smax*3/4)
        cs(i)=4;
    elseif abs(sx1(i))==Smax
        cs(i)=5;
    end

    if abs(tx1(i))==Tmax/4
        ct(i)=2;
    elseif abs(tx1(i))==Tmax/2
        ct(i)=3;
    elseif abs(tx1(i))==(Tmax*3/4)
        ct(i)=4;
    elseif abs(tx1(i))==Tmax
        ct(i)=5;
    end

    if abs(rz1(i))==Rmax/4
        cr(i)=2;
    elseif abs(rz1(i))==Rmax/2
        cr(i)=3;
    elseif (abs(rz1(i))>Rmax/2 && abs(rz1(i))<Rmax)
        cr(i)=4;
    elseif abs(rz1(i))==Rmax
        cr(i)=5;
    end
end
ci=cs/10+ct/100+cr/1000;

u=1;
```

```
for i=1:5
    for j=1:5
        for k=1:5
           S(u)=(i-1)/4;
           T(u)=(j-1)/4;
           R(u)=(k-1)/4;
           C(u)=i/10+j/100+k/1000;
           CS(u)=i;
           CT(u)=j;
           CR(u)=k;

           w1=1;
           for w=1:2601
               if ci(w)==C(u)
                   temp_res(w1)=results(w,7);%/results(1,7);
                   temp_res_UCV(w1)=results(w,6);
                   temp_res_RCV(w1)=results(w,2);
                   temp_class(w1)=w;
                   w1=w1+1;
               end
           end
           [Cmin(u),Cloctemp]=min(temp_res);
           [UCVmin(u),Uloctemp]=max(temp_res_UCV);
           [RCVmin(u),Rloctemp]=max(temp_res_RCV);

            CN(u)=temp_class(Cloctemp);
            UN(u)=temp_class(Uloctemp);
            RN(u)=temp_class(Rloctemp);
           temp_res=0;
           temp_res_UCV=0;
           temp_res_RCV=0;
           u=u+1;
        end
    end
end
%%
u=1;
for i=1:5
    for k=1:5
        CS1(i,k)=Cmin(u);
        CS2(i,k)=Cmin(u+25);
        CS3(i,k)=Cmin(u+50);
        CS4(i,k)=Cmin(u+75);
        CS5(i,k)=Cmin(u+100);

        UCVS1(i,k)=UCVmin(u);
        UCVS2(i,k)=UCVmin(u+25);
        UCVS3(i,k)=UCVmin(u+50);
        UCVS4(i,k)=UCVmin(u+75);
        UCVS5(i,k)=UCVmin(u+100);

        RCVS1(i,k)=RCVmin(u);
        RCVS2(i,k)=RCVmin(u+25);
        RCVS3(i,k)=RCVmin(u+50);
        RCVS4(i,k)=RCVmin(u+75);
        RCVS5(i,k)=RCVmin(u+100);
```

```
        u=u+1;
    end
end

%%%%%%%%%%%%%%%%%%%%%%%%%%%%%%%%%%%%%%%%%%%%%%%%%%%%%%%%%%%%%%%%%%%%%%%%
%%%
%%%%%%%%%%%%%%%%%%%%%%% colormap and alphamap
%%%%%%%%%%%%%%%%%%%%%%%%%%%%
%%%%%%%%%%%%%%%%%%%%%%%%%%%%%%%%%%%%%%%%%%%%%%%%%%%%%%%%%%%%%%%%%%%%%%%%
%%%
  cmap=[linspace(1,1,50)' linspace(0,.75,50)' zeros(50,1)
        linspace(1,0,50)' linspace(1,1,50)' zeros(50,1)];

  cmap2=[linspace(0,1,400)' linspace(1,1,400)' zeros(400,1)
      linspace(1,1,600)' linspace(0.75,0,600)' zeros(600,1)];

  cmap3=[linspace(0,1,400)' linspace(1,1,400)' zeros(400,1)
      linspace(1,1,600)' linspace(0.75,0,600)' zeros(600,1)];

    amap=linspace(min(Cmin),1,1000);%linspace(.00,.00,773)
linspace(1,1,1000-773)];/max(Cmin)
    amapU1=linspace(min(UCVmin),1,1000);
    amapR1=linspace(min(RCVmin),1,1000);
    for i=1:1000
        if amap(i)>=0.90
            amap(i)=1;%amap(i);
        else amap(i)=0;
        end

        if amapU1(i)<=0.15
            amapU(i)=1;
        else amapU(i)=0;
        end

        if amapR1(i)<0.149
            amapR(i)=1;
        else amapR(i)=0;
        end
    end

    rot_=[0,.1,.2,.3,.4];
    tilt_=[0, 1, 2, 3, 4];
    shift_=[0, .0025, .005, .0075, 0.01];
    [rot,tilt]=meshgrid(rot_,tilt_);


%%%%%%%%%%% Interpolation %%%%%%%%%%%%%%%

[CR_,CT_,CS_]=meshgrid((0:4)*Rmax/4,(0:4)*Tmax/4,(0:4)*Smax/4);
Cmin_(:,:,1)=CS1;Cmin_(:,:,2)=CS2;Cmin_(:,:,3)=CS3;Cmin_(:,:,4)=CS4;Cmi
n_(:,:,5)=CS5;

[crq,ctq,csq]=meshgrid((0:.1:4)*Rmax/4,(0:.1:4)*Tmax/4,(0:.1:4)*Smax/4)
;
cminq=interp3(CR_,CT_,CS_,Cmin_,crq,ctq,csq);
```

```
UCVmin_(:,:,1)=UCVS1;UCVmin_(:,:,2)=UCVS2;UCVmin_(:,:,3)=UCVS3;UCVmin_(
:,:,4)=UCVS4;UCVmin_(:,:,5)=UCVS5;
UCVminq=interp3(CR_,CT_,CS_,UCVmin_,crq,ctq,csq);

RCVmin_(:,:,1)=RCVS1;RCVmin_(:,:,2)=RCVS2;RCVmin_(:,:,3)=RCVS3;RCVmin_(
:,:,4)=RCVS4;RCVmin_(:,:,5)=RCVS5;
RCVminq=interp3(CR_,CT_,CS_,RCVmin_,crq,ctq,csq);

%%%%%%%%%%% Slices %%%%%%%%%%%%%%%
sx=[3.5 3 2.5 2 1.5 1 .5 0.001]*Rmax/4;
sy=[3.5 3 2.5 2 1.5 1 .5 0.001]*Tmax/4;
sz=[3.5 3 2.5 2 1.5 1 .5 0.001]*Smax/4;


figure(1)
slice(CR_,CT_,CS_,Cmin_,[0 .2],0,0)
xlabel('Z Axis Rotation (deg)'),ylabel('X-Y Axis Tilt
(deg)'),zlabel('X-Y Lateral Shift (mm)')
colormap(cmap),caxis([0.85,1]),view(157,62),
c=colorbar;c.Label.String='Correlation Degree';

%%
figure(2)
p1a=slice(crq,ctq,csq*1000,cminq,sx,sy,sz*1000);

set(p1a,'EdgeColor','none','EdgeAlpha','interp','AlphaDataMapping','sca
led','FaceColor','interp','FaceAlpha','interp')
       alpha('color'),alphamap(amap)
    hold on
p1b=slice(crq,ctq,csq*1000,cminq,0,0,0);
    set(p1b,'EdgeColor','none','FaceColor','interp')
       alpha(p1b,.75)
    hold off
        xlabel('Rotational (deg)'),ylabel('Tilt
(deg)'),zlabel('Displacement (um)')

colormap(cmap),caxis([0.80,1]),c=colorbar;c.Label.String='Correlation
Degree';
        view(143,34),ylim([0 Tmax]),xlim([0 Rmax]),zlim([0 Smax*1000])

 figure(3)
p1aU=slice(crq,ctq,csq*1000,UCVminq,sx,sy,sz*1000);

set(p1aU,'EdgeColor','none','EdgeAlpha','interp','AlphaDataMapping','sc
aled','FaceColor','interp','FaceAlpha','interp')
       alpha('color'),alphamap(amapU)
    hold on
p1bU=slice(crq,ctq,csq*1000,UCVminq,0,0,0);
    set(p1bU,'EdgeColor','none','FaceColor','interp')
       alpha(p1bU,.75)
    hold off
        xlabel('Rotational (deg)'),ylabel('Tilt
(deg)'),zlabel('Displacement (um)')
```

```
colormap(cmap2),c=colorbar;caxis([0.05,0.3]);c.Label.String='Uniformity
Error CV';
        view(143,34),ylim([0 Tmax]),xlim([0 Rmax]),zlim([0 Smax*1000])

 figure(4)
p1aR=slice(crq,ctq,csq*1000,RCVminq,sx,sy,sz*1000);

set(p1aR,'EdgeColor','none','EdgeAlpha','interp','AlphaDataMapping','sc
aled','FaceColor','interp','FaceAlpha','interp')
       alpha('color'),alphamap(amapR)
    hold on
p1bR=slice(crq,ctq,csq*1000,RCVminq,0,0,0);
    set(p1bR,'EdgeColor','none','FaceColor','interp')
       alpha(p1bR,.75)
    hold off
        xlabel('Rotational (deg)'),ylabel('Tilt
(deg)'),zlabel('Displacement (um)')
%

colormap(cmap3),caxis([0.05,0.3]),c=colorbar;c.Label.String='Shape
Error CV';
        view(143,34),ylim([0 Tmax]),xlim([0 Rmax]),zlim([0 Smax*1000])
```

A.4 Surface form tolerancing

A.4.1 Surface form error generation (combined height and slope scale) – pre simulation

```
% Beam shaper: combined_scales_form_error_generator_for_dissertation.m
% Surface form error generation (combined height and slope scale) - pre
simulation
% Author: Jason Shultz
% Date: 2/21/17

clear all
fclose('all');

%load reference surface
Z_freeform_L1=load('BS_reference_surface.txt');
Zref=Z_freeform_L1;

nx=301;nxf=299; %number of data points in surface
r=linspace(-6,6,nx);%radial vector
x(2:nx+1)=r;
delx=abs(r(1)-r(2));
x(1)=-6-delx;
x(nx+2)=6+delx;

[X,Y]=meshgrid(r,r);
X=X+7.25*0; Y=Y+7.25*0;
R=sqrt(X.^2+Y.^2);
 th=atan2(Y,X);

%%create aperture
 aperture14mm=ones(nx,nx);
 R_=sqrt((X-7.25*0).^2+(Y-7.25*0).^2);
for i=1:(nx)
    for k=1:(nx)
        if R_(i,k)>6
            aperture14mm(i,k)=0;
        end
    end
end

Zref_max=max(max(Zref.*aperture14mm));
Zref_min=min(min(Zref.*aperture14mm));
diff=abs(Zref_min)-Zref_max;
Zref=Zref+diff/2;

[FX,FY]=gradient(Zref);
dzdx_ref=FX/delx;
dzdy_ref=FY/delx;

dzdth=R.*(-dzdx_ref.*sin(th)+dzdy_ref.*cos(th));
dzdr_ref=sqrt(dzdx_ref.^2+dzdy_ref.^2);

maxdzdr=max(max(abs(dzdr_ref.*aperture14mm)));
```

```
maxdzdrth=atan(maxdzdr);


%%%%deviated surfaces
slope=linspace(-.0018,.006,21);
scale=linspace(-.05,.02,21);

m=0;
tic
for u=1:21
     for v=1:21
m=m+1
for ii=1:nx
    for ki=1:nx
        offset=(abs(dzdr_ref(ii,ki))/maxdzdr)^2*slope(u);
        Z_1(ii,ki)=Zref(ii,ki)*(1+scale(v))+offset;
    end
end

errdiff(m)=max(max(abs(Z_1-Zref).*aperture14mm));

PV_baseR(m)=max(max(abs(Zref-Z_1).*aperture14mm));
rms_baseR(m)=rmse(zeros(nx,nx),(Z_1-Zref).*aperture14mm);
PV_irreg(m)=max(max(abs(Z_1-Zref*(1+scale(v))).*aperture14mm));
rms_irreg(m)=rmse(zeros(nx,nx),(Z_1-Zref*(1+scale(v))).*aperture14mm);

Z_2=-Z_1(:,nx:-1:1);

%%%%%%%%%%%%%%%%%%_____data file for L1_____%%%%%%%%%%%%%
      % nx ny delx dely unitflag xdec ydec
      % z dz/dx dz/dy d2z/dxdy nodata
%  k=1;
  first_line=[nxf nxf delx delx 0 0 0];
%   filename=sprintf('SA_Alvarez_L1_scaleoffset_%d.dat',m);
  filename=sprintf('FE_BS_SA_combined_scale_051017_L1_%d.dat',m);

  fid=fopen(filename,'w');
  fprintf(fid,'%f %f %f %f %f %f %f \r\n',first_line);

  for j=2:nxf+1
  for i=2:nxf+1
          dzdx=(Z_1(j,i+1)-Z_1(j,i-1))/(delx*2);
          dzdy=(Z_1(j-1,i)-Z_1(j+1,i))/(delx*2);
          d1dxy=(Z_1(j-1,i+1)-Z_1(j-1,i-1))/(delx*2);
          d2dxy=(Z_1(j+1,i+1)-Z_1(j+1,i-1))/(delx*2);
          dzdxy=(d1dxy-d2dxy)/(delx*2);
  next_line=[Z_1(j,i) dzdx dzdy dzdxy];
  fprintf(fid,'%f %f %f %f \r\n',next_line);
  end
  end

 fclose(fid);

%%%%%%%%%%%%%%%%%%_____data file for L2_____%%%%%%%%%%%%%
  first_line=[nxf nxf delx delx 0 0 0];
```

```
%   filename=sprintf('SA_Alvarez_L2_scaleoffset_%d.dat',m);
  filename=sprintf('FE_BS_SA_combined_scale_051017_L2_%d.dat',m);

  fid=fopen(filename,'w');
  fprintf(fid,'%f %f %f %f %f %f %f \r\n',first_line);

  for j=2:nxf+1
  for i=2:nxf+1
          dzdx=(Z_2(j,i+1)-Z_2(j,i-1))/(delx*2);
          dzdy=(Z_2(j-1,i)-Z_2(j+1,i))/(delx*2);
          d1dxy=(Z_2(j-1,i+1)-Z_2(j-1,i-1))/(delx*2);
          d2dxy=(Z_2(j+1,i+1)-Z_2(j+1,i-1))/(delx*2);
          dzdxy=(d1dxy-d2dxy)/(delx*2);
  next_line=[Z_2(j,i) dzdx dzdy dzdxy];
  fprintf(fid,'%f %f %f %f \r\n',next_line);
  end
  end

fclose(fid);

HS(m)=scale(v);
SS(m)=slope(u);
toc
     end
end
toc
dev_index=[[1:m]' HS' SS' PV_baseR' rms_baseR' PV_irreg' rms_irreg'];
save('FE_BS_SA_combined_scale_051017_dev_index.txt','dev_index','-
ascii');
```

A.4.2 Combined error analysis – post simulation

```
% BS_FE_combined_error_results_for_dissertation.m
% Beam shaper: Combined error analysis - post simulation
% Author: Jason Shultz
% Date: 2/21/17

clear all
fclose('all');

devs=load('FE_BS_SA_combined_scale_051017_dev_index.txt');
results=load('FE_BS_combined_error_results_D1mm_051017_N_RU_RUCV_Rsig_R
CV_Usig_UCV_C_CCA.txt');
m=0;
for i=1:21
    for k=1:21
        m=m+1;
        HS(i,k)=devs(m,2);
        SS(i,k)=devs(m,3)*0.10977^2;
        PVbase(i,k)=devs(m,4);
        rmsbase(i,k)=devs(m,5);
        PVI(i,k)=devs(m,6);
        rmsI(i,k)=devs(m,7);

        UCV(i,k)=results(m,7);
        RCV(i,k)=results(m,3);
        C(i,k)=results(m,8);
        C_passed(i,k)=C(i,k);
        if C(i,k)<0.9
            C_passed(i,k)=0;
        end
    end
end

%%%%custom colormap%%%%
  cmap=[linspace(1,1,667)' linspace(0,.75,667)' zeros(667,1)
        linspace(1,0,333)' linspace(1,1,333)' zeros(333,1)];

  cmap2=[linspace(0,1,500)' linspace(1,1,500)' zeros(500,1)
         linspace(1,1,500)' linspace(0.75,0,500)' zeros(500,1)];

figure(1)
surf(HS,SS*-1,C)
ylabel('Slope Scale'),xlabel('Height Scale'),zlabel('Correlation
Degree')
colormap(cmap),caxis([0.7 1]),shading
interp,alpha(.8),set(gca,'GridAlpha',1)
c=colorbar;c.Label.String='Correlation Degree';
axis square,grid on,view(0,90)
xlim([-0.0,.011]),ylim([-0.00,0.000017])


figure(2)
surf(HS,SS,UCV)
```

```
axis square,grid on,colormap(cmap2),caxis([0 .3]),colorbar,shading
interp
xlim([-0.012,.012]),ylim([-0.0014,0.0014])
ylabel('Slope Scale'),xlabel('Height Scale')

figure(3)
surf(HS,SS,RCV)
axis square,grid on,colormap(cmap2),caxis([0 .3]),colorbar,shading
interp
xlim([-0.012,.012]),ylim([-0.0014,0.0014])
ylabel('Slope Scale'),xlabel('Height Scale')

figure(4)
 PVI(6:21,:)=PVI(6:21,:)*-1;
surf(HS*100,PVI*1000,RCV)
ylabel('Irregularity PV (um)'),xlabel('Power Percentage
(%)'),zlabel('Shape Deviation CV')
colormap(cmap2),caxis([0 .3]),colorbar,shading
interp,alpha(.8),set(gca,'GridAlpha',1)
c=colorbar;c.Label.String='Shape Deviation CV';
 xlim([-0.00,1.1]),ylim([0,1.4]),view(0,90) ,axis square

figure(5)
surf(HS*100,PVI*1000,UCV)
ylabel('Irregularity PV (um)'),xlabel('Power Percentage
(%)'),zlabel('Uniformity CV')
colormap(cmap2),caxis([0 .3]),colorbar,shading
interp,alpha(.8),set(gca,'GridAlpha',1)
c=colorbar;c.Label.String='Uniformity CV';
 xlim([-0.00,1.1]),ylim([0,1.4]),view(0,90),axis square

figure(6)
%  PVI(6:21,:)=PVI(6:21,:)*-1;
surf(HS,PVI*1000,C)
ylabel('Irregularity PV (um)'),xlabel('Height
Scale'),zlabel('Correlation Degree')
colormap(cmap),caxis([0.7 1]),colorbar,shading
interp,alpha(.8),set(gca,'GridAlpha',1)
c=colorbar;c.Label.String='Correlation Degree';
 xlim([-0.00,.011]),ylim([0,1.4]),view(0,90),axis square
```

APPENDIX B: LIST OF PEER-REVIEWED PUBLICATIONS, CONFERENCE PROCEEDINGS, AND PATENTS

[1] T. J. Suleski, **J. Shultz**, and P. J. Smilie, "Design of Dynamic Freeform Optics," in Renewable Energy and the Environment, OSA Technical Digest (online), paper FW2B.2, Optical Society of America, 2013.

[2] M. Liu, **J. Shultz**, J. Owen, M. Davies, T. J. Suleski, "Moth's eye anti-reflection gratings on germanium freeform surfaces," Proc. SPIE 9192, Current Developments in Lens Design and Optical Engineering XV, 91920L, September, 2014.

[3] **J. Shultz**, P. J. Smilie, B. Dutterer, M. Davies, T. J. Suleski, "Experimental characterization of variable output refractive beamshapers using freeform elements," Proc. SPIE 9194, Laser Beam Shaping XV, 91940M, September, 2014.

[4] T. J. Suleski, **J. Shultz**, P. J. Smilie, "Dynamic beam shaping with freeform optics," Proc. SPIE 9194, Laser Beam Shaping XV, 91940K, September, 2014.

[5] P. J. Smilie, **J. Shultz**, and T. J. Suleski, "Dynamic laser beam shaping methods and systems", U. S. Patent No. 9,238,577 (2015).

[6] **J. Shultz**, M. Davies, and T. J. Suleski, "Effects of MSF errors on performance of freeform optics: Comparison of diamond turning and diamond milling," in Imaging and Applied Optics 2015, OSA Technical Digest (online), paper FT4B.3, Optical Society of America, 2015.

[7] J. Troutman, D. Barnhardt, **J. Shultz**, J. Owen, M. Davies and T. J. Suleski, "Pre-process error mapping and correction for ultraprecision manufacturing of freeform optics by slow tool servo," in 7th CIRP Conference on High Performance Cutting, Accepted, Chemnitz, Germany, 2016.

[8] **J. Shultz**, H. Aryan, J. Owen, M. Davies, and T. J. Suleski, "Impacts of sub-aperture manufacturing techniques on the performance of freeform optics," Proc. ASPEN/ASPE Topical Meeting, Manufacture and Metrology of Structured and Freeform Surfaces for Functional Applications, 2017.

[9] **J. Shultz**, P. Smilie, M. Davies, and T. J. Suleski, "Optomechanical tolerancing of dynamic freeform optical systems," Proc. ASPEN/ASPE Topical Meeting, Manufacture and Metrology of Structured and Freeform Surfaces for Functional Applications, 2017.

[10] **J. Shultz**, M. Davies, and T. J. Suleski, "Simplified tolerancing of alignment errors in dynamic freeform optical systems," in Optical Design and Fabrication 2017, paper JTh1C.3, Optical Society of America, 2017.

[11] **J. Shultz**, and T. J. Suleski, "Design of a variable toric lens using laterally shifted freeform elements," in Optical Design and Fabrication 2017, paper JW2C.2, Optical Society of America, 2017.